Novel three-dimensional nanostructured carbon materials as electrocatalyst support in low-temperature fuel cells

by

Ayyappan Elangovan

B.Tech., CSIR-Central Electrochemical Research Institute, 2015

AN ABSTRACT OF A DISSERTATION

submitted in partial fulfillment of the requirements for the degree

DOCTOR OF PHILOSOPHY

Department of Chemistry
College of Arts and Sciences

KANSAS STATE UNIVERSITY
Manhattan, Kansas

2020

Abstract

Human sustainability and fossil fuel depletion are driving the demand for alternative energy sources. Low-temperature fuel cells (LTFCs) can be an alternative sustainable energy source owing to their high energy conversion efficiency, environmental friendliness, and ability to use renewable fuels. Despite the success, the high cost, poor durability, and susceptibility to fuel poison of the Pt-based electrocatalysts limit the widespread applications of LTFCs. Therefore, numerous efforts have been devoted to developing novel nanostructured carbon materials as electrocatalyst support to address the issues faced by the commercial Pt-based catalysts. This research focuses on a unique three-dimensional carbon support in this direction.

In the first approach, a systematic study has been carried out on oxygen reduction reaction (ORR) with ion-beam sputtered Pt catalyst (at Pt loadings of 6.5 – 43.0 μg cm^{-2}) on a vertically aligned carbon nanofiber (VACNF) array, consisting of conically stacked graphitic microstructures. Rotating disk electrode (RDE) studies reveal that thick 3D architecture of VACNFs exhibits enhanced limiting current density that deviates from the Levich equation for conventional thin-film catalysts. Nevertheless, useful information can be derived from RDE experiments with such systems. Molecular models representing VACNFs have been constructed to explore their capability as catalyst supports for ORR. Platinum atoms form strong bonds at the open graphitic edges in VACNFs, corroborating the role of VACNF in stabilizing Pt. Density Functional Theory (DFT) calculations further elucidate the two-electron and four-electron ORR pathways on the bare VACNF and Pt/VACNF catalysts, respectively. Furthermore, the Pt/VACNF catalysts show enhanced tolerance to methanol oxidation and a higher ability to recover from carbon monoxide poisoning in comparison to the benchmark Pt/C catalysts.

Following the success of VACNFs for the ORR, in the second approach, the role of additional nitrogen doping into the three-dimensional VACNF array by NH_3 plasma annealing in improving the durability of the Pt catalysts towards the ORR has been explored. The additional nitrogen present in N-VACNF support enhances the metal-support interaction which helps in reducing the Pt particle size from 3.1 nm to 2.3 nm. Pt/N-VACNF catalyst shows better durability when compared to the Pt/VACNF and Pt/C with similar Pt loading. DFT calculations validate the increase in stability of the Pt NPs with an increase in pyridinic N and illustrate the molecular ORR pathway for Pt/N-VACNF. Moreover, the Pt/N-VACNF catalyst is also found to have an enhanced tolerance towards the methanol crossover.

In the third approach, the role of three-dimensionally architectured in-situ N-doped VACNFs as a catalyst support for methanol oxidation reaction (MOR) has been studied in acidic and alkaline media. The abundant graphitic edge sites at the sidewall of N-doped VACNF strongly anchor the deposited platinum group metal (PGM) catalysts and induce a partial electron transfer between the PGM catalysts and support. DFT calculations reveal that the strong metal-support interaction substantially increases the adsorption energy of OH, particularly near the N-doping sites, which helps to compete and remove the adsorbed intermediate species generated during MOR. The PGM catalysts on N-doped VACNF support exhibit CO stripping at lower potentials comparing to the commercial Vulcan carbon support and present an enhanced electrocatalytic performance and better durability for MOR.

Novel three-dimensional nanostructured carbon materials as electrocatalyst support in low-temperature fuel cells

by

Ayyappan Elangovan

B.Tech., CSIR-Central Electrochemical Research Institute, 2015

A DISSERTATION

submitted in partial fulfillment of the requirements for the degree

DOCTOR OF PHILOSOPHY

Department of Chemistry
College of Arts and Sciences

KANSAS STATE UNIVERSITY
Manhattan, Kansas

2020

Approved by:

Major Professor

Dr. Jun Li.

Copyright

Abstract

Human sustainability and fossil fuel depletion are driving the demand for alternative energy sources. Low-temperature fuel cells (LTFCs) can be an alternative sustainable energy source owing to their high energy conversion efficiency, environmental friendliness, and ability to use renewable fuels. Despite the success, the high cost, poor durability, and susceptibility to fuel poison of the Pt-based electrocatalysts limit the widespread applications of LTFCs. Therefore, numerous efforts have been devoted to developing novel nanostructured carbon materials as electrocatalyst support to address the issues faced by the commercial Pt-based catalysts. This research focuses on a unique three-dimensional carbon support in this direction.

In the first approach, a systematic study has been carried out on oxygen reduction reaction (ORR) with ion-beam sputtered Pt catalyst (at Pt loadings of 6.5 – 43.0 µg cm^{-2}) on a vertically aligned carbon nanofiber (VACNF) array, consisting of conically stacked graphitic microstructures. Rotating disk electrode (RDE) studies reveal that thick 3D architecture of VACNFs exhibits enhanced limiting current density that deviates from the Levich equation for conventional thin-film catalysts. Nevertheless, useful information can be derived from RDE experiments with such systems. Molecular models representing VACNFs have been constructed to explore their capability as catalyst supports for ORR. Platinum atoms form strong bonds at the open graphitic edges in VACNFs, corroborating the role of VACNF in stabilizing Pt. Density Functional Theory (DFT) calculations further elucidate the two-electron and four-electron ORR pathways on the bare VACNF and Pt/VACNF catalysts, respectively. Furthermore, the Pt/VACNF catalysts show enhanced tolerance to methanol oxidation and a higher ability to recover from carbon monoxide poisoning in comparison to the benchmark Pt/C catalysts.

Following the success of VACNFs for the ORR, in the second approach, the role of additional nitrogen doping into the three-dimensional VACNF array by NH_3 plasma annealing in improving the durability of the Pt catalysts towards the ORR has been explored. The additional nitrogen present in N-VACNF support enhances the metal-support interaction which helps in reducing the Pt particle size from 3.1 nm to 2.3 nm. Pt/N-VACNF catalyst shows better durability when compared to the Pt/VACNF and Pt/C with similar Pt loading. DFT calculations validate the increase in stability of the Pt NPs with an increase in pyridinic N and illustrate the molecular ORR pathway for Pt/N-VACNF. Moreover, the Pt/N-VACNF catalyst is also found to have an enhanced tolerance towards the methanol crossover.

In the third approach, the role of three-dimensionally architectured in-situ N-doped VACNFs as a catalyst support for methanol oxidation reaction (MOR) has been studied in acidic and alkaline media. The abundant graphitic edge sites at the sidewall of N-doped VACNF strongly anchor the deposited platinum group metal (PGM) catalysts and induce a partial electron transfer between the PGM catalysts and support. DFT calculations reveal that the strong metal-support interaction substantially increases the adsorption energy of OH, particularly near the N-doping sites, which helps to compete and remove the adsorbed intermediate species generated during MOR. The PGM catalysts on N-doped VACNF support exhibit CO stripping at lower potentials comparing to the commercial Vulcan carbon support and present an enhanced electrocatalytic performance and better durability for MOR.

Table of Contents

List of Figures

List of Tables

List of Schemes

Acknowledgements

Ph.D. journey is a strenuous climb of resilience and perseverance. Reaching the finishing line is not possible without the support, guidance, and encouragement from the professors, supporting staff, friends, and families. I want to express my deepest gratitude to all the following people.

First and foremost, I would like to express my sincere gratitude to my advisor and mentor, Professor Jun Li, for his tremendous support, valuable advice, and guidance throughout these years. I would also like to thank my collaborators; Jiayi Xu and Professor Bin Liu for their support and valuable discussions. I would also like to thank my supervisory committee; Professor Daniel Higgins, Professor Christer Aakeröy, Professor Bin Liu, and Professor Caterina Scoglio for their invaluable time and advice. I would also like to thank my undergraduate advisor, Professor Subrata Kundu of CSIR-Central Electrochemical Institute for his support and guidance.

I would like to extend a special thank you to Dr. Dan Boyle of Kansas State University and Dr. Prem Thapa of the University of Kansas for their help with TEM measurements; Dr. Balamurugan Balasubramanian of the University of Nebraska Lincoln for his help with XPS analysis. I also want to acknowledge Michael Hinton for his help in teaching lab skills. I would like to extend my appreciation to Jim Hodgson, Ron Jackson, Tobe Eggers, Mary Dooley, Bart Bath, and Kimberly Ross for making my research life smooth over the past five years.

I would like to thank all the present and past Jun Li group members with a special mention to Dr. Emery Brown, Yang Song, Archana Sekar, Zachary Johnson, and Jerry Williams for being supportive and helping throughout these years. A special thanks to my two friends in the Chemistry

Department; Dr. Nandini Sarkar and Dr. Bhupinder Sandhu for being there and supporting me in every step.

I wish to acknowledge the funding supported by NSF-CBET-1703263, NSF-DMR-1707585, and DOE-DE-EE0008440 and the matching support from the state of Kansas through Kansas Technology Enterprise Corporation. I would like to thank the Chemistry department for providing me with Graduate Teaching Assistantship; Phi Lambda Upsilon, K-State Graduate School and K-State College of Arts and Sciences for proving me with the funds to present my research work in various conferences; K-state Alumni Association for providing me with the International Student Scholarship and honoring me with the International Leadership Award 2020. Thank you to the Analytical Chemistry professors for recognizing me with the Meloan Award for my research.

I want to thank the Indian Student Association, Graduate Student Council, International Buddies, Phi Lambda Upsilon, Wildcats for International Development, Diversity Programming Committee, and Intercultural Leadership Council for giving me an opportunity to serve the K-State community.

I am blessed to have some amazing friends encouraging and motivating me all the time, without whom I feel the Ph.D. journey would have been more difficult. Thank you Arun S. Siddarth, Aathithya Raja, Aswin Prathap, Meenu, Anbu & Thiba, Balaji Aravindhan, Arvind Kannan, Azhagiya Singam, Sinthiya, Chandru & Brinda, Manickam & Karthika, Arun & Priya, Roshan & Reshma, Vivek, Zayed, Shashank, Asrar, Abhishek, Mahesh, Sowmya, Sravya, Nikitha, Nirupama, Mahima, Joydeep, Sabari, Agni, Niharika, Ryan and Joshnika. Thank you all for the wonderful times and I will cherish our memories for the rest of my life.

Finally, I would like to share my deep eternal gratitude to my wonderful parents Mr. Elangovan Karuppaiah and Mrs. Ramu Thirunavukkarasu; sister Ms. Kannathal Elangovan for believing in me and supporting me to pursue an education of my choice halfway across the world. You all have given the most and expected the least in return. Your endless sacrifices, motivation, and prayers have helped me overcome any obstacle and move forward in my life. You three are my strength and without you all I would not be the person I am today.

Dedication

To my father, mother, and sister!

For their unconditional love and continuous support…

Preface

The dissertation focuses on understanding the role of vertically aligned carbon nanofibers with three-dimensional architecture as an electrocatalyst support for the oxygen reduction and methanol oxidation reactions in low-temperature fuel cells. The dissertation comprises of the following sections:

Chapter 1: This chapter gives an overview of the fuel cells and discusses the working principle, importance, and challenges of proton exchange membrane fuel cells and direct methanol fuel cells. This is followed by the introduction of oxygen reduction and methanol oxidation reaction, and emphasizing on the PGM electrocatalysts employed, reaction mechanism for the PGM catalysts, and advantages and disadvantages of PGM electrocatalysts. In addition, the use of nanostructured carbon materials and the importance of vertically aligned carbon nanofibers as electrocatalyst support is introduced.

Chapter 2: This chapter describes the methodology and procedures employed to grow vertically aligned carbon nanofibers and deposit catalyst particles. The electrochemical experimental setup and techniques such as cyclic voltammetry, linear sweep voltammetry, rotating disk electrode, rotating ring disk electrode, and chronoamperometry are briefly discussed.

Chapter 3: An accepted paper published in *The Journal of Electrochemical Society*. This chapter is a report on the systematic study on oxygen reduction reaction with Pt catalyst deposited on vertically aligned carbon nanofibers. The resulting Pt/VACNF catalysts catalyze oxygen reduction through a four-electron pathway and exhibit enhanced tolerance to methanol oxidation in a mixed environment and a higher ability to recover from carbon monoxide poisoning in comparison to the benchmark Pt/C catalyst. This work provides new insights into the roles of 3D architectured carbon supports and their graphitic microstructures on the fundamental electrocatalytic properties of the catalyst.

Chapter 4: In this chapter, we demonstrate a NH_3 plasma annealing approach to introduce additional nitrogen into vertically aligned carbon nanofibers (N-VACNF) and explore its role as an electrocatalyst and electrocatalyst support. The additional nitrogen content alters the electronic structure of the VACNF support and improves the interaction between metal nanoparticles and VACNF support. The resulting Pt/N-VACNF shows better durability after 5000 accelerated stress cycles and better tolerance to methanol oxidation in a mixed environment when comparing to the benchmark Pt/C catalyst.

Chapter 5: A manuscript submitted to *ChemCatChem*. This chapter is a report on the role of in-situ nitrogen-doped vertically aligned carbon nanofibers as an electrocatalyst support for the methanol oxidation reaction in acidic and alkaline media. The resulting Pt/VACNF and PtRu/VACNF catalysts have strong metal-support interaction and exhibit enhanced electrocatalytic performance and better durability for the methanol oxidation reaction. This work provides new insights into the role of nitrogen-doped three-dimensional graphitic carbon supports in enhancing the MOR catalytic activity.

Chapter 6: This chapter provides a short discussion of the current ongoing projects.

Chapter 7: This chapter summarizes the main findings of three major studies presented in the dissertation and draws overarching conclusions.

Chapter 1 - Introduction

1.1 Motivation

The global population continues to grow and is predicted to increase by 2.0 billion over the next three decades[1]. Rising population, developing economies, and improving standards of living will drive an increase in the global energy demand. The world's energy demand is projected to have a 50% increase by 2050[2]. Fossil fuels continue to play a dominant role in the global energy supply and around 80% of the present global energy comes from oil, natural gas, and coal. As a result, an increase in energy demands will eventually lead to the depletion of fossil fuels. Also, higher consumption of energy from fossil fuels results in global warming, increased pollution, and affecting public health[3]. To meet the future energy needs alongside addressing environmental challenges and climate change, clean and sustainable energy is required[4]. Renewable energy continues to grow and is predicted to supply the majority of the global energy usage by 2050[2]. However, renewable energy sources are intermittent and highly dependent on geographic locations. Because of the intermittency of the renewable energy sources such as wind and solar irradiation, it requires additional energy storage systems like batteries for backup, which makes the overall system more expensive. Therefore, a sustainable energy future requires a change in the way we produce, deliver, and consume energy[5]. Fuel cells are identified as a potential solution to the energy crisis and a promising alternative to standard energy sources[6]. Fuel cells can provide clean, reliable, and consistent energy with high efficiency. In addition, they are significantly lighter, more compact, environmentally beneficial with little to no harmful pollutant emissions and can serve as both primary and standby power sources. It's clear that fuel cells have several advantages over conventional fossil fuel systems, however, they have challenges that must be overcome to be a successful and competitive alternative.

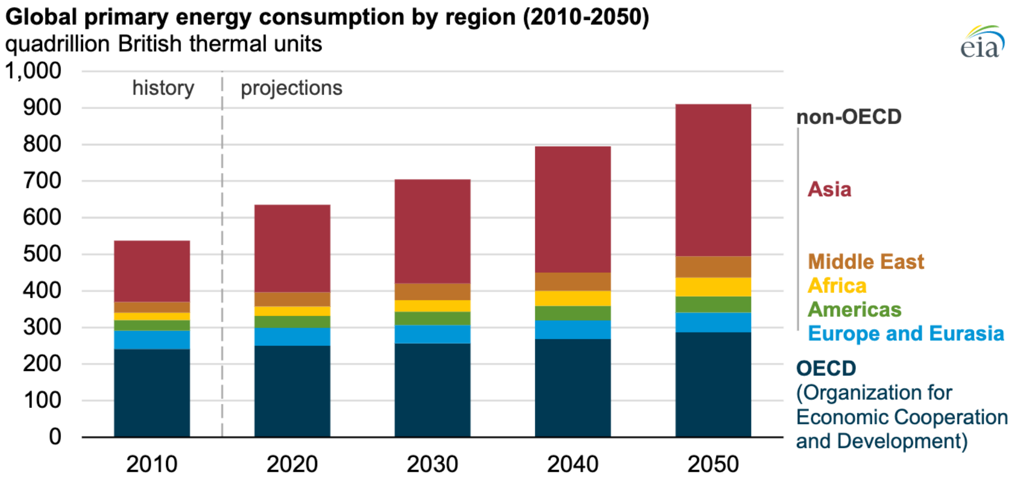

Figure 1.1: Global primary energy consumption by region (2010-2050). Source: U.S. Energy Information Administration, *International Energy Outlook 2019*[2].

1.2 Fuel Cells

Fuel cells are electrochemical devices that convert chemical energy into electrical energy. Fuel cells operate like batteries, but they do not need recharging and can provide electricity as long as a continuous supply of the fuel and the oxidizer is available. Fuel cells have high energy density and are more efficient than current means of energy conversion. In general, a fuel cell consists of two electrodes-a negative electrode (anode) and a positive electrode (cathode) and an electrolyte. The fuel gets oxidized at the anode and the generated ions migrate through the polymer electrolyte membrane (PEM) where they react with oxygen and the electrons that go through the external circuit to produce heat and electricity. The PEM also serves as a barrier to prevent the mixing of products generated at the electrodes. Fuel cells can operate in a wide range of temperatures which makes them suitable for a variety of portable devices, transportation, and stationary systems.

1.3 Types of Fuel Cells

Based on the operating temperature, nature of electrolyte, fuel required, and kind of catalysts required fuel cells can be classified into six different types. These six different types of fuel cells can be broadly divided into low-temperature and high-temperature fuel cells. The different types of fuel cells with their operating temperature, electrolyte, anode fuel, oxidation agent, and reaction by-product are illustrated in Figure 1.2[7].

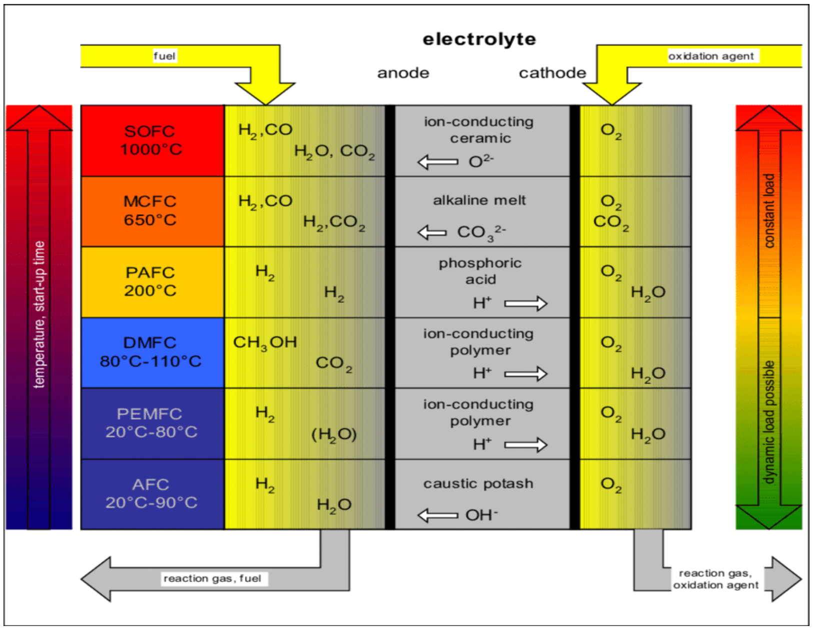

Figure 1.2: Illustration of the different types of fuel cell technologies (Reproduced from 2nd European PV-Hybrid and Mini-Grid Conference, Kassel, Germany, 2003, pp 232-239. © OTTI Energie Kolleg. All rights reserved)

Low-temperature fuel cells (LTFCs), i.e. alkaline fuel cell (AFC), polymer electrolyte membrane fuel cell (PEMFC), direct methanol fuel cell (DMFC), and phosphoric acid fuel cell (PAFC) operate at a temperature range between 20-200 °C. LTFCs are small and light weighted which enables them to be more suitable for transport and portable applications. Also, they have a quick start-up or shut-down time. However, the downside is that they require highly active noble-metal catalysts to decrease the activation energy of the half-cell electrochemical reactions. High-temperature fuel cells (HTFCs), i.e. molten carbonate fuel cell (MCFC) and solid oxide fuel cell (SOFC) operate at temperature range between 600-1000 °C. HTFCs have high fuel flexibility such as reformed hydrocarbon, gasified biomass, or gasified coal as fuel on the anode side. In addition, they don't require noble metal-based catalysts. However, their high operating temperature results in longer start-up time and breakdown of cell components. The range of fuel cell technologies, possible fuels, and different applications are given in Figure 1.3.

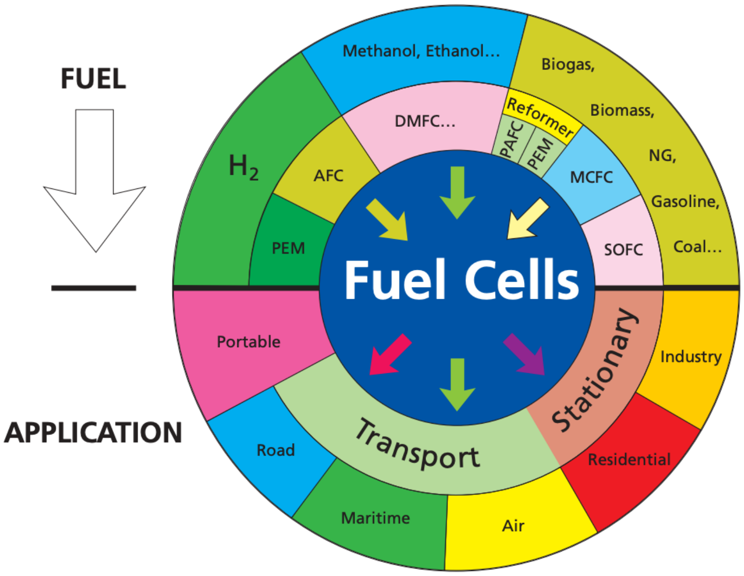

Figure 1.3: Different fuel cell technologies with its possible fuels and applications[8].

1.3.1 Polymer Electrolyte Membrane Fuel Cells

1.3.1.1 Working Principle

The PEMFC employs hydrogen as a fuel on the anode side and oxygen on the cathode side which is electrochemically oxidized and reduced to generate heat and electricity. Figure 1.4 presents the schematic illustration of a PEMFC. Platinum (Pt) and Pt-alloy nanoparticles supported on the high surface area carbon support catalysts facilitate the electrochemical reactions on both anode and cathode. Nafion is the most commonly used electrolyte in PEMFC. As shown, the electrolyte is a proton exchange membrane that allows only H^+ to pass through and blocks H_2 from entering into the cathode side. Among the LTFC technologies, PEMFC is the cleanest and economically viable power source.

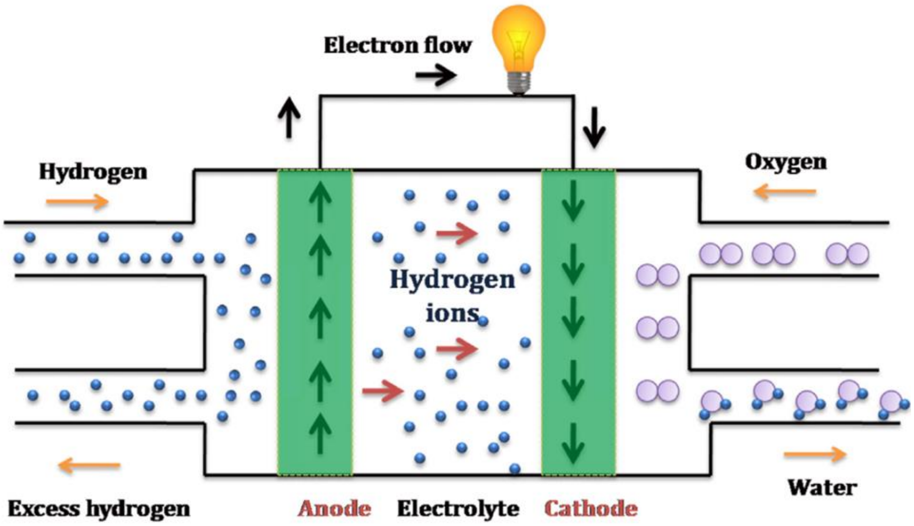

Figure 1.4: **Schematic illustration of a PEMFC. (Reproduced with permission from *Elsevier*: 2018; pp 751-767. © 2017 Elsevier Inc. All rights reserved.)**

The electrochemical half-cell reactions and the overall reaction in the PEMFC are given as follows:

Anode: $2H_2 \rightarrow 4H^+ + 4e^-$ $E^o_a = 0.0$ V (1.1)

Cathode: $O_2 + 4H^+ + 4e^- \rightarrow 2H_2O$ $E^o_c = 1.23$ V (1.2)

Overall: $2H_2 + O_2 \rightarrow 2H_2O$ $E^o_{Cell} = 1.23$ V (1.3)

Alkaline PEMFC involving anion exchange membrane is the new class of fuel cells as the reaction kinetics can be improved in alkaline medium and it offers flexibility in using non-noble metal catalysts[9]. These fuel cells are similar to acidic-PEMFC, and the only difference is the OH^- ions pass through the electrolyte from cathode to anode where they react with hydrogen to produce water. The electrochemical half-cell reactions and the overall reaction in the alkaline PEMFC are given as follows:

Anode: $2H_2 + 4OH^- \rightarrow 4H_2O + 4e^-$ $E^o{}_a = 0.40$ V (1.4)

Cathode: $O_2 + 2H_2O + 4e^- \rightarrow 4OH^-$ $E^o{}_c = -0.83$ V (1.5)

Overall: $2H_2 + O_2 \rightarrow 2H_2O$ $E^o{}_{Cell} = 1.23$ V (1.6)

1.3.1.2 Challenges with PEMFC

In principle, the oxidation of hydrogen happens when the anode potential is above 0.0 V, with respect to the standard hydrogen electrode (SHE). Similarly, the oxygen is reduced spontaneously when the cathode assumes a potential below 1.23 V vs. SHE. Hence, the thermodynamic potential for the operation of PEMFC is 1.23 V vs SHE. However, a real PEMFC has a cell voltage less than that due to various losses which could be attributed to the fuel crossover, poor cathode reaction kinetics, slow mass transport, and ohmic loss due to the electrical resistance of different components[10]. The typical polarization curve indicating the different overpotential sources is shown in Figure 1.5. At lower current densities, the drop in cell voltage is rapid due to the activation loss. At moderate current densities, the cell voltage drops linearly due to the ohmic loss. At higher current densities, the cell voltage drops faster due to the mass transport loss.

The proton conductivity in PEMFC decreases with a lower humidification content and it causes the increase in cell resistance[11]. So, the electrolyte needs to be in a hydrated condition to maintain the overall performance. At the same time, an excess amount of water on the cathode side can cause water flooding which limits O_2 transportation through the gas diffusion layer[12]. This limits the PEMFCs to operate at a temperature below 100 ^{o}C. The performance of the PEMFC is affected by the presence of CO. As hydrogen is generated from the reforming of hydrocarbons or alcohol fuels which invariably introduce carbon monoxide (CO). Even at a very low CO concentration of 5-10 ppm, CO present in the anode can preferentially adsorb on the Pt surface and block the active sites[13]. In addition, the hydrogen storage pose severe challenge as the conventional storage methods are expensive, inefficient, bulky, and pose safety concerns[14].

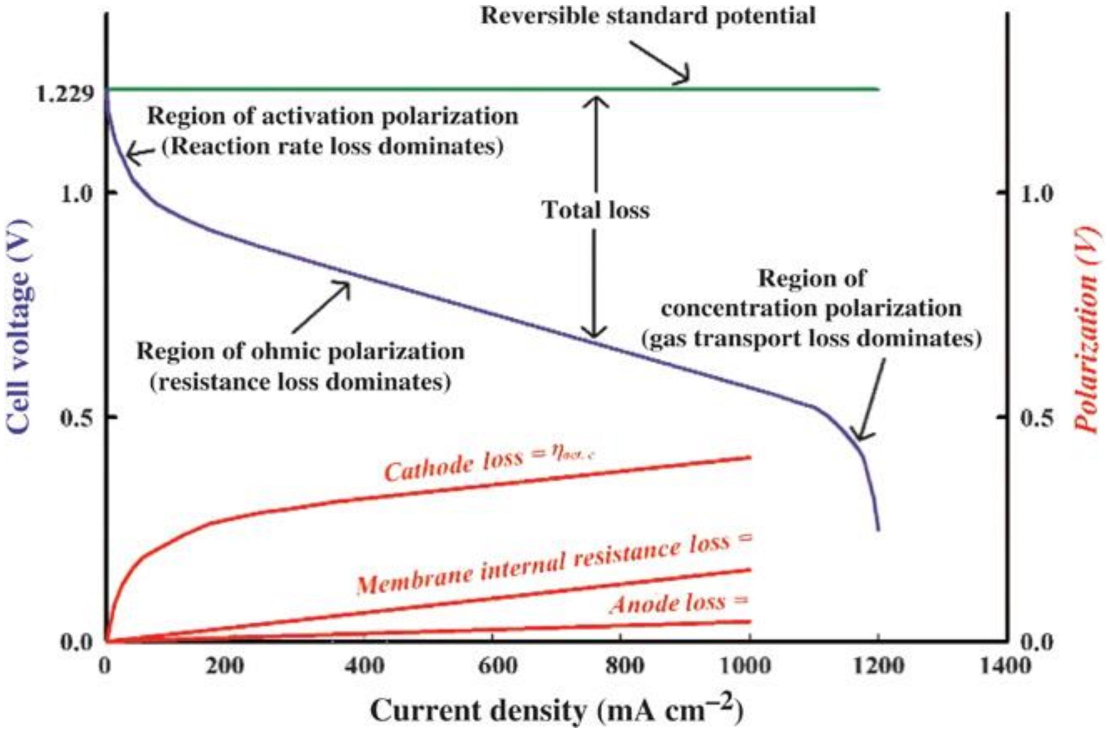

Figure 1.5: Polarization curve of PEMFC. (Adapted from *Electrochem. Soc. Interface* 2004, 13 (3), 17-19. © The Electrochemical Society. All rights reserved.)

Despite the advantages of alkaline PEMFC, there are still some challenges associated with it. The OH^- ions diffusion coefficient is lower than the H^+ ions and they suffer from low anionic conductivity[15]. As a result, the alkaline PEMs require a higher ion exchange capacity, but this can lead to polymer swelling and affect the mechanical properties[16]. The alkaline PEM degrades faster due to its instability at higher pH and higher temperature and this results in the performance decline of alkaline PEMFC[16]. In addition, water is one of the major reactants in alkaline PEMFC, and if it suffers from low water retention, there will not be enough water available to react at the cathode which will result in decreased fuel cell performance[17].

1.3.2 Direct Methanol Fuel cell

1.3.2.1 Working Principle

DMFC uses methanol and oxygen from the air to produce electricity. They tend to have lower efficiency than PEMFC due to the longer startup time and poor anode and cathode reaction kinetics. However, it is highly attractive towards application in portable electronic devices as it employs methanol, a liquid fuel that is easy to transport, store, and distribute. Methanol has a volumetric energy density of 4.82 kWh/L and a gravimetric energy density of 6.1 kWh/kg[18]. DMFC operates at a low and intermediate temperature up to (150 ^{o}C). In the DMFC, a methanol /water mixture should be fed as the fuel input and platinum group metals (PGM) are employed as electrocatalysts. The methanol gets oxidized by a bimetallic, usually platinum/ruthenium catalyst at the anode producing carbon dioxide which leaves the cell in the direction of the fuel reservoir, $6e^-$ which travel along the external circuit to the cathode, $6H^+$ which migrate through the PEM and react with oxygen supplied at the cathode side to produce water and heat.

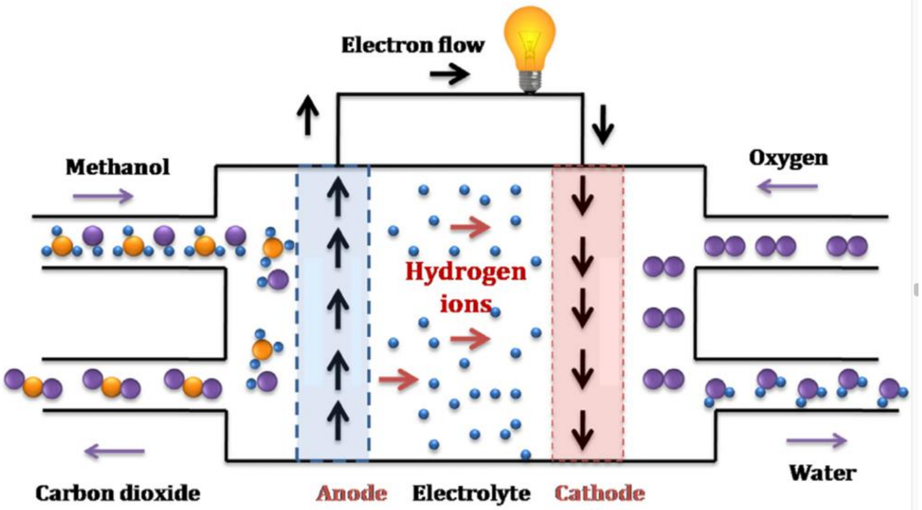

Figure 1.6: Schematic illustration of DMFC. (Reproduced with permission from *Elsevier*: 2018; pp 751-767. © 2017 Elsevier Inc. All rights reserved.)

The electrochemical half-cell reactions and the overall reaction in the acidic DMFC can be given as follows:

Anode: $CH_3OH + H_2O \rightarrow CO_2\uparrow + 6H^+ + 6e^-$ $E^o_a = 0.02$ V (1.7)

Cathode: $\frac{3}{2}O_2 + 6H^+ + 6e^- \rightarrow 3H_2O$ $E^o_c = 1.23$ V (1.8)

Overall: $CH_3OH + \frac{3}{2}O_2 \rightarrow CO_2\uparrow + 2H_2O$ $E^o_{Cell} = 1.21$ V (1.9)

In the case of alkaline DMFC, the reactions can be given by the following equations:

Anode: $CH_3OH + 6OH^- \rightarrow CO_2\uparrow + 5H_2O + 6e^-$ $E^o_a = -0.81$ V (1.10)

Cathode: $\frac{3}{2}O_2 + 5H_2O + 6e^- \rightarrow 3H_2O$ $E^o_c = 0.40$ V (1.11)

Overall: $CH_3OH + \frac{3}{2}O_2 \rightarrow CO_2\uparrow + 2H_2O$ $E^o_{Cell} = 1.21$ V (1.12)

1.3.1.2 Challenges with DMFC

In principle, the oxidation of methanol happens when the anode potential is above 0.02 V vs. SHE. Similarly, the oxygen reduction occurs at a potential below 1.23 V vs. SHE. So, the overall cell voltage of DMFC is roughly about 1.21 V vs. SHE. But in reality, it is impossible to attain the ideal cell voltage and poor electrode kinetics cause the electrode reaction to deviate from the ideal thermodynamic values which result in the reduction of the overall cell voltage[19]. The real behavior of the DMFC in practical conditions is shown by the polarization curve in Figure 1.6. In Practice, a far more positive potential is required to oxidize methanol and a more negative potential to reduce oxygen. The polarization curve of DMFC can be divided into three regions. Region 1 is called activation polarization and the voltage loss is due to the reaction kinetics. Region 2 is called ohmic polarization and the voltage loss is due to the internal resistance from the fuel cell. Region 3 is called concentration polarization and the voltage loss is due to the depletion of the reactant species. Hence, the overall output of the DMFC is lower than that of the ideal cell voltage at any current rating.

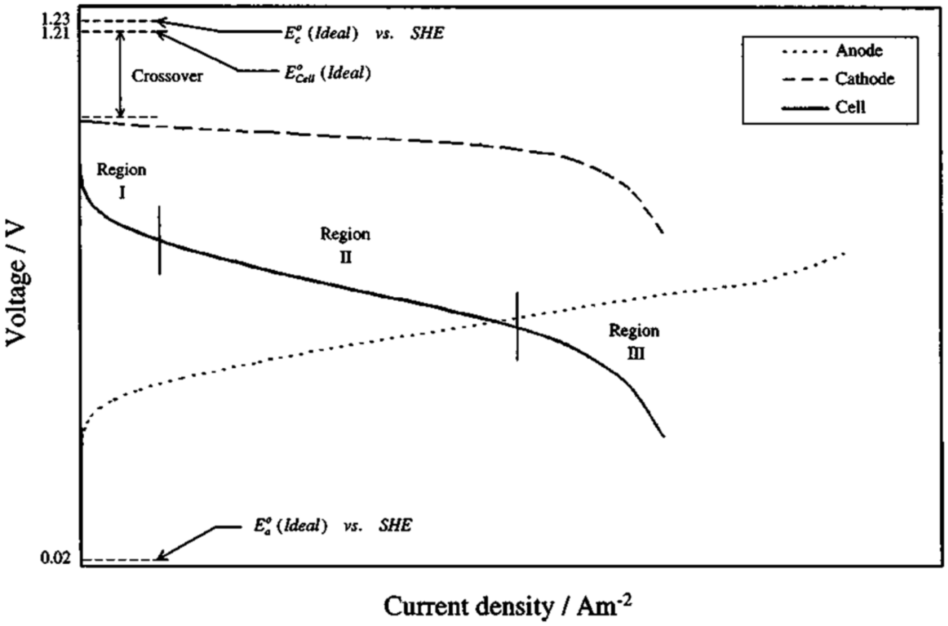

Figure 1.7: Polarization curve of DMFC. (Reproduced with permission from *J. Electrochem. Soc.* 2003, *150* (9), A1231-A1245. © The Electrochemical Society. All rights reserved.)

In the present hydrogen-fueled PEMFC, the kinetics of hydrogen oxidation reaction at the anode is relatively fast and most losses occur at the cathode. This enables the PEMFC to attain a very high power density of roughly 500 to 600 mW/cm^2 at an efficient cell voltage between 0.6 to 0.7 V. Due to the additional poor kinetics of the DMFC anode, it gets harder to achieve a very high-power density (closer to that of PEMFC) at a practical cell voltage. Using a fuel reformer may convert the methanol to hydrogen fuel and use the normal, but it accounts for the volume and efficiency losses. In general, there is a trend to remove the fuel reformer and develop DMFCs. It is believed that the overall performance of DMFC can be competitive with the hydrogen-fueled PEMFC. In the actual system, the electrochemical reactions are much more complex than the reaction scheme given by equations 1.7, 1.9, 1.10, 1.11 which results in the poor electrode kinetics at the anode and cathode and causes the formation of intermediates. These intermediates get adsorbed on the Pt surface and block the active site which reduces the overall catalytic activity of platinum towards the methanol oxidation. Therefore, these intermediates need to be removed by using advanced catalyst materials.

The major technical barrier with DMFC is the methanol crossover. Methanol has a very high solubility in water and the Nafion membrane used in DMFC can easily absorb the methanol and water mixture which results in the methanol transport from the anode to the cathode[20]. Once the methanol reaches the cathode, it starts to get oxidized, partially cancel the oxygen reduction current and results in a mixed potential, leading to a significant decrease in the performance of DMFC[21]. To reduce methanol crossover, methanol can be diluted to a very low concentration of about 1M-2M.[22] But the lower concentration of methanol suffers from the mass transfer limitations and cannot obtain current density beyond a certain value. The dilution of methanol makes it not possible to utilize the high energy density of methanol. As a result of methanol crossover, not all the methanol is converted to electrical current and the overall chemical to electrical conversion efficiency is roughly about 40%[23]. DMFC produces CO_2 as a by-product and CO_2 build-up in the fuel cell system should be avoided with an effective ventilation system. Otherwise, the CO_2 can dissolve in the water and form carbonic acid which can cause corrosion in the fuel cell components[24]. In alkaline DMFCs, the carbonation due to CO_2 can cause a decrease in the anionic conductivity leading to a further drop in the DMFC performance[25].

1.4 Electrochemical Reactions

1.4.1 Oxygen Reduction Reaction

The oxygen reduction reaction (ORR) occurring at the cathode is one of the limiting factors in PEMFC due to its slow reaction kinetics. The thermodynamic redox potential of the ORR is

1.23 V vs. SHE. However, the ORR has an onset potential of about 1.0 V vs. SHE. with around 230 mV overpotential due to the fuel crossover and internal currents[26]. The ORR process is complex, and it involves the formation of several intermediates depending on the pH, type of electrolyte, and employed catalyst material. The reaction can either proceed through a four electron (4-e$^-$) or a two-electron (2-e$^-$) or a one-electron (1-e$^-$) reduction pathway. Based on the applications, these different pathways have unique significance. The 4-e$^-$ reduction pathway is highly preferred in fuel cells. The 2-e$^-$ reduction pathway is used in industry to produce H_2O_2. The 1-e$^-$ reduction pathway is the main process in lithium-air batteries. In an aqueous acidic environment, the reaction pathways can be given by equations 1.13-1.16[27, 28]

1) 4-e$^-$ reduction pathway

$$O_2 + 4H^+ + 4e^- \rightarrow 2H_2O \qquad E^o = 1.23\ V \qquad (1.13)$$

2) 2-e$^-$ reduction pathway

$$O_2 + 2H^+ + 2e^- \rightarrow H_2O_2 \qquad E^o = 0.70\ V \qquad (1.14)$$

followed by either 2-e$^-$ reduction:

$$H_2O_2 + 2H^+ + 2e^- \rightarrow 2H_2O \qquad E^o = 1.76\ V \qquad (1.15)$$

or a decomposition reaction:

$$2H_2O_2 \rightarrow 2H_2O + O_2 \qquad (1.16)$$

In an aqueous alkaline environment, the reaction pathways can be given by equations 1.17-1.20[27, 28].

1) 4-e$^-$ reduction pathway

$$O_2 + 2H_2O + 4e^- \rightarrow 4OH^- \qquad E^o = 0.401\ V \qquad (1.17)$$

2) 2-e$^-$ reduction pathway

$$O_2 + H_2O + 2e^- \rightarrow HO_2^- + OH^- \qquad E^o = -0.065\ V \qquad (1.18)$$

followed by either 2-e$^-$ reduction:

$$HO_2^- + H_2O + 2e^- \rightarrow 3OH^- \qquad E^o = 0.867\ V \qquad (1.19)$$

or a decomposition reaction:

$$2HO_2^- \rightarrow 2OH^- + O_2 \qquad (1.20)$$

In a non-aqueous aprotic solvent, the ORR happens through a 1-e$^-$ reduction pathway forming superoxide followed by a 1-e$^-$ reduction to O_2^{2-} as expressed by equations 1.21 and 1.22[28]. The thermodynamic potentials of these reduction reactions are highly dependent on the employed solvent.

$$O_2 + e^- \rightarrow O_2^- \qquad (1.21)$$

$$O_2 + e^- \rightarrow O_2^{2-} \qquad (1.22)$$

1.4.2 Methanol Oxidation Reaction

The methanol oxidation reaction (MOR) requires 6-e$^-$ to be completely oxidized to CO_2. The thermodynamic potential of the reaction (0.02 V) is very close to the hydrogen oxidation reaction. However, in reality, it's not possible to get all the 6-e$^-$ at once and the reaction kinetics of MOR is several orders of magnitude slower than the HOR. So, the reaction occurs through several steps with generating a number of intermediate species. The MOR mechanism can be given by the parallel pathway shown in Figure 1.8. The indirect oxidation pathway involves the oxidation of methanol through the formation of poisoning CO_{ads} species[29]. The direct oxidation pathway involves oxidation of methanol through the formation of soluble intermediates such as formaldehyde, formate, and methyl formate[29]. These intermediate species can either diffuse into the electrolyte or re-absorb onto the catalyst surface to form CO_2.

The CO can be adsorbed onto the catalyst surface through a linear-bonded or bridge bonded models[30]. The CO_{ads} species react with the O-containing species on the adjacent surface to form

CO_2 following a Langmuir-Hinshelwood mechanism[31]. The O-containing species are produced from the dissociation of water molecules at the electrode surface. The formation of OH_{ads} is limited to a few sites at lower potentials, and therefore the dissociation of water molecules to generate OH_{ads} species is the rate-determining step (RDS). The reaction mechanism for converting CO_{ads} to CO_2 can be given by equations 1.23-1.25[32].

$$H_2O + * \Leftrightarrow OH_{ads} + H^+ + e^- \tag{1.23}$$

$$CO_{ads} + OH_{ads} \rightarrow COOH_{ads} \tag{1.24}$$

$$COOH_{ads} \rightarrow CO_2 + H^+ + e^- + 2^* \tag{1.25}$$

where * denotes an adjacent free site on the catalyst surface.

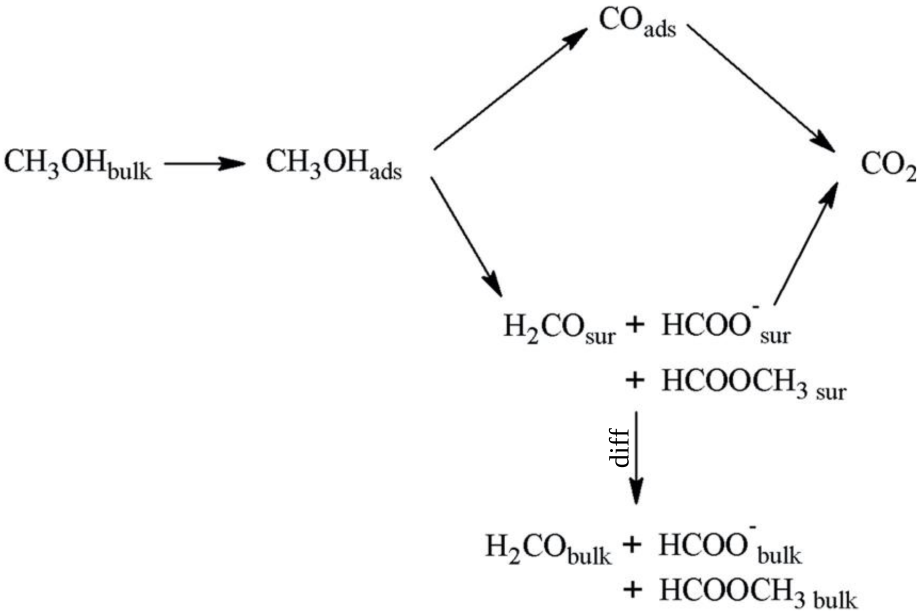

Figure 1.8: Simplified reaction mechanism of methanol oxidation showing the parallel pathway. (Reproduced with permission from *J. Power Sources* 2018, *375*, 320-334. © 2017 Elsevier B.V. All rights reserved.)

1.5 Electrocatalysts for LTFCs

1.5.1 Electrocatalysts for ORR

Platinum is recognized as the more efficient electrocatalyst for the ORR in both acidic and alkaline environments. The ORR catalyzed by Pt usually proceeds through a 4-e^- reduction pathway with multi-step protonation process. Initially, the O_2 gets adsorbed on the catalyst surface followed by hydrogenation of the adsorbed species which can happen through either an associative or a dissociative mechanism. An associative mechanism involves the adsorption of O_2 molecule followed by a direct proton and electron transfer to produce OOH, which breaks into O and OH. In a dissociative mechanism, the O_2 adsorption splits the O-O bond and forms adsorbed atomic O, which gets further hydrogenated to form OH and then H_2O. The ORR mechanism on Pt electrode can be given by the modified Wroblowa et al. scheme in Figure 1.9[33].

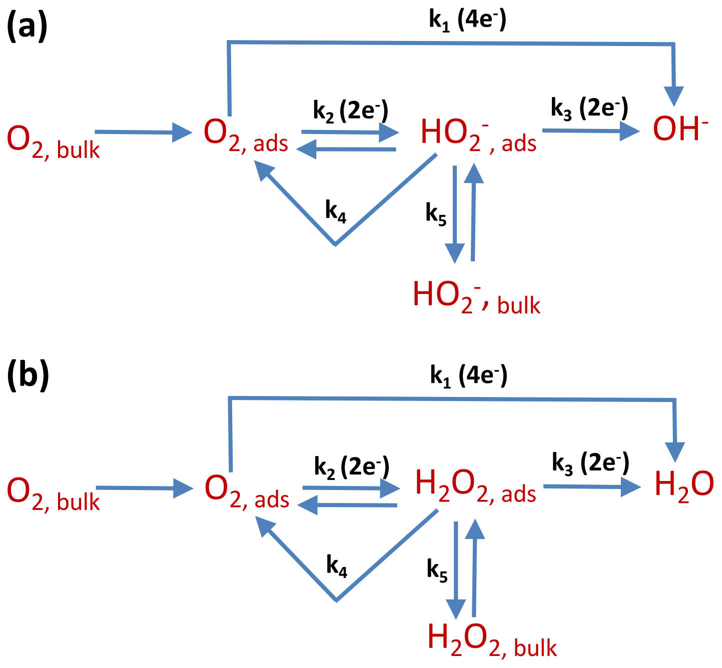

Figure 1.9: ORR mechanism on Pt surface in (a) alkaline and (b) acidic environment. (Adapted from *J. Electroanal. Chem.*, 1976, 69 (2), 195-201. © 1976 Elsevier B.V. All rights reserved.)

As shown in Figure 1.9, the ORR can produce the 4-e^- product by a direct (k_1) or a series (k_2+k_3) pathway. The $H_2O_{2,\ ads}$/ $HO_2^{-}{}_{,\ ads}$ can chemically decompose on the electrode surface (k_4) or diffuse into the electrolyte (k_5). Experimental results suggest that on Pt surface the majority of the ORR product is either H_2O/OH^- or $H_2O_{2,\ ads}$/ $HO_2^{-}{}_{,\ ads}$. However, a small amount of H_2O_2/HO_2^- could be observed during ORR with the electron transfer number still close to 4. The reaction kinetics and mechanism of ORR on Pt surface get affected by the anions in the electrolyte, Pt particle sizes, and crystal structure[34-38].

The RDS of the ORR depend on the active sites, pH of the electrolyte, and reaction temperature. Even though, the complete mechanism of ORR is still not clear, it is widely accepted that the O_2 adsorption on to the metal surface is the crucial step for ORR[39-41]. Nørskov et al. proposed a method for calculating the adsorption energy of ORR intermediates using electronic structure calculations. They employed Density Functional Theory (DFT) calculations to calculate the bond energies of oxygen and hydroxyl for different metals and generated a volcano plot as shown in Figure 1.10a.

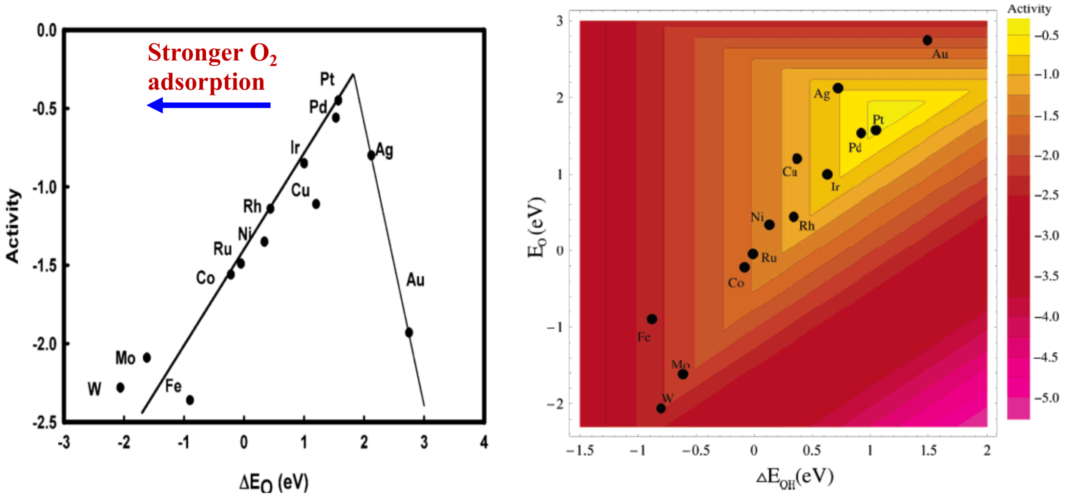

Figure 1.10: (a) Trends in oxygen reduction activity plotted as a function of the oxygen binding energy; (b) Trends in oxygen reduction activity plotted as a function of both oxygen and hydroxyl binding energy. (Reproduced with permission from *J. Phys. Chem. B* 2004, *108* (46), 17886-17892. © 2004 American Chemical Society. All rights reserved.)

As it appears, pure Pt(111) is at the top of the plot, making it the most effective ORR catalyst. However, if a metal binds O_2 too strong, the reaction is limited by the removal of adsorbed O and OH species and if a metal binds O_2 too weak, the reaction is limited by the transfer of electrons and protons to adsorbed O_2. So, an efficient ORR catalyst must bind O_2 strongly enough for the reaction to take place, but weakly enough that the product will dissociate, and the catalyst surface will not be poisoned by either the reactant or intermediates. As seen from Figure 1.10a, the metal that binds O_2 slightly weaker than Pt will have a higher activity. Apart from the O_2 binding energy, the OH binding energy also plays a significant role in determining the ORR activity. As presented in Figure 1.10b the binding energy of O_2 and OH are roughly linearly correlated for the elemental surfaces[39]. It is found that the better electrocatalyst proceeding a through a 4-e- reduction pathway should have oxygen binding energy lower than Pt by 0.2 eV and hydroxyl binding energy lower than Pt by 0.1 eV[42].

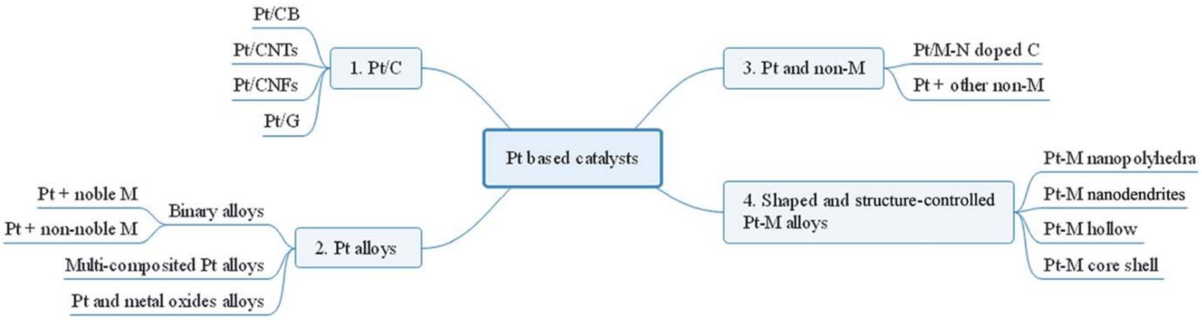

Figure 1.11: Current representative class of Pt-based catalysts for LTFCs. (Reproduced from *Sustain. Energy Fuels* 2020, *4* (1), 15-30 with permission from The Royal Society of Chemistry. All rights reserved.)

Several efforts have been made to find alternatives for Pt catalysts, however, the other precious or non-precious metal-based catalysts cannot match the performance of Pt catalyst in practical applications[43-45]. A significant improvement has been made to the Pt single-atom electrocatalysts by employing different carbon supports, employing hetero atom doping, forming Pt alloys, and forming shape and structure controlled Pt alloys[41-47]. The representative class of Pt-based catalysts for LTFCs can be illustrated in Figure 1.11.

1.5.2 Electrocatalysts for MOR

Pt is the most involved metal in catalyzing the MOR. On Pt surface dehydrogenation of methanol happens through dissociating the C-H bond and involves the formation of multiple intermediates as shown in Figure 1.12[48, 49].

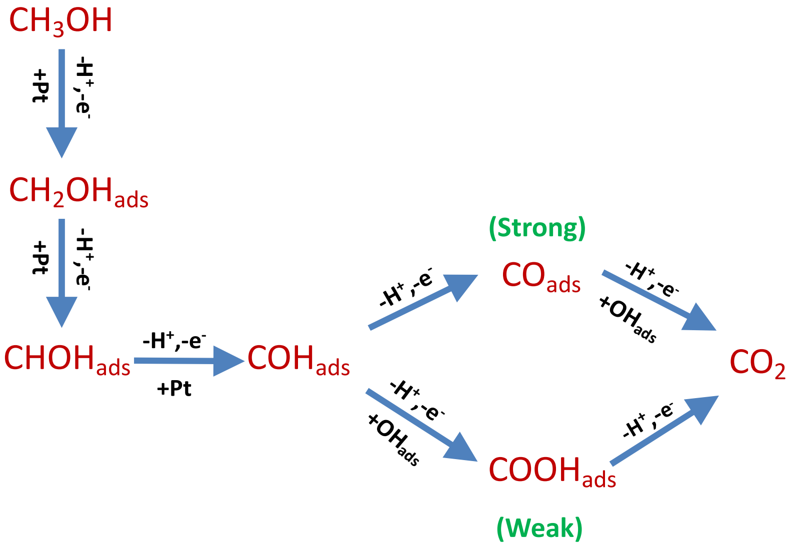

Figure 1.12: MOR reaction pathways on Pt surface in acidic medium.

The reaction on Pt surface can happen through CO_{ads} or $COOH_{ads}$ involved reaction routes and it has been accepted that CO_{ads} is the primary intermediate poisoning the active surface of Pt, which ultimately results in sluggish reaction kinetics for MOR in acidic electrolyte. The strongly attached CO_{ads} intermediate species can be removed by OH_{ads} species on the neighboring Pt site that was generated from the dissociation of water molecules. However, the water dissociation happens at a higher potential (0.6 V vs RHE) on Pt surface[50]. In alkaline electrolyte, the presence of additional OH^- species in the electrolyte enables relatively easier removal of CO_{ads} when compared to the acid electrolyte. The strongly adsorbed intermediates affect further adsorption of methanol and thus limiting the activity. Therefore, an ideal catalyst should not only assist in breaking the C-H bond, but it should also facilitate the dissociation of water molecules at a lower potential to remove the strongly adsorbed CO species.

A more interesting alternative to the Pt catalysts can be created by combining Pt with secondary metals such as ruthenium (Ru), copper (Cu), cobalt (Co), tin (Sn), and a few more. These secondary metals should be hydrophilic so that they can generate OH_{ads} species at a lower potential which helps in removing the adsorbed intermediates such as CO_{ads}. Among the secondary metals, Ru is by far considered to be the most effective hydrophilic metal in facilitating the MOR effectively through a bifunctional mechanism[51] expressed by equation 1.26 and 1.27. The water activation on Ru surface occurs at much lower potential (0.2 V vs RHE). Currently, Pt-Ru with an atomic ratio of 1:1 is found to be the most promising catalyst for efficient methanol and CO_{ads} oxidation.[52]

$$Ru + H_2O \longrightarrow RuOH_{ads} + H^+ + e^- \qquad (1.26)$$

$$PtCO_{ads} + RuOH_{ads} \longrightarrow CO_2 + H^+ + e^- + Pt + Ru \qquad (1.27)$$

1.5.3 Challenges with PGM Electrocatalysts

Generally, Pt and PtRu nanoparticles (NPs) supported on amorphous carbon support such as carbon black (Pt/C) is the most widely used catalyst in LTFC. Due to the sluggish reaction kinetics, a large amount of Pt is required to accelerate the oxygen reduction process and the methanol oxidation process and meet the performance requirement of LTFCs. The cost of the fuel cell is the most important factor affecting the widespread commercialization of the technology and undoubtedly, the cost of PGM catalysts is the major component contributing to the overall fuel cell cost. In small-scale production, the cost of the catalysts is around 26% and 41% for PEMFC and DMFC, respectively assuming 1000 PEMFC systems and 200 DMFC systems produced per year[53, 54]. The majority of the fuel cell cost comes from components like bipolar plates and gas diffusion layers as they are produced in small-scale which makes them expensive. So, when a large number of systems are produced, the mass production of these components can bring down their cost. However, the cost of the catalysts is not significantly reduced, and it increases when a larger number of systems are produced per year as the catalyst cost comes from the material cost, it’s processing and availability. Figure 1.13 presents the fuel cell stack cost for PEMFC and DMFC.

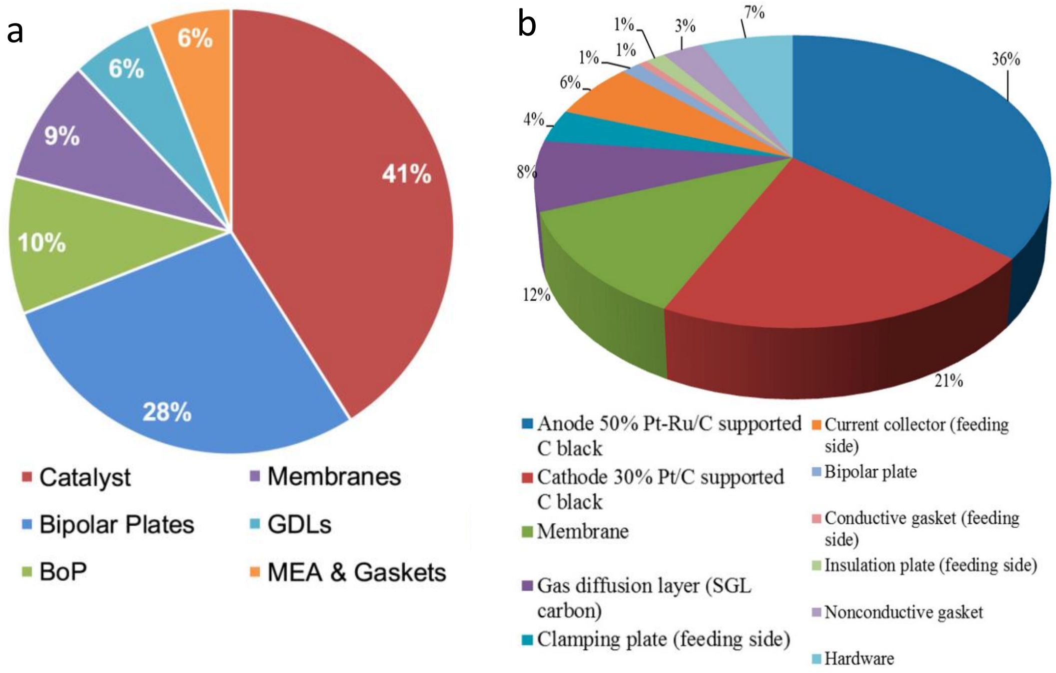

Figure 1.13: Fuel cell stack cost by component for (a) PEMFC at 500,000 systems per year manufacturing rate[55] and (b) DMFC at 10,000 systems per year manufacturing rate[53]. (Adapted from *Current Opinion in Electrochemistry* 2019, *16*, 90-95 and *Energies* 2016, *9* (12), 1008. All rights reserved.)

As presented in Figure 1.13a, the Pt catalysts have a major contribution of around 41% in the total fuel cell cost assuming a total production of 500,000 systems per year[55]. In DMFC due to the high PGM loading, the catalysts contribute to 57% of the total DMFC cost assuming 10,000 systems produced per year as shown in Figure 1.13b[53]. Hence, lowering the catalyst loading while maintaining the performance is important. The DOE 2020 target for the Pt loading of 0.025 mg/cm^2 and < 0.1 mg/cm^2 for the anode and cathode, respectively. In DMFC, the anode catalyst loading is significantly high, and the DOE 2020 target to bring the overall PGM catalysts loading to < 4mg/cm^2.

Apart from cost and availability, the Pt-based catalysts suffer from degradation. The degradation occurs through dissolution, agglomeration, and detachment of the catalyst NPs[56]. The Pt dissolution happens at a potential of 1.00 V vs RHE[57]. The Pt dissolution from the catalyst's surface can be given by the equations 1.28-1.30[58, 59]. The presence of PtO on the catalyst's surface accelerates the degradation of the Pt catalysts[60].

$$Pt \longrightarrow Pt^{2+} + 2e^- \tag{1.28}$$

$$Pt + H_2O \longrightarrow PtO + 2H^+ + 2e^- \tag{1.29}$$

$$PtO + 2H^+ \longrightarrow Pt^{2+} + H_2O \tag{1.30}$$

In addition to degradation, the commercial Pt/C suffers from carbon corrosion. The carbon black is known to electrochemically oxidize to form surface oxides which finally creates CO_2[56, 60]. The carbon conversion to CO_2 can be given by equation 1.31.

$$C + H_2O \longrightarrow CO_2 + 4H^+ + 4e^- \tag{1.31}$$

The standard potential of the carbon oxidation/corrosion is 0.207 V vs SHE, but the kinetics of the reaction is slow and the carbon shows little corrosion at low voltage[61]. However, when the potential raises above 1.0 V vs. SHE the carbon corrosion rate increases. Carbon corrosion is more dominating when the cell potential may rise as high as 1.5 V during start-up/shut down cycle due to fuel starvation, H_2/air boundary at the anode, and slower ORR kinetics[60, 62, 63]. Even for a shorter period of time, this high potential can further accelerate the carbon corrosion. Also, at such high potential, the carbon corrosion is also enhanced by the higher O_2 concentrations and elevated temperature[60, 64]. The presence of oxygen-containing groups on the carbon surface can weaken the interaction between the Pt NPs and the carbon support which results in the dissolution or agglomeration of the weakly attached Pt NPs[60, 65]. It is also found that the Pt NPs catalyze the carbon corrosion at high potential[66]. So, the Pt degradation and carbon corrosion or somewhat interrelated. Also, the Pt/C is susceptible to the methanol crossover in the DMFCs and poisoned by the CO present in the H_2 fuel in the PEMFCs. As a result of methanol crossover and CO poisoning, the overall performance decreases. Hence, an ideal catalyst support should mitigate all these problems.

1.6 Nanostructured Carbon Supports

Nanostructured carbon materials are the ideal electrocatalysts support owing to their high electrical conductivity, high porosity, high electrochemical stability, resistance to carbon corrosion, ability to strongly support catalysts particles, flexibility for surface modification, and accelerated electron transfer at the electrode-electrolyte interface[62, 67-69]. The nanostructured carbon supports can help to reduce the Pt loading and improve the overall catalytic performance and enhance the catalyst’s tolerance to methanol crossover and CO poisoning. Nanostructured carbon materials such as carbon nanotubes[70, 71], carbon nanofibers[72-74], graphene[75-77], graphene nanoribbons[78, 79], reduced graphene oxide[80, 81], carbon aerogels[82], carbon nanohorns[83], carbon nanocoils[84], carbon nanocages[85], ordered mesoporous carbon spheres[86] have been widely employed as electrocatalyst supports. Introducing heteroatoms, such as N, S, B, and P into the nanostructured carbon materials can further improve the performance of the resulting electrocatalyst towards various electrochemical reactions in low-temperature fuel cells.

1.7 Vertically Aligned Carbon Nanofibers

Vertically aligned carbon nanofibers (VACNF) is a special type of multi-walled carbon nanotube (MWCNT) distinct by its internal morphology consisting of conically stacked graphitic layers rather than cups as shown in Figure 1.14[87-90]. The stacked conical structure is often referred to as herringbone or fishbone structure. The angle (α) between the fiber axis and the graphitic sheets at the sidewall can distinguish the nanofibers and nanotubes. The carbon nanotubes (CNTs) have $\alpha = 0^o$ and the carbon nanofibers (CNFS) have $\alpha > 0^o$[88]. As a result, they possess different mechanical, electrical, and chemical properties. The VACNF with herringbone structure, has both "in-plane" and "interplane" charge transport components, which slightly reduces the electron conductivity along the axis to $\sigma = 2.5x10^5$ S/m, compared to multi-walled CNTs with $\sigma = 10^6$-10^7 S/m[88, 91]. They also have good electrochemical stability and high mechanical strength due to the internal graphitic microstructures. The VACNF array forms a brush-like structure with each nanofiber vertically aligned and free standing on the surface of the substrate. The diameter of the fibers can be varied between ~50 to 300 nm and the length can also be varied from a few hundreds of nanometers to well over 20 microns, through varying the growth time and several other parameters. In addition, the fibers are well separated from each other on the order of ~100 to 300 nm which allows the uniform deposition of catalyst particles. VACNF contains numerous broken graphitic edges around the sidewall and these exposed graphitic edges act as nucleation sites for other active materials to bind with CNFs, unlike the smooth basal plane surface of a CNT[92, 93]. The graphitic edges in the side wall of the VACNFs is ideal for improving the catalyst particles interactions due to the intrinsic nature of the carbon supports which is found to be critical in carbon corrosion and NPs detachment. The catalyst particles deposited on the graphitic edge sites of the

VACNFs will have better utilization and hence VACNFs can help in reducing the overall catalyst loading.

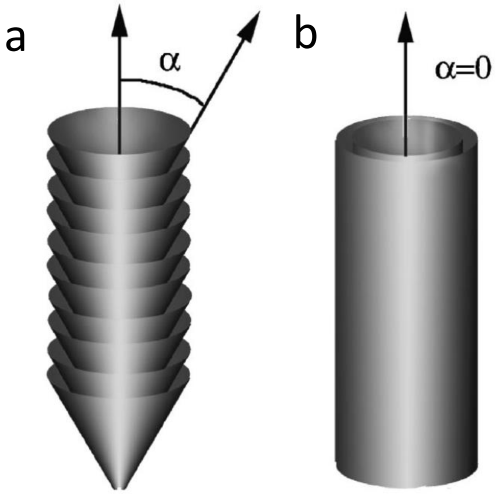

Figure 1.14: Schematic illustration of (a) carbon nanofibers with herringbone structure and (b) carbon nanotubes. (Reproduced with permission from *J. Appl. Phys.* 2005, 97 (4), 041301. © AIP Publsihing. All rights reserved.)

1.8 References

1. Growing at a slower pace, world population is expected to reach 9.7 billion in 2050 and could peak at nearly 11 billion around 2100. June 17, 2019.
2. *International Energy Outlook*; U.S. Energy Information Administration: September 24, 2019.
3. Lelieveld, J.; Klingmüller, K.; Pozzer, A.; Burnett, R.; Haines, A.; Ramanathan, V., Effects of fossil fuel and total anthropogenic emission removal on public health and climate. *PNAS* **2019,** *116* (15), 7192-7197.
4. Hussain, A.; Arif, S. M.; Aslam, M., Emerging renewable and sustainable energy technologies: State of the art. *Renew. Sust. Energ. Rev.* **2017,** *71*, 12-28.
5. Gielen, D.; Boshell, F.; Saygin, D.; Bazilian, M. D.; Wagner, N.; Gorini, R., The role of renewable energy in the global energy transformation. *Energy Strategy Rev.* **2019,** *24*, 38-50.
6. O'hayre, R.; Cha, S.-W.; Colella, W.; Prinz, F. B., *Fuel cell fundamentals*. John Wiley & Sons: 2016.
7. Roth, W.; Benz, J.; Ortiz, B.; Sauer, D.; Steinhüser, A., Fuel cells in photovoltaic hybrid systems for stand-alone power Supplies. In *2nd European PV-Hybrid and Mini-Grid Conference*, Kassel, Germany, 2003; pp 232-239.
8. *Hydrogen energy and fuel cells - a vision of our future*; European Commission: 2003.

9. Zhang, X.; Chen, J., Maximum equivalent power output and performance optimization analysis of an alkaline fuel cell/heat-driven cycle hybrid system. *J. Power Sources* **2011,** *196* (23), 10088-10093.
10. Ramani, V.; Kunz, H. R.; Fenton, J. M., The polymer electrolyte fuel cell. *Interface* **2004,** *13* (3), 17-19.
11. Bose, S.; Kuila, T.; Nguyen, T. X. H.; Kim, N. H.; Lau, K.-t.; Lee, J. H., Polymer membranes for high temperature proton exchange membrane fuel cell: recent advances and challenges. *Prog. Polym. Scie.* **2011,** *36* (6), 813-843.
12. Bazylak, A., Liquid water visualization in PEM fuel cells: A review. *Int. J. Hydrog. Energy* **2009,** *34* (9), 3845-3857.
13. Yan, W.-M.; Chu, H.-S.; Lu, M.-X.; Weng, F.-B.; Jung, G.-B.; Lee, C.-Y., Degradation of proton exchange membrane fuel cells due to CO and CO2 poisoning. *J. Power Sources* **2009,** *188* (1), 141-147.
14. Thangavelautham, J., Degradation in PEM Fuel Cells and Mitigation Strategies Using System Design and Control. In *Proton Exchange Membrane Fuel Cell*, IntechOpen: 2018.
15. Agel, E.; Bouet, J.; Fauvarque, J. F., Characterization and use of anionic membranes for alkaline fuel cells. *J. Power Sources* **2001,** *101* (2), 267-274.
16. Wang, Y.-J.; Qiao, J.; Baker, R.; Zhang, J., Alkaline polymer electrolyte membranes for fuel cell applications. *Chem. Soc. Rev.* **2013,** *42* (13), 5768-5787.
17. Olson, T. S.; Pylypenko, S.; Atanassov, P.; Asazawa, K.; Yamada, K.; Tanaka, H., Anion-Exchange Membrane Fuel Cells: Dual-Site Mechanism of Oxygen Reduction Reaction in Alkaline Media on Cobalt−Polypyrrole Electrocatalysts. *J. Phys. Chem. C* **2010,** *114* (11), 5049-5059.
18. Joghee, P.; Malik, J. N.; Pylypenko, S.; O'Hayre, R., A review on direct methanol fuel cells – In the perspective of energy and sustainability. *MRS Energy Sustain.* **2015,** *2*, E3.
19. Murgia, G.; Pisani, L.; Shukla, A. K.; Scott, K., A Numerical Model of a Liquid-Feed Solid Polymer Electrolyte DMFC and Its Experimental Validation. *J. Electrochem. Soc.* **2003,** *150* (9), A1231-A1245.
20. Cruickshank, J.; Scott, K., The degree and effect of methanol crossover in the direct methanol fuel cell. *J. Power Sources* **1998,** *70* (1), 40-47.
21. Li, Q.; Wang, T.; Havas, D.; Zhang, H.; Xu, P.; Han, J.; Cho, J.; Wu, G., High-Performance Direct Methanol Fuel Cells with Precious-Metal-Free Cathode. *Adv. Sci.* **2016,** *3* (11), 1600140.
22. Aricò, A. S.; Cretì, P.; Kim, H.; Mantegna, R.; Giordano, N.; Antonucci, V., Analysis of the Electrochemical Characteristics of a Direct Methanol Fuel Cell Based on a Pt-Ru/C Anode Catalyst. *J. Electrochem. Soc.* **1996,** *143* (12), 3950-3959.
23. Gao, L.; Abeysiri, M. C.; Winfield, Z. C., Evaluating the Energy Consumption and Emissions of Direct Alcohol Fuel Cells. *Int. J. Energy Sci.* **2012,** *2* (5), 211-216.
24. Hacquard, A. Improving and understanding direct methanol fuel cell (DMFC) performance. Worcester Polytechnic Institute, 2005.

25. Lu, S.; Pan, J.; Huang, A.; Zhuang, L.; Lu, J., Alkaline polymer electrolyte fuel cells completely free from noble metal catalysts. *PNAS* **2008,** *105* (52), 20611-20614.
26. Vilekar, S. A.; Datta, R., The effect of hydrogen crossover on open-circuit voltage in polymer electrolyte membrane fuel cells. *J. Power Sources* **2010,** *195* (8), 2241-2247.
27. Bard, A. J.; Faulkner, L. R., *Electrochemical methods: fundamentals and applications*. Wiley New York: 1980; Vol. 2.
28. Song, C.; Zhang, J., Electrocatalytic oxygen reduction reaction. In *PEM fuel cell electrocatalysts and catalyst layers*, Springer: 2008; pp 89-134.
29. Kübler, M.; Jurzinsky, T.; Ziegenbalg, D.; Cremers, C., Methanol oxidation reaction on core-shell structured Ruthenium-Palladium nanoparticles: Relationship between structure and electrochemical behavior. *J. Power Sources* **2018,** *375*, 320-334.
30. Kunimatsu, K.; Seki, H.; Golden, W.; Gordon, J.; Philpott, M., Carbon monoxide adsorption on a platinum electrode studied by polarization-modulated FT-IR reflection-absorption spectroscopy: II. Carbon monoxide adsorbed at a potential in the hydrogen region and its oxidation in acids. *Langmuir* **1986,** *2* (4), 464-468.
31. Lebedeva, N.; Rodes, A.; Feliu, J.; Koper, M.; Van Santen, R., Role of crystalline defects in electrocatalysis: CO adsorption and oxidation on stepped platinum electrodes as studied by in situ infrared spectroscopy. *J. Phys. Chem. B* **2002,** *106* (38), 9863-9872.
32. Herrero, E.; Álvarez, B.; Feliu, J. M.; Blais, S.; Radovic-Hrapovic, Z.; Jerkiewicz, G., Temperature dependence of the COads oxidation process on Pt (1 1 1), Pt (1 0 0), and Pt (1 1 0) electrodes. *J. Electroanal.* **2004,** *567* (1), 139-149.
33. Wroblowa, H. S.; Yen Chi, P.; Razumney, G., Electroreduction of oxygen: A new mechanistic criterion. *J. Electroanal. Chem.* **1976,** *69* (2), 195-201.
34. Sun, S.; Zhang, G.; Geng, D.; Chen, Y.; Li, R.; Cai, M.; Sun, X., A highly durable platinum nanocatalyst for proton exchange membrane fuel cells: multiarmed starlike nanowire single crystal. *Angew. Chem. Int. Ed. Engl.* **2011,** *123* (2), 442-446.
35. Marković, N.; Schmidt, T.; Stamenković, V.; Ross, P., Oxygen reduction reaction on Pt and Pt bimetallic surfaces: a selective review. *Fuel cells* **2001,** *1* (2), 105-116.
36. Rizo, R.; Herrero, E.; Feliu, J. M., Oxygen reduction reaction on stepped platinum surfaces in alkaline media. *Phys. Chem. Chem. Phys.* **2013,** *15* (37), 15416-15425.
37. Schmidt, T. J.; Paulus, U. A.; Gasteiger, H. A.; Behm, R. J., The oxygen reduction reaction on a Pt/carbon fuel cell catalyst in the presence of chloride anions. *J. Electroanal. Chem.* **2001,** *508* (1), 41-47.
38. Liu, S.; White, M. G.; Liu, P., Mechanism of Oxygen Reduction Reaction on Pt(111) in Alkaline Solution: Importance of Chemisorbed Water on Surface. *J. Phys. Chem. C* **2016,** *120* (28), 15288-15298.
39. Nørskov, J. K.; Rossmeisl, J.; Logadottir, A.; Lindqvist, L.; Kitchin, J. R.; Bligaard, T.; Jónsson, H., Origin of the Overpotential for Oxygen Reduction at a Fuel-Cell Cathode. *J. Phys. Chem. B* **2004,** *108* (46), 17886-17892.

40. Tripković, V.; Skúlason, E.; Siahrostami, S.; Nørskov, J. K.; Rossmeisl, J., The oxygen reduction reaction mechanism on Pt(111) from density functional theory calculations. *Electrochim. Acta* **2010,** *55* (27), 7975-7981.

41. Wang, X. X.; Swihart, M. T.; Wu, G., Achievements, challenges and perspectives on cathode catalysts in proton exchange membrane fuel cells for transportation. *Nat. Catal.* **2019,** *2* (7), 578-589.

42. Nie, Y.; Li, L.; Wei, Z., Recent advancements in Pt and Pt-free catalysts for oxygen reduction reaction. *Chem. Soc. Rev.* **2015,** *44* (8), 2168-2201.

43. Ren, X.; Lv, Q.; Liu, L.; Liu, B.; Wang, Y.; Liu, A.; Wu, G., Current progress of Pt and Pt-based electrocatalysts used for fuel cells. *Sustain. Energy Fuels* **2020,** *4* (1), 15-30.

44. Sui, S.; Wang, X.; Zhou, X.; Su, Y.; Riffat, S.; Liu, C.-j., A comprehensive review of Pt electrocatalysts for the oxygen reduction reaction: Nanostructure, activity, mechanism and carbon support in PEM fuel cells. *J. Mater. Chem. A* **2017,** *5* (5), 1808-1825.

45. Jung, N.; Chung, D. Y.; Ryu, J.; Yoo, S. J.; Sung, Y.-E., Pt-based nanoarchitecture and catalyst design for fuel cell applications. *Nano Today* **2014,** *9* (4), 433-456.

46. Shao, M.; Chang, Q.; Dodelet, J.-P.; Chenitz, R., Recent advances in electrocatalysts for oxygen reduction reaction. *Chem. Rev.* **2016,** *116* (6), 3594-3657.

47. Shin, D.; Jeong, B.; Choun, M.; Ocon, J. D.; Lee, J., Diagnosis of the measurement inconsistencies of carbon-based electrocatalysts for the oxygen reduction reaction in alkaline media. *RSC Adv.* **2015,** *5* (2), 1571-1580.

48. Minteer, S., *Alcoholic Fuels*. 2006.

49. Hamnett, A., Mechanism and electrocatalysis in the direct methanol fuel cell. *Catalysis Today* **1997,** *38* (4), 445-457.

50. Wieckowski, A.; Nørskov, J. K., *Fuel cell science: Theory, Fundamenatals, and Biocatalysis*. Wiley: 2010.

51. Moura, A. S.; Fajín, J. L.; Mandado, M.; Cordeiro, M. N. D., Ruthenium–platinum catalysts and direct methanol fuel cells (DMFC): a review of theoretical and experimental breakthroughs. *Catalysts* **2017,** *7* (2), 47.

52. Li, B.; Higgins, D. C.; Zhu, S.; Li, H.; Wang, H.; Ma, J.; Chen, Z., Highly active Pt–Ru nanowire network catalysts for the methanol oxidation reaction. *Catal. Commun.* **2012,** *18,* 51-54.

53. Sgroi, M. F.; Zedde, F.; Barbera, O.; Stassi, A.; Sebastián, D.; Lufrano, F.; Baglio, V.; Aricò, A. S.; Bonde, J. L.; Schuster, M., Cost analysis of direct methanol fuel cell stacks for mass production. *Energies* **2016,** *9* (12), 1008.

54. Wilson, A. K., Gregory. Papageorgopoulos, Dimitrios *Fuel Cell System Cost - 2017*; DOE Hydrogen and Fuel Cells Program November, 30, 2017.

55. Pollet, B. G.; Kocha, S. S.; Staffell, I., Current status of automotive fuel cells for sustainable transport. *Curr. Opin. Electrochem.* **2019,** *16,* 90-95.

56. Du, L.; Shao, Y.; Sun, J.; Yin, G.; Liu, J.; Wang, Y., Advanced catalyst supports for PEM fuel cell cathodes. *Nano Energy* **2016,** *29,* 314-322.

57. Noël, J.-M.; Yu, Y.; Mirkin, M. V., Dissolution of Pt at Moderately Negative Potentials during Oxygen Reduction in Water and Organic Media. *Langmuir* **2013,** *29* (5), 1346-1350.
58. Holby, E. F.; Morgan, D., Application of Pt Nanoparticle Dissolution and Oxidation Modeling to Understanding Degradation in PEM Fuel Cells. *J. Electrochem. Soc.* **2012,** *159* (5), B578-B591.
59. Darling, R. M.; Meyers, J. P., Kinetic model of platinum dissolution in PEMFCs. *J. Electrochem. Soc.* **2003,** *150* (11), A1523.
60. Shao, Y.; Yin, G.; Gao, Y., Understanding and approaches for the durability issues of Pt-based catalysts for PEM fuel cell. *J. Power Sources* **2007,** *171* (2), 558-566.
61. Vasquez, L., *Fuel cell research trends*. Nova Publishers: 2007.
62. Anwar, M. T.; Yan, X.; Asghar, M. R.; Husnain, N.; Shen, S.; Luo, L.; Zhang, J., Recent advances in hybrid support material for Pt-based electrocatalysts of proton exchange membrane fuel cells. *Int. J. Energy Res.* **2019,** *43* (7), 2694-2721.
63. Paul, T. Y.; Gu, W.; Makharia, R.; Wagner, F. T.; Gasteiger, H. A., The impact of carbon stability on PEM fuel cell startup and shutdown voltage degradation. *ECS Trans.* **2006,** *3* (1), 797.
64. Shao, Y.; Yin, G.; Wang, Z.; Gao, Y., Proton exchange membrane fuel cell from low temperature to high temperature: material challenges. *J. Power Sources* **2007,** *167* (2), 235-242.
65. Wang, J.; Yin, G.; Shao, Y.; Zhang, S.; Wang, Z.; Gao, Y., Effect of carbon black support corrosion on the durability of Pt/C catalyst. *J. Power sources* **2007,** *171* (2), 331-339.
66. Dam, V.; Jayasayee, K.; De Bruijn, F., Determination of the potentiostatic stability of PEMFC electro catalysts at elevated temperatures. *Fuel Cells* **2009,** *9* (4), 453-462.
67. Candelaria, S. L.; Shao, Y.; Zhou, W.; Li, X.; Xiao, J.; Zhang, J.-G.; Wang, Y.; Liu, J.; Li, J.; Cao, G., Nanostructured carbon for energy storage and conversion. *Nano Energy* **2012,** *1* (2), 195-220.
68. Shao, Y.; Liu, J.; Wang, Y.; Lin, Y., Novel catalyst support materials for PEM fuel cells: current status and future prospects. *J. Mater. Chem.* **2009,** *19* (1), 46-59.
69. Antolini, E., Carbon supports for low-temperature fuel cell catalysts. *Appl. Catal B* **2009,** *88* (1), 1-24.
70. Wang, D.-W.; Su, D., Heterogeneous nanocarbon materials for oxygen reduction reaction. *Energy Environ. Sci.* **2014,** *7* (2), 576-591.
71. Tong, X.; Zhang, J.; Zhang, G.; Wei, Q.; Chenitz, R. g.; Claverie, J. P.; Sun, S., Ultrathin carbon-coated Pt/carbon nanotubes: a highly durable electrocatalyst for oxygen reduction. *Chem. Mater.* **2017,** *29* (21), 9579-9587.
72. Bessel, C. A.; Laubernds, K.; Rodriguez, N. M.; Baker, R. T. K., Graphite Nanofibers as an Electrode for Fuel Cell Applications. *J. Phys. Chem. B* **2001,** *105* (6), 1115-1118.
73. Lee, K.; Zhang, J.; Wang, H.; Wilkinson, D. P., Progress in the synthesis of carbon nanotube- and nanofiber-supported Pt electrocatalysts for PEM fuel cell catalysis. *J. Appl. Electrochem.* **2006,** *36* (5), 507-522.

74. Li, W.; Waje, M.; Chen, Z.; Larsen, P.; Yan, Y., Platinum nanopaticles supported on stacked-cup carbon nanofibers as electrocatalysts for proton exchange membrane fuel cell. *Carbon* **2010,** *48* (4), 995-1003.

75. Seo, M. H.; Choi, S. M.; Kim, H. J.; Kim, W. B., The graphene-supported Pd and Pt catalysts for highly active oxygen reduction reaction in an alkaline condition. *Electrochem. Commun.* **2011,** *13* (2), 182-185.

76. Zhu, C.; Dong, S., Recent progress in graphene-based nanomaterials as advanced electrocatalysts towards oxygen reduction reaction. *Nanoscale* **2013,** *5* (5), 1753-1767.

77. Shao, Y.; Zhang, S.; Wang, C.; Nie, Z.; Liu, J.; Wang, Y.; Lin, Y., Highly durable graphene nanoplatelets supported Pt nanocatalysts for oxygen reduction. *J. Power Sources* **2010,** *195* (15), 4600-4605.

78. Fortunato, G. V.; de Lima, F.; Maia, G., Oxygen-reduction reaction strongly electrocatalyzed by Pt electrodeposited onto graphene or graphene nanoribbons. *J. Power Sources* **2016,** *302*, 247-258.

79. Lim, D.-H.; Wilcox, J., Mechanisms of the oxygen reduction reaction on defective graphene-supported Pt nanoparticles from first-principles. *J. Phys. Chem. C* **2012,** *116* (5), 3653-3660.

80. Li, Y.; Li, Y.; Zhu, E.; McLouth, T.; Chiu, C.-Y.; Huang, X.; Huang, Y., Stabilization of high-performance oxygen reduction reaction Pt electrocatalyst supported on reduced graphene oxide/carbon black composite. *J. Am. Chem. Soc.* **2012,** *134* (30), 12326-12329.

81. Tiwari, J. N.; Kemp, K. C.; Nath, K.; Tiwari, R. N.; Nam, H.-G.; Kim, K. S., Interconnected Pt-nanodendrite/DNA/reduced-graphene-oxide hybrid showing remarkable oxygen reduction activity and stability. *ACS Nano* **2013,** *7* (10), 9223-9231.

82. Marie, J.; Chenitz, R.; Chatenet, M.; Berthon-Fabry, S.; Cornet, N.; Achard, P., Highly porous PEM fuel cell cathodes based on low density carbon aerogels as Pt-support: Experimental study of the mass-transport losses. *J. Power Sources* **2009,** *190* (2), 423-434.

83. Hamoudi, Z.; Brahim, A.; El Khakani, M. A.; Mohamedi, M., Electroanalytical Study of Methanol Oxidation and Oxygen Reduction at Carbon Nanohorns-Pt Nanostructured Electrodes. *Electroanalysis* **2013,** *25* (2), 538-545.

84. Celorrio, V.; Flórez-Montaño, J.; Moliner, R.; Pastor, E.; Lázaro, M., Fuel cell performance of Pt electrocatalysts supported on carbon nanocoils. *Int. J. Hydrog. Energy* **2014,** *39* (10), 5371-5377.

85. Wang, X. X.; Tan, Z. H.; Zeng, M.; Wang, J. N., Carbon nanocages: A new support material for Pt catalyst with remarkably high durability. *Sci. Rep.* **2014,** *4*, 4437.

86. Zhang, C.; Xu, L.; Shan, N.; Sun, T.; Chen, J.; Yan, Y., Enhanced electrocatalytic activity and durability of Pt particles supported on ordered mesoporous carbon spheres. *ACS Catal.* **2014,** *4* (6), 1926-1930.

87. Merkulov, V. I.; Melechko, A. V.; Guillorn, M. A.; Lowndes, D. H.; Simpson, M. L., Alignment mechanism of carbon nanofibers produced by plasma-enhanced chemical-vapor deposition. *Appl. Phys. Lett.* **2001,** *79* (18), 2970-2972.

88. Melechko, A. V.; Merkulov, V. I.; McKnight, T. E.; Guillorn, M. A.; Klein, K. L.; Lowndes, D. H.; Simpson, M. L., Vertically aligned carbon nanofibers and related structures: Controlled synthesis and directed assembly. *J. Appl. Phys.* **2005,** *97* (4), 041301.

89. Meyyappan, M.; Delzeit, L.; Cassell, A.; Hash, D., Carbon nanotube growth by PECVD: a review. *Plasma Sources Sci. Technol.* **2003,** *12* (2), 205.

90. Li, J.; Pandey, G. P., Advanced physical chemistry of carbon nanotubes. *Annu. Rev. Phys. Chem.* **2015,** *66*, 331-56.

91. Ngo, Q.; Yamada, T.; Suzuki, M.; Ominami, Y.; Cassell, A. M.; Li, J.; Meyyappan, M.; Yang, C. Y., Structural and Electrical Characterization of Carbon Nanofibers for Interconnect Via Applications. *IEEE Trans. Nanotechol.* **2007,** *6* (6), 688-695.

92. Li, W.; Waje, M.; Chen, Z.; Larsen, P.; Yan, Y., *Platinum nanopaticles supported on stacked-cup carbon nanofibers as electrocatalysts for proton exchange membrane fuel cell*. 2010; Vol. 48, p 995-1003.

93. Landis, E. C.; Klein, K. L.; Liao, A.; Pop, E.; Hensley, D. K.; Melechko, A. V.; Hamers, R. J., Covalent Functionalization and Electron-Transfer Properties of Vertically Aligned Carbon Nanofibers: The Importance of Edge-Plane Sites. *Chem. Mater.* **2010,** *22* (7), 2357-2366.

Chapter 2 - Experimental Methods and Characterization

2.1 Overview of PECVD Growth Process

VACNFs were grown on the graphite paper (0.2 mm thick) substrate using a Black Magic DC-biased Plasma Enhanced Chemical Vapor Deposition (PEVCD) system manufactured by Aixtron, CA. The kinetics of VACNF growth, ratio of feedstock, plasma chemistry, growth conditions, and the impact of different growth parameters have been discussed thoroughly in the previous reports[1-3]. The major advantage of the PECVD system over the conventional thermal CVD is that the plasma enhancement controls the direction of the growth of nanostructures and reduces the activation energy required for the deposition process. The vertical alignment of the CNF is a result of uniform tensile stress created across the entire catalyst/CNF interface by its interaction with the high electric field. The growth of VACNF arrays requires a catalyst and Fe, Ni, Co are found to be efficient in breaking the bonds in the carbon precursor. For all our studies, we used a Ni thin film as a catalyst for CNF growth as Ni catalyst is found to create the herringbone type structure and the Fe and Co catalysts create nanotubes[4]. The deposited catalyst thin film needs to be sintered to form discrete Ni nanoparticles (NPs) to grow fibers when the carbon source is introduced. The resulting fiber diameter and distribution of fibers are determined by the Ni NPs which depends on the catalyst film thickness. A thinner catalyst film results in smaller fiber diameter. We kept the thickness of Ni catalyst film to 22 nm in all our studies to get an optimized uniform growth of VACNFs. The Ni NPs are pushed upwards once the carbon flux is introduced and it becomes elongated. As the growth continues, the Ni NPs forms a teardrop shape, and this results in the deposited graphitic layers being conically stacked. During the growth process, we used ammonia (NH_3) as a reducing agent and an etchant gas to remove the amorphous carbon deposited during the growth, hence achieving better growth. The fibers resulting from each Ni NP is well separated and hence creating an open-3D brush-like structure. This open space allows an easy deposition of active materials and hence finding its application as catalyst support. Figure 2.1 shows the PECVD reactor.

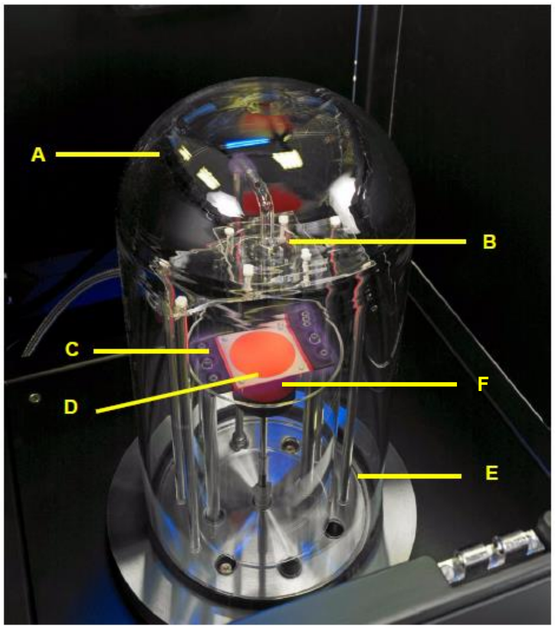

A – Quartz Belljar
B – Showerhead
C – Graphite Heater
D – Sample Stage
E – Baseplate
F – Plasma directing disks

Figure 2.1: PEVCD reactor (Blackmagic, Aixtron, Germany).

2.2 Procedure for the VACNF Growth

The procedure for the growth of VACNFs was modified based on the previously reported procedure[1, 2, 5]. The growth chamber was purged with UHP N_2 (1000 sccm) for 600 s and the chamber was vacuumed to 13 mTorr before starting the recipe. At first, the Ni coated graphite paper substrate was heated to 500^{o}C in 250 sccm NH_3 at a pressure of 3.9 Torr for 150 s and then followed by a 40 W DC plasma treatment for 60 s. This pretreatment procedure has combined effects of thermal dewetting and NH_3 plasma etching which helped to break down the 22 nm Ni film into randomly distributed Ni NPs that catalyzed the growth of VACNFs in a tip growth mode.

After the initial pretreatment, a mixture of acetylene (63 sccm) and NH_3 (250 sccm) was introduced at a pressure of 6.2 Torr as the precursors for the growth of VACNFs at a substrate temperature of 750 ^{o}C. The plasma power was kept at 45 W for 30 min to grow the VACNFs with an average length of 5 μm, 60 min to grow the VACNFs with an average length of 8 μm, and 90 min to grow the VACNFs with an average length of 11 μm. Finally, the substrate with VACNFs was allowed to cool until 140 ^{o}C in the presence of N_2 (1000 sccm), and they are removed from the vacuum once the temperature reaches 90 ^{o}C. Figure 2.2 illustrates the schematic of the VACNF growth process. For a 30 min growth, the system yields VACNF arrays with an areal density of 1.0 x 10^9 CNF/cm^2 and average diameter of ~150 nm[6].

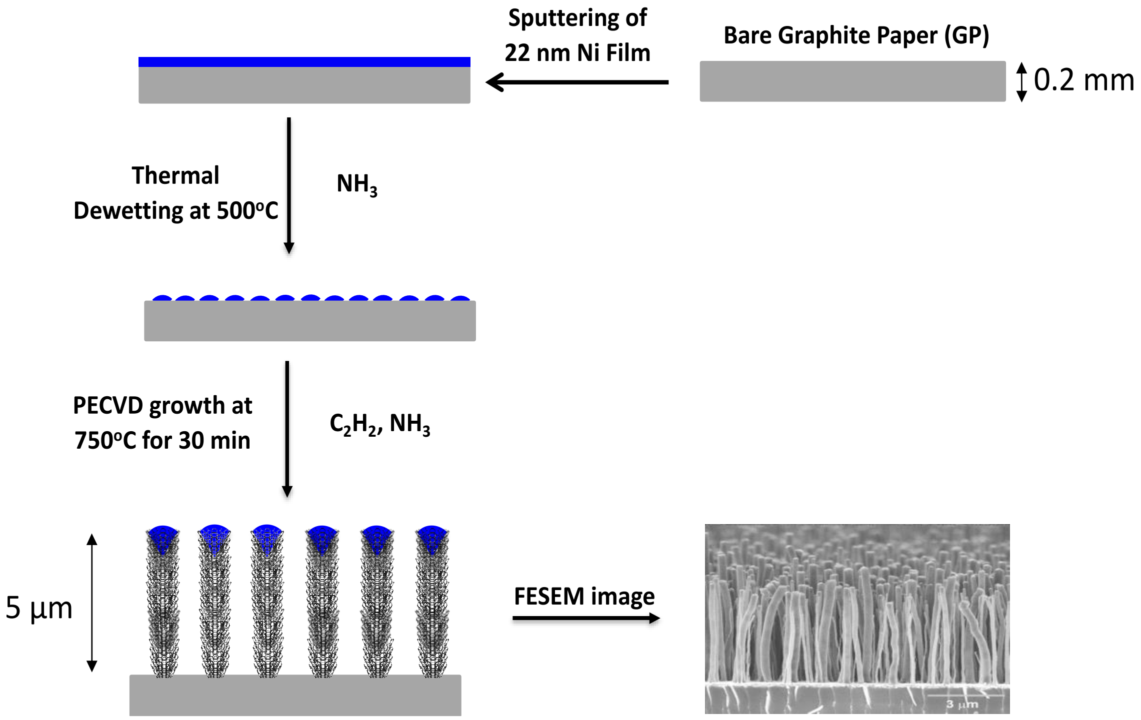

Figure 2.2: Schematic illustration of the VACNF growth process.

The mass of carbon on the VACNFs can't be reliably measured by weighing the sample before and after growth due to various factors. So, the mass of VACNFs can be estimated using equation 2.1:

$$Mass\ of\ VACNFs = Dx\ V \quad (2.1)$$

where D and V are the density and volume of the CNFs. D = 2.26 g/cm^3 assuming that the fibers are graphitic in nature. For a 5 μm, 8 μm, and 11 μm long VACNF array, the mass of carbon was estimated to be 177, and 283, and 389 μg/cm^2, respectively. It needs to be noted that this method is quite conservative and likely the carbon mass can be less. The mass of VACNFs is used to calculate the wt% of metal catalysts after sputter deposited.

2.3 Catalysts Deposition

There are multiple ways to deposit catalyst particles on the substrate/support material and we have employed ion beam sputtering technique for the preparation of pure and highly effective catalysts film/particles. Ion beam sputtering has advantages such as the ease of sputtering any material with high purity, good adhesion to the substrate, controlled sputtering rate, and an accurate estimation of metal loading. Ion beam sputtering uses an ion source (Ar^+) to generate a focused ion beam that sputters a target material (metal or dielectric) onto a substrate. An inert gas like argon is introduced into the system at a pressure of 2.0 x 10^{-4} Torr to purge the two penning ion guns. Then, the high electric field at the penning ion causes the introduced Ar gas to get ionized, creating a plasma. The resulting Ar+ ions are accelerated towards the target, and via momentum transfer between the ion and target, the target material gets sputtered towards the substrate. Figure 3.3 presents the schematic illustration of ion beam sputtering.

The Ni catalyst film was sputtered at a rate of 0.5 Å/s by applying an 8 keV beam energy. The substrate holder was set and a rock angle of 7^o with 8 rocks/sec and rotated at a constant speed of 30 rpm. For the sputtering of Pt/PtRu NPs, the sputtering rate was maintained at 0.5 Å/s by applying a 4.5 keV beam energy, and the substrate holder was fixed at an angle of 5^o and rotated at a constant speed of 15 rpm. Due to the shadow effect, the sample stage can't be tilted at any angle >5° for after growth depositions. All the sputtering was done under a system pressure between 8.0 x 10^{-5} and 1.0 x 10^{-4} Torr.

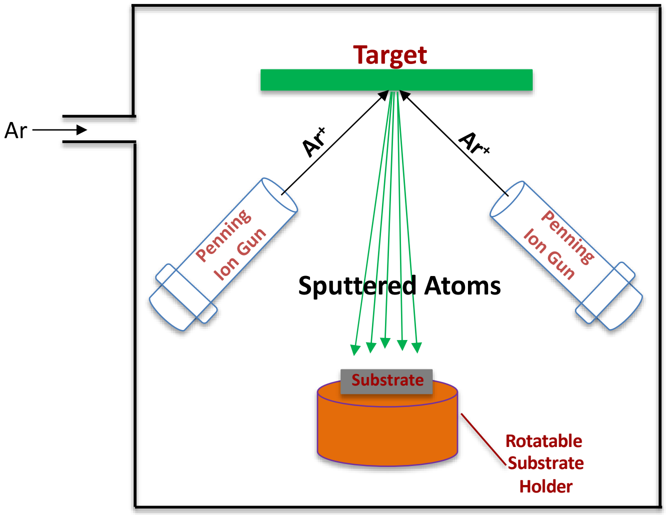

Figure 2.3: Schematic illustration of ion beam sputtering.

2.4 Experimental Setup for Electrochemical Characterization

All the electrochemical characterizations were performed in a three-electrode electrochemical cell using a rotating disk electrode (RDE) with a glassy carbon (GC) disk of 0.078 cm^2 embedded in PEEK surface or a rotating ring disk electrode (RRDE) with a GC disk of 0.125 cm^2 and a Pt disk (O.D. 7.0 mm and I.D. 5.0 mm) of 0.189 cm^2 in PEEK surface controlled by a CHI 760D electrochemical workstation. Figures 2.4a-2.4c displays the schematic of an RDE, RRDE, and CHI 760D potentiostat. The RDE or RRDE is controlled by the RRDE-3A Rotating Ring Disk Electrode Apparatus Ver.2.0. (Figure 2.4d) when using in the hydrodynamic conditions. The working electrode involved in this thesis is either a VACNF based catalyst modified RDE or a catalyst thin film formed on RDE/RRDE from the catalyst powders. For any VACNF based catalyst, the working electrode was prepared by punching out a 6.0 mm disk and mounting it on the RDE using a silver conductive epoxy paste. The modified RDE electrode was dried at 70 °C for 2 hours prior to use. For any powder catalysts, the required amount of catalysts powder was mixed with a mixture of organic/water/Nafion solution and sonicated for 1 hour. Then a few μL of the formed ink solution was deposited to get a thin catalyst film. The deposited electrode was dried at RT prior to use. Before drop casting the catalyst ink, the glassy carbon surface was polished using an alumina slurry with 50 nm particles to get a mirror finish. A coiled Pt wire with surface area 10 times higher than the working electrode was employed as a counter electrode. A silver-silver chloride (Ag/AgCl) dipped in 1.0 M KCl or 4.0 M KCl was used as the reference electrode in acidic condition, and a mercury-mercuric oxide (Hg/HgO) dipped in 1.0 M NaOH was used as the reference electrode in alkaline condition. We used different electrolytes such as 0.10 M KOH, 0.50 M H_2SO_4, and 0.10 M $HClO_4$ to study the activity of the catalysts.

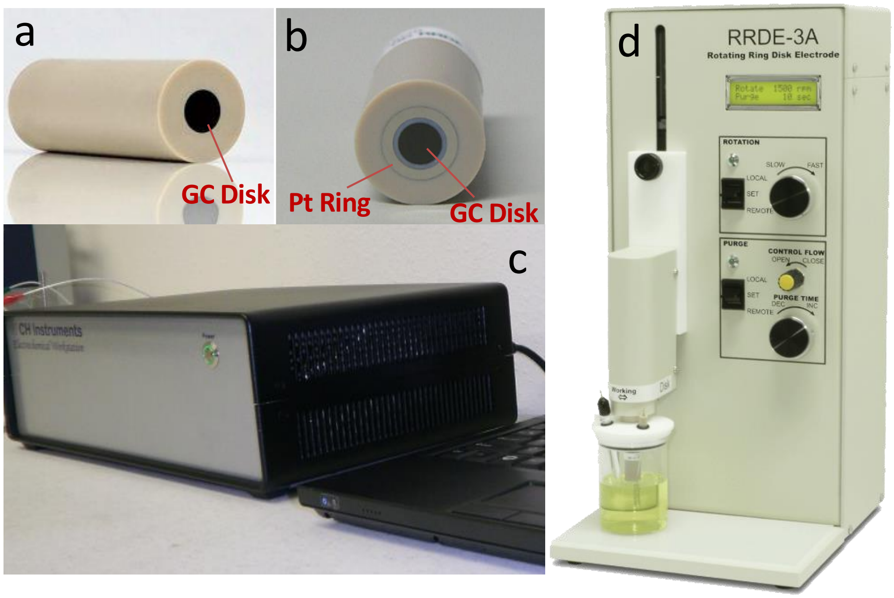

Figure 2.4: (a) Rotating disk electrode, (b) Rotating ring disk electrode; (c) CHI 760D electrochemical workstation from CH Instruments, and (d) RRDE-3A Rotating ring disk electrode apparatus from ALS, Japan.

The measured potentials versus the reference electrode were converted versus the reversible hydrogen electrode (RHE) for easy comparison with the literature. The electrode potential values versus the Hg/HgO reference electrode (in experiments carried out in 0.10 M KOH solution, pH = 13.00) are converted to the values versus the reversible hydrogen electrode (RHE) using the following equation:

$$E_{(\text{vs. RHE})} = E_{(\text{vs. Hg/HgO})} + E_{\text{Hg/HgO vs. NHE}} + 0.059\ \text{pH} = E_{(\text{vs. Hg/HgO})} + 0.907\ \text{V} \qquad (2.2)$$

where $E_{(\text{vs. Hg/HgO})}$ is the experimentally measured potential versus the Hg/HgO reference electrode (with 1.0 M NaOH filling solution), and $E_{\text{Hg/HgO vs. NHE}}$ = 0.140 V is the Hg/HgO reference electrode potential versus the NHE.

Similarly, the electrode potential values versus the Ag/AgCl reference electrode (in experiments carried out in 0.50 M H_2SO_4 solution, pH = 0.00) are converted to the values versus the RHE using the following equation:

$$E_{(\text{vs. RHE})} = E_{(\text{vs. Ag/AgCl})} + E_{\text{Ag/AgCl vs. NHE}} + 0.059\ \text{pH} = E_{(\text{vs. Ag/AgCl})} + 0.200\ \text{V} \qquad (2.3)$$

where $E_{(\text{vs. Ag/AgCl})}$ is the experimentally measured potential versus the Ag/AgCl reference electrode (with 4.0 M KCl filling solution), and $E_{\text{Ag/AgCl vs. NHE}}$ = 0.200 V is the Ag/AgCl reference electrode potential versus the NHE.

Similarly, the electrode potential values versus the Ag/AgCl reference electrode (in experiments carried out in 0.10 M $HClO_4$ solution, pH = 1.00) are converted to the values versus the RHE using the following equation:

$$E_{(\text{vs. RHE})} = E_{(\text{vs. Ag/AgCl})} + E_{\text{Ag/AgCl vs. NHE}} + 0.059\ \text{pH} = E_{(\text{vs. Ag/AgCl})} + 0.281\ \text{V} \qquad (2.4)$$

where $E_{(\text{vs. Ag/AgCl})}$ is the experimentally measured potential versus the Ag/AgCl reference electrode (with 1.0 M KCl filling solution), and $E_{\text{Ag/AgCl vs. NHE}}$ = 0.222 V is the Ag/AgCl reference electrode potential versus the NHE.

The experimental setup for all the electrochemical characterizations is illustrated in Figure 2.5. We modified the purging system by using a bottom purge that has a glass porous frit at the bottom of the electrochemical cell which breaks the gas bubbles into smaller ones. This ensures effective purging in a short time. Before evaluating the electrochemical properties of the prepared catalyst, the solution was bottom purged with Ar/O_2 depending on the measurements for 5 to 10 minutes or until its completely saturated. All the initial purging mentioned in this thesis was done by bottom purging unless and until its mentioned. During electrochemical measurements, the respective gas was purged from the top through Teflon tube to maintain a particular atmosphere. The gas flow rate was 60 sccm for both the bottom and top purge.

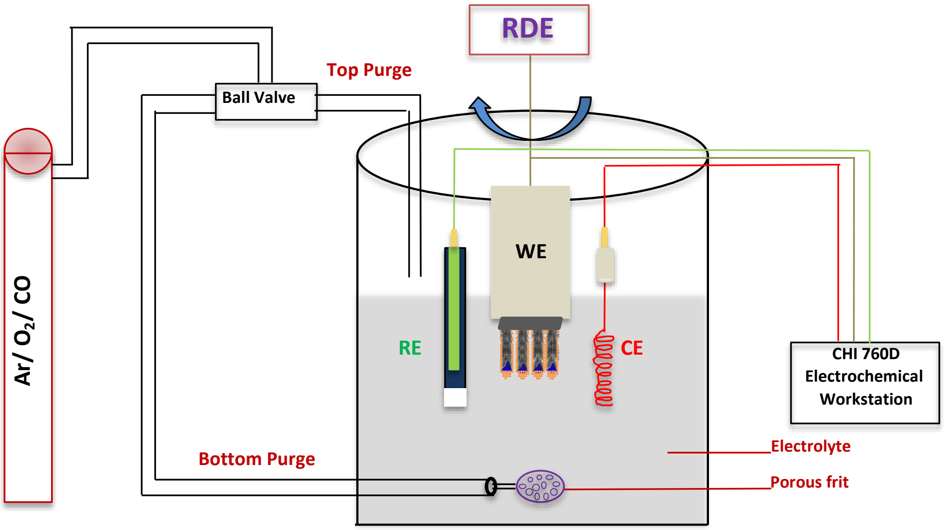

Figure 2.5: Schematic representation of the three-electrode electrochemical experiment setup.

2.5 Electrochemical Characterization Techniques

The catalysts were evaluated using different electrochemical techniques such as cyclic voltammetry (CV), linear sweep voltammetry (LSV), amperometric i-t curve, CO-stripping voltammetry, and electrochemical impedance spectroscopy (EIS). The catalyst activity towards the ORR was studied using the RDE and RRDE technique. All these techniques were performed using a CHI-760D electrochemical workstation controlled by a CHI electrochemical software. The electrodes were not rotated while performing steady-state measurements.

2.5.1 Cyclic Voltammetry

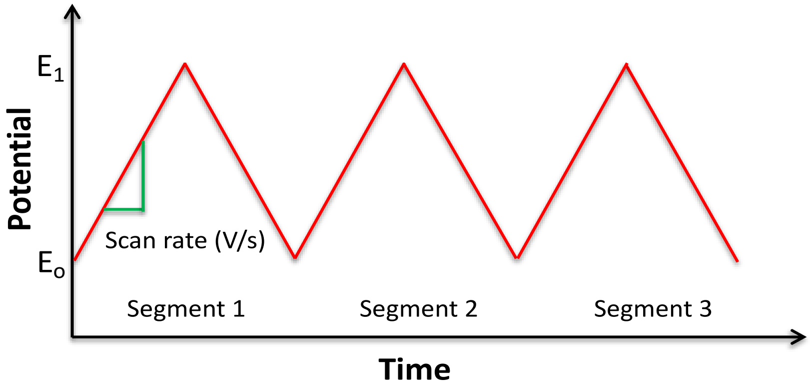

Figure 2.6: Applied potential waveform for the CV.

Cyclic Voltammetry is a useful technique to obtain both qualitative and quantitative information about the catalysts being tested and the involved electrochemical reactions in the applied potential range. In general, CV is performed by sweeping the potential between two defined points where the catalyst is repeatedly oxidized or reduced, and the current responses are recorded against the applied potential. Figure 2.6 shows the applied potential waveform as a function of time. The sign of the recorded current tells if the occurring electrochemical reaction is a reduction or oxidation reaction. Apart from oxidation or reduction, there are some other electrochemical reactions that occur on Pt-based catalysts, which acts as a signature characteristic feature for it. Figure 2.7 shows a typical CV of Pt/C recorded at a scan rate of 50 mV/s between 0.00 and 1.20 V (vs. RHE). The recorded CV can be divided into different regions as denoted. Integrating the hydrogen adsorption or desorption peak area can lead to the estimation of electrochemical active surface area (ECSA) which is a quantitative measure of the catalyst surface area available for electron transfer.

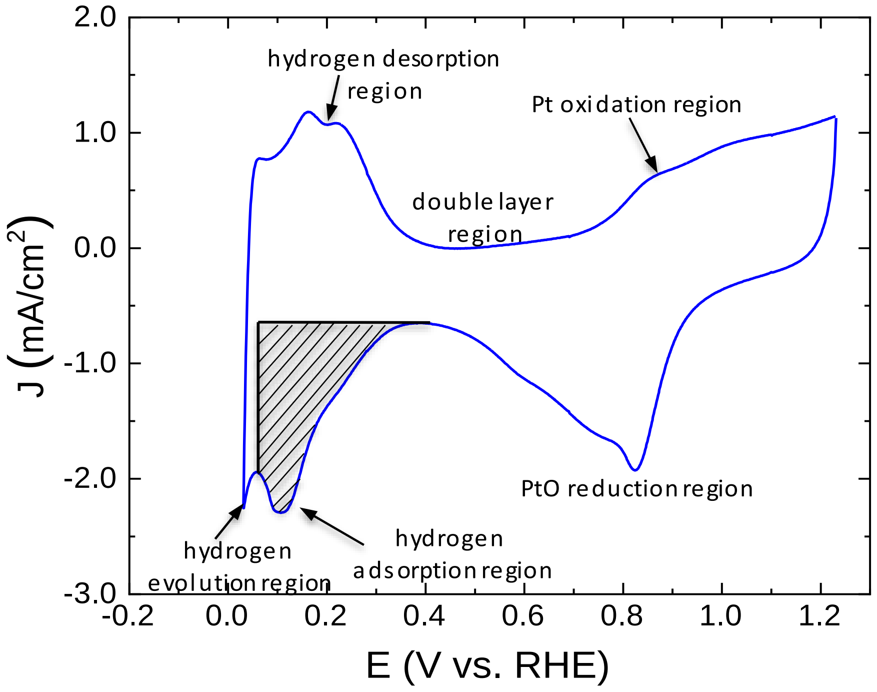

Figure 2.7: A typical Cyclic Voltammetry of 20 % Pt/C recorded in Ar-saturated 0.10 M $HClO_4$ solution with a scan rate of 50 mV/s.

ECSA can be calculated by using the following formula:

$$ECSA = \frac{Q_{Hads}}{Q_C * m_{Pt}} \qquad (2.5)$$

where Q_{Hads} is the charge for one monolayer of hydrogen adsorption on the metal surface, $Q_C = 210\ \mu C/cm^2$ is the charge associated with forming a close-packed monolayer of hydrogen atoms on 1 cm^2 of Pt surface and m_{Pt} is the mass of platinum.

2.5.2 Linear Sweep Voltammetry

In LSV, the current is recorded as a function of potential by scanning the potential between two different points. The potential is scanned from a lower limit to a higher limit for an oxidation reaction and scanned vice versa for the reduction reaction. Figure 2.8 shows the applied potential waveform as a function of time.

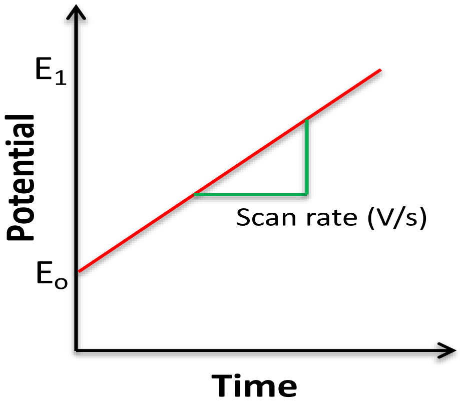

Figure 2.8: Applied potential waveform for the LSV.

2.5.3 Rotating Disk Electrode

The newly developed catalysts need to be evaluated to identify its electrochemical performance towards a particular electrocatalytic reaction. However, testing the prepared catalysts by assembling an MEA every single time requires abundant materials and time-consuming, and also the full cell testing can be affected by various factors which makes it difficult to evaluate the catalytic activity. Therefore, a rapid screening technique is required to evaluate the catalysts without any complications. RDE is the commonly used electrochemical technique at lab scale for testing the ORR activity of the catalysts in a half-cell setup. It can give detailed information about the kinetics and mechanism of the electrode reaction (i.e. ORR). Diffusion and convection are the two major processes for material transport in the electrochemical cell. When the RDE is rotated in the solution, the spinning disk drags a steady stream of solution from the bulk to the surface of the electrode and the resulting centrifugal force flings the solution away from the electrode surface as shown in Figure 2.9. The fluid at the surface is constantly replenished by the fresh solution flowing up perpendicular to the surface. As a result of convection, a thin layer of the solution near the electrode surface tends to rotate with the electrode. The convection velocity of the solution is improved as the rotation rate increases, and more flux of reactant reaches the electrode surface. The diffusion layer gets thinner as the rotation rate increases. The electrode rotation rate can be precisely controlled by RDE through which the quantitatively control of diffusion layer thickness can be realized, resulting in feasible quantitative analysis of the electrode reaction kinetics. In the absence of convection, the thickness of diffusion layer near the electrode surface will keep increasing which prolongs the reaction time, resulting in non-steady-state current density.

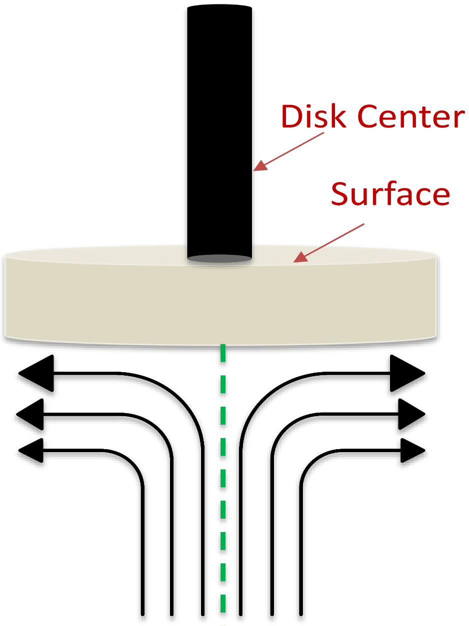

Figure 2.9: Schematic illustration of the solution flow pattern near the RDE surface.

The RDE experiment is done by recording a series of LSV at different rotation speeds between 500 and 3000 rpm and a scan rate of 10 mV/s. The resulting LSV curves have a sigmoidal shape as presented in Figure 2.10a. The current is controlled by the reaction kinetics at the initial potential and as the potential is increased or decreased, the current measured is now controlled by both the kinetics and mass transport. Finally, when the potential is high enough, the measured current is completely controlled by the mass transport. Beyond this point, any further increase in the potential does not change the current and it creates a diffusion-controlled current plateau as shown in Figure 2.10a. The measured diffusion-controlled current is described by the following Levich equation[7]:

$$I_d = 0.20nFA_{geo}[O_2]{D_{O_2}}^{2/3}\nu^{-1/6}\omega^{1/2} \tag{2.6}$$

where n is the electron transfer numbers in ORR, F is the Faraday constant (96,485 C mol^{-1}), A is the geometric electros area, $[O_2]$ is the concentration of dissolved O_2, D_{O_2} is the diffusion coefficient of O_2, ν is the kinematic viscosity of the electrolyte solution, and ω is the angular rotation rate.

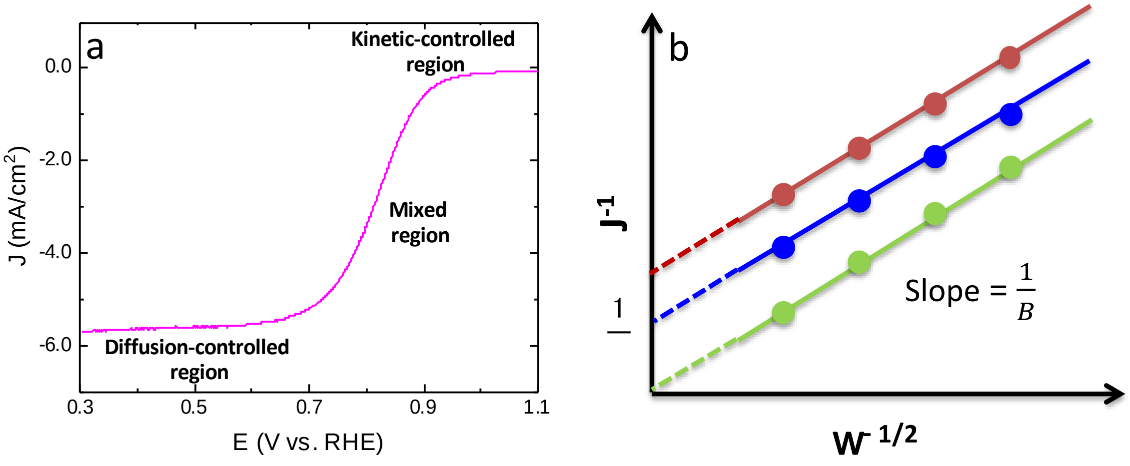

Figure 2.10: ORR polarization curve for 20% Pt/C in 0.10 M $HClO_4$ and (b) A model of KL plot derived from the RDE voltammogram.

The overall measured current density in the entire potential region can be given by the Koutecky-Levich equation as below[7]:

$$\frac{1}{J} = \frac{1}{B\omega^{1/2}} + \frac{1}{J_k} \tag{2.7}$$

where J_k is the kinetic-controlled current density and B is the Levich constant. From the set of LSVs recorded at different rpm, a Koutecky-Levich (KL) plot can be constructed between the inverse of measure current density versus the inverse of the square root of ω as shown in Figure

2.10b. From this plot, we can extract the slope (1/B) and inverse of kinetic-controlled current density. From the slope (1/B) of the KL plot, the n value can be calculated as given in equation 2.8. The determined n number can help in identifying the reaction mechanism of the ORR.

$$B = 0.20nF[O_2]{D_{O_2}}^{2/3}\nu^{-1/6} \qquad (2.8)$$

2.5.4 Rotating Ring Disk Electrode

RRDE can be used to analyze the nature of the electrode reaction products generated. In RRDE the product generated by the electrode reaction at the disk electrode is transported into the ring electrode by centrifugal force and it is detected at the ring electrode. Overall a reduction occurs reaction occurs at the disk electrode and an oxidation reaction occurs at the ring electrode. The electrochemical reaction at the ring and disk electrode is mentioned as below:

At disk electrode, $Ox \longrightarrow Red + e^-$ (2.9)

At ring electrode, $Red + e^- \longrightarrow Ox$ (2.10)

During ORR reaction if the catalysts are not effective in the direct reduction of O_2, it may generate some amount of peroxide or peroxide ion as intermediates. This peroxide or peroxide ion is transported to the ring electrode where they get oxidized back to O_2 which leads to a ring current. Therefore, the ring electrode is always kept at a constant potential (1.20 V vs RHE) to ensure complete oxidation of the transported reduced species. However, in an RRDE not all the products generated at the disk electrode will make its way to the ring electrode. The percentage of material detected/collected at the ring electrode is called the collection efficiency (N), and it can be calculated as expressed in equation 2.11. The obtained collection efficiency is the same for the particular RRDE irrespective of the electrode reaction being studied and can be given in terms of disk current (I_D) and ring current (I_R) as below:

$$N = \frac{|I_R|}{|I_D|} \qquad (2.11)$$

The collection efficiency was calculated by using a well-behaved electrochemical system like ferrocyanide/ferricyanide system. The RRDE electrode was dipped into 0.10 M KOH solution containing 10 mmol/L of $K_3[Fe(CN)_6]$. The electrode was rotated from 500 to 2000 rpm, and the disk electrode was scanned from 0.65 V to -0.50 V (vs. Hg/HgO) at a scan rate of 20 mV/s. The ring electrode was kept at a constant potential of 0.65 V (vs. Hg/HgO). The ratio of $|I_R|/|I_D|$ is almost constant under various ω. Using equation 2.11, the collection efficiency N was calculated to be 0.44. The LSV curves recorded for the Pt RRDE in 0.10 M KOH with $K_3[Fe(CN)_6]$ is presented in Figure 2.11. The percentage of peroxide or peroxide ion generated from the ORR can be determined from the RRDE measurements by using equation 2.12. Equation 2.13 can be used to calculate the electron transfer number, n from the RRDE voltammogram.

$$H_2O_2 \ or \ OH_2^-\% = 100 \ x \ \frac{2\frac{I_R}{N}}{I_D+\frac{I_R}{N}} \qquad (2.12)$$

$$n = \frac{4I_D}{I_D+\frac{I_R}{N}} \qquad (2.13)$$

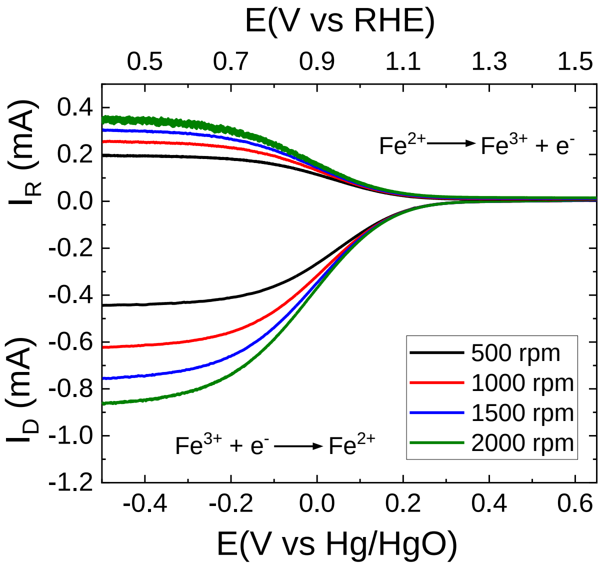

Figure 2.11: LSV curves of the disk and ring electrode recorded for the calculation of collection efficiency (N) at a Pt RRDE in 0.10 M KOH with 10mM $K_3[Fe(CN)_6]$ at a scan rate of 20 mV/s.

2.5.5 Amperometric i-t curve

In the amperometric i-t curve, the current is recorded by applying a constant potential on the working electrode as a function of time. Figure 2.12 displays the potential waveform applied as a function of time. A quiet time of 10 s is always employed before recording the current. For measuring the methanol tolerance ability of the catalyst, a small volume of methanol solution is added in steps to see its impact in the recorded current.

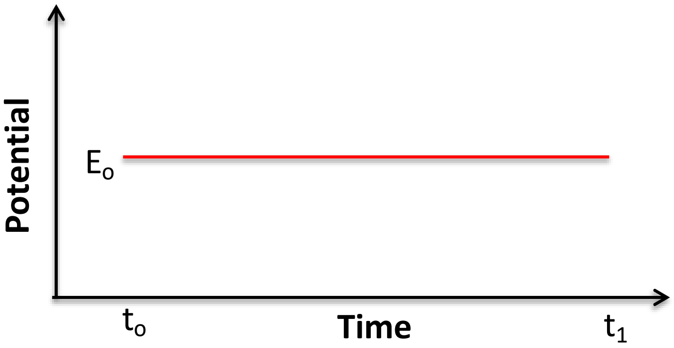

Figure 2.12: The applied potential waveform for the amperometric i-t curve.

2.5.6 CO Stripping Voltammetry

CO stripping voltammetry is an effective method for calculating the ECSA of the catalyst. In this method, the catalyst being tested is initially poisoned with CO by purging the electrolyte with 100% pure CO under a constant potential. As the electrolyte is purged with CO, a monolayer of CO gets adsorbed on the electrode surface and is electrochemically oxidized between 0.50 and 0.90 V (vs. RHE) depending upon the surface of the catalyst sites, its surface plane, and also on the pH of the electrolyte employed[8]. The CO stripping experiment was done as follows: 1) purge the solution with Ar for 600 s to remove any dissolved O_2 species and a CV was recorded between 0.00 and 1.20 V (vs. RHE) for 15 cycles in Ar-saturated solution. 2) adsorb CO by purging 100% pure CO for 300 s while holding the potential at 0.10 V or 0.20 V (vs. RHE) using the amperometric i-t technique. 3) purge the electrolyte solution with Ar for 1800 s to completely remove any CO present in the electrolyte while still holding the potential. 4) three CV cycles (CO stripping curves) were recorded by positively sweeping the potential between 0.00 V and 1.30 V (vs. RHE) at a scan rate of 10 mV/s starting from the constant potential at which the electrode was held to adsorb CO. The resulting CO oxidation peak was integrated and the ECSA was further calculated based on the following equation:

$$ECSA_{CO} = \frac{Q_{CO}}{Q_a{}^* \, m_{Pt}} \qquad (2.14)$$

where Q_{CO} is the charge associated with the desorption of CO from the Pt active sites, Q_a (420 μC/cm^2) is the charge required to oxidize a monolayer of CO adsorbed on 1 cm^2 of Pt surface and m_{Pt} is the mass loading of platinum.

2.6 References

1. Melechko, A. V.; Merkulov, V. I.; McKnight, T. E.; Guillorn, M. A.; Klein, K. L.; Lowndes, D. H.; Simpson, M. L., Vertically aligned carbon nanofibers and related structures: Controlled synthesis and directed assembly. *J. Appl. Phys.* **2005,** *97* (4), 041301.
2. Cruden, B. A.; Cassell, A. M.; Ye, Q.; Meyyappan, M., Reactor design considerations in the hot filament/direct current plasma synthesis of carbon nanofibers. *J. Appl. Phys.* **2003,** *94* (6), 4070-4078.
3. Meyyappan, M.; Delzeit, L.; Cassell, A.; Hash, D., Carbon nanotube growth by PECVD: a review. *Plasma Sources Sci. Technol.* **2003,** *12* (2), 205-216.
4. Dong, L.; Jiao, J.; Pan, C.; Tuggle, D., Effects of catalysts on the internal structures of carbon nanotubes and corresponding electron field-emission properties. *Applied Physics A* **2004,** *78* (1), 9-14.
5. Liu, J.; Essner, J.; Li, J., Hybrid Supercapacitor Based on Coaxially Coated Manganese Oxide on Vertically Aligned Carbon Nanofiber Arrays. *Chem. Mater.* **2010,** *22* (17), 5022-5030.
6. Klankowski, S. A.; Rojeski, R. A.; Cruden, B. A.; Liu, J.; Wu, J.; Li, J., A high-performance lithium-ion battery anode based on the core–shell heterostructure of silicon-coated vertically aligned carbon nanofibers. *J. Mater. Chem. A* **2013,** *1* (4), 1055-1064.
7. Bard, A. J.; Faulkner, L. R., *Electrochemical methods: fundamentals and applications*. Wiley New York: 1980; Vol. 2.
8. García, G.; Koper, M. T. M., Stripping voltammetry of carbon monoxide oxidation on stepped platinum single-crystal electrodes in alkaline solution. *Phys. Chem. Chem. Phys.* **2008,** *10* (25), 3802-3811.

Chapter 3 - Fundamental Electrochemical Insights of Vertically Aligned Carbon Nanofiber Architecture as a Catalyst Support for ORR

Reproduced with permission from A. Elangovan, J. Xu, E. Brown, B. Liu, J. Li, Journal. of the Electrochemical Society, **2020,** 167 (6), 066523. DOI: 10.1149/1945-7111/ab86c1 © The Electrochemical Society.

3.1 Introduction

Low-temperature fuel cells (LTFCs) are attractive environmentally friendly alternatives to fossil fuel powered devices[1-3]. It directly converts oxygen and fuels into H_2O at moderate temperatures to release electrical energy. Even though the overall reaction is thermodynamically favored, the sluggish kinetics leads to the high electrochemical overpotential and low power density[2]. To enable broader impacts, the power density and durability of LTFCs need to be significantly improved while the cost is reduced. Highly efficient electrocatalysts are key to achieving these goals. Particularly, the electrocatalytic ORR is one of the important reactions occurring in LTFCs[2, 4]. ORR proceeds either by a direct four-electron (4-e^-) reduction pathway to form H_2O (in acidic media) or OH^- (in alkaline media) or by a less efficient two-step two-electron (2-e^-) reduction pathway involving the formation of corrosive intermediate species H_2O_2 (in acidic media) or HO_2^- (in alkaline media)[2-5]. Platinum (Pt) nanoparticles (NPs) supported on Vulcan carbon, denoted as Pt/C, is the most effective ORR catalyst[2, 4-6]. However, the high cost and limited supply of Pt poses severe challenges for broader applications. In addition, the current Pt/C catalyst suffers from poor durability, CO poisoning, and methanol crossover reactions (in DMFC – a type of LTFC)[7-9]. As a result, there is a strong demand to improve these properties[2, 3, 10, 11]. This study focuses on exploring vertically aligned carbon nanofiber (VACNF) arrays as a unique carbon-based catalyst support for Pt catalyst, with an emphasis on understanding its fundamental electrochemical properties in ORR using a rotating disk electrode (RDE) and its capability in improving Pt catalyst's tolerance to methanol crossover.

Vulcan carbon support in commercial Pt/C catalyst is so far quite successful. However, in the presence of oxygen at high electrode potentials, carbon corrosion occurs, leading to the detachment of Pt NPs from the carbon support and decline in fuel cell performance[12-14]. One of the approaches in solving these issues is to develop highly graphitic carbon materials as novel catalyst supports, such as graphene[15-17], carbon nanotubes (CNTs)[18, 19], carbon nanofibers (CNFs)[20-22] and carbon NPs[23]. These carbon materials exhibit higher chemical stability, high specific surface area, large structural variety, tailorable surface chemistry, wide potential window, and high electrical conductivity[19, 24], which can reduce carbon corrosion and improve the durability of Pt NPs. Some studies indicated that Pt deposited on CNT or CNF supports also show higher CO tolerance[25, 26]. In most studies, these CNT or CNF supports are in the form of randomly stacked dense networks. A few studies explored vertically aligned organic whiskers as catalysts support in so-called nanostructured thin-film (NSTF) catalysts[27-29]. Such vertically aligned structures allow the deposition of a low Pt mass (at ~0.1-0.22 mg/cm^2) via simple ion sputtering[27-29], which has been found to present higher activity than the commercial Pt/C catalyst. Tian et al.[30] further explored vertically aligned CNTs sputtered with ~ 35 μg/cm^2 Pt in membrane electrode assemblies (MEAs) and the hydrogen fuel cell made of such MEAs matched the performance of the Pt/C catalyst with 10 times of Pt loading. In another direction, Gong et al.[7] reported that vertically aligned nitrogen-doped CNT arrays can serve as a metal-free catalyst with superior catalytic activities.

While the above results are encouraging, it still lacks a good understanding of the fundamental electrochemical properties of such 3D electrodes in ORR. This is challenging because the large thickness and the porous 3D structure are substantially different from the conventional thin-film RDE electrodes (< 200 nm in thickness) in ORR studies. It is noteworthy that voltammetry measurements with RDE are an essential technique for evaluating ORR electrocatalysts due to the low O_2 solubility in electrolytes (~ 1.2 mM) and sluggish kinetics. The well-defined hydrodynamic conditions based on the Levich equation in thin-film RDE measurements enable deconvolution of mass transport and kinetic effects and thus allow determination of the electrochemical kinetics and ORR mechanisms[31]. These cannot be achieved with other electrochemical techniques such as cyclic voltammetry (CV) or full cell studies. Herein, we present a systematic study using a well-defined model system, i.e. vertically aligned carbon nanofiber (VACNF) arrays, an interesting vertical 3D architecture with conically stacked graphitic microstructures. Density functional theory (DFT) calculations further support the electrocatalytic properties of Pt/VACNF derived from RDE measurements. We believe that this fundamental understanding would provide important insights to guide the design and characterization of future 3D architectured catalyst supports.

In this study, we prepared VACNF arrays using a DC-biased plasma-enhanced chemical vapor deposition (PECVD) system[32, 33] and used it as a 3D architectured support for ion-beam sputtered Pt catalysts. The overall ORR catalytic activity, tolerance to methanol crossover, and recovery from CO poisoning were evaluated. It is noteworthy that many studies in literature reported similar materials such as vertically aligned CNTs[7] or MWCNTs[7, 30], refer to as "VACNTs". Here we use the terminology "VACNFs" following the relevant previous studies[32-34] to stress two important differences from those CNT materials. First, in a typical VACNF array, each nanofiber freely stands on the conductive substrate with an areal density of 1.0 x 10^9 CNFs/cm^2 (corresponding to an average inter-fiber distance of ~340 nm). Such an open structure allows Pt to be sputter-deposited from above and spread along the full length of individual nanofibers, hence enabling effective utilization of the Pt catalyst. In contrast, the VACNTs have about 4 to 10 times higher areal density, smaller diameter (20-30 nm) and larger length (10s to 1000s μm). Thus, VACNTs are wavy and heavily entangled, giving much smaller open spaces that can be accessed directly from above. Second, VACNFs consist of graphitic cones stacked on top of each other along the fiber axis and present a high density of graphitic edge sites at the sidewall[32, 33, 35]. This is critically different from the graphite basal plane-like sidewall in CNTs or amorphous structure in common carbon nanofibers by pyrolysis. These exposed graphitic edges act as the active sites and are expected to improve the durability of Pt catalysts as demonstrated with materials of similar structures[22, 36, 37]. DFT calculations based on the atomic model of conically stacked VACNF structure successfully validates the stronger binding between Pt and graphitic edges and illustrates the molecular ORR pathways. Furthermore, the 3D architectured Pt/VACNF catalyst presents interesting new phenomena in RDE studies and displayed a notable resistance to methanol oxidation reaction and a higher capability to recover from CO poisoning

3.2 Experimental

3.2.1 Preparation of Pt/VACNFs

A graphite paper (GP) of 1 x 1 $inch^2$ was coated with a nominal thickness (equivalent to the film thickness on a flat surface) of 22 nm nickel film as the catalyst for VACNF growth using a high-resolution ion beam coater. VACNFs were grown on the graphite paper using a PECVD system following the procedure mentioned in Chapter 2 for 30, 60, and 90 min to obtain VACNFs with an average length of 5, 8, and 11 µm, respectively. Pt of 99.99% purity was deposited on the as-grown VACNFs using the high-resolution ion beam coater. The deposition was precisely controlled to the nominal thickness of 3, 5, 10, and 20 nm, respectively, using an in-situ quartz crystal microbalance (QCM) and was further validated with scanning electron microscopy (SEM). The error of the nominal thickness is generally lower than 5%.

3.2.3 Materials Characterization

The surface morphology of the as-grown VACNF arrays was characterized by a Field-emission scanning electron microscope (FESEM) (Versa 3D Dual Beam, FEI, Hillsboro, OR) at a 15-kV accelerating voltage. The microstructure of the Pt/VACNF was analyzed using field-emission scanning/transmission electron microscopy (S/TEM, FEI Tecnai F20 XT, Hillsboro, OR) at a 200-kV accelerating voltage. Elemental analysis and mapping were done using energy-dispersive X-ray spectroscopy (EDS) in the S/TEM. Raman spectra were obtained using a DXR Raman microscope (Thermo Scientific, Waltham, MA) at an excitation laser wavelength of 532 nm.

3.2.3 Working Electrode Preparation

A RDE with a glassy carbon disk of 0.078 cm^2 in a 12 mm diameter polyether ether ketone (PEEK) shroud was used for characterizing the catalysts. The Pt/VACNF on graphite paper was punched into 6.0 mm diameter discs and attached on the RDE using a conductive silver paste followed by drying at 70 ^oC before use. The Pt/VACNF electrode with 3, 5, 10, and 20 nm nominal Pt thicknesses have a Pt mass loading of 6.5, 10.8, 21.5, and 43.0 $\mu g/cm^2$, respectively. For comparison, the commercial Pt/C catalyst was deposited onto the RDE as a conventional thin-film electrode from a catalyst ink. The standard ink solution consisted of 5.0 mg of the commercial Pt/C catalyst dispersed in 2.5 ml water, isopropanol and Nafion (at 200:49:1 volume ratio) mixture and was sonicated for 1 h before use. About 5.0 µL of this ink solution was drop cast on the RDE electrode to give a Pt loading of 25.6 µg/cm^2. After drying at room temperature, it forms a uniform thin catalyst film. For other Pt loadings, the concentration of the Pt/C ink was adjusted proportionally.

3.2.4 Electrochemical Measurements

The electrochemical properties and the catalytic activity of the Pt/VACNFs were studied using a CHI 760D electrochemical workstation (CH Instruments, Austin, TX) and a rotating ring disk electrode controller (RRDE-3A, ALS Co., Ltd, Japan). For comparison, the commercial Pt/C catalyst was also examined under the same conditions. The electrochemical tests were done in a three-electrode configuration consisting of the catalyst-coated RDE as the working electrode, a coiled Pt wire as the counter electrode, and a mercury-mercuric oxide (Hg/HgO) electrode with 1.0 M NaOH filling solution as the reference electrode. The electrolyte for most studies were 0.10 M KOH solution. For direct comparison with literature, the measured electrode potential (vs. Hg/HgO) in this electrolyte at 25 ^{o}C is converted to the value versus the reversible hydrogen electrode (RHE), by adding 0.907 V. Cyclic voltammetry (CV) was conducted between 0.30 V and -0.90 V (vs. Hg/HgO) at a scan rate of 50 mV/s. Linear sweep voltammetry (LSV) from 0.20 V to -0.50 V (vs. Hg/HgO) at a scan rate of 10 mV/s was carried out with the RDE at the rotation speed from 500 to 3,000 rpm. The details in converting potentials versus different reference electrodes are mentioned in Chapter 2. The derivation of the limiting current density J_{lim}, the half-wave potential $E_{1/2}$ and electrochemical surface area (ECSA) are described in Section 1 and Figures A.1 and A.2 in the Appendix-A. The accelerated stress test (AST) was carried out by performing continuous potential cycling between 0.293 V and -0.307 V (vs. Hg/HgO), i.e., between 1.20 V and 0.60 V versus RHE as used in the literature[38], at a scan rate of 100 mV/s for 5,000 cycles. Ar or O_2 was purged into the solution depending upon the type of measurements.

CV curves and ORR polarization curves were collected at various cycle intervals during the AST to record the degradation of the electrocatalysts.

3.2.5 Computational Methods

Computation work done by our collaborators Dr. Bin Liu and Mr. Jiayi Xu in the Tim Taylor Department of Chemical Engineering of Kansas State University was used to gain insights into the experimental work. Spin-polarized density functional theory (DFT) calculations were performed using the Vienna *Ab initio* Simulation Package (VASP).[39] The Generalized Gradient Approximation (GGA) Perdew-Burke-Ernzerhof (PBE) functional was used to account for the Kohn-Sham electron exchange-correlation interactions[40]. The projector augmented wave (PAW) method was used to represent the ionic cores[41]. A cut-off for the plane wave basis set expansion up to 400 eV was used for all calculations. The break condition for the self-consistent iteration was set to be 1×10^{-6} eV. Ionic relaxation was stopped when the forces on all atoms are smaller than 0.05 eV/Å. Monkhorst-Pack-based k-point meshes[42] were employed. The relaxed lattice constants for bulk graphite obtained from this setting are a = b = 2.47 Å and c = 6.80 Å, and in very good agreement with reported literature values of 2.46 Å, and 6.78 Å, respectively[43]. Moreover, Grimme's DFT-D3 method was used to account for the dispersion interactions[44].

3.2.6 DFT Models

The semi-periodic *fishbone* models (periodic along the carbon edge) were built by cleaving the graphite layers to represent the VACNF architecture. Given the large diameter of the VACNF (~50 to 250 nm), the small curvature of the VACNF was neglected in this model[45]. The dangling bonds at the broken graphitic edges at the VACNF sidewall were passivated by OH groups, which are energetically favorable in alkaline conditions. The deposited Pt NPs are located at the graphitic edge sites. The Pt atoms interact with the open-edge C atoms directly. Furthermore, Pt structures with different numbers of atoms, from Pt_4 to Pt_{20}, were constructed. It was shown that the formation energies (per Pt atom) converged (within 0.06 eV) at Pt_{12}, which was thus selected for the modeling of ORR pathways.

3.3 Results and Discussion

3.3.1 Catalyst/Support Design

Scheme 3.1 shows the design of the ORR catalyst, where the hierarchical architecture of VACNFs is used as the catalyst support. This open vertically aligned 3D structure is significantly different from the commercial Pt/C catalyst in which the catalyst nanoparticles and carbon supports are tightly packed in a random fashion and bound through Nafion ionomer. Moreover, the microstructure of the VACNFs consists of a stack of conical graphitic cups on top of each other, providing abundant broken graphitic edges at the sidewall. The vertical array feature and the internal graphitic stacking of the VACNFs are illustrated by FESEM and TEM images in Figure 3.1. The red lines in Figure 3.1c are the visual guide of the stack of a few representative graphitic sheets. The broken graphitic edges at the sidewalls are known to be the active ORR catalytic sites,[46] which helps to anchor the Pt nanoparticles (NPs (Figures 3.1d and 3.1f).

Panels (c) and (d) of Scheme 3.1 illustrate the atomic cross-sections of the proposed conically stacked VACNF architectures that are generated by cutting graphite crystal along the ($\bar{1}$ 1 10) facet. After sputtering Pt atoms onto the VACNF arrays, it formed Pt NPs firmly attached to the exposed edge sites (as pointed by the red arrows in Figure 3.1e). The large spacing (~ 300 nm) between the neighboring VACNFs allows the Pt NPs to spread along the fibers and reach till the bottom. The catalytic activities of the bare VACNFs and Pt/VACNFs have been studied systematically to reveal the contributions of each component. It is noteworthy that this vertically aligned architecture is free of Nafion binder, which facilitates a faster mass transport of O_2 via diffusion into the open structure during RDE measurements as shown in Scheme 3.1. In contrast, in conventional ORR catalysts, O_2 molecules have to diffuse through the Nafion binder to reach Pt/C catalyst inside the film, thus requiring very thin films (< 200 nm). These differences make it necessary to modify the algorithm to extract useful information from RDE experiments with the thick 3D catalyst architectures comparing to conventional thin-film catalysts. To make it clear, the methods to calculate electrochemical surface area (ECSA) and to derive critical ORR catalytic parameters such as the limiting current density (J_{lim}) and half-wave potential ($E_{1/2}$) are defined in Section 2.5.1, Section 1 in Appendix-A, and Figures A.1 and A.2.

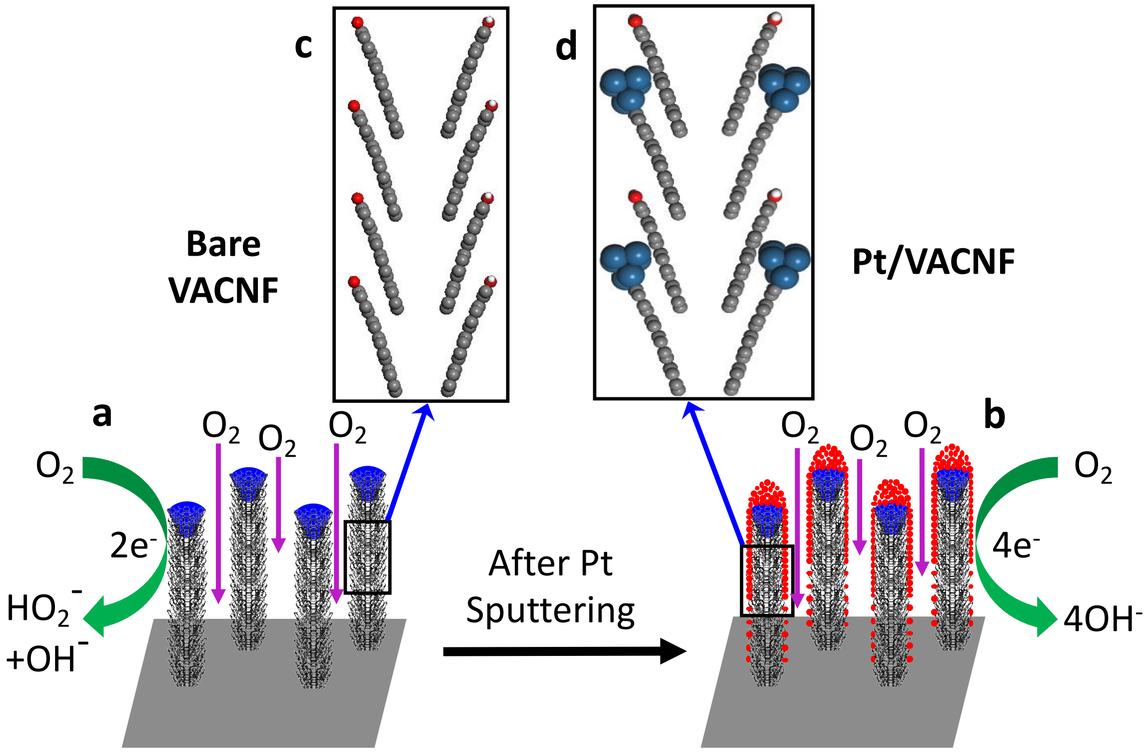

Scheme 3.1: Schematic illustration of the catalyst structure: (a) bare VACNFs, (b) Pt/VACNF, (c) the atomic cross-sections of the conically stacked VACNF architectures that are generated by cutting graphite crystal along the ($\bar{1}$ 1 10) facet, and (d) Pt nanoparticles bound to the graphitic edges of the VACNFs. (Reproduced with permission from *J. Electrochem. Soc.* 2020, 167, 066523. © The Electrochemical Society. All rights reserved)

3.3.2 Structural Characterization of the Pt/VACNF Catalysts

The FESEM images of the as-grown VACNFs presented in Figures 3.1a and 3.1b show that the VACNFs are firmly attached to the surface of the graphite paper (GP) in a uniform vertical alignment and are fully separated from each other. The VACNFs are randomly distributed with the average inter-fiber spacing of ~340 nm (corresponding to an areal density of ~1x10^9 CNFs/cm^2). The diameter of VACNFs spreads from 50 nm to 250 nm with the average value of ~150 nm and the length ranges from 5 µm to 11 µm depending on the growth time as shown by the cross-sectional FESEM images in Figure A.3. This unique brush-like structure is different from the dense and entangled vertically aligned CNTs in other studies[7, 30, 47]. In VACNF arrays, each CNF consists of a stack of conical graphitic cups under the Ni catalyst NPs as shown in Figure 6.1c. The basal planes of the graphitic layers are stacked and buried inside the VACNFs leaving mainly the edge sites exposed at the sidewall. The Ni catalyst presents in the form of an 'inverse teardrop' at the tip of each VACNF and acts as a cap to the bamboo-like hollow core. The Ni NPs were found to have no effects on the ORR catalysis in control experiments after removing them by soaking in 0.10 M HNO_3. The TEM image in Figure 3.1d shows the tiny Pt NPs deposits on the sidewall of the VACNF array by ion-beam sputtering at a nominal thickness of 5.0 nm (corresponding to 10.8 µg/cm^2 Pt loading relative to the geometric surface area). The enlargement of the indicated region (in red rectangle) is given in Figure 3.1e, which together with the histogram in Figure A.4a indicate that the Pt NPs have an average diameter of ~1.1 nm. The high magnification TEM image shown in Figure 3.1f shows the lattice fringes of d=0.34 nm, which confirms the graphitic nature of the VACNFs.

Since the individual fibers are well separated, the sputtered Pt can reach deep into the 3D structure. Tilting the substrate surface normal at an angle of 5^o off from the incoming Pt flux was found to give the most effective Pt deposition onto the VACNF array. Increasing the nominal thickness of the Pt deposition was found to increase the Pt nanoparticle size on the VACNF sidewall, as confirmed by the TEM images in Figure A.4. The average diameter of the Pt NPs is 1.14 ± 0.25, 1.69 ± 0.50, and 3.10 ± 0.43 nm for the 5, 10, and 20 nm nominal thickness (corresponding to the Pt loading of 10.8, 21.5, and 43.0 μg/cm^2), respectively. These sizes are in the right range for highly active Pt catalysts[48]. Above 20 nm nominal Pt thickness, the deposited Pt NPs start to extend into secondary nanowhiskers anchored on the VACNFs. The high-angle annular dark-field scanning transmission electron microscope (HAADF-STEM) and the EDS elemental mapping in the selected region of a sample deposited with 5.0 nm nominal thickness of Pt (Figure A.5) further reveal the uniform distribution of Pt NPs on the VACNF surface. The wt% of Pt on the Pt/VACNF can be calculated by estimating the mass of carbon present in the VACNFs and the amount of Pt deposited on the VACNFs. The mass of carbon in the VACNFs can be calculated from the average structure observed by FESEM (Figures 6.1a, 6.1b and A.3b), giving ~177 μg/cm^2 for a VACNF array with 5 μm average length and 150 nm average fiber diameter. As the Pt loading increases, the wt% of Pt on VACNF increases. The Pt wt% on VACNFs are estimated to be ~3.5, 5.8, 10.8, and 19.8 wt% for the Pt loading of 6.5, 10.8, 21.5, and 43.0 μg/cm^2, respectively. It needs to emphasize that the internal microstructure of VACNFs are critically different from multi-walled carbon nanotubes (MWCNTs) in literature[7, 30], which is reflected by the drastically different Raman spectra in Figure A.6. The VACNF array shows a much stronger D-band peak at 1341 cm^{-1}, whose intensity is close to that of the G-band peak at 1580 cm^{-1}. The 2D band shifts up to ~2850 cm^{-1} and becomes much broader. These evidences indicate that more sp^3 carbon present in the VACNFs, most likely at the broken graphitic edges on the sidewall of VACNFs, which is consistent with the conical stacked graphitic structure revealed by the TEM images in Figures 3.1c-

3.1f. The uniform vertical alignment, much lower areal density and free of entanglement between the neighbors make it possible to deposit Pt more uniformly along the VACNFs instead of accumulating near the tips[30].

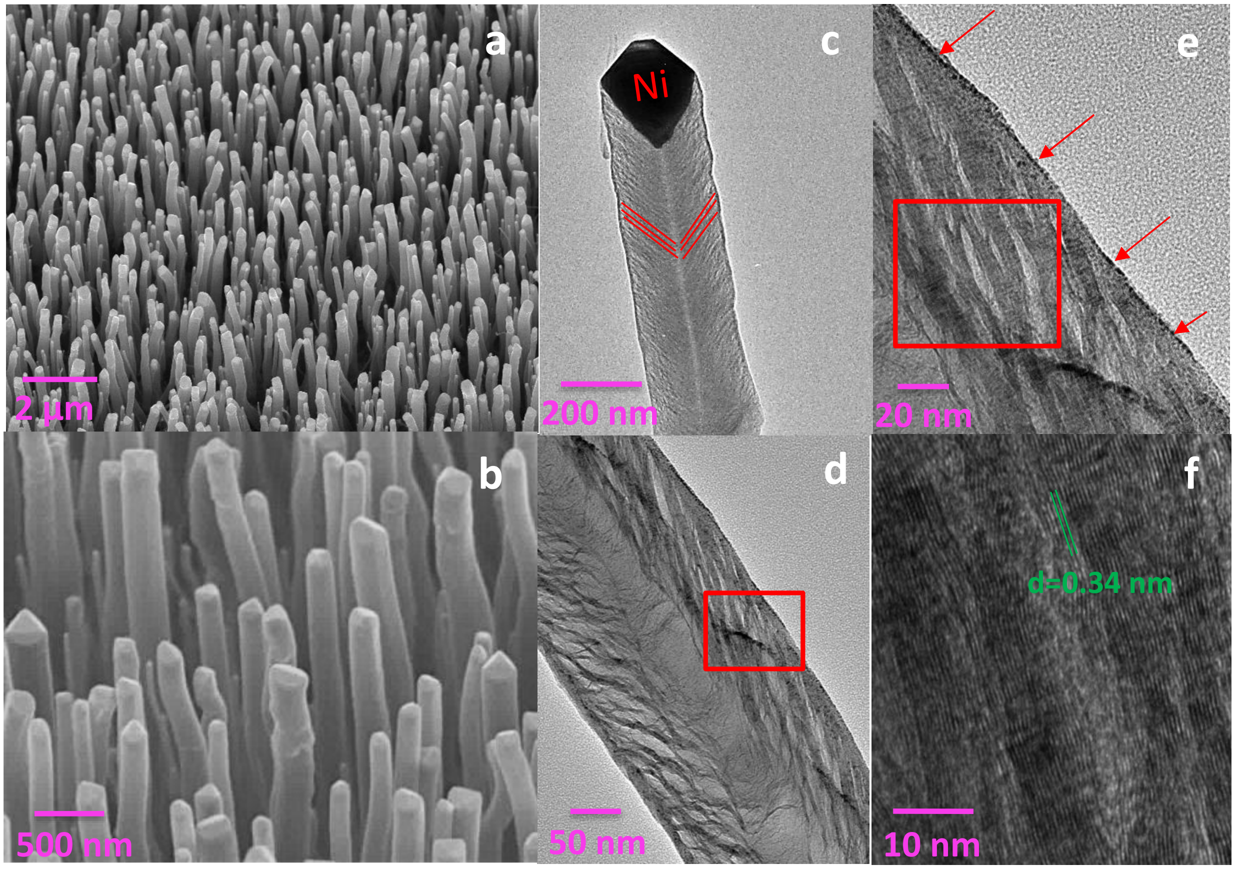

Figure 3.1: FESEM images of VACNF at (a) low magnification and (b) high magnification; (c) a low-magnification TEM image of a bare VACNF; TEM images of Pt/VACNF (10.8 µg/cm^2) at (d) low magnification, (e) high magnification, and (f) high magnification showing the lattice fringe of the graphitic layers. The red boxes in panels (d) and (e) indicate the area in the next enlarged TEM images. (Reproduced with permission from *J. Electrochem. Soc.* 2020, 167, 066523. © The Electrochemical Society. All rights reserved.)

3.3.3 Assessment of the Fundamental Electrocatalytic Properties of Pt/VACNF in ORR

The electrocatalytic activity of the 3D architectured catalysts was first evaluated with CV in Ar-saturated and O_2-saturated 0.10 M KOH solution. Figures 3.2a and 3.2b are representative

CVs of the commercial Pt/C catalyst with a Pt loading of 25.6 µg/cm^2 (denoted as 25.6 Pt/C) and in-house prepared Pt/VACNF catalyst with a Pt loading of 21.5 µg/cm^2 (denoted as 21.5 Pt/VACNF), respectively. The current density is relative to the geometric area of the working electrode. In Figure 3.2a, the reduction peak at -0.20 V (vs. Hg/HgO) in Ar corresponds to reducing Pt oxide to Pt whereas the reduction peaks between -0.45 V and -0.75 V correspond to the hydrogen underpotential deposition (UPD) on the Pt surface. The increased reduction current observed at potentials below 0.0 V (vs. Hg/HgO) in O_2–saturated solution is attributed to ORR. The 21.5 Pt/VACNF catalyst in Figure 3.2b shows similar ORR and hydrogen adsorption features, but they are superimposed on a higher baseline current due to the larger capacitive current. The CVs for Pt/VACNF at other Pt loadings in Figure A.7 show similar features. As the Pt loading increases, the oxygen reduction and hydrogen UPD current density increases.

The CV curves indicate that the Pt/VACNF has about 50% higher capacitance contribution compared to the Pt/C catalyst. The high capacitive contribution of Pt/VACNF catalysts arises mainly from the graphite paper that is used as the substrate to grow VACNFs. Figure A.8a presents the CV curves in Ar-saturated 0.1 M KOH for bare GP alone and those of VACNFs grown on GP with PECVD growth time of 30, 60 and 90 min. The capacitance relative to the geometric surface area of these electrodes is summarized in Figures A.8b and A.8c. The bare 200 µm thick graphite paper has a very high capacitance of 10080 ± 105 µF/cm^2, which is about 50% higher than the capacitive background of Pt/C catalyst. After the VACNFs are grown on the substrate, the capacitance is slightly higher, and it increases with the VACNF length. With 11 µm long VACNFs (90 min growth time), the capacitance increases by ~11% compared to the bare graphite paper.

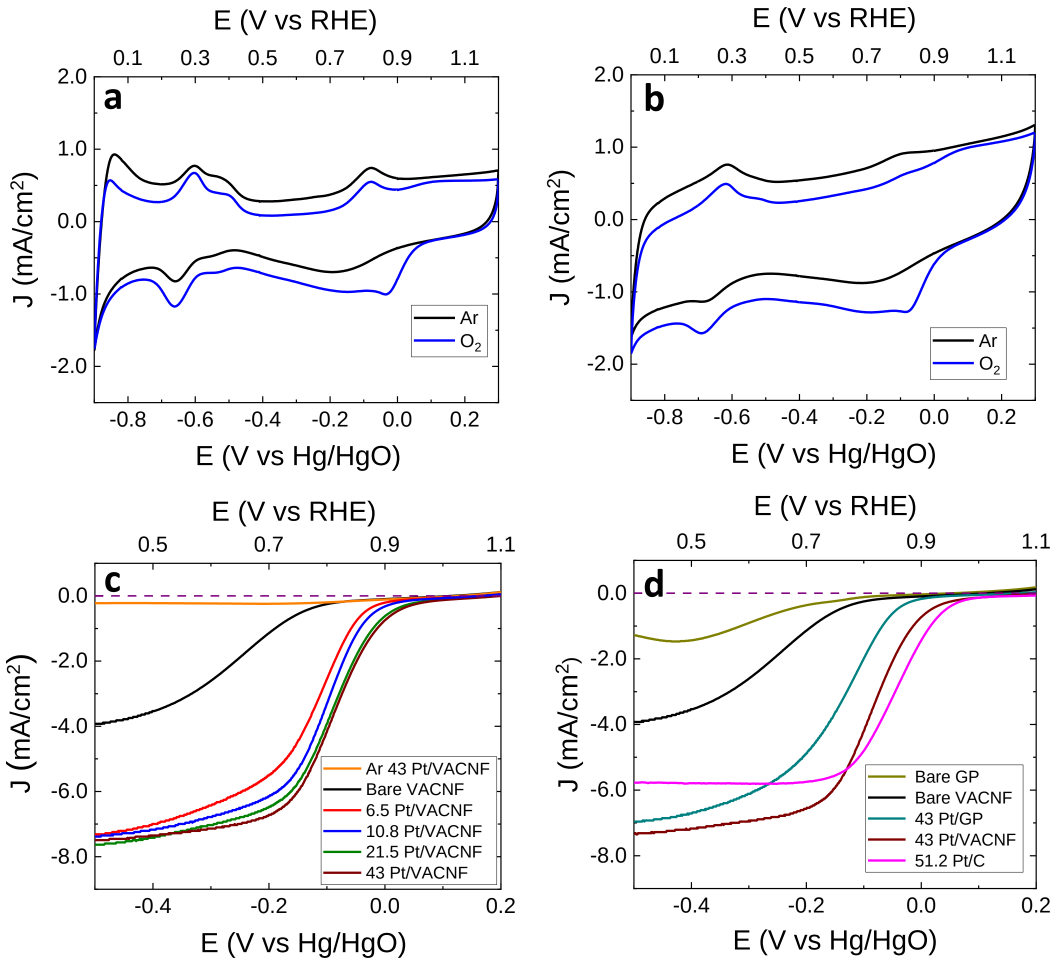

Figure 3.2: CV curve of (a) Pt/C (25.6 µg/cm^2) and (b) Pt/VACNF (21.5 µg/cm^2) recorded in Ar-saturated (black line) and O_2-saturated (blue line) 0.10 M KOH solution at a scan rate of 50 mV/s ; LSV curves recorded at a scan rate of 10 mV/s and a rotation speed of 1,600 rpm in O_2-saturated 0.10 M KOH solution for (c) various VACNF catalysts (with a Pt loading of 0, 6.5, 10.8, 21.5 and 43.0 µg/cm^2) and (d) bare graphite paper, bare VACNF, Pt on graphite paper (43.0 µg/cm^2) , Pt/VACNF (43.0 µg/cm^2) and Pt/C (51.2 µg/cm^2). The purple dash lines mark the zero current density. (Reproduced with permission from *J. Electrochem. Soc.* 2020, 167, 066523. © The Electrochemical Society. All rights reserved.)

Table A.1 summarizes the length and capacitance for just VACNFs after correcting the contribution from bare graphite paper. The baseline of the CV in Pt/VACNF shows a slope about two times of that of the Pt/C catalyst (see Figures 3.2a and 3.2b), indicating a smaller ohmic resistance of the Pt/VACNF electrode due to the larger surface area and absence of Nafion coating. It is noted that the graphite paper substrate obscures some details of CVs and it gets difficult to extract the ECSA for low Pt loadings. But for 20 nm nominal thickness of Pt (43.0 µg/cm^2) on the VACNFs, the ECSA was estimated to be 23.5 m^2/g as shown in Figure A.2. This is lower than the 28.6 m^2/g obtained with commercial Pt/C, which is mainly due to the larger Pt NPs on the VACNF tip surface which approximately accounts for about ~20% of the deposited Pt in proportion to its geometric surface area. More uniform Pt distribution and higher ECSA can be achieved in the future using other deposition techniques like atomic layer deposition (ALD).

The linear sweep voltammetry (LSV) curves of the bare VACNF and Pt/VACNF catalysts (at 6.5, 10.8, 21.5, and 43.0 µg/cm^2 Pt loading) recorded with the RDE from +0.20 V to -0.50 V (vs. Hg/HgO) at a rotating speed of 1,600 rpm in O_2-saturated 0.10 M KOH is shown in Figure 3.2c. All LSVs in the O_2-saturated solution present the characteristic sigmoidal curves indicating the formation of the steady-state. However, compared to the commercial Pt/C catalyst, the baseline in the diffusion-controlled region is slanted downward to the negative potential. Nevertheless, the limiting current density J_{lim} and the half-wave potential $E_{1/2}$ can be derived from each LSV curve by extrapolating the linear segments as described in Figure A.1 of the Appendix-A. Table 3.1 summarizes the J_{lim} (background-corrected) and $E_{1/2}$ (vs. both Hg/HgO and RHE) for different catalysts. Quantitatively, the capacitive current arising from the VACNF structure and the GP in Pt/VACNF is similar in both CV and LSV measurements and can be calculated from the total capacitance derived from Figure A.8a. It was found to be only about -0.1 mA/cm^2 in the LSV curve in Figure 3.2c, which is negligible compared to the measured ORR limiting current density (~6.0 mA/cm^2). The LSV of 43.0 Pt/VACNF recorded in the absence of O_2 (in Ar-saturated solution) shows only a small maximum current density of -0.2 mA/cm^2 at -0.50 V (vs. Hg/HgO) (indicated by the orange solid line), which accounts for the total contribution from surface redox reactions, ohmic current, and capacitive current. This is subtracted from the ORR LSVs in data analyses. It is clear that the LSV curves of Pt/VACNF samples slightly vary with the Pt loadings at low values but almost superimpose on each other when the Pt loading is above 21.5 µg/cm^2. Interestingly, the bare VACNF/graphite paper alone also shows a sigmoidal curve, but the much lower J_{lim} and > 120 mV negative shift of $E_{1/2}$ than the Pt/VACNF catalysts indicates that the bare VACNF arrays act as an inefficient ORR catalyst, possibly through the 2-e$^-$ reduction pathway.

Table 3.1: Summary of the limiting current density J_{lim} (background-corrected) and half-wave potential $E_{1/2}$ for different catalysts. The LSVs in Ar-saturated electrolyte is subtracted from the ORR LSVs measured in O_2-saturated electrolyte before quantitative analyses. (© The Electrochemical Society. (Reproduced with permission from *J. Electrochem. Soc.* 2020, 167, 066523. © The Electrochemical Society. All rights reserved.)

Catalyst	J_{lim} **(mA/cm^2)**	$E_{1/2}$ **(V vs. Hg/HgO)**	$E_{1/2}$ **(V vs. RHE)**
Bare GP	1.2	-0.291	0.616
Bare VACNF	3.5	-0.247	0.660
6.5 Pt/VACNF	6.3	-0.118	0.789
10.8 Pt/VACNF	6.5	-0.102	0.805
21.5 Pt/VACNF	6.6	-0.091	0.816
43 Pt/VACNF	6.7	-0.086	0.821
43 Pt/GP	5.8	-0.131	0.776
51.2 Pt/C	5.7	-0.045	0.862

It is noteworthy that the J_{lim} values (6.3 – 6.7 mA/cm^2) of all the Pt/VACNF catalysts are higher than the value of ~5.7 mA/cm^2 by Levich equation at 1,600 rpm for the benchmark system, i.e. the conventional ultrathin Pt/C catalyst films. To reveal the reasons, systematic LSV experiments were performed with the bare graphite paper (GP), bare VACNFs grown on GP, and VACNFs on GP sputter-coated with 43.0 µg/cm^2 Pt. The LSV data in RDE experiments are systematically compared with the commercial Pt/C thin film catalyst at 51.2 µg/cm^2 Pt loading. As shown in Figure 3.2d, the 51.2 µg/cm^2 Pt/C catalyst shows an ORR J_{lim} = 5.7 mA/cm^2 which matches the theoretical value and exhibits an expected $E_{1/2}$ = -0.045 V vs Hg/HgO (i.e. 0.862 V vs. reversible hydrogen electrode (RHE)). These benchmark characteristics validate that the experimental conditions are appropriate.

Interestingly, even the bare GP shows a low ORR activity (J_{lim} = 1.2 mA/cm^2) at lower potentials with $E_{1/2}$ = -0.291 V vs Hg/HgO (0.616 V vs. RHE). After the growth of VACNF arrays on the GP, the ORR current substantially increases to J_{lim} = 3.5 mA/cm^2 and the LSV curve positively shifts to $E_{1/2}$ = -0.247 V vs Hg/HgO (0.660 V vs. RHE). After sputtering 43.0 µg/cm^2 Pt onto the VACNF array, the ORR J_{lim} value jumps up to ~ 6.7 mA/cm^2, exceeding the theoretical value for thin-film Pt/C catalyst by ~18%. In the meantime, the LSV curve significantly shifts to higher potentials with $E_{1/2}$ = -0.086 V vs. Hg/HgO (0.821 V vs. RHE). The $E_{1/2}$ value of Pt/VACNF with 43.0 µg/cm^2 Pt loading is only 41 mV lower than the commercial Pt/C catalyst with 51.2 µg/cm^2 Pt loading. For comparison, the bare GP (without VACNFs) sputtered with 43.0 µg/cm^2 Pt gives much more negative $E_{1/2}$ = -0.131 V vs. Hg/HgO (0.776 V vs. RHE). It is noteworthy that the current density at E < -0.2 V is much higher than the theoretical limiting current density (~5.7 mA/cm^2 at 1,600 rpm) given by the Levich equation and the LSV is slanted. Using the linear extrapolating method in Figure A.1, the J_{lim} value is determined to be 5.8 mA/cm^2 matching well with the theoretical value. The more positive $E_{1/2}$ value of Pt/VACNF in comparison with Pt/GP confirms that the VACNFs are able to support the majority of the Pt NPs, leading to the ORR activity comparable to the well-dispersed commercial Pt/C system. However, it is surprising that both Pt/GP and Pt/VACNF (grown on GP) give high J_{lim} values exceeding the diffusion limited theoretical value obtained for Pt/C thin films. Understanding the fundamental principles behind this phenomenon is critical for design and electrochemical studies of future 3D catalyst supports. So far, little efforts have been made to reveal the unique RDE features of the 3D catalyst films.

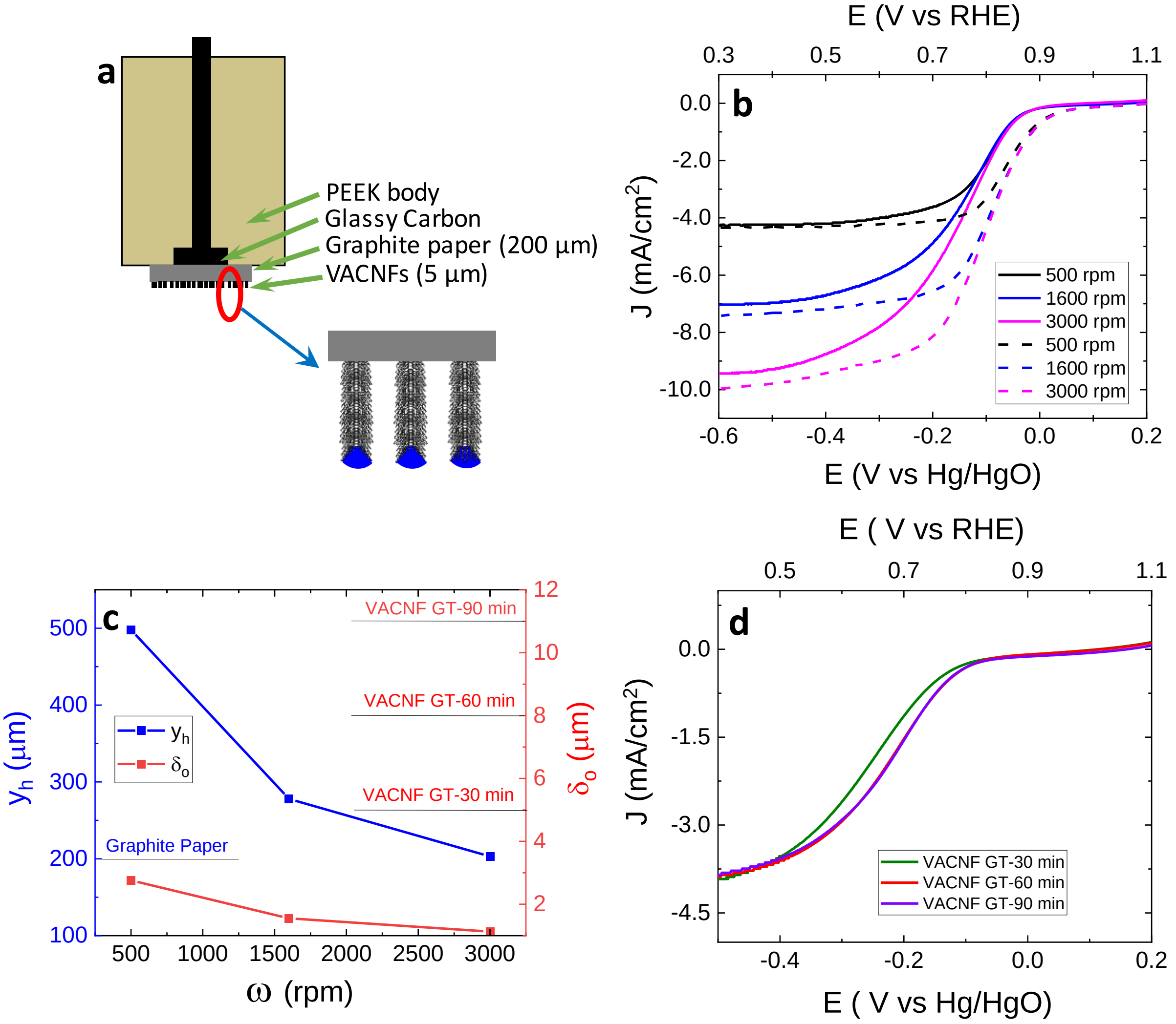

Figure 3.3: (a) Schematic illustration of the working electrode set up; (b) LSV curves of 43.0 µg/cm^2 Pt on GP disks (solid lines) and 43.0 µg/cm^2 Pt/VACNF on GP disks (dashed lines) recorded in O$_2$-saturated 0.10 M KOH solution with a scan rate of 10 mV/s in the negative direction and at a rotation speed from 500, 1600 & 3000 rpm, respectively; (c) The plot of y_h (left scale)) and δ_o (right scale) of a flat thin-film RDE vs. the rotation speed (rpm). The black horizontal lines indicate the thickness of the GP substrate (left scale) and the average length of VACNF arrays produced by different growth time (right scale) for comparison with y_h and δ_o, respectively; (d) LSV curves of bare VACNF arrays on the GP substrate with different growth time in O$_2$-saturated 0.10 M KOH solution at a scan rate of 10 mV/s and a rotation speed of 1600 rpm. (Reproduced with permission from *J. Electrochem. Soc.* 2020, 167, 066523. © The Electrochemical Society. All rights reserved.)

ORR catalysts are normally studied by drop-casting a uniform thin film (< 200 nm) of the catalyst material onto the inlaid RDE. The vertically aligned 3D catalyst support is much thicker (5-11 µm) and poses a highly porous open structure. Thus, it is substantially different from the conventional Pt/C system. Also, as shown in Figure 3.3a, it is necessary to mount the VACNF arrays along with the GP substrate onto the RDE to retain the intact vertically aligned structure. Similar methods have been reported in other studies using polymer transferring films[7, 47, 49], but the processes were not easy to control and it was hard to quantify the RDE voltammetry data. Alternatively, some studies use recessed RDEs for the non-conventional porous materials[31, 50]. However, this approach also has its limitations such as larger ohmic resistance and altered hydrodynamics due to the large recessing depth (typically > 500 µm). Hence it is necessary to explore RDE studies using the raised VACNF array electrodes as illustrated in 3.3a.

Here we systematically link the observed RDE voltammetry results with all the possible structural factors illustrated in Figure 3.3a. First, the silver paste used for mounting the VACNF/GP disk onto RDE was found to have a negligible contribution towards the ORR. There is no measurable difference in LSV curves between the bare glassy carbon RDE and that applied with the Ag paste. Second, the bare GP substrate did increase the baseline current. A peak current of ~1.2 mA/cm^2 is observed with the bare GP disk in Figure 3.2d, which increases with the rotation rate. This low ORR is at rather negative potentials. Third, after growing VACNFs on the GP disks, LSV shows a tilt sigmoidal curve with substantially higher ORR current at slightly higher potentials than the bare GP disk. Fourth, Pt/VACNF samples show LSVs approaching that of the commercial Pt/C catalyst but with a higher J_{lim} than the theoretical value by Levich equation. The control experiment using 43.0 µg/cm^2 Pt directly deposited on a GP also shows higher J_{lim} than the theoretical value but with a negative shift in $E_{1/2}$ than Pt/VACNF (Figure 3.3b).

As shown in Figure 3.3a, when the GP disks are mounted on the RDE, the electrode surface is raised above the surrounding PEEK insulator by about 200 μm due to the GP thickness. This is considerably larger than the thickness of the catalyst film (~ 0.2 μm)[51] in traditional thin-film RDE experiments. Therefore, the resulted hydrodynamic conditions need to be re-examined. The raised GP edge is expected to give a Reynolds number larger than the critical Reynolds number[52] and thus will induce turbulent flow at the GP disk edge. Accordingly, the mass transfer of O_2 is larger than the ideal linear diffusion described by the Levich equation. This effect becomes more evident at higher rotation rates, as revealed by the larger tilt of the LSV curves in Figure A.9b.

The fundamental hydrodynamics of a thin-film RDE can be further illustrated with two parameters, namely the hydrodynamic boundary layer thickness y_h and the steady-state diffusion layer thickness δ_o, which are given as following[52]:

$$y_h = 3.6(\nu/\omega)^{1/2} \tag{3.1}$$

$$\delta_o = 1.61 D_o^{\frac{1}{3}} \omega^{-\frac{1}{2}} \nu^{-\frac{1}{6}} \tag{3.2}$$

where ω is the angular frequency in s^{-1} and D_o is the diffusion coefficient in cm^2/s. The values of these two parameters are plotted versus the rotation rate in Figure 3.3c. The hydrodynamic boundary layer thickness y_h indicates the thickness of the solution rotating with the RDE. In 0.10 M KOH ($\nu = 0.01$ cm^2/s) at $\omega = 1600$ rpm or 167.5 s^{-1}, y_h is roughly 278 μm using Equation (3.1). In this study, the 200 μm thick GP substrate is close to y_h. Therefore, the deviation from the Levich equation is expected. This explains the slanted LSVs in the diffusion-controlled regime, which can be partially corrected by the linear extrapolating method illustrated in Figure A.1.

The second parameter δ_o describes the steady-state diffusion layer thickness of a thin-film RDE in the diffusion-controlled regime in RDE LSVs. Based on Equation (3.2), δ_o is 1.55 µm at 1600 rpm, which is considerably larger than the conventional 200 nm catalyst film thickness. In contrast, the average thickness of the VACNF arrays at different growth times in this study is 5, 8 and 11 µm, respectively, much larger than δ_o. Hence, the open 3D structure of VACNF poses a secondary effect causing the LSVs in RDE experiments to deviate from the Levich model. Figure 3.3b indeed show that Pt/VACNFs on GP exhibit slightly higher J_{lim} than the Pt/GP catalyst and the difference increases with the rotation rate. Interestingly, the LSVs of the bare VACNF/GP samples (Figure 3.3d) only show slight changes versus the VACNF length, clearly not in a proportional relationship. It is likely that the diffusion layer is mainly disturbed by the roughness at the outer surface (~0.5-1.0 µm) rather than the full 3D brush-like VACNF structures.

Overall, the obtained high limiting current density and the tilt LSV curves of the Pt/VACNF catalysts can be rationalized with the deviation from the Levich equation by the turbulent flow at the raised GP substrate edge and the disturbance to the stagnant diffusion layer by the surface roughness of the VACNF arrays. The linear extrapolating method (see Figure A.1) can partially correct the tilt of LSVs. Thus, the general principles of RDE measurements are still applicable to such complicated 3D systems. We just need to be cautious in quantitative interpretation of the enhanced limiting current density comparing to the thin-film Pt/C catalyst. In the Pt/VACNF system, even though the ORR catalytic activity is primarily attributed to Pt NPs, the VACNF array not only provides the 3D open architecture to support Pt catalyst but also presents the synergistic ORR catalytic activity at more negative potentials.

3.3.4 Analyses of the Rotating Disk Electrode Measurements

The RDE polarization curves (after background correction) at a series of rotation speed from 500 to 3,000 rpm for the commercial Pt/C catalyst at 25.6 µg/cm^2 Pt loading and the Pt/VACNF catalyst at 21.5 µg/cm^2 Pt loading are displayed in Figures 3.4a and 3.4b, respectively. The J_{lim} for ORR increases with the rotation speed while the steady-state diffusion layer thickness δ_o is reduced. The RDE polarization curves (after background correction) for the Pt/C and Pt/VACNF catalysts (with Pt loadings of 6.5, 10.8 and 43.0 µg/cm^2) are displayed in Figure A.9.Clearly, all Pt/VACNF catalysts show consistent higher J_{lim} values than the benchmark Pt/C catalyst, but the tilt of the curve in the diffusion-controlled region becomes smaller as the Pt loading increases.

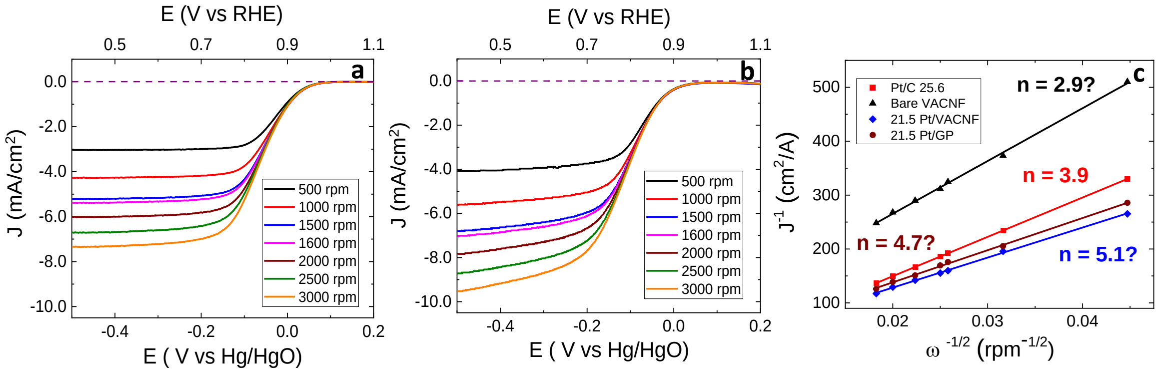

Figure 3.4: Rotating disk electrode voltammogram with background-corrected for (a) Pt/C (25.6 µg/cm^2) and (b) Pt/VACNF (21.5 µg/cm^2) recorded in 0.10 M KOH solution with a scan rate of 10 mV/s at a series of rotation speed from 500 to 3,000 rpm. The purple dash line marks the zero current density; (c) KL plot derived using background-corrected J_{lim} at -0.4 V (vs. Hg/HgO) for Pt/C (25.6 µg/cm^2) and J_{lim} calculated as described in supplementary information for Bare VACNF, Pt/GP (21.5 µg/cm^2) and Pt/VACNF (21.5 µg/cm^2). (Reproduced with permission from *J. Electrochem. Soc.* 2020, 167, 066523. © The Electrochemical Society. All rights reserved.)

The Koutecky-Levich (KL) equation has been commonly used to evaluate the kinetic parameters of the ORR reaction with conventional catalysts and is adopted for the Pt/VACNF system here. Figure A.10 shows the KL plots (i.e. 1/j vs. 1/ω$^{1/2}$) for various catalysts derived at different potentials based on Equation (3.3):

$$\frac{1}{J} = \frac{1}{J_k} + \frac{1}{B\omega^{1/2}} \tag{3.3}$$

where J is the measured current density (mA/cm^2), J_k is the kinetic limited current density (mA/cm^2) and ω is the electrode rotation speed (rpm). The KL plots within the potential range from -0.2 V to -0.5 V (vs. Hg/HgO) presented in Figure A.10 exhibit linear lines nearly parallel to each other for each catalyst, confirming the reaction is diffusion-controlled. From the slope (1/B) of the KL plots, the overall electron transfer number (n) can be calculated using the Levich equation:

$$B = 0.20nF[O_2]{D_{O_2}}^{2/3}\nu^{-1/6} \tag{3.4}$$

where n is the electron transfer numbers in ORR, F is the Faraday constant (96,485 C mol^{-1}), [O_2] = 1.2 x 10^{-6} mol cm^{-3} is the dissolved O_2 concentration in 0.10 M KOH, D_{O_2} = 1.90 x 10^{-5} cm^2 s^{-1} is the diffusion coefficient of O_2 in 0.10 M KOH and ν = 0.01 cm^2 s^{-1} is the kinematic viscosity of 0.10 M KOH solution. Figure 3.4c shows the KL plot derived using the J_{lim} at -0.4 V (vs. Hg/HgO) for 25.6 Pt/C and J_{lim} derived from the linear extrapolation method (see Figure A.1) for bare VACNF, 21.5 Pt/GP and 21.5 Pt/VACNF. The derived n values are 2.9, 3.9, 4.7 and 5.1, respectively. The 25.6 µg/cm^2 Pt/C catalyst gives n = 3.9, close to the benchmark value of 4.0 for the direct reduction of O_2 through the 4-e$^-$ pathway. This validates the experimental conditions and the algorithm of the KL analyses. However, the as-derived value n = 2.9 for the bare VACNF array is greater than n = 2 for the 2-e$^-$ ORR pathway while n = 4.7 for 21.5 Pt/GP and n = 5.1 for Pt/VACNF are greater than n = 4 for the 4-e$^-$ pathway. As discussed above, this is associated with the enhanced J_{lim} by the thick GP substrate, which causes the LSV to deviate from the Levich equation. Modification to the Levich equation is needed to apply the KL analyses on 3D catalyst structures. The contribution of the 3D morphology[53] and their effects on KL analyses of carbon-based electrocatalysts[54] have indeed received attention recently. While more accurate algorithms need to be developed in the future, here we hypothesize that the Pt catalysts on the 3D VACNF support follow the direct 4-e$^-$ transfer ORR pathway similar to traditional Pt/C catalyst.

3.3.5 DFT Simulation of the ORR Mechanism of the VACNF Catalyst Support

The dissociative and associative 4-e$^-$ ORR mechanisms on Pt (111) in alkaline solutions are adopted in this study.[55-58] As shown by Equations (3.5-3.8), the dissociative ORR pathway follows a direct O–O bond cleavage of O_2^*. For each dissociated O*, one H is abstracted from liquid H_2O(l), coupled with the charge transfer of one electron to form OH$^-$ ion and OH* (Equation 3.8). The combination of OH* coupled with a second charge forms a second OH$^-$ ion.

$$O_2(g) + * \rightarrow\ O_2^* \tag{3.5}$$

$$O_2^* + * \rightarrow\ 2O^* \tag{3.6}$$

$$O^*\ +\ H_2O(l) +\ e^- \rightarrow\ OH^*\ +\ OH^-(aq) \tag{3.7}$$

$$OH^*\ +\ e^- \rightarrow * \ + OH^-\ (aq) \tag{3.8}$$

In the associative mechanism shown in Equations (3.9-3.10), O_2* first abstracts one H atom from H_2O (l) producing OOH* and an OH$^-$ ion (first charge transfer), followed by the O–O bond cleavage to produce OH* and O*. Both O* and OH* proceed to form OH$^-$ by following steps as in Equations (3.7-3.8).

$$O_2^*\ +\ H_2O(l) +\ e^- \rightarrow\ OOH^*\ + OH^-(aq) \tag{3.9}$$

$$OOH^* + * \rightarrow OH^*\ + O^* \tag{3.10}$$

Over the Pt-free VACNF, both 2-e$^-$ and 4-e$^-$ pathways were also considered. According to Choi et al.[59], it has been shown that O_2 adsorption is not crucial because the charge transfer initiating ORR may occur in the outer Helmholtz plane. Thus, the process involving OOH* formation can be summarized by Equation (3.11). In the 2-e$^-$ pathway, OOH* will desorb upon receiving the second electron, as in Equation (3.12). In the 4-e^- pathway, OOH^- further undergoes the O–O bond cleavage to form OH* and O*. At the OH-passivated VACNF edge, the formation of O* is likely to result in H_2O formation from the passivating OH groups, as described by Equation (3.13 -3.14), where OH_{edge} and O_{edge} denote the passivating OH and O species at the graphitic edge.

$$O_2(g) + * + H_2O(l) + e^- \rightarrow OOH^* + OH^- \tag{3.11}$$

$$OOH^* + e^- \rightarrow * + OOH^-(aq) \tag{3.12}$$

$$OOH^* + 3OH_{edge} \rightarrow 3O_{edge} + 2H_2O(aq) \tag{3.13}$$

$$\boldsymbol{O_{edge}} + \boldsymbol{H_2O(l)} + \boldsymbol{e^-} \rightarrow * + \boldsymbol{OH^-(aq)} \tag{3.14}$$

Analogous to the Computational Hydrogen Electrode (CHE) model under acidic condition[56], the elementary charge transfer step in an alkaline environment is represented by Equation (3.15). In the same way, the step involving $OOH^-(aq)$ is represented by Equation (3.16).

$$OH^-(aq) + \frac{1}{2}H_2(g) \rightarrow H_2O(l) + e^- \tag{3.15}$$

$$OOH^-(aq) + \frac{1}{2}H_2(g) \rightarrow H_2O(l) + \frac{1}{2}O_2(g) + e^- \tag{3.16}$$

Both zero-point energy (ZPE) corrections and entropic contributions were estimated based on the simple harmonic approximation[60]. For liquid phase water, $H_2O(l)$, the solvation energies (the free energy difference between their gas-phase and aqueous-phase states) were taken from the handbook by Dean[61].

As shown in Figure A.11, the dangling bonds at the graphitic edges are passivated with OH groups. Free energy diagrams corresponding to the 2-e^- and 4-e^- ORR pathways over bare VACNFs, along with the configurations of reaction intermediates, are presented in Figure 3.5. As indicated in Figure 3.5, the formation of OOH* from O_2 (g) via the first charge transfer in Equation

(9), is an exothermic process. For the 4-e$^-$ process (blue line in Figure 3.4), O* destabilizes the passivating OH and converts it into oxygen atoms according to Equation (3.13). This step is highly exothermic (-5.19 eV corresponding to the formations of 3 edge sites without the passivating H, as indicated by the inset Figure in Figure 3.5). However, the regeneration of passivating OH groups in Equation (3.14) will be a highly endothermic step (1.16 eV). Thus, the 2-e$^-$ process, simply involving the desorption of OOH* (as OOH$^-$ indicated by red lines in Figure 3.5) is more competitive and is consistent with the experimental results in this work.

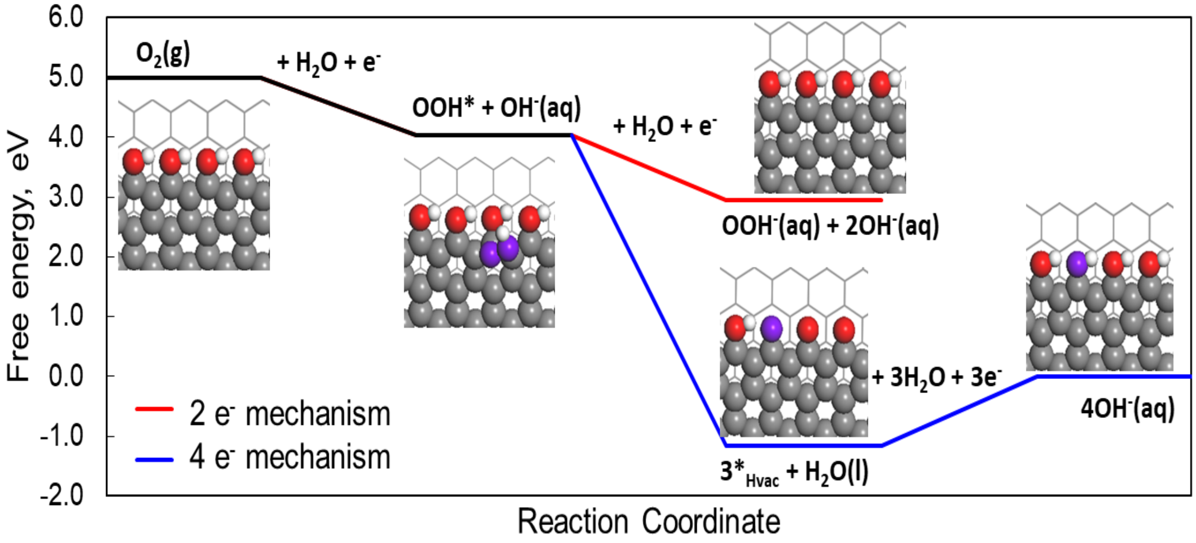

Figure 3.5: Free energy diagram comparing the 2-e$^-$ associative pathway (red) with 4-e$^-$ pathway (blue) on as-grown VACNFs. Color code: white - H, red – O, gray – C, purple – O from the reactant. (Reproduced with permission from *J. Electrochem. Soc.* 2020, 167, 066523. © The Electrochemical Society. All rights reserved.)

DFT calculations based on the Pt/VACNF model confirmed that Pt atoms preferentially bind at the edge. The sputtered Pt atoms form strong Pt–C bonds with the C atoms at the graphitic edge, which stabilizes the ORR active sites. As shown in Figure A.12, the strong Pt–C interaction enables Pt to easily replace the original O species passivating the graphitic edge. Other evidence from modeling has been reported by Cheng and coworkers.[62, 63] More detailed structures of Pt catalysts supported on VACNF models are shown in Figures A.11-A.13. Upon optimization, the

Pt structure becomes somewhat corrugated and also compressed due to the mismatch between Pt and graphene lattices, i.e. 2.51 Å in graphene versus 2.81 Å nearest neighbor Pt-Pt distance in Pt (111) surface.

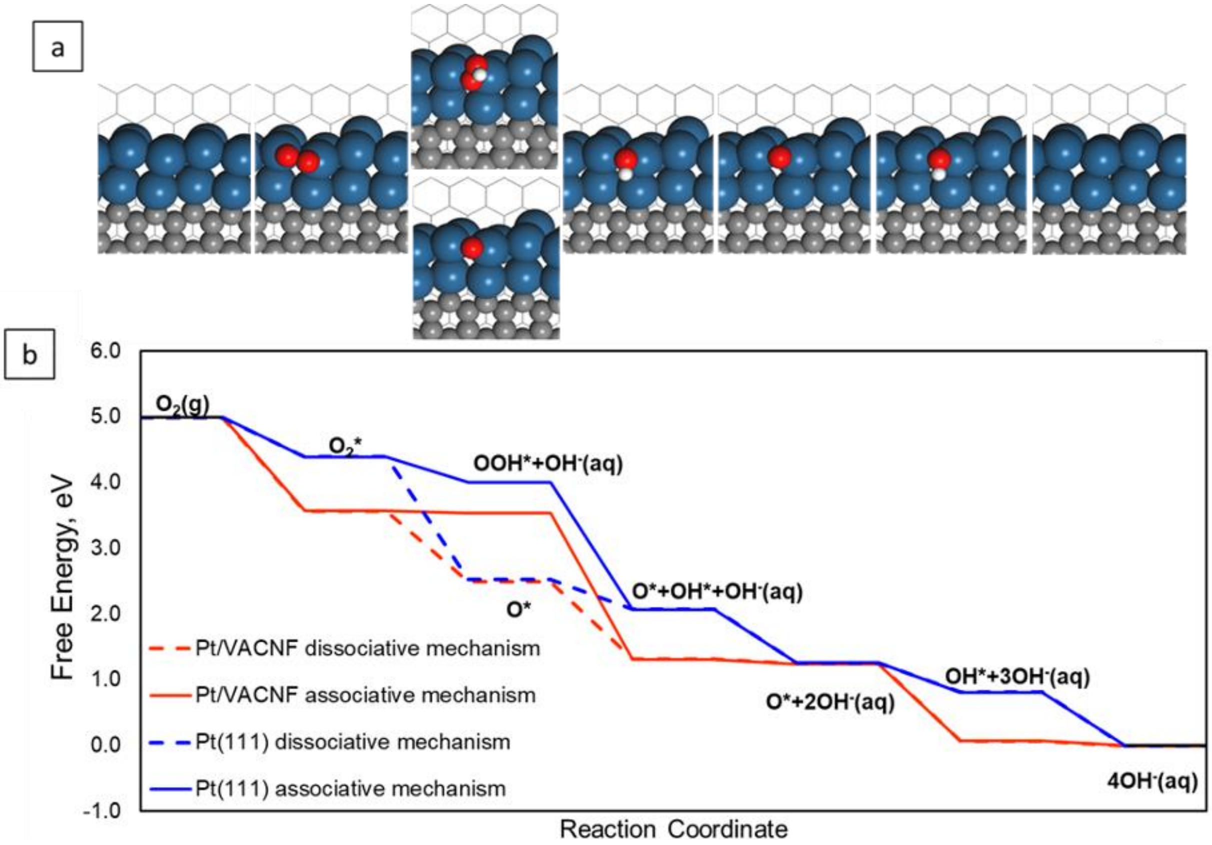

Figure 3.6: a) Molecular structures of ORR reaction intermediates and (b) free energy profiles of the 4-e$^-$ pathway for ORR on Pt/VACNF (red) comparing with Pt (111) (blue) by both dissociative (dashed lines) and associative mechanisms (solid lines). Color code: white – H, red – O, gray – C, blue – Pt. (Reproduced with permission from *J. Electrochem. Soc.* 2020, 167, 066523. © The Electrochemical Society. All rights reserved.)

Here, these Pt atoms are also considered to be the primary site for ORR. The molecular configurations of the most stable intermediates associated with the proposed mechanism for Pt/VACNF are shown in Figure 3.6a. All ORR intermediates prefer to bind at the Pt site. The free energy diagram (Figure 3.6b) shows that O_2 adsorption over Pt/VACNF becomes much stronger (-1.45 eV) than on Pt (111) (-0.60 eV). Thus, the overall ORR free energy profile for the

Pt/VACNF system shifts notably downward. The O–O bond cleavage is also an exothermic step (-1.19 eV). Subsequent formation of OH* (a one-electron transfer step, Equation (3.7)) and its desorption to form $OH^-(aq)$ (Equation (8)) are both exothermic at -1.12 eV and -0.05 eV, respectively. In comparison, over Pt/VACNF, the associative mechanism proceeds through the formation of OOH* in Equation (3.9), with a free energy change of -0.01 eV. As shown in Figure 3.6, the formation of atomic O species via the dissociative mechanism would be much more thermodynamically favorable. Interestingly, by applying a potential bias of 1.23 V, the free energy diagram (Figure A.14) suggests that the OH desorption step becomes strongly endothermic (1.18 eV) and likely the rate-limiting step. Furthermore, the limiting potential calculated on Pt/VACNF is 0.05 V, which is lower than 0.45 V on Pt (111), due to the strong OH binding at the low coordinated Pt sites in our Pt/VACNF model (see Figure 3.5). The DFT calculations are consistent with the -41 mV shift in $E_{1/2}$ with Pt/VACNF comparing to the Pt/C (see Figure 3.2d).

3.3.6 Evaluation of the Durability of Pt/VACNF Electrocatalysts

After rationalizing the RDE LSVs, we can now adapt RDE for further studies. One of the objectives is to understand whether Pt/VACNF catalysts show better durability due to the strong binding of Pt NPs on the graphic edge sites as revealed by the DFT calculations. To evaluate the durability of the synthesized Pt/VACNF catalysts in comparison with the commercial Pt/C catalysts, low Pt loading (10.0-13.0 μg/cm^2) has been studied with the accelerated stress test (AST) in O_2-saturated 0.10 M KOH between 0.293 V and -0.307 V vs. Hg/HgO (i.e. 1.200 V and 0.600 V vs. RHE) at a scan rate of 100 mV/s. After every 1,000 cycles of AST, LSV (at 1,600 rpm) is recorded with RDE (Figures 3.7a and 3.7b). Two parameters, the shift of the potential (ΔE) to maintain the original half-wave current and the % loss in the limiting current density J_{lim}, are derived and shown in Figures 3.7c and 3.7d.

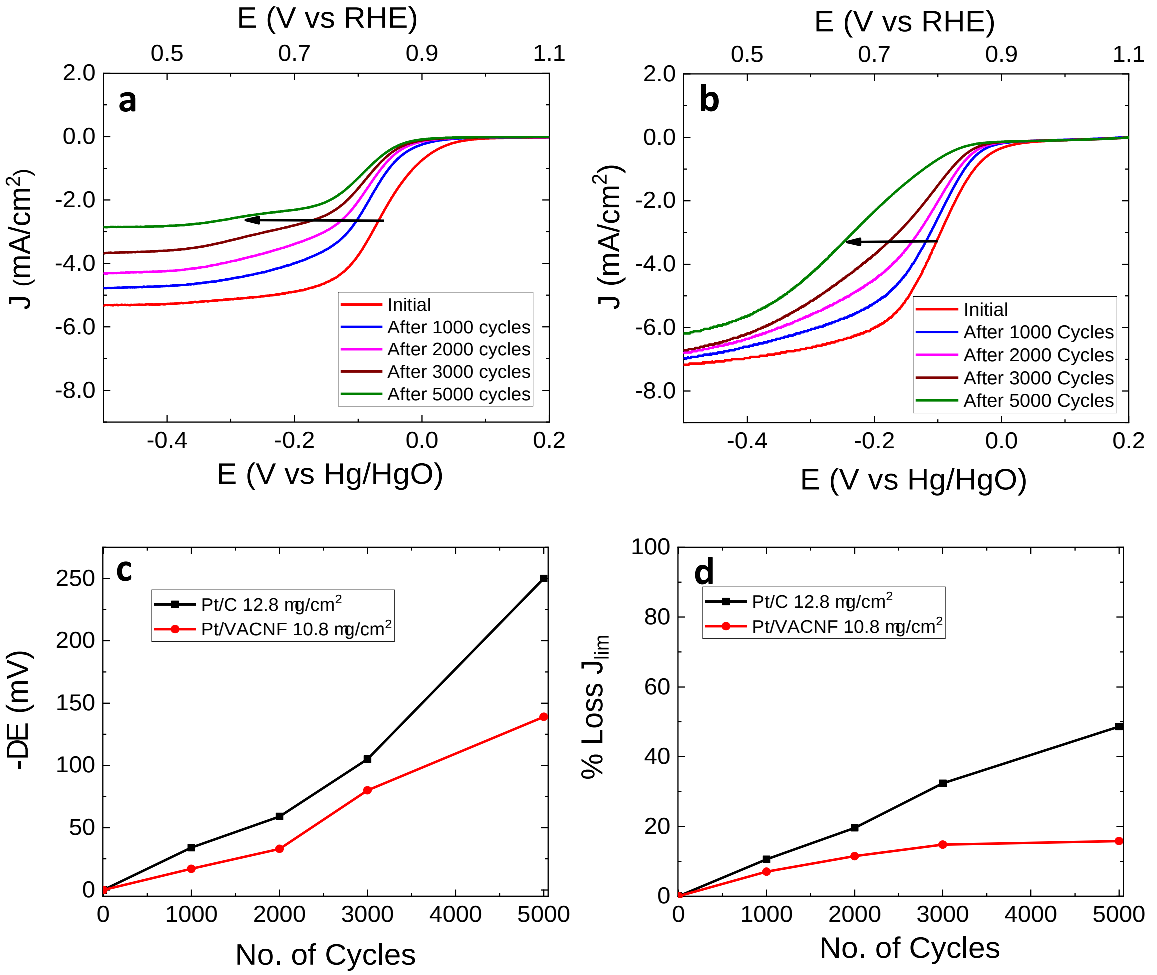

Figure 3.7: **LSV curves of (a) Pt/C (12.8 µg/cm^2) and (b) Pt/VACNF (10.8 µg/cm^2) after every 1000 AST cycles in O_2-saturated 0.10 M KOH solution at a scan rate of 10 mV/s and a rotation speed of 1600 rpm ; (C) Changes in the potential in the LSV curves across the original half-wave current level vs. the number of AST cycles for both the catalysts; (d) The percentage loss in J_{lim} measured with LSVs using a RDE at 1600 rpm in 0.10 M KOH vs. the number of AST cycles for both the catalysts. J_{lim} for the Pt/VACNF is calculated as shown in Figure A.1. (Reproduced with permission from *J. Electrochem. Soc.* 2020, 167, 066523. © The Electrochemical Society. All rights reserved.)**

As presented in Figures 3.7a and 3.7b, the Pt/VACNF catalyst with 10.8 µg/cm^2 Pt loading shows much more stable LSV curves than the commercial Pt/C catalyst with a slightly higher Pt loading of 12.8 µg/cm^2. The potential shift ΔE after 5,000 AST cycles is about -140.0 mV with the Pt/VACNF whereas it is -250 mV for the commercial Pt/C catalyst. The percentage loss of J_{lim} in the Pt/VACNF catalyst is only ~18% after 5,000 AST cycles in contrast to 50% in Pt/C catalyst.

The average sizes of the Pt nanoparticles in Pt/VACNF catalyst and Pt/C catalyst are about 1.1 nm and 3.5 nm, respectively. Even the smaller Pt NPs on the VACNF exhibit better durability than the Pt/C catalyst. This could be likely attributed to the strong interactions between Pt NPs and the graphitic edges. The durability can be further improved by increasing the Pt loading as shown in Figure A.15, and it is clear that 43.0 µg/cm^2 Pt/VACNF is still better than 51.2 µg/cm^2 Pt/C. The TEM images before and after 5,000 AST cycles in Figure A.16 further shows the severe dissolution and agglomeration of Pt in Pt/C whereas much smaller changes were observed in Pt/VACNFs.

3.3.7 Tolerance to Methanol Crossover Reaction

For DMFCs, the ideal ORR catalyst should exhibit higher tolerance to methanol crossover from the anode. These have been investigated by a side-by-side comparison of the Pt/VACNF catalyst (at 10.8 and 21.5 µg/cm^2 Pt loadings) with the commercial Pt/C catalyst (at 12.8 and 25.6 µg/cm^2 Pt loadings). The methanol tolerance was evaluated by performing amperometric measurements and record *j*-t curves while adding 3.0 M methanol into 0.10 M KOH in 20 steps at 0.2 ml/step followed by 8 steps at 2.0 ml/step. The final methanol concentration was 0.75 M in the electrolyte solution. Two fixed potentials, -0.30 V and -0.10 V (vs. Hg/HgO), were chosen for the amperometric measurements, corresponding to the diffusion-controlled and mixed kinetic-diffusion controlled ORR regions of the LSV curves in Figure 3.2c. As shown in Figure 3.8a, at -0.30 V, the commercial Pt/C is very sensitive to methanol, with the current density dropping from about -5.0 mA/cm^2 to -2.0 mA/cm^2 after adding methanol. In contrast, the current density of Pt/VACNF only drops from -6.5 mA/cm^2 to -4.4 mA/cm^2, retaining 67% of the original ORR current. At -0.1 V (Figure 3.8b), where there is stronger methanol oxidation, the difference between the commercial Pt/C and the Pt/VACNF is even more evident. For the commercial Pt/C, the current density changes from -4.4 mA/cm^2 (dominated by ORR) to +3.6 mA/cm^2 (dominated by methanol oxidation). In contrast, with the Pt/VACNF, the current density is dominated by ORR even after reaching the final methanol concentration of 0.75 M though the magnitude is reduced by ~50%, from -3.4 mA/cm^2 to -1.7 mA/cm^2. This demonstrates that the VACNF support can significantly improve the tolerance to methanol crossover.

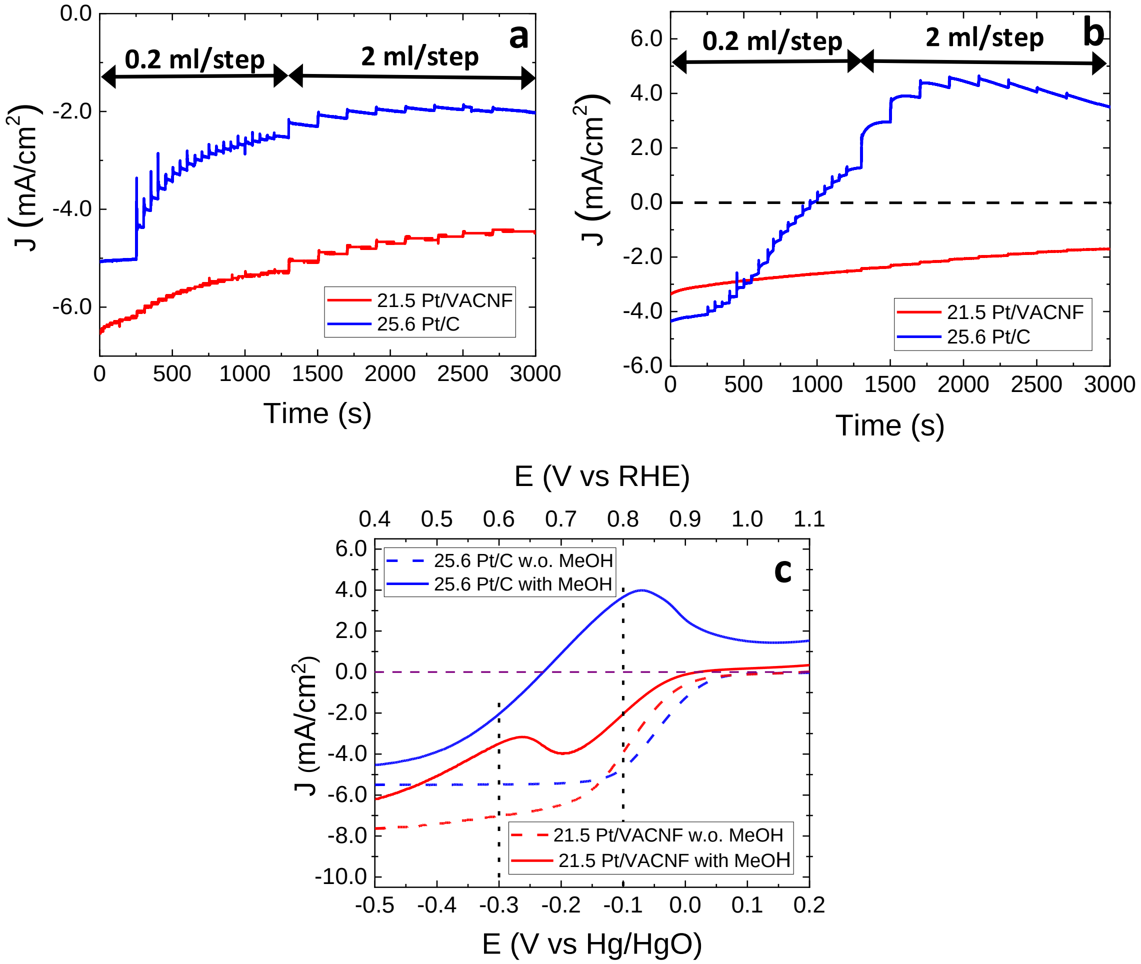

Figure 3.8: Amperometric j-t curves of Pt/C (25.6 μg/cm^2) and Pt/VACNF (21.5 μg/cm^2) recorded at 1,600 rpm in O2-saturated 0.10 M KOH solution with successive addition of 3.0 M methanol to give the final concentration of 0.75 M at the potential of (a) -0.3 V (vs. Hg/HgO) and (b) -0.1 V (vs. Hg/HgO); (c) LSV curves recorded at a scan rate of 10 mV/s and 1,600 rpm in 0.10 M KOH with and without the presence of 0.75 M MeOH for Pt/C (25.6 μg/cm^2) and Pt/VACNF (21.5 μg/cm^2). The purple dash lines mark the zero current density and black dot lines mark the potential at which amperometric j-t curve was recorded. (Reproduced with permission from *J. Electrochem. Soc.* 2020, 167, 066523. © The Electrochemical Society. All rights reserved.)

Figure 3.8c presents the LSV curves at 1600 rpm for the two types of catalysts in the presence and absence of 0.75 M methanol. For the Pt/C catalyst with 25.6 μg/cm^2 Pt loading, the LSV curve in presence of methanol is dominated by methanol oxidation at the potential above -0.23 V (vs. Hg/HgO). In contrast, the Pt/VACNF catalyst with 21.5 μg/cm^2 Pt loading exhibits a reduction current in the full ORR potential range (up to 0.0 V vs. Hg/HgO) and the methanol oxidation is significantly suppressed even up to 0.0 V (vs. Hg/HgO), which explains why a large ORR current density can be observed at -0.1 V even after reaching 0.75 M methanol concentration (as shown in Figure 3.8b). Figures A.17 and A.18 show similar results for Pt/VACNF catalysts with 10.8 and 43.0 μg/cm^2 Pt loading, respectively. The methanol oxidation is suppressed in both amperometric j-t and LSV curves compared to the Pt/C catalysts at similar Pt loadings. Not surprisingly, as the Pt loading increases, the methanol crossover reactions become more dominant in the Pt/C catalyst. The observed high tolerance to methanol oxidation could be related to the stronger O_2 binding on Pt/VACNF than on Pt (111) as revealed by the DFT calculations in Figure 3.6. The presence of O species on the VACNF-supported Pt NPs hinders the methanol chemisorption in the mixed environment of O_2 and methanol. Overall, the adsorption of methanol on active Pt sites in Pt/VACNF is weaker than that of Pt/C. Thus, the Pt/VACNF catalysts show higher selectivity for ORR.

3.3.8 Resistance to CO Poisoning

An ideal catalyst should be completely immune to CO poisoning or able to rapidly recover the activity after desorbing CO. This has been evaluated for the Pt/VACNF catalyst (at 10.8 and 21.5 μg/cm^2 Pt loadings) in comparison with the commercial Pt/C catalyst (at 12.8 and 25.6 μg/cm^2 Pt loadings) by recording LSVs at 1600 rpm in 0.10 M KOH solution at three different conditions: (1) the initial system purged with pure O_2 for standard ORR; (2) the system purged with 10% CO mixed in 90% O$_2$ for poisoning effects; and (3) the system re-purged with pure O$_2$ for the recovering capability. Steps (2) and (3) are alternately repeated 5 times.

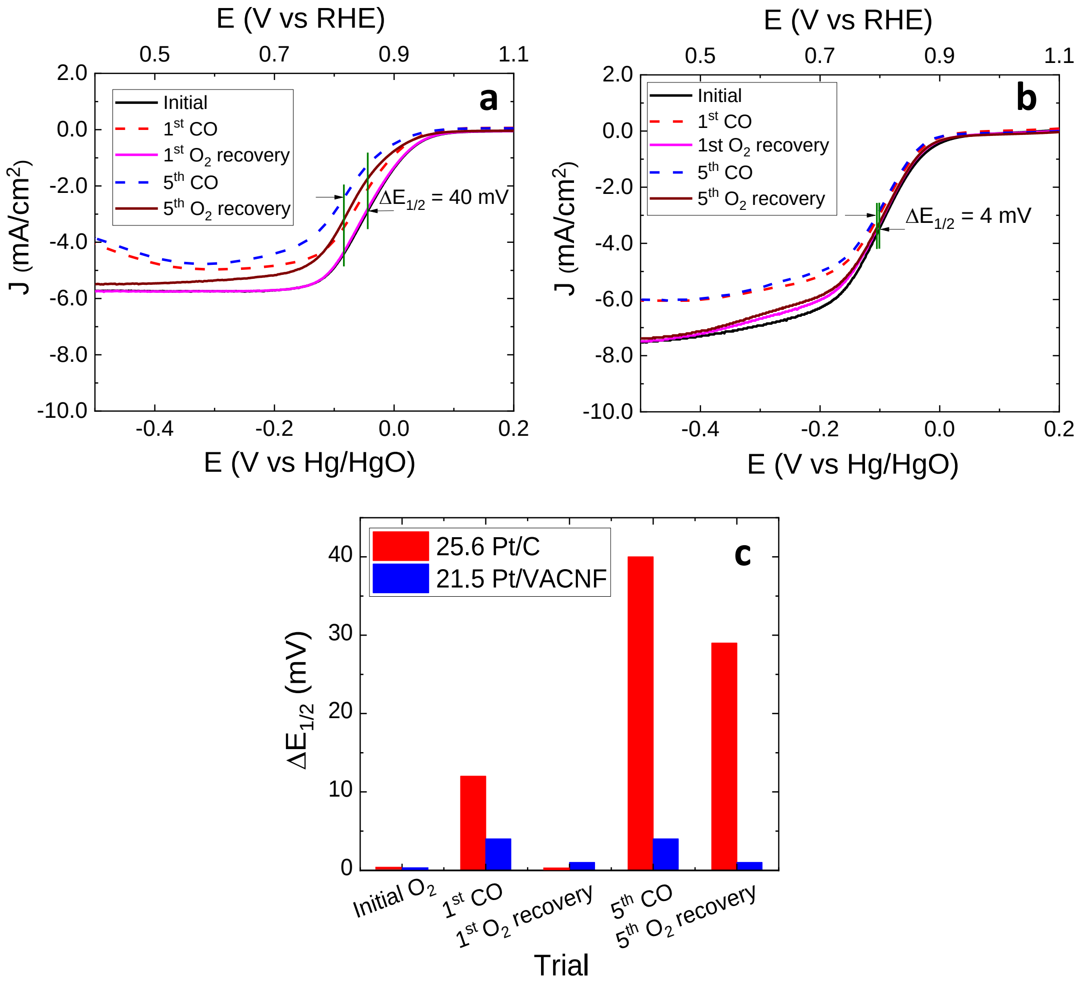

Figure 3.9: LSV curves recorded at a scan rate of 10 mV/s and 1,600 rpm in 0.10 M KOH initially purged with pure O$_2$, then with 10 % CO and 90% O$_2$ (CO poisoning), and re-purged with pure O$_2$ (O$_2$ recovery) for (a) Pt/C (25.6 μg/cm^2) and (b) Pt/VACNF (21.5 μg/cm^2). (The initial and 1st O$_2$ recovery LSV curve is overlapped in Figure 7a). The purging sequence was repeated 5 times and only the data from the first and fifth sets are presented. (c) Plot of the negative shift of the half-wave potential (ΔE$_{1/2}$) vs. the different purging conditions. (Reproduced with permission from *J. Electrochem. Soc.* 2020, 167, 066523. © The Electrochemical Society. All rights reserved.)

As shown in Figure 3.9a and 3.9b, it is clear that the ORR limiting current density drops when the system is first exposed to CO and it completely recovers to the initial performance after re-purging with pure O_2 for both the 25.6 μg/cm^2 Pt/C catalyst and the 21.5 μg/cm^2 Pt/VACNF catalyst. But after the 5th purge with 10% CO, the limiting current density of the Pt/C catalyst drops much more and is not completely recovered after re-purge with O_2. In contrast, the limiting current of the Pt/VACNF catalyst in 5th CO purge drops by about the same amount as in the first CO purge and is nearly fully recovered when re-purged with O_2. Figure 3.9c presents the change in half-wave potential between the initial LSV curve and LSV curves recorded at different purging conditions. After the fifth trial of CO poisoning, the $E_{1/2}$ has only a small shift of -4 mV in the Pt/VACNF catalyst whereas it is -40 mV in the Pt/C catalyst. Figure A.19 shows a similar behavior observed at lower Pt loading with 12.8 μg/cm^2 Pt/C and 10.8 μg/cm^2 Pt/VACNF during the CO and pure O_2 purging cycles. These results indicate that Pt/VACNF has clearly a better recovery capability from CO poisoning than the commercial Pt/C catalyst and it can be attributed to either the stronger O_2 adsorption or the presence of O species on the VACNF-supported Pt NPs which help to remove CO.

3.4 Conclusions

In summary, the VACNF array grown by PECVD has been demonstrated as a unique 3D architecture to support ion-sputtered Pt catalysts for ORR. The linear sweep voltammetry of ORR based on such 3D structures on RDE has been found to deviate from the Levich equation. The raised edge and the roughness at the top surface of the nanostructured VACNF array alter the hydrodynamic conditions and the stagnant diffusion layer thickness, resulting in a slanted ORR curve and an increased limiting current density in the Pt/VACNF system. Despite this complication, useful information can be extracted from the RDE measurements. The half-wave potential of the Pt/VACNF catalysts is comparable to the benchmark commercial Pt/C catalyst at similar Pt loadings following a 4-e^- ORR pathway. DFT calculations have validated the strong binding of Pt atoms with the graphitic edge sites in Pt/VACNF catalysts. Based on these models, we have concluded that ORR proceeds via a 2-e^- pathway on bare VACNFs and a 4-e^- pathway on Pt/VACNF, respectively. The Pt/VACNF catalyst has shown better durability in accelerated stress tests than the commercial Pt/C catalyst at similar loading. Furthermore, the Pt/VACNF catalysts have shown enhanced tolerance to methanol oxidation. The ORR is the dominant reaction in the full potential range with the Pt/VACNF catalysts in the presence of 0.75 M methanol while methanol oxidation surpasses ORR above -0.2 V (vs. Hg/HgO) with the commercial Pt/C catalyst. The Pt/VACNF system has also shown improved capability to recover from CO poisoning. These results provide new insights into the critical roles of 3D nanostructured carbon supports and their graphitic microstructures on the fundamental electrocatalytic properties of the catalyst.

3.5 References

1. Wee, J.-H., Applications of Proton Exchange Membrane Fuel Cell Systems. *Renew. Sust. Energy Rev.* **2007,** *11* (8), 1720-1738.
2. Rabis, A.; Rodriguez, P.; Schmidt, T. J., Electrocatalysis for Polymer Electrolyte Fuel Cells: Recent Achievements and Future Challenges. *ACS Catal.* **2012,** *2* (5), 864-890.
3. Antolini, E., Carbon supports for low-temperature fuel cell catalysts. *Appl. Catal. B: Environ.* **2009,** *88* (1), 1-24.
4. Gewirth, A. A.; Thorum, M. S., Electroreduction of Dioxygen for Fuel-Cell Applications: Materials and Challenges. *Inorg. Chem.* **2010,** *49* (8), 3557-3566.
5. Morozan, A.; Jousselme, B.; Palacin, S., Low-platinum and platinum-free catalysts for the oxygen reduction reaction at fuel cell cathodes. *Energy Environ. Sci.* **2011,** *4* (4), 1238-1254.
6. Peng, Z.; Yang, H., Designer platinum nanoparticles: Control of shape, composition in alloy, nanostructure and electrocatalytic property. *Nano Today* **2009,** *4* (2), 143-164.
7. Gong, K.; Du, F.; Xia, Z.; Durstock, M.; Dai, L., Nitrogen-doped carbon nanotube arrays with high electrocatalytic activity for oxygen reduction. *Science* **2009,** *323* (5915), 760-4.
8. Koenigsmann, C.; Wong, S. S., Tailoring Chemical Composition To Achieve Enhanced Methanol Oxidation Reaction and Methanol-Tolerant Oxygen Reduction Reaction Performance in Palladium-Based Nanowire Systems. *ACS Catal.* **2013,** *3* (9), 2031-2040.
9. Shukla, A. K.; Raman, R. K., Methanol-resistant oxygen-reduction catalysts for direct methanol fuel celms. *Annu. Rev. Mater. Res.* **2003,** *33*, 155-168.

10. Debe, M. K., Electrocatalyst approaches and challenges for automotive fuel cells. *Nature* **2012,** *486* (7401), 43-51.
11. Wang, X. X.; Swihart, M. T.; Wu, G., Achievements, challenges and perspectives on cathode catalysts in proton exchange membrane fuel cells for transportation. *Nat. Catal.* **2019,** *2* (7), 578-589.
12. Nie, Y.; Li, L.; Wei, Z., Recent advancements in Pt and Pt-free catalysts for oxygen reduction reaction. *Chem. Soc. Rev.* **2015,** *44* (8), 2168-2201.
13. Yu, X.; Ye, S., Recent advances in activity and durability enhancement of Pt/C catalytic cathode in PEMFC: Part I. Physico-chemical and electronic interaction between Pt and carbon support, and activity enhancement of Pt/C catalyst. *J. Power Sources* **2007,** *172* (1), 133-144.
14. Yu, X.; Ye, S., Recent advances in activity and durability enhancement of Pt/C catalytic cathode in PEMFC: Part II: Degradation mechanism and durability enhancement of carbon supported platinum catalyst. *J. Power Sources* **2007,** *172* (1), 145-154.
15. Seo, M. H.; Choi, S. M.; Kim, H. J.; Kim, W. B., The graphene-supported Pd and Pt catalysts for highly active oxygen reduction reaction in an alkaline condition. *Electrochem. Commun.* **2011,** *13* (2), 182-185.
16. Zhu, C.; Dong, S., Recent progress in graphene-based nanomaterials as advanced electrocatalysts towards oxygen reduction reaction. *Nanoscale* **2013,** *5* (5), 1753-1767.
17. Shao, Y.; Zhang, S.; Wang, C.; Nie, Z.; Liu, J.; Wang, Y.; Lin, Y., Highly durable graphene nanoplatelets supported Pt nanocatalysts for oxygen reduction. *J. Power Sources* **2010,** *195* (15), 4600-4605.
18. Tang, H.; Chen, J. H.; Huang, Z. P.; Wang, D. Z.; Ren, Z. F.; Nie, L. H.; Kuang, Y. F.; Yao, S. Z., High dispersion and electrocatalytic properties of platinum on well-aligned carbon nanotube arrays. *Carbon* **2004,** *42* (1), 191-197.
19. Wang, D.-W.; Su, D., Heterogeneous nanocarbon materials for oxygen reduction reaction. *Energy Environ. Sci.* **2014,** *7* (2), 576-591.
20. Bessel, C. A.; Laubernds, K.; Rodriguez, N. M.; Baker, R. T. K., Graphite Nanofibers as an Electrode for Fuel Cell Applications. *J. Phys. Chem. B* **2001,** *105* (6), 1115-1118.
21. Lee, K.; Zhang, J.; Wang, H.; Wilkinson, D. P., Progress in the synthesis of carbon nanotube- and nanofiber-supported Pt electrocatalysts for PEM fuel cell catalysis. *J. Appl. Electrochem.* **2006,** *36* (5), 507-522.
22. Li, W.; Waje, M.; Chen, Z.; Larsen, P.; Yan, Y., Platinum nanopaticles supported on stacked-cup carbon nanofibers as electrocatalysts for proton exchange membrane fuel cell. *Carbon* **2010,** *48* (4), 995-1003.
23. Chung, H. T.; Won, J. H.; Zelenay, P., Active and stable carbon nanotube/nanoparticle composite electrocatalyst for oxygen reduction. *Nat. Commun.* **2013,** *4*, 1922.
24. Wang, Y.-J.; Zhao, N.; Fang, B.; Li, H.; Bi, X. T.; Wang, H., Carbon-Supported Pt-Based Alloy Electrocatalysts for the Oxygen Reduction Reaction in Polymer Electrolyte Membrane Fuel Cells: Particle Size, Shape, and Composition Manipulation and Their Impact to Activity. *Chem. Rev.* **2015,** *115* (9), 3433-3467.

25. Kongkanand, A.; Kuwabata, S.; Girishkumar, G.; Kamat, P., Single-Wall Carbon Nanotubes Supported Platinum Nanoparticles with Improved Electrocatalytic Activity for Oxygen Reduction Reaction. *Langmuir* **2006,** *22* (5), 2392-2396.

26. Shaijumon, M. M.; Ramaprabhu, S.; Rajalakshmi, N., Platinum/multiwalled carbon nanotubes-platinum/carbon composites as electrocatalysts for oxygen reduction reaction in proton exchange membrane fuel cell. *Appl. Phys. Lett.* **2006,** *88* (25), 253105.

27. Debe, M. K.; Schmoeckel, A. K.; Vernstrom, G. D.; Atanasoski, R., High voltage stability of nanostructured thin film catalysts for PEM fuel cells. *J. Power Sources* **2006,** *161* (2), 1002-1011.

28. Debe, M. K.; Steinbach, A. J.; Vernstrom, G. D.; Hendricks, S. M.; Kurkowski, M. J.; Atanasoski, R. T.; Kadera, P.; Stevens, D. A.; Sanderson, R. J.; Marvel, E.; Dahn, J. R., Extraordinary Oxygen Reduction Activity of Pt3Ni7. *J. Electrochem. Soc.* **2011,** *158* (8), B910-B918.

29. Debe, M. K., Nanostructured Thin Film Electrocatalysts for PEM Fuel Cells - A Tutorial on the Fundamental Characteristics and Practical Properties of NSTF Catalysts. *ECS Trans.* **2012,** *45* (2), 47-68.

30. Tian, Z. Q.; Lim, S. H.; Poh, C. K.; Tang, Z.; Xia, Z.; Luo, Z.; Shen, P. K.; Chua, D.; Feng, Y. P.; Shen, Z.; Lin, J., A Highly Order-Structured Membrane Electrode Assembly with Vertically Aligned Carbon Nanotubes for Ultra-Low Pt Loading PEM Fuel Cells. *Adv. Energy Mater.* **2011,** *1* (6), 1205-1214.

31. Wakabayashi, R. H.; Paik, H.; Murphy, M. J.; Schlom, D. G.; Brützam, M.; Uecker, R.; van Dover, R. B.; DiSalvo, F. J.; Abruña, H. D., Rotating Disk Electrode Voltammetry of Thin Films of Novel Oxide Materials. *J. Electrochem. Soc.* **2017,** *164* (14), H1154-H1160.

32. Melechko, A. V.; Merkulov, V. I.; McKnight, T. E.; Guillorn, M. A.; Klein, K. L.; Lowndes, D. H.; Simpson, M. L., Vertically aligned carbon nanofibers and related structures: Controlled synthesis and directed assembly. *J. Appl. Phys.* **2005,** *97* (4), 041301.

33. Cruden, B. A.; Cassell, A. M.; Ye, Q.; Meyyappan, M., Reactor design considerations in the hot filament/direct current plasma synthesis of carbon nanofibers. *J. Appl. Phys.* **2003,** *94* (6), 4070-4078.

34. Li, J.; Pandey, G. P., Advanced Physical Chemistry of Carbon Nanotubes. *Annu. Rev. Phys. Chem.* **2015,** *66* (1), 331-356.

35. Biddinger, E. J.; Ozkan, U. S., Role of Graphitic Edge Plane Exposure in Carbon Nanostructures for Oxygen Reduction Reaction. *J. Phys. Chem. C* **2010,** *114* (36), 15306-15314.

36. Kim, C.; Kim, Y. J.; Kim, Y. A.; Yanagisawa, T.; Park, K. C.; Endo, M.; Dresselhaus, M. S., High performance of cup-stacked-type carbon nanotubes as a Pt–Ru catalyst support for fuel cell applications. *J. App. Phys.* **2004,** *96* (10), 5903-5905.

37. Endo, M.; Kim, Y. A.; Ezaka, M.; Osada, K.; Yanagisawa, T.; Hayashi, T.; Terrones, M.; Dresselhaus, M. S., Selective and Efficient Impregnation of Metal Nanoparticles on Cup-Stacked-Type Carbon Nanofibers. *Nano Lett.* **2003,** *3* (6), 723-726.

38. Zhou, Z.-M.; Shao, Z.-G.; Qin, X.-P.; Chen, X.-G.; Wei, Z.-D.; Yi, B.-L., Durability study of Pt–Pd/C as PEMFC cathode catalyst. *Int. J. Hydrogen Energy* **2010,** *35* (4), 1719-1726.

39. Kresse, G.; Furthmüller, J., Efficient iterative schemes for ab initio total-energy calculations using a plane-wave basis set. *Phys. Rev. B* **1996,** *54* (16), 11169-11186.

40. Perdew, J. P.; Burke, K.; Ernzerhof, M., Generalized Gradient Approximation Made Simple. *Phys. Rev. Lett.* **1996,** *77* (18), 3865-3868.

41. Blöchl, P. E., Projector augmented-wave method. *Phys. Rev. B* **1994,** *50* (24), 17953-17979.

42. Monkhorst, H. J.; Pack, J. D., Special points for Brillouin-zone integrations. *Phys. Rev. B* **1976,** *13* (12), 5188-5192.

43. Ooi, N.; Rairkar, A.; Adams, J. B., Density functional study of graphite bulk and surface properties. *Carbon* **2006,** *44* (2), 231-242.

44. Grimme, S.; Antony, J.; Ehrlich, S.; Krieg, H., A consistent and accurate ab initio parametrization of density functional dispersion correction (DFT-D) for the 94 elements H-Pu. *J. Chem. Phys.* **2010,** *132* (15), 154104.

45. Zhu, Y. A.; Sui, Z. J.; Zhao, T. J.; Dai, Y. C.; Cheng, Z. M.; Yuan, W. K., Modeling of fishbone-type carbon nanofibers: A theoretical study. *Carbon* **2005,** *43* (8), 1694-1699.

46. Hou, X.; Hu, Q.; Zhang, P.; Mi, J., Oxygen reduction reaction on nitrogen-doped graphene nanoribbons: A density functional theory study. *Chem. Phys. Lett.* **2016,** *663*, 123-127.

47. Wang , S.; Iyyamperumal , E.; Roy, A.; Xue, Y.; Yu, D.; Dai, L., Vertically Aligned BCN Nanotubes as Efficient Metal-Free Electrocatalysts for the Oxygen Reduction Reaction: A Synergetic Effect by Co-Doping with Boron and Nitrogen. *Angew. Chem.* **2011,** *50* (49), 11756-11760.

48. Scofield, M. E.; Liu, H.; Wong, S. S., A concise guide to sustainable PEMFCs: recent advances in improving both oxygen reduction catalysts and proton exchange membranes. *Chem. Soc. Rev.* **2015,** *44* (16), 5836-5860.

49. Cai, X.; Xia, B. Y.; Franklin, J.; Li, B.; Wang, X.; Wang, Z.; Chen, L.; Lin, J.; Lai, L.; Shen, Z., Free-standing vertically-aligned nitrogen-doped carbon nanotube arrays/graphene as air-breathing electrodes for rechargeable zinc–air batteries. *J. Mater. Chem. A* **2017,** *5* (6), 2488-2495.

50. Dinan, T. E.; Matlosz, M.; Landolt, D., Experimental Investigation of the Current Distribution on a Recessed Rotating Disk Electrode. *J. Electrochem. Soc.* **1991,** *138* (10), 2947-2951.

51. Garsany, Y.; Baturina, O. A.; Swider-Lyons, K. E.; Kocha, S. S., Experimental Methods for Quantifying the Activity of Platinum Electrocatalysts for the Oxygen Reduction Reaction. *Anal. Chem.* **2010,** *82* (15), 6321-6328.

52. Bard, A. J.; Faulkner, L. R., *Electrochemical methods: fundamentals and applications*. Wiley New York: 1980; Vol. 2.

53. Masa, J.; Batchelor-McAuley, C.; Schuhmann, W.; Compton, R. G., Koutecky-Levich analysis applied to nanoparticle modified rotating disk electrodes: Electrocatalysis or misinterpretation. *Nano Res.* **2014,** *7* (1), 71-78.

54. Shin, D.; Jeong, B.; Choun, M.; Ocon, J. D.; Lee, J., Diagnosis of the measurement inconsistencies of carbon-based electrocatalysts for the oxygen reduction reaction in alkaline media. *RSC Adv.* **2015,** *5* (2), 1571-1580.

55. Liu, S.; White, M. G.; Liu, P., Mechanism of Oxygen Reduction Reaction on Pt(111) in Alkaline Solution: Importance of Chemisorbed Water on Surface. *J. Phys. Chem. C* **2016,** *120* (28), 15288-15298.

56. Nørskov, J. K.; Rossmeisl, J.; Logadottir, A.; Lindqvist, L.; Kitchin, J. R.; Bligaard, T.; Jónsson, H., Origin of the Overpotential for Oxygen Reduction at a Fuel-Cell Cathode. *J. Phys. Chem. B* **2004,** *108* (46), 17886-17892.

57. Rizo, R.; Herrero, E.; Feliu, J. M., Oxygen reduction reaction on stepped platinum surfaces in alkaline media. *Phys. Chem. Chem. Phys.* **2013,** *15* (37), 15416-15425.

58. Xu, J.; Liu, B., Intrinsic properties of nitrogen-rich carbon nitride for oxygen reduction reaction. *Appl. Surf. Sci.* **2020,** *500*, 144020.

59. Choi, C. H.; Lim, H.-K.; Chung, M. W.; Park, J. C.; Shin, H.; Kim, H.; Woo, S. I., Long-Range Electron Transfer over Graphene-Based Catalyst for High-Performing Oxygen Reduction Reactions: Importance of Size, N-doping, and Metallic Impurities. *J. Am. Chem. Soc.* **2014,** *136* (25), 9070-9077.

60. Shan, N.; Zhou, M.; Hanchett, M. K.; Chen, J.; Liu, B., Practical principles of density functional theory for catalytic reaction simulations on metal surfaces – from theory to applications. *Mol Simul.* **2017,** *43* (10-11), 861-885.

61. Dean, J. A., *Lange's Handbook of Chemistry*. McGraw-Hill: New York: 1985.

62. Cheng, H.; Zhu, Y.-A.; Chen, D.; Åstrand, P.-O.; Li, P.; Qi, Z.; Zhou, X.-G., Evolution of Carbon Nanofiber-Supported Pt Nanoparticles of Different Particle Sizes: A Molecular Dynamics Study. *J. Phys. Chem. C* **2014,** *118* (41), 23711-23722.

63. Cheng, H.-Y.; Zhu, Y.-A.; Åstrand, P.-O.; Chen, D.; Li, P.; Zhou, X.-G., Evolution of Pt Nanoparticles Supported on Fishbone-Type Carbon Nanofibers with Cone–Helix Structures: A Molecular Dynamics Study. *J. Phys. Chem. C* **2013,** *117* (27), 14261-14271.

Chapter 4 - Evaluation of the Catalyst Activity and Durability towards ORR using Nitrogen-doped Vertically Aligned Carbon Nanofibers

4.1 Introduction

Platinum NPs supported on amorphous carbon (Pt/C) is still considered to be the effective catalyst for catalyzing the ORR with sluggish reaction kinetics. The high-cost Pt and its limited reserve seems to be a drawback for Pt-based catalysts. Besides the cost issue, they also suffer from long-term durability, which is another technical barrier for the commercialization of fuel cells[1]. The performance of the Pt/C deteriorates when operated for a longer time due to the agglomeration of Pt NPs and dissolution of Pt from the carbon support[1, 2]. The other factor that affects the long-term performance is the oxidation of the underlying carbon support, i.e. carbon corrosion[3]. The fuel cells are operated under harsh conditions and sometimes during startup/shutdown cell voltage can rise as high as 1.5 V to counter effect the hydrogen starvation which can result in increasing the potential of the cathode reaction[4, 5]. At very high cathode potentials the carbon starts to degrade and form CO_2, and the corrosion rate increases drastically with the potential[6]. Also, the presence of more Pt on the surface can further catalyze the oxidation of carbon and there may be increase in agglomeration and dissolution of Pt as the amount of carbon decreases[7]. To address these various issues with Pt catalysts it is reported to reduce the Pt loading or replace it completely with non-noble metal catalysts. However, when the Pt loading is reduced or replaced it is very challenging to maintain catalytic activity and durability.

Introducing strain and electronic effects by alloying with other noble/transition metals[7-9], designing of Pt catalysts in the form of nanowires, nanodendrites and nanotubes[10-14], development of new methods for catalyst synthesis[15], developing support materials such as TiO_2[16, 17], IrO_2[18, 19], SnO_2[20], SiC[21, 22], W_2C[23], heteroatom-doped carbon materials[24-26] are the various methods that have been adopted to solve the durability issue with still employing Pt catalysts. However, among these different methods, N-doped into carbon nanomaterials such as carbon nanotubes[27], carbon nanofibers[28, 29], carbon nanocages[30], graphene[31], graphene paper[32], reduced graphene oxide[33], porous carbon[34], ordered mesoporous carbon[35] as the catalysts support is considered to be a better choice for improving the catalyst durability. The role of nitrogen species in carbon materials has been investigated and found out that nitrogen doping altered the electronic and structural properties of the employed carbon material and created a stronger metal-support interaction, and thereby enhancing the catalytic activity and durability with reduced Pt loading[3, 24, 36]. Nitrogen doping can be achieved by using in-situ or ex-situ methods and both resulting in nitrogen doping with different N-functionalities[24]. Previous reports have suggested that, among different N-functionalities, the presence of pyridinic N increases the available ORR active sites and hence contributing to the improved ORR activity and increasing the Pt stability[28, 32, 33, 37]. However, there is no report on employing pyridinic N rich VACNFs with lower Pt particle size as catalysts support to address the durability of the Pt catalyst.

In this study, we prepared a N-doped three-dimensional VACNF array using a DC-biased PECVD system[38, 39] coupled with NH_3 plasma annealing (PA) and employed it as a catalyst support to improve the durability of the Pt catalysts towards the ORR. We previously conducted a series of studies to emphasize the role of VACNFs as a catalyst support for ORR as given in Chapter 3. The resulting Pt/VACNF catalysts exhibit considerable durability and higher tolerance to methanol crossover when compared to the commercial Pt/C catalyst. Herein, we further explore the role of additional nitrogen introduced into the VACNF structures and its influence in the catalyst activity and durability. Initially, the VACNF arrays are prepared using PECVD with an average diameter between 50 and 250 nm and an average length of ~5 μm. Additional nitrogen is introduced into the VACNF arrays by using NH_3 plasma annealing at 550 ^{o}C for different time intervals. After plasma annealing, the surface morphology of the resulting N-VACNF changes, and with the assistance of HRTEM and EDX mapping we verified that the plasma annealing creates NiO particles as the secondary nanostructures on the catalyst surface. The change in the nature of the carbon surface is characterized using Raman analysis. The % of Nitrogen increases with the plasma annealing time and the increase in nitrogen content alters the electronic structure of the VACNF support. As a result, when the N-VACNF is sputtered with Pt, the nitrogen present in the support reduces the Pt particle size, modifies the Pt binding energy, and improves the interaction between Pt NPs and the VACNF support. In addition, the nitrogen doping leads to a partial electron transfer between the carbon support and Pt NPs, as verified by XPS analysis. As a result, Pt/N-VACNF catalyst is found to have better durability when compared to the Pt/VACNF and counterpart Pt/C with similar loading. Density Functional Theory (DFT) calculations validate the increase in stability of the Pt NPs with an increase in pyridinic N and illustrate the molecular ORR pathway for Pt/N-VACNF. Moreover, the resulting Pt/N-VACNF catalyst is also found to have an enhanced tolerance towards the methanol crossover and its highly selective to the ORR in a mixed environment.

4.2 Experimental Section

4.2.1 N-VACNF Growth

Graphite paper with 1 x 1 inch^2 was coated with the nickel catalyst for a nominal thickness of 22 nm using a high-resolution ion beam coater and VACNFs with an average length of 5 μm was grown on the graphite paper substrate using DC-biased PECVD by following the procedure mentioned in Chapter 2.

The N-VACNFs was prepared by introducing nitrogen-doping into the as-grown VACNF samples in two different ways: thermal and plasma annealing. Thermal annealing was done by heat treating the as-grown samples in the presence of NH_3 (400 sccm) at a temperature range between 600-800 ^oC for 1 h. Plasma annealing was done by treating the as-grown samples in NH_3 (400 sccm) plasma with 45 W power at temperatures of 550, 600, and 650 ^oC for a time period of 5, 15, and 30 min. Both the annealing was done immediately after preparing the VACNFs

4.2.2 Preparation of Pt/N-VACNF

Among different N-VACNF samples, the one that was plasma annealed at 550 ^oC for 5 min was used as the catalyst support for Pt. Pt was deposited on the N-VACNFs from a Pt target of 99.99% purity using the high-resolution ion beam coater under a pressure of 1.5×10^{-4} Torr. The sample stage was inclined at an angle of 5^o and rotated at a constant speed of 15 rpm to ensure uniform deposition of Pt along the fibers. The deposition was maintained at a constant rate of 0.5 Å/s and was precisely controlled to a nominal thickness of 20 nm using an in-situ quartz crystal microbalance with less than 5% error to get the desired Pt mass loading. The Pt/N-VACNF with a nominal thickness of 20 nm has a Pt loading of 43.0 $\mu g/cm^2$ and an overall wt % of ~19.8 %.

4.2.3 Materials Characterization

The surface topography of the N-VACNF catalysts was obtained using the DS 130F FESEM (Topcon, Tokyo, Japan) at a 15 KV accelerating voltage. The microstructure of the N-VACNF and Pt/N-VACNF was analyzed using a CM 100 transmission electron microscope

(TEM) (FEI, Hillsboro, OR) at a 100 kV accelerating voltage and Tecnai F20 XT high-resolution TEM (HRTEM) (FEI, Hillsboro, OR) at a 200 kV accelerating voltage. Elemental mapping and analysis were obtained using EDS in the Tecnai Osiris S/TEM (FEI, Hillsboro, OR) at a 200 kV accelerating voltage and Tecnai F20 XT field-emission S/TEM (FEI, Hillsboro, OR). Raman spectra were obtained using a DXR Raman microscope (Thermo Scientific, Waltham, MA) at an excitation laser wavelength of 532 nm. Surface composition and chemical environments of the catalysts were obtained using a K-Alpha X-ray photoelectron spectrometer system (Thermo Scientific, Waltham, MA) with a monochromated Al Kα source (1486.7 eV). All the X-ray photoelectron spectroscopy (XPS) measurements were obtained using a 400 μm spot size. Survey spectra were recorded using a pass energy of 200.0 eV, a step size of 1.00 eV, and a dwell time of 10 ms. The high-resolution spectra were recorded using a pass energy of 50.0 eV, a step size of 0.10 eV, and a dwell time of 50 ms. The high-resolution XPS spectra were deconvoluted using OriginPro and the peak fitting was done using Gaussian-Lorentzian curves and a Shirley background subtraction.

4.2.4 Electrochemical Characterization

The study of the electrochemical properties and the catalytic activity towards the ORR were performed by a three-electrode setup using a CHI 760D electrochemical workstation (CH Instruments, Austin, TX) and a rotating ring disk electrode controller (RRDE-3A, ALS Co., Ltd, Japan). The commercial Pt/C catalyst was studied under the same conditions to make a fair comparison. A coiled Pt wire and a mercury-mercuric oxide (Hg/HgO) electrode (0.198 V vs Hg/HgO) with 1.0 M NaOH filling solution was used as the counter and reference electrode, respectively. The working electrode for the N-VACNF and Pt/N-VACNF catalysts were prepared by punching out a 6.0 mm disks, pasting it on the RDE using a conductive silver paste, and drying at 70 ^{o}C for 2 h. For Pt/C, the working electrode was prepared by drop casting 5.0 µL of the catalyst ink on a glassy-carbon RDE (3.15 mm diameter) and drying the electrode at RT to get a uniform thin film. The catalyst ink was prepared by dispersing 10.0 mg of the catalyst in a 2.5 ml mixture of water, isopropanol, and 5 wt% Nafion followed by sonication for 1 h. The amount of Pt/C on the RDE was optimized to match the Pt loading on Pt/N-VACNF. The electrolyte for most of the studies was 0.10 M KOH solution saturated with Ar or O_2. CV was conducted between 0.30 V and -0.90 V (vs. Hg/HgO) at a scan rate of 50 mV/s. The RDE polarization curves were obtained using LSV technique in a potential range of 0.20 V to -0.70 V (vs. Hg/HgO) at different rotation speeds, from 500 to 3000 rpm, and at a scan rate of 10 mV/s. The details in converting potentials versus the RHE is mentioned in Chapter 2. The derivation of the limiting current density (J_{lim}) and the half-wave potential ($E_{1/2}$) electrochemical are described in Sections 1 and 2 and Figures A.1 and A.2 in Appendix-A. The durability of the catalysts were evaluated using AST carried out for both Pt/N-VACNF and Pt/C in O_2-saturated 0.10 M KOH solution by performing continuous potential cycling between 0.293 V and -0.307 V (vs. Hg/HgO), i.e., between 1.20 V and 0.60 V versus RHE, for 5,000 cycles with a scan rate of 100 mV/s. CV curves and LSV curves at a rotation speed of 1600 rpm were collected at every 1000 cycles interval during the AST to record the degradation of the electrocatalysts. The methanol tolerance ability was evaluated by performing amperometric measurements and record *j*-t curves at -0.1 V (vs. Hg/HgO) while adding 3.0 M methanol into 0.10 M KOH in 20 steps at 0.2 ml/step followed by 8 steps at 2.0 ml/step. LSV was recorded between -0.20 and -0.50 V (vs. Hg/HgO) at 1600 rpm after completely addition of 20 ml of 3.0 M methanol to identify the ORR activity in a mixed environment.

4.2.5 Computational Methods

Computation work done by our collaborators Dr. Bin Liu and Mr. Jiayi Xu in the Tim Taylor Department of Chemical Engineering of Kansas State University was used to gain insights into the experimental work. Spin-polarized density functional theory (DFT) calculations were performed using the Vienna *Ab initio* Simulation Package (VASP).[40] The Generalized Gradient Approximation (GGA) Perdew-Burke-Ernzerhof (PBE) functional was used to account for the Kohn-Sham electron exchange-correlation interactions[41]. The projector augmented wave (PAW) method was used to represent the ionic cores[42]. A cut-off for the plane wave basis set expansion up to 400 eV was used for all calculations. The break condition for the self-consistent iteration was set to be 1×10^{-6} eV. Ionic relaxation was stopped when the forces on all atoms are smaller than 0.05 eV/Å. Monkhorst-Pack-based k-point meshes[43] were employed. The relaxed lattice constants for bulk graphite obtained from this setting are a = b = 2.47 Å and c = 6.80 Å, and in very good agreement with reported literature values of 2.46 Å, and 6.78 Å, respectively[44]. Moreover, Grimme's DFT-D3 method was used to account for the dispersion interactions[45].

4.3 Results and Discussion

4.3.1 Structural Characterization

The morphology of the N-VACNFs prepared by both thermal and plasma annealing is first observed by FESEM. As shown in Figure B.1, the heat treatment to VACNF thus changes the morphology of the material based on the temperature. The difference between the as-grown and 650 ^{o}C annealed are not big at this lower magnification. However, when the as-grown VACNFs were heat-treated at temperatures higher than 650 ^{o}C, we start to see the deformation in the vertical alignment (Figure B.1c) and at a very high temperature around 800 ^{o}C (Figure B.1d), the unique architecture was completely collapsed and the carbon fibers started to be etched away. The initial

FESEM assessment on the thermally annealed samples gave an idea on the maximum temperature that can be applied to prepare N-VACNF with maintaining its unique 3D architecture. The morphology change due to plasma annealing can be identified from the FESEM images in Figure B.2. As the VACNFs were plasma annealed, the NH_3 plasma starts to etch the sidewalls of carbon fibers which is clearly seen from the decrease in its diameter. Apart from the diameter decrease, Figures B.2c and B.2d also shows that some kind of secondary structures is created on the surface of the VACNF due to the plasma annealing at the temperature between 600-650 ^{o}C. The plasma annealing between 500-650 ^{o}C retained the original vertical alignment along with the unique brush-like structure.

TEM images as shown in Figures 4.1 a-d was taken to further identify the microstructure of N-VACNFs and Pt/N-VACNFs. TEM images 4.1a and 4.1b show the clear difference between the single carbon fiber before and after plasma annealing for 5 min. The diameter of the carbon nanofiber decreases as the result of the plasma annealing and leaving a larger Ni head at the tip (resembling a matchstick). Besides, the plasma annealed samples also have secondary structures of 5 to 10 nm in diameter and 10 to 15 nm in length on both the sidewalls and surface. Figure 4.1c shows the presence of small Pt NPs deposited on the sidewall of VACNF by ion-beam sputtering of 20 nm nominal thickness Pt metal. The TEM image with higher magnification in Figure 4.1d further confirms the presence of Pt NPs and together with Figure B.3 indicates that the Pt NPs have an average diameter of 2.26 ± 0.45 nm. We saw in Section 3.3.2 that the diameter of Pt NPs on VACNF with Pt deposited for 20 nm nominal thickness was 3.10 ± 0.43 nm. The smaller particle size on Pt/N-VACNFs can be ascribed to the presence of additional nitrogen which gives rise to enhanced metal-support interaction.

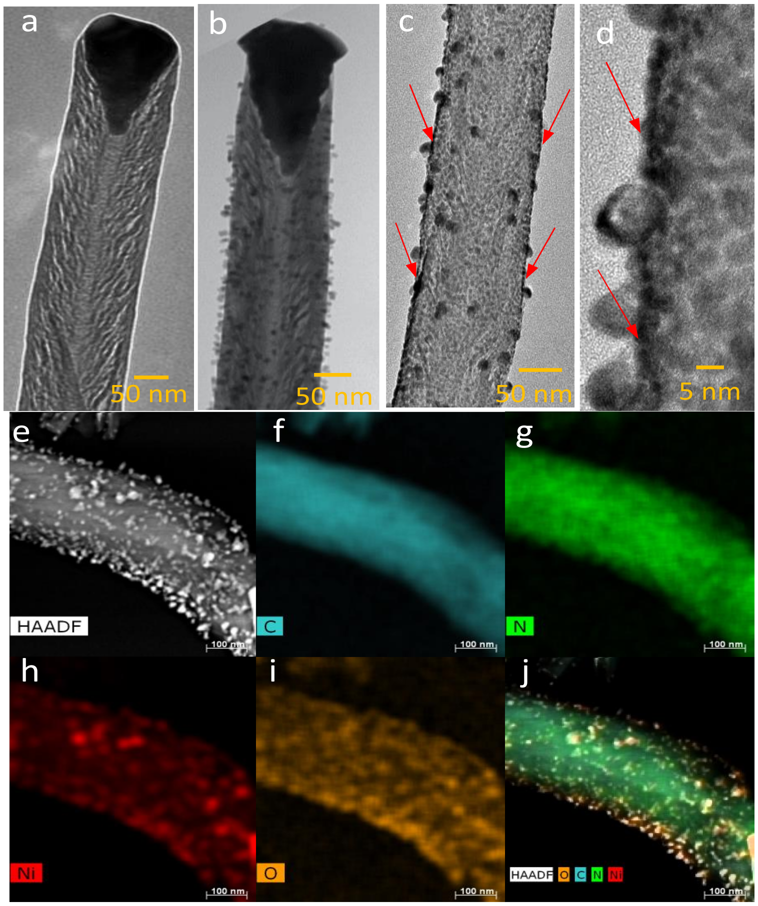

Figure 4.1: TEM image of bare VACNF (a) before and (b) after plasma annealing; TEM image of Pt/N-VACNF PA 5 min (43.0 μg/cm^2) at (c) low and (d) high magnification. The red arrow indicates the Pt NPs deposited on the sidewalls; (e) HAADF-STEM image and (f-j) STEM-EDX elemental mapping of bare N-VACNF (PA 15 min).

To identify the presence of different elements and nature of the secondary structures we used a high-angle annular dark-field scanning transmission electron microscope (HAADF-STEM) and EDS elemental mapping in the selected region. Figures 4.1e-j and B.4 confirm the presence of C, N, Ni, and O in the N-VACNFs annealed at 5 and 15 min. Based on the elemental mapping it is clear that the carbon and nitrogen are present throughout the fiber. It is also found that the secondary structures on the surface of VACNFs are possibly NiO (Figures 4.1h and 4.1i). We anticipate that this could be deposited during plasma annealing from the Ni head at the tip or from some of the unreacted Ni left on the substrate. The TEM EDX spectrum in Figure B.4a confirms the presence of only C, N, O, and Ni in the selected area (as shown by the orange rectangle) and the tabulated results in the inset reveals that carbon was the majority element with 96.26 at%. It was found that there is 0.53 at% of Ni present in the selected area, which further confirms that the secondary structures are Ni-based. The TEM EDX spectrum in Figure B.5 of Pt/N-VACNF PA 5 min (43.0 μg/cm^2) reveals the presence of C, O, Pt with C being the majority of about 78.18 %. The Cu signal comes from the TEM grid. The wt% of Pt in the selected area for EDX analysis was 18.54% which is close to the actual wt% of Pt (19.8%) calculated earlier. Elemental mapping of Pt/N-VACNF PA 5 min reveals that the carbon and nitrogen were present throughout the fiber, Ni presents on the surface alongside oxygen, and Pt presents on the sidewalls as shown in Figure B.6.

Figure B.7a. displays the Raman spectra recorded for bare VACNF and VACNF samples plasma annealed at 550 ^{o}C for 5, 15, and 30 min. All four samples exhibit the signature peaks at 1365 cm^{-1}, 1580 cm^{-1}, and 2695cm^{-1} corresponding to the D-band, G-band, and 2D-band. The I_D/I_G ratio of bare VACNF, N-VACNF (PA 5 min), N-VACNF (PA 15 min), and N-VACNF (PA-30min) is calculated to be 0.93, 0.92, 0.89, and 0.70, respectively. The decreased I_D/I_G ratio indicates that the sp^3 carbon present in the VACNFs decreases, which is expected as the NH3 plasma etch the sidewalls of carbon nanofibers. In addition to that, when the sample is plasma annealed for longer time (30 min) it gives rise to a sharp 2D-band which further correlates with the reduced number of graphitic layers as a result of plasma annealing.

4.3.2 XPS Analysis

XPS measurements were taken further to evaluate the chemical features and composition of the prepared catalysts. The survey spectrum was recorded within the range of 0-1400 eV as shown in Figure B.7b for bare VACNF, N-VACNF (PA 5min), N-VACNF (PA 15 min), and N-VACNF (30 min). The survey spectra reveal the presence of C, N, O, and Ni in all the catalysts which further confirms the successful doping of nitrogen into the VACNFs. The at% of different chemical components of all the catalysts are listed in Table B.1. To obtain more information about the nitrogen functionalities and its content in the plasma annealed samples the high-resolution N 1s spectra are deconvoluted as shown in Figures 4.2a-d.

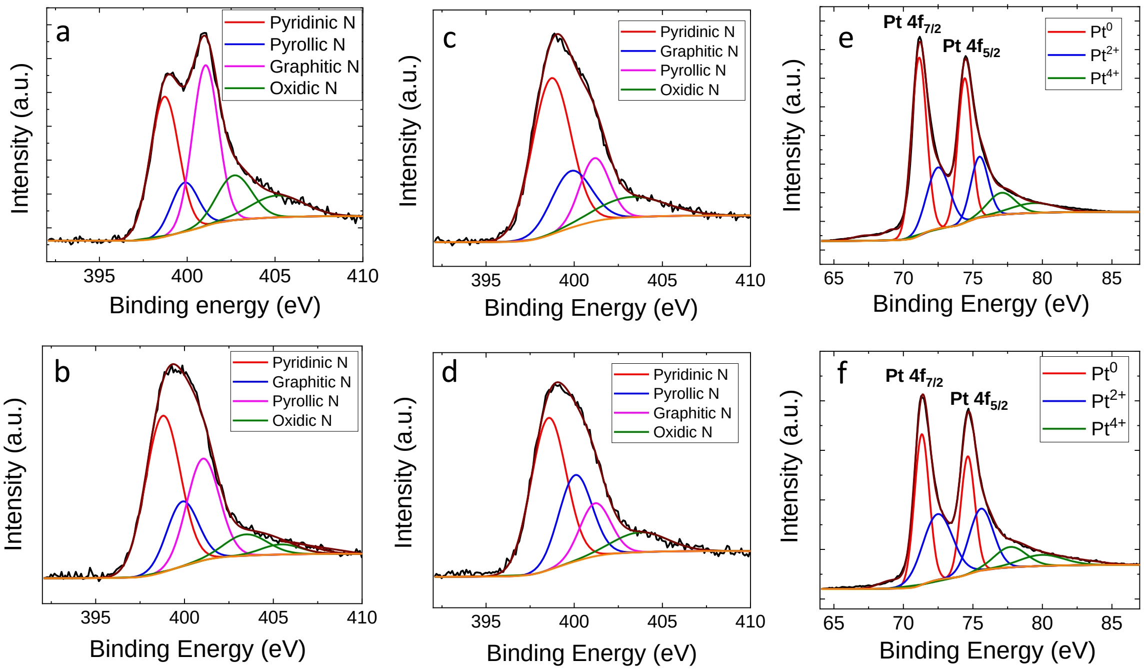

Figure 4.2: N 1s XPS spectra of (a) bare VACNF and VACNF samples plasma annealed for (b) 5 min, (c) 15 min, and (d) 30 min; Pt 4f XPS spectra for (e) Pt/N-VACNF and (f) Pt/C.

The N 1s spectra is deconvoluted into four components: pyridinic N (398.80 ± 0.3 eV), pyrrolic N (400.1± 0.3 eV), graphitic N (401.20 ± 0.2 eV), and pyridinic N-oxide (oxidic N) (402.00-406.00 eV)[37, 46]. The bare VACNF is mostly dominated with pyridinic N (ca. 32.9%) and graphitic N (ca. 34.0%) with some amount of pyrrolic N (10.9%) and oxidic N (22.2%). As the VACNFs are plasma annealed the % N increases in the sample and also the relative % of N functionalities change. For the N-VACNF PA for 5 min, the at % of N increases from 7.4 to 8.5% along with the increase in % of pyridinic N. As shown in Figure 4.2b, it is deconvoluted into pyridinic N (ca. 45.2 %), pyrrolic N (16.8), graphitic N (27.4 %), and oxidic N (10.6 %). When the plasma annealing time was further increased to 15 min, the % N content increased to 8.6 % with an increase in the pyridinic N (ca. 53.1 %) along with pyrrolic N (ca. 9.4 %), graphitic N (ca. 16.4 %), and oxidic N (12.1%). However, a further increase of plasma annealing time to 30 min resulted in a decrease in the total % N content to 7.4% with a slight decrease in the pyridinic N (ca. 49.1 %). The N-VACNF (PA 30 min) also contains pyrrolic N (26.1 %), graphitic N (15.0 %), and oxidic N (9.8 %). Figure 4.3a presents the total N and at % of different nitrogen species for all the four catalysts. Figure 4.3b presents the ratio between C and different species of N in all the four catalysts.

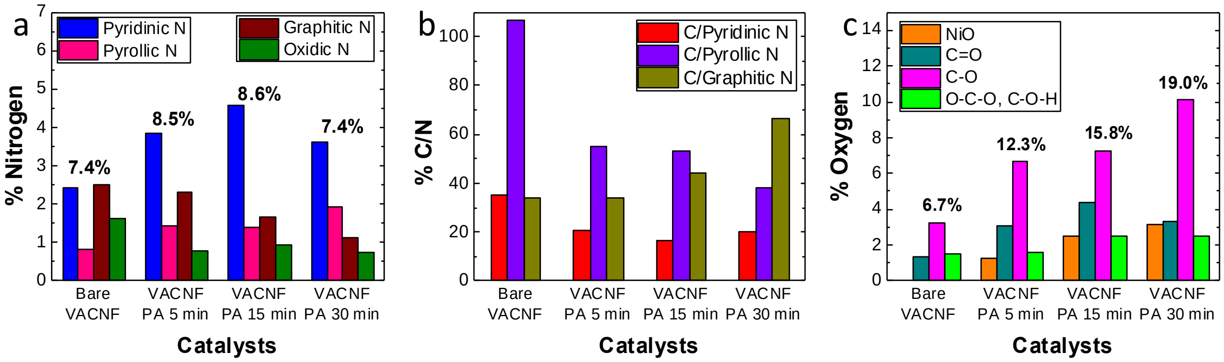

Figure 4.3: (a) Atomic % of different types of N, (b) % ratio of C to N , and (c) atomic % of different types of oxygen in bare VACNF and VACNF samples Plasma annealed for different time intervals.

Figure D.8 presents the O 1s spectra of bare VACNF, N-VACNF (PA 5min), N-VACNF (PA 15 min), and N-VACNF (30 min). As the plasma annealing time increases, O at % increases in the sample. The O 1s spectra of bare VACNF can be deconvoluted into four different peaks with binding energies (BE) of 531.28, 532.26, 533.64, and 534.72 eV corresponding to the C=O, C-O, C-O-H/C-O-C bonds, and physisorbed water, which accounts for 20.7, 47.7, 23.0 and 8.6 % of total oxygen atoms, respectively[47]. After plasma annealing, the N-VACNF samples show C=O, C-O, and C-O-H/C-O-C peaks at almost the same binding energy with a small change in their relative % between samples. However, all three plasma annealed samples have an additional peak at ~529.60 eV which can be ascribed to the Ni-O bond[48]. This further confirms the presence of NiO particles on the surface of VACNFs which is quite different from the Ni head at the tip. The relative % of NiO is found to be 10.3, 15.0, and 16.4 % for N-VACNF (PA 5min), N-VACNF (PA 15 min), and N-VACNF (30 min), respectively. Figure 4.3c illustrates the total O content and at % of different oxygen species present in all the four catalysts. Table B.2 summarizes the BE and relative area % of the individual chemical components derived from O 1s and N 1s high-resolution spectra for all the catalysts.

To identify the type of Nitrogen functionalities, present after Pt sputtering, the N 1s high-resolution spectra of Pt/N-VACNF PA for 5 min (43.0 µg/cm^2) is deconvoluted as shown in Figure B.9a. The peaks at 398.81, 400.13, and 401.20 eV are allocated to the pyridinic N, pyrrolic N, and graphitic N which accounts for 45.3, 17.6, and 11.1% of total nitrogen, respectively. However, an additional peak at 397.75 eV is required to perfectly fit the N 1s spectra which is originally not present in either the bare VACNF or N-VACNFs PA for 5 min. The peak at 397.75 eV (ca. 33.9 %) can be attributed to the presence of Pt-N bond as previously reported in the literature[49, 50]. This gives stronger evidence for the presence of Pt and N interaction in the Pt/N-VACNF sample. In Pt/VACNF, the Pt-N bond was present at 398.00 eV and it corresponds to about 26.0% of total N as presented in Figure B.9b. It is important to note that the presence of additional pyridinic N in the Pt/N-VACNF sample shifted the BE of Pt-N peak negatively by 0.25 eV when compared to Pt/VACNF and increased the relative % of Pt-N bond. These findings validate the electron transfer between N and Pt, and they are in good agreement with the smaller Pt particle size obtained from the TEM image (Figure B.3) resulting from the stronger interaction between N and Pt.

Figures 4.2e and 4.2d present the Pt 4f XPS spectra of 20 % Pt/C and Pt/N-VACNF. The Pt 4f spectrum consists of two spin-orbit splits, namely Pt 4f$_{7/2}$ and Pt 4f$_{5/2}$ with a peak ratio of 4:3, and each of them can be further deconvoluted into 3 peaks that are assigned to Pt^0, Pt^{2+} (PtO or $Pt(OH)_2$), and Pt^{4+} (PtO_2) species, respectively. The BE and relative area % of each of the components in the Pt 4f spectra of Pt/C and Pt/N-VACNF is summarized in Table B.3. As it is seen from Figures 4.2e, 4.2f and Table B.3, the BE of metallic Pt (Pt^0 $4f_{7/2}$ and Pt^0 $4f_{5/2}$) shifted to a lower value by about 0.19 and 0.22 eV. This observed negative shift is attributed to the electron transfer from the carbon support to Pt. In addition to that, the presence of N helps to increase the relative concentration of Pt^0 (57.2 %) when compared to that of Pt/C (45.6 %) which has no nitrogen. Overall, the XPS results confirm the increase of pyridinic N content in the sample with PA, presence of NiO in the plasma annealed samples, stronger metal-support interaction, and partial electron transfer between Pt and N.

4.3.3 Evaluation of the Catalytic Activity for ORR

Figure 4.4a presents the cyclic voltammetry (CV) curves recorded in Ar-saturated and O_2-saturated 0.10 M KOH solution for N-VACNF PA for 5 min. In the presence of O_2, there is a reduction peak at -0.252 V (vs. Hg/HgO) which was not present in the absence of O_2 indicating the ORR activity of the catalyst. As the Pt was sputtered on the N-VACNF (PA 5 min) sample, the O_2 reduction peak shifts to a positive potential of about -0.099 V (vs. Hg/HgO) indicating an increase in the activity resulting from the Pt deposition. As shown in Figure 4.4b there is an additional peak around -0.70 V (vs. Hg/HgO) due to the hydrogen adsorption on Pt surfaces similar to the one obtained for Pt/VACNF catalysts in Section 3.3.3. The impact of a larger capacitive current on the Pt/N-VACNF is discussed earlier in Chapter 3. Figure B.10 displays the CV curves recorded for Pt/N-VACNF catalysts with different Pt loadings. As the Pt loading decreases, the current density of the O_2 reduction peak and H_2 adsorption peak decreases.

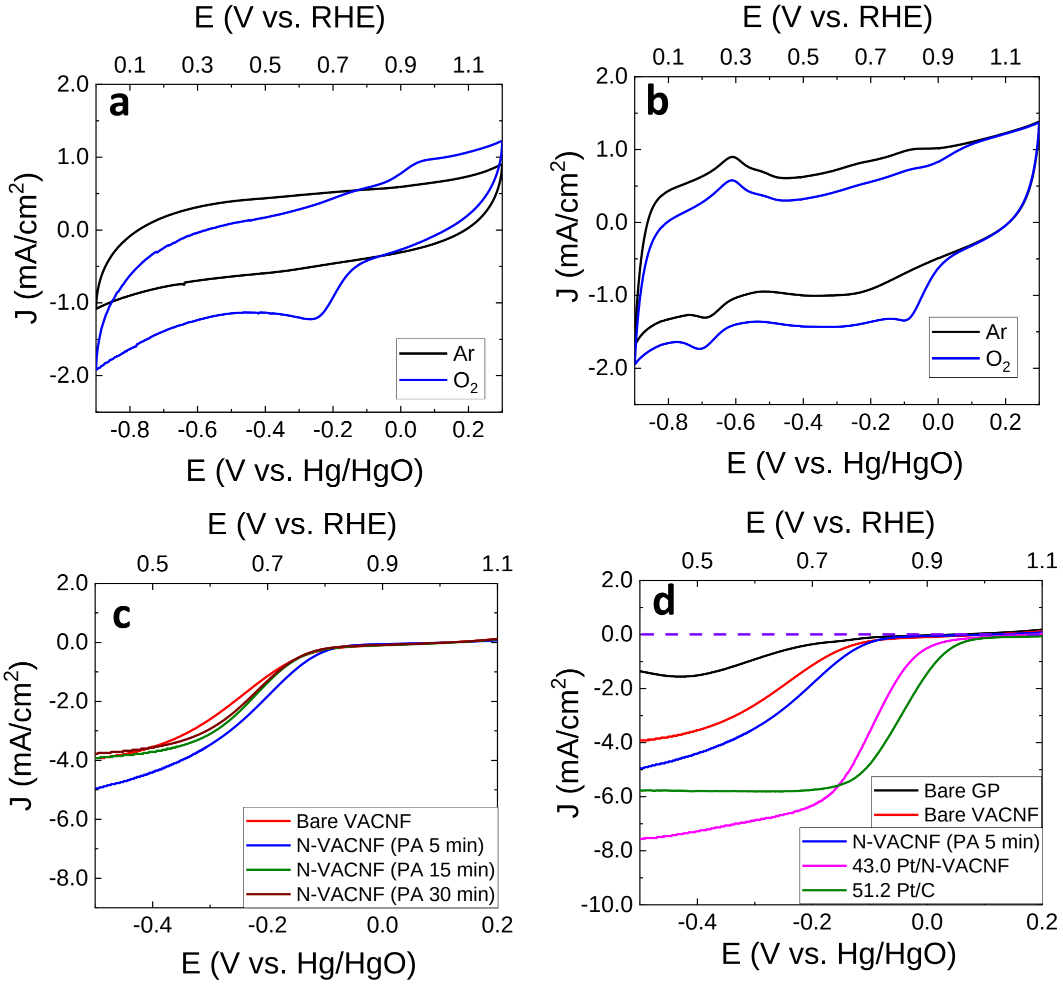

Figure 4.4: Cyclic voltammogram of (a) N-VACNF (PA 5 min) and (b) Pt/N-VACNF (43.0 μg/cm^2) recorded in Ar-saturated (black line) and O_2-saturated (blue line) 0.10 M KOH solution at a scan rate of 50 mV/s; LSV curves recorded at a scan rate of 10 mV/s and a rotation speed of 1,600 rpm (c) for various N doped VACNF catalysts and (d), bare graphite paper, bare VACNF, N-VACNF (PA 5 min), 43.0 Pt/N-VACNF, and 51.2 Pt/C.

Figure 4.4c shows the linear sweep voltammetry (LSV) curves recorded at a rotation speed of 1600 rpm between +0.20 V and -0.50 V (vs. Hg/HgO) in O_2-saturated 0.10 M KOH solution for bare VACNF and VACNF plasma annealed samples. All the LSV's have almost similar onset potential and they overlap in the kinetic region. The difference comes in the mixed and diffusion-limited region. Once the sample is plasma annealed for 5 min the $E_{1/2}$ shifted positively to -0.205 V (vs. Hg/HgO) which was about 42 mV higher when compared to the bare VACNF (-0.247 V vs. Hg/HgO). Also, the current density at -0.50 V for N-VACNF PA 5 min has an almost 20% increase when compared to the bare VACNF. However, the ORR activity did not significantly improve when the PA time is increased. We attribute that this could be due to the presence of larger Ni particles blocking the ORR active sites. So, for further studies involving Pt deposition we used the N-VACNF PA 5 min as the support.

Figure 4.4 d shows that after sputtering 20 nm of Pt there is clearly a positive shift in the $E_{1/2}$ and an increase in the current density indicating the improvement in the catalytic activity with still maintaining the sigmoidal shape representing the steady-state condition. However, compared to the commercial catalyst Pt/C, the baseline in the diffusion-limited region is slanted towards the negative potential. A similar feature was noticed for Pt/VACNF and a detailed study is reported in Chapter 2. The 43.0 Pt/N-VACNF has a J_{lim} value of 6.7 mA/cm^2 which is the same as 43.0 Pt/VACNF with same Pt loading. The difference comes with the negative shift in the ORR curve. For 43.0 Pt/N-VACNF, the value of $E_{1/2}$ is -0.096 V (vs. Hg/HgO) which shifted negatively by 10 mV when compared to the 43.0 Pt/VACNF (-0.086 V vs. Hg/HgO). We wanted to identify if the observed negative shift is due to the presence of NiO particles on the VACNF surface. As shown in Figures B.11a-c, the NiO particles diameter increases when the PA time increase. The NiO particles present on the surface can be removed by leaving the catalysts in 1.0 M HNO_3 for 20 min. Figures B.11d-f confirms that the NiO particles were successfully removed including the Ni head at the top. Before sputtering Pt on the N-VACNF PA 5 min after treatment with HNO_3, the sample was dried in vacuum at 70^{o}C. After completely dried Pt of about 20 nm nominal thickness is sputtered followed by the testing of ORR activity. As presented in Figure B.12a the Pt sputtered after HNO_3 treatment has $E_{1/2}$ shifted more negative when compared to the Pt/N-VACNF without any treatment in HNO_3. This negative shift can be attributed to the other factors introduced after the treatment in HNO_3. After the samples are in contact with the solution and when they are removed from it due to the capillary force the individual VACNFs bundle up together as shown in Figures B.12b and B.12c and loose its unique architecture. It is clear that removing Ni particles from the surface and testing the ORR activity of the catalysts start to introduce additional factors, and hence we can’t confirm the influence of NiO in the ORR activity of the Pt/N-VACNF catalyst based on these results. The RDE voltammogram at a series of rotation speed between 500 and 3000 rpm is recorded for the bare VACNF, N-VACNF with PA for different time intervals, and Pt/N-VACNF PA 5 min with different Pt loadings (6.5, 10.8, 21.5, and 43.0 μg/cm^2) and the results are presented in Figures B.13 and B.14. As the rotation speed increases, the J_{lim} increases as more O_2 flux reaching the electrode surface. This is in good agreement with the RDE results observed in Chapter 2. All the Pt/VACNF catalysts show consistent higher J_{lim} values than the benchmark Pt/C catalyst, but the tilt of the curve in the diffusion-controlled region becomes smaller as the Pt loading increases.

4.3.4 DFT Analysis

As shown in Figure B.15, with the presence of more pyridinic nitrogen dopants, the formation energy becomes more negative. This indicates that the stability of the Pt NPs increases when the pyridinic N content increase. Pt atoms are considered to be the primary binding site for O_2 which is similar to the undoped fishbone edge and the most stable ORR intermediates over Pt supported by pyridinic N (N_p)-doped edge are given in Figure 4.5a. According to the free energy diagram in Figure 4.5b, the overall energy profile for the ORR over Pt supported by N_p-doped edge is very much similar to the undoped edge with the rate-limiting step still being the OH desorption step and the reaction following a 4-e^- pathway. However, the Pt supported by N_p-doped edge shows slightly stronger adsorption of ORR intermediates. In addition to that, the limiting potential calculated on PtN_p/VACNF is -0.06 V, which is lower than 0.05 V on Pt/VACNF and 0.45 V on Pt (111) due to the stronger binding of OH. Based on these results, we can confirm that the -10 mV shift in $E_{1/2}$ of Pt/N-VACNF is due to the stronger binding of OH and may not be due to the presence of NiO particles.

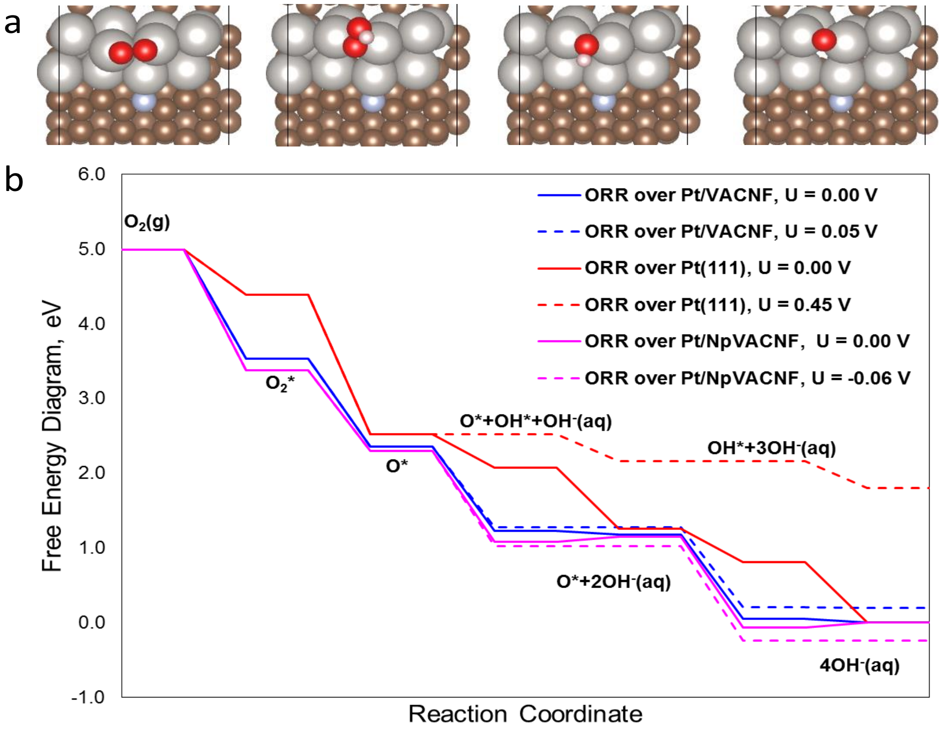

Figure 4.5: (a) Molecular structures of the most stable ORR intermediates over Pt/N_pVACNF; (b) Free energy diagram of the 4-e^- reduction pathway for ORR on Pt/N_pVACNF (pink) comparing with Pt (111) (red) and Pt/VACNF (blue) by both dissociative mechanisms. Color code: white – H, red – O, brown – C, gray – Pt, cool gray - N.

4.3.5 Durability test for Pt/N-VACNF

The durability test of the prepared Pt/N-VACNF, Pt/VACNF, and Pt/C catalyst are studied using the accelerated stress test (AST) which is done by fast potential cycling (100mV/s) between 0.293 V and -0.307 V. The ORR activity was tested for all the catalysts by recording the CV and LSV at 1600 rpm for every 1000 AST cycles. We evaluate the durability of the catalyst by calculating the value of shift in potential (ΔE) to maintain the original half-wave current density and the results are displayed in Figure 4.6d .

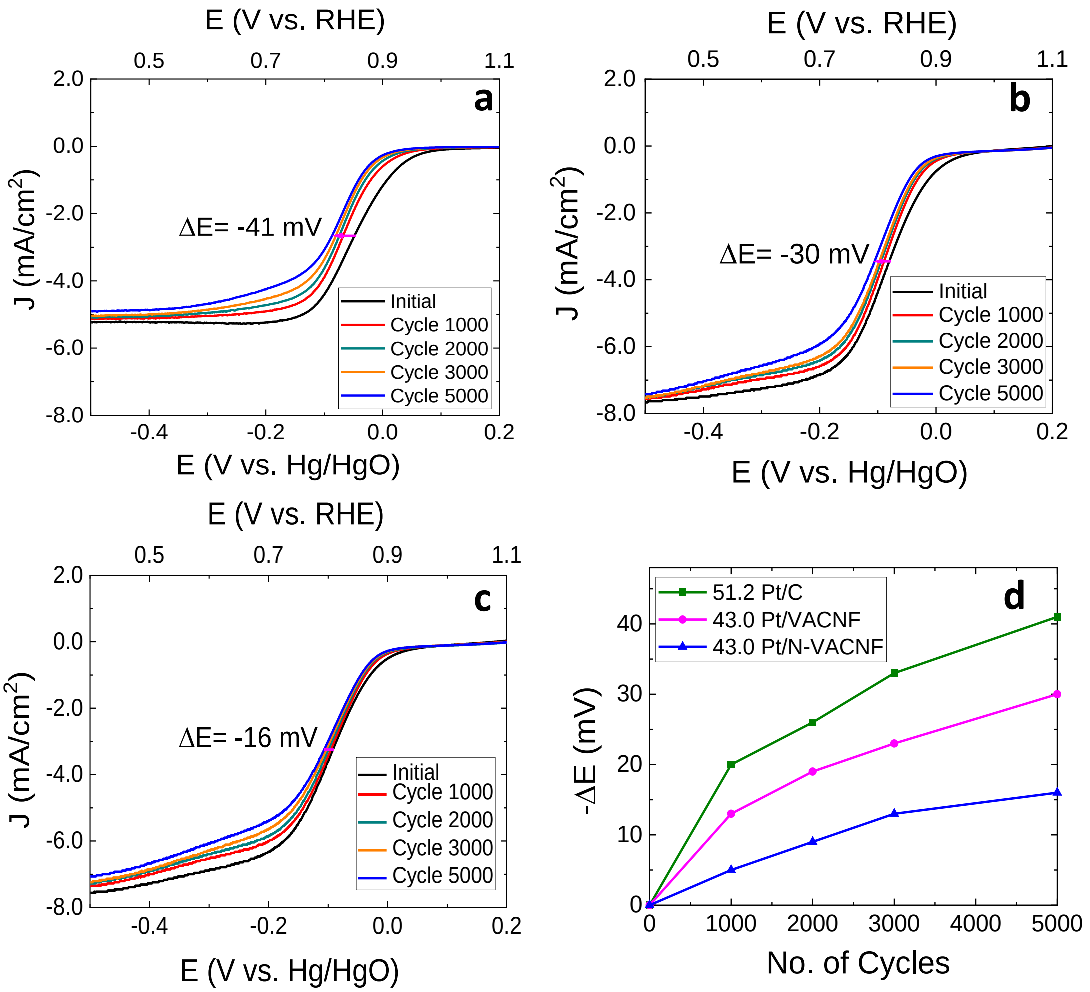

Figure 4.6: LSV curves of (a) Pt/C (51.2 μg/cm^2) and (b) Pt/VACNF (43.0 μg/cm^2) and (c) Pt/N-VACNF (43.0 μg/cm^2) after every 1000 AST cycles in O_2-saturated 0.10 M KOH solution at a scan rate of 10 mV/s and a rotation speed of 1600 rpm; (d) Change in the half-wave potential of the LSV curves vs. the number of AST cycles for all the catalysts.

As presented in Figures 4.6a-c, the Pt/N-VACNF catalyst shows much more stable LSV curves than the one for Pt/VACNF and Pt/C. The potential shift ΔE after 5,000 AST cycles is about -16.0 mV with the Pt/N-VACNF whereas it is -30.0 mV for the Pt/VACNF and -41.0 mV for the commercial Pt/C catalyst. This lower shift in ΔE indicates that the Pt NPs deposited on N-

VACNF PA 5 min is much more stable than the Pt NPs deposited on bare VACNF. Besides, the particle size is ~2.3 nm for Pt/N-VACNF which is much smaller than the ~3.1 nm for Pt/VACNF and ~3.5 nm for Pt/C. The better durability with even smaller Pt particle size on Pt/N-VACNF can be ascribed to the presence of additional pyridinic N which increases the stability of the Pt NPs as verified by the DFT analysis and a strong interaction between the Pt and catalysts support as verified by XPS analysis. Even at a lower Pt loading of 21.5 µg/cm^2 Pt/N-VACNF catalyst shows only -27 mV shift in ΔE when compared to the -43 mV shift for Pt/C after 3000 cycles as displayed in Figure B.16. Overall it is clear that the presence of additional N increases the durability of the catalyst and at the end of AST cycles the Pt/N-VACNF is better than Pt/VACNF and Pt/C will similar Pt loadings.

4.3.6 Methanol Tolerance of Pt/N-VACNF

Ability to withstand the methanol crossover seems to be an important criterion for the ORR catalyst especially when employed in direct methanol fuel cells. The methanol tolerance was evaluated by employing amperometric measurements. The potential used to record the amperometric *j*-t curve is -0.10 V (vs. Hg/HgO) as it is found to be the more critical potential at which the Pt catalysts are sensitive to methanol. Figure 4.7a displays the amperometric *j*-t curve recorded for 43.0 Pt/N-VACNF and 51.2 Pt/C. The 43.0 Pt/N-VACNF catalysts lost only about 21 % of the ORR current density after adding 0.75 M of methanol whereas the 51.2 Pt/C has the % loss in negative (-300 %) which tells that the commercial Pt/C catalyst has almost lost all its current density generated by the ORR and resulted in current density obtained from methanol oxidation reaction. Besides, the high tolerance towards methanol oxidation for Pt/N-VACNF can further be confirmed using the LSV curves as presented in Figure 4.7b. For the Pt/N-VACNF catalyst with 43.0 µg/cm^2 Pt loading, the LSV curve in the presence of methanol exhibits a reduction current in the full ORR potential range and the methanol oxidation is significantly suppressed, which explains why a large ORR current density is observed at -0.10 V even after adding methanol for about 0.75 M. In contrast, for the Pt/C catalyst with 51.2 µg/cm^2 the LSV curve is dominated by the methanol oxidation at the potential above -0.30 V (vs. Hg/HgO) indicating a poor tolerance to methanol crossover. Overall, the Pt/N-VACNF is highly selective towards the ORR in a mixed environment indicating a higher tolerance to methanol crossover.

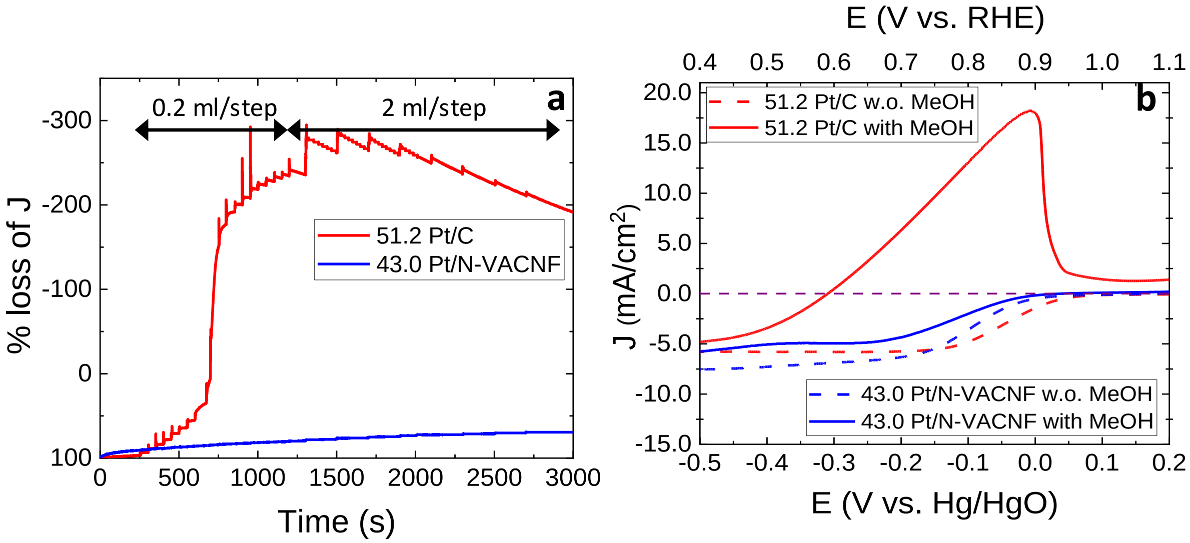

Figure 4.7: (a) Amperometric *j-t* curve of Pt/C (51.2 µg/cm^2) and Pt/N-VACNF (43.0 µg/cm^2) recorded at 1,600 rpm in O_2-saturated 0.10 M KOH solution with successive addition of 3.0 M methanol to the final concentration of 0.75 M at the potential of -0.10 V (vs. Hg/HgO); (b) LSV curves recorded at a scan rate of 10 mV/s and 1,600 rpm in 0.10 M KOH + 0.75 M MeOH for Pt/C (51.2 µg/cm^2) and Pt/N-VACNF (43.0 µg/cm^2). The purple dash line marks the zero current density.

4.4 Conclusions

In summary, a new N-doped VACNF has been prepared by NH_3 plasma annealing at 550 °C using PECVD and successfully employed as a unique catalyst support to improve the durability of the Pt catalysts towards the ORR. The structural characterization results have identified the morphological change, indicated the presence of NiO particles on the catalyst surface, and confirmed the anchoring of Pt nanoparticles. The presence of nitrogen species and different oxygen functionalities present in the VACNFs as a result of plasma annealing is revealed by the XPS analysis. The presence of nitrogen induced a partial electron transfer between the Pt particles and N-VACNF support which resulted in a strong metal-support interaction. As a result, the Pt/N-VACNF with 43.0 µg/cm^2 Pt loading and a Pt particle size of ~2.3 nm exhibited only a -16 mV shift in ΔE indicating a better durability when compared to the Pt/VACNF and Pt/C catalysts. DFT calculations have validated the strong binding of Pt atoms with the pyridinic N-doped edge and confirmed the 4-e$^-$ reduction pathway for Pt/N-VACNF catalyzed ORR. In addition, the Pt/N-VACNF catalysts have shown excellent tolerance to methanol oxidation with the oxygen reduction being more dominant in the full potential range. Altogether, the increased N content improves the durability of the Pt/N-VACNF catalysts and the prepared N-VACNF catalysts with NiO particles on the catalyst surface can be further explored as a noble metal-free electrocatalyst for other electrochemical reactions in fuel cells and water splitting owing to the advantage of metal oxide modified heteroatom-doped carbon nanomaterials.

4.5 References

1. Shao, Y.; Yin, G.; Gao, Y., Understanding and approaches for the durability issues of Pt-based catalysts for PEM fuel cell. *J. Power Sources* **2007,** *171* (2), 558-566.
2. Zhang, C.; Shen, X.; Pan, Y.; Peng, Z., A review of Pt-based electrocatalysts for oxygen reduction reaction. *Front. Energy* **2017,** *11* (3), 268-285.
3. Zhou, Y.; Holme, T.; Berry, J.; Ohno, T. R.; Ginley, D.; O'Hayre, R., Dopant-Induced Electronic Structure Modification of HOPG Surfaces: Implications for High Activity Fuel Cell Catalysts. *J. Phys. Chem. C* **2010,** *114* (1), 506-515.
4. Reiser, C. A.; Bregoli, L.; Patterson, T. W.; Yi, J. S.; Yang, J. D.; Perry, M. L.; Jarvi, T. D., A Reverse-Current Decay Mechanism for Fuel Cells. *Electrochem. Solid-State Lett.* **2005,** *8* (6), A273.
5. Gasteiger, H. A.; Kocha, S. S.; Sompalli, B.; Wagner, F. T., Activity benchmarks and requirements for Pt, Pt-alloy, and non-Pt oxygen reduction catalysts for PEMFCs. *Appl. Catal. B* **2005,** *56* (1), 9-35.

6. Yu, X.; Ye, S., Recent advances in activity and durability enhancement of Pt/C catalytic cathode in PEMFC: Part II: Degradation mechanism and durability enhancement of carbon supported platinum catalyst. *J. Power Sources* **2007,** *172* (1), 145-154.
7. Li, X.; Park, S.; Popov, B. N., Highly stable Pt and PtPd hybrid catalysts supported on a nitrogen-modified carbon composite for fuel cell application. *J. Power Sources* **2010,** *195* (2), 445-452.
8. Su, L.; Jia, W.; Li, C.-M.; Lei, Y., Mechanisms for Enhanced Performance of Platinum-Based Electrocatalysts in Proton Exchange Membrane Fuel Cells. *ChemSusChem* **2014,** *7* (2), 361-378.
9. Greeley, J.; Stephens, I. E. L.; Bondarenko, A. S.; Johansson, T. P.; Hansen, H. A.; Jaramillo, T. F.; Rossmeisl, J.; Chorkendorff, I.; Nørskov, J. K., Alloys of platinum and early transition metals as oxygen reduction electrocatalysts. *Nat. Chem.* **2009,** *1* (7), 552-556.
10. Liang, H.-W.; Cao, X.; Zhou, F.; Cui, C.-H.; Zhang, W.-J.; Yu, S.-H., A Free-Standing Pt-Nanowire Membrane as a Highly Stable Electrocatalyst for the Oxygen Reduction Reaction. *Adv. Mater.* **2011,** *23* (12), 1467-1471.
11. Xia, B. Y.; Wu, H. B.; Yan, Y.; Lou, X. W.; Wang, X., Ultrathin and Ultralong Single-Crystal Platinum Nanowire Assemblies with Highly Stable Electrocatalytic Activity. *J. Am. Chem. Soc.* **2013,** *135* (25), 9480-9485.
12. Chen, Z.; Waje, M.; Li, W.; Yan, Y., Supportless Pt and PtPd Nanotubes as Electrocatalysts for Oxygen-Reduction Reactions. *Angew. Chem.* **2007,** *46* (22), 4060-4063.
13. Lim, B.; Jiang, M.; Camargo, P. H. C.; Cho, E. C.; Tao, J.; Lu, X.; Zhu, Y.; Xia, Y., Pd-Pt Bimetallic Nanodendrites with High Activity for Oxygen Reduction. *Science* **2009,** *324* (5932), 1302-1305.
14. Liu, M.; Zhao, Z.; Duan, X.; Huang, Y., Nanoscale Structure Design for High-Performance Pt-Based ORR Catalysts. *Adv. Mater.* **2019,** *31* (6), 1802234.
15. Wang, H.-H.; Zhou, Z.-Y.; Yuan, Q.; Tian, N.; Sun, S.-G., Pt nanoparticle netlike-assembly as highly durable and highly active electrocatalyst for oxygen reduction reaction. *Chem. Comm.* **2011,** *47* (12), 3407-3409.
16. Ando, F.; Tanabe, T.; Gunji, T.; Tsuda, T.; Kaneko, S.; Takeda, T.; Ohsaka, T.; Matsumoto, F., Improvement of ORR Activity and Durability of Pt Electrocatalyst Nanoparticles Anchored on TiO2/Cup-Stacked Carbon Nanotube in Acidic Aqueous Media. *Electrochim. Acta* **2017,** *232*, 404-413.
17. Elezović, N. R.; Babić, B. M.; Radmilovic, V. R.; Vračar, L. M.; Krstajić, N. V., Novel Pt catalyst on ruthenium doped TiO2 support for oxygen reduction reaction. *Appl. Catal. B* **2013,** *140-141*, 206-212.
18. Samad, S.; Loh, K. S.; Wong, W. Y.; Lee, T. K.; Sunarso, J.; Chong, S. T.; Wan Daud, W. R., Carbon and non-carbon support materials for platinum-based catalysts in fuel cells. *Int. J. Hydrog. Energy* **2018,** *43* (16), 7823-7854.
19. Antolini, E., Iridium As Catalyst and Cocatalyst for Oxygen Evolution/Reduction in Acidic Polymer Electrolyte Membrane Electrolyzers and Fuel Cells. *ACS Catal.* **2014,** *4* (5), 1426-1440.

20. Zhang, P.; Huang, S.-Y.; Popov, B. N., Mesoporous tin oxide as an oxidation-resistant catalyst support for proton exchange membrane fuel cells. *J. Electrochem. Soc.* **2010,** *157* (8), B1163.
21. Lv, H.; Mu, S.; Cheng, N.; Pan, M., Nano-silicon carbide supported catalysts for PEM fuel cells with high electrochemical stability and improved performance by addition of carbon. *Appl. Catal. B* **2010,** *100* (1), 190-196.
22. Paraknowitsch, J. P.; Thomas, A., Doping carbons beyond nitrogen: an overview of advanced heteroatom doped carbons with boron, sulphur and phosphorus for energy applications. *Energy Environ. Sci.* **2013,** *6* (10), 2839-2855.
23. Wang, Y.; Song, S.; Maragou, V.; Shen, P. K.; Tsiakaras, P., High surface area tungsten carbide microspheres as effective Pt catalyst support for oxygen reduction reaction. *Appl. Catal. B* **2009,** *89* (1), 223-228.
24. Zhou, Y.; Neyerlin, K.; Olson, T. S.; Pylypenko, S.; Bult, J.; Dinh, H. N.; Gennett, T.; Shao, Z.; O'Hayre, R., Enhancement of Pt and Pt-alloy fuel cell catalyst activity and durability via nitrogen-modified carbon supports. *Energy Environ. Sci.* **2010,** *3* (10), 1437-1446.
25. Asefa, T.; Huang, X., Heteroatom-Doped Carbon Materials for Electrocatalysis. *Chem. Eur.* **2017,** *23* (45), 10703-10713.
26. Li, J.-C.; Hou, P.-X.; Liu, C., Heteroatom-Doped Carbon Nanotube and Graphene-Based Electrocatalysts for Oxygen Reduction Reaction. *Small* **2017,** *13* (45), 1702002.
27. Liang, L.; Xiao, M.; Zhu, J.; Ge, J.; Liu, C.; Xing, W., Low-temperature synthesis of nitrogen doped carbon nanotubes as promising catalyst support for methanol oxidation. *J. Energy Chem.* **2019,** *28*, 118-122.
28. Peera, S. G.; Arunchander, A.; Sahu, A. K., Platinum nanoparticles supported on nitrogen and fluorine co-doped graphite nanofibers as an excellent and durable oxygen reduction catalyst for polymer electrolyte fuel cells. *Carbon* **2016,** *107*, 667-679.
29. Sebastián, D.; Ruíz, A. G.; Suelves, I.; Moliner, R.; Lázaro, M. J.; Baglio, V.; Stassi, A.; Aricò, A. S., Enhanced oxygen reduction activity and durability of Pt catalysts supported on carbon nanofibers. *Appl. Catal. B* **2012,** *115-116*, 269-275.
30. Wang, X. X.; Tan, Z. H.; Zeng, M.; Wang, J. N., Carbon nanocages: A new support material for Pt catalyst with remarkably high durability. *Sci. Rep.* **2014,** *4* (1), 4437.
31. Vinayan, B. P.; Nagar, R.; Rajalakshmi, N.; Ramaprabhu, S., Novel Platinum–Cobalt Alloy Nanoparticles Dispersed on Nitrogen-Doped Graphene as a Cathode Electrocatalyst for PEMFC Applications. *Adv. Funct. Mater.* **2012,** *22* (16), 3519-3526.
32. Bang, G. S.; Shim, G. W.; Shin, G. H.; Jung, D. Y.; Park, H.; Hong, W. G.; Choi, J.; Lee, J.; Choi, S.-Y., Pyridinic-N-Doped Graphene Paper from Perforated Graphene Oxide for Efficient Oxygen Reduction. *ACS Omega* **2018,** *3* (5), 5522-5530.
33. Li, Z.; Gao, Q.; Zhang, H.; Tian, W.; Tan, Y.; Qian, W.; Liu, Z., Low content Pt nanoparticles anchored on N-doped reduced graphene oxide with high and stable electrocatalytic activity for oxygen reduction reaction. *Sci. Rep.* **2017,** *7* (1), 43352.

34. Guo, L.; Jiang, W.-J.; Zhang, Y.; Hu, J.-S.; Wei, Z.-D.; Wan, L.-J., Embedding Pt Nanocrystals in N-Doped Porous Carbon/Carbon Nanotubes toward Highly Stable Electrocatalysts for the Oxygen Reduction Reaction. *ACS Catal.* **2015,** *5* (5), 2903-2909.

35. Prithi, J. A.; Rajalakshmi, N.; Ranga Rao, G., Nitrogen doped mesoporous carbon supported Pt electrocatalyst for oxygen reduction reaction in proton exchange membrane fuel cells. *Int. J. Hydrog. Energy* **2018,** *43* (9), 4716-4725.

36. Quílez-Bermejo, J.; Melle-Franco, M.; San-Fabián, E.; Morallón, E.; Cazorla-Amorós, D., Towards understanding the active sites for the ORR in N-doped carbon materials through fine-tuning of nitrogen functionalities: an experimental and computational approach. *J. Mater. Chem. A* **2019,** *7* (42), 24239-24250.

37. Guo, D.; Shibuya, R.; Akiba, C.; Saji, S.; Kondo, T.; Nakamura, J., Active sites of nitrogen-doped carbon materials for oxygen reduction reaction clarified using model catalysts. *Science* **2016,** *351* (6271), 361-5.

38. Cruden, B. A.; Cassell, A. M.; Ye, Q.; Meyyappan, M., Reactor design considerations in the hot filament/direct current plasma synthesis of carbon nanofibers. *J. Appl. Phys.* **2003,** *94* (6), 4070-4078.

39. Melechko, A. V.; Merkulov, V. I.; McKnight, T. E.; Guillorn, M. A.; Klein, K. L.; Lowndes, D. H.; Simpson, M. L., Vertically aligned carbon nanofibers and related structures: Controlled synthesis and directed assembly. *J. Appl. Phys.* **2005,** *97* (4), 041301.

40. Kresse, G.; Furthmüller, J., Efficient iterative schemes for ab initio total-energy calculations using a plane-wave basis set. *Phys. Rev. B* **1996,** *54* (16), 11169-11186.

41. Perdew, J. P.; Burke, K.; Ernzerhof, M., Generalized Gradient Approximation Made Simple. *Phys. Rev. Lett.* **1996,** *77* (18), 3865-3868.

42. Blöchl, P. E., Projector augmented-wave method. *Phys. Rev. B* **1994,** *50* (24), 17953-17979.

43. Monkhorst, H. J.; Pack, J. D., Special points for Brillouin-zone integrations. *Phys. Rev. B* **1976,** *13* (12), 5188-5192.

44. Ooi, N.; Rairkar, A.; Adams, J. B., Density functional study of graphite bulk and surface properties. *Carbon* **2006,** *44* (2), 231-242.

45. Grimme, S.; Antony, J.; Ehrlich, S.; Krieg, H., A consistent and accurate ab initio parametrization of density functional dispersion correction (DFT-D) for the 94 elements H-Pu. *J. Chem. Phys.* **2010,** *132* (15), 154104.

46. Bae, G.; Youn, D. H.; Han, S.; Lee, J. S., The role of nitrogen in a carbon support on the increased activity and stability of a Pt catalyst in electrochemical hydrogen oxidation. *Carbon* **2013,** *51*, 274-281.

47. Ganguly, A.; Sharma, S.; Papakonstantinou, P.; Hamilton, J., Probing the Thermal Deoxygenation of Graphene Oxide Using High-Resolution In Situ X-ray-Based Spectroscopies. *J. Phys. Chem.C* **2011,** *115* (34), 17009-17019.

48. Jeerage, K. M.; Candelaria, S. L.; Stavis, S. M., Rapid Synthesis and Correlative Measurements of Electrocatalytic Nickel/Iron Oxide Nanoparticles. *Sci. Rep.* **2018,** *8* (1), 4584.

49. Ma, J.; Habrioux, A.; Luo, Y.; Ramos-Sanchez, G.; Calvillo, L.; Granozzi, G.; Balbuena, P. B.; Alonso-Vante, N., Electronic interaction between platinum nanoparticles and nitrogen-doped reduced graphene oxide: effect on the oxygen reduction reaction. *J. Mater. Chem. A* **2015,** *3* (22), 11891-11904.

50. Xiong, Y.; Ma, Y.; Zou, L.; Han, S.; Chen, H.; Wang, S.; Gu, M.; Shen, Y.; Zhang, L.; Xia, Z.; Li, J.; Yang, H., N-doping induced tensile-strained Pt nanoparticles ensuring an excellent durability of the oxygen reduction reaction. *J. Catal.* **2020,** *382*, 247-255.

Chapter 5 - Enhancing Methanol Oxidation Reaction with Platinum-based Catalysts Using a N-Doped Three-dimensional Graphitic Carbon Support

5.1 Introduction

The depletion of fossil-fuels and ever-increasing global energy demands have driven researchers to identify sustainable and efficient energy conversion devices, including fuel cells[1, 2]. Among the several types of fuel cells, direct methanol fuel cells (DMFCs) are considered to be a promising candidate for automotive, portable applications, and stationary systems, owing to their high energy density, low operating temperatures, high energy conversion efficiency, and environmental friendliness[3-5]. However, the widespread applications of DMFCs are limited by the sluggish reaction kinetics of anodic methanol oxidation and large overpotentials[6, 7]. Platinum (Pt) and platinum group metals (PGM) are the most commonly used catalysts for methanol oxidation reaction (MOR) due to their high ability to enable methanol dehydrogenation[8-10]. The MOR catalyzed by Pt mainly occurs through an indirect pathway and produces carbon monoxide (CO) and other carbonaceous intermediates which are known to adsorb strongly on the catalyst surface, thus poisoning the active sites and hindering further oxidation of methanol[9-11]. The poisoning of the Pt catalyst can be decreased by alloying it with a secondary metal such as Ru, Cu, Au, Fe, and so on[12]. These secondary metals are identified to adjust the electronic and chemical properties of the Pt atoms and enhance the overall catalytic performance towards MOR[12]. Alloying with Ru is one of the best strategies for the removal of CO_{ads} species. Ru can supply OH_{ads} species at lower potentials which facilitate the oxidative removal of CO_{ads} and thus, weakening the interaction between Pt and CO intermediates[13, 14].

In other circumstances, CO poisoning can also be suppressed by employing support materials that can provide a synergistic effect of enhanced electron transfer and stronger metal anchoring[15-18]. Among various support materials, the N-doped carbon structures are attractive due to their outstanding electrical conductivity, excellent chemical stability, and enhanced catalytic activity[19]. N-doping into the carbon networks can change the nucleation and growth behavior of Pt nanoparticles (NPs) and reduce their agglomeration through the strong interaction with Pt, resulting in enhanced electrocatalytic activity and long-term stability for MOR[20]. In addition, N-doped carbon materials with graphitic properties can withstand carbon corrosion at high potentials, which is a common problem in commercial carbon supports such as carbon black. Nitrogen can be introduced into the carbon networks in two ways: in-situ doping and post-synthesis doping. The *in-situ* doping includes methods such as arc discharge, pyrolysis, and chemical vapor deposition using nitrogen-containing precursors[21]. The post-synthesis doping approach involves the treatment of pre-synthesized materials in the nitrogen-containing atmosphere at elevated temperatures[22]. Among these two types, in-situ N-doping is assumed to create uniformly distributed nitrogen species in high concentrations, which can improve the electrocatalytic activity and further increase the tolerance towards CO poisoning[20]. Recently, Ma *et al.* have reported that Pt NPs supported on nitrogen-doped graphene nanocomposite derived from pyrolysis exhibited both higher MOR activity and improved tolerance to CO poisoning in acidic media[23]. Liang *et al*. fabricated the N-doped CNTs (N-MOCNTs) that are moderately oxidized using the hydrothermal reaction and the resulting Pt/N-MONCNT catalysts showed the best catalytic performance toward MOR in acidic media comparing to other catalysts employed in the study[24]. Ding *et al*. synthesized N-doped macro/oversized mesoporous carbon support using N-doped carbon nanotubes as spacers for N-doped carbon nanosheets. Pt NPs supported on these 3D architectured N-doped supports exhibited enhanced activity and stability for MOR in acidic media relative to the other nanoporous carbon catalysts reported in their study[25]. Zhang *et al*. prepared a honeycomb-like mesoporous nitrogen-doped carbon spheres (MNCS) using dopamine as the carbon and nitrogen precursor and identified that Pt/MNCS catalyst was electrochemically more active and more stable than the conventional Pt/C catalyst in alkaline media[20]. Hence, the in-depth investigation of in-situ N-doped three-dimensional (3D) graphitic carbon structure as a support material for methanol oxidation reaction in both acidic and alkaline media is required to understand the catalyst-support interactions and further improve the performance.

Herein, we report a study using vertically aligned carbon nanofibers (VACNFs) as a catalyst support for MOR in acidic and alkaline media. VACNFs are a robust brush-like array of carbon nanofibers consisting of conically stacked graphitic microstructures and are aligned vertically in a 3D architecture[26]. The 3D architectured VACNFs can be used as a unique catalyst support for PGM catalysts. Previously, we reported a systematic study explaining the role of VACNFs as a catalyst support for the oxygen reduction reaction (ORR) in alkaline media[27]. The Pt-sputtered VACNF catalysts exhibit longer durability, higher tolerance to methanol crossover, and a faster recovery from CO poisoning comparing to the traditional Pt/C catalyst. This study further reveals the potentials of this 3D architecture as highly effective support for the deposited Pt and PtRu NPs for MOR in both acidic and alkaline electrolytes. The synthesized catalysts exhibit stronger metal-support interactions and higher electrocatalytic activities. In addition, the catalysts have an improved MOR activity and better long-term durability. We prepared VACNF arrays using DC-biased plasma-enhanced chemical vapor deposition (PECVD), which possesses an area density of ~1.0 x 10^9 CNF/cm^2 with a variable average diameter between 50 to 250 nm and an average length of ~5 μm. The individual fibers in the VACNF arrays are separated by an average distance of ~340 nm, forming an open structure which allows the PGM NPs to be sputter-deposited from above and spread along the full length of individual nanofibers. VACNFs offer distinctive advantages over other carbon materials owing to their high density of graphitic edge sites at the sidewall. In addition, the inherent nitrogen heteroatom doping in the VACNFs can lead to the partial electron transfer between carbon support and the deposited PGM NPs, as verified by the XPS analysis, and a stronger metal-support interaction, which enhanced the OH adsorption to compete with CO poison on the catalyst surface in Pt/VACNF and PtRu/VACNF systems. The resulting catalysts are found to have quite different CO stripping and MOR catalytic properties from commercial Pt/C catalysts. Density Functional Theory (DFT) calculations have been employed to obtain molecular insights. Bader charge analyses aid the understanding of charge transfers taking place between the MOR catalysts and their VACNF support. The influence of such charge transfers on the relevant binding of CO and OH at the same MOR active sites was investigated as well. This study on PGM catalysts deposited on the 3D architectured support emphasizes the role of N-doped graphitic edge of VACNFs in enhancing the removal of adsorbed intermediate species and improving catalytic performance towards MOR.

5.2 Experimental Section

5.2.1 VACNF Growth

Graphite paper with 1 x 1 inch^2 was coated with the nickel catalyst for a nominal thickness of 22 nm using a high-resolution ion beam coater and VACNFs with an average length of 5 μm was grown on the graphite paper substrate using DC-biased PECVD by following the procedure mentioned in Chapter 2.

5.2.2 Preparation of Pt/VACNFs and PtRu/VACNFs

Pt was deposited on the as-grown VACNFs from a Pt target of 99.99% purity using the high-resolution ion beam coater under a pressure of 1 x 10^{-4} Torr. The sample stage was inclined at an angle of 5^{o} and rotated at a constant speed of 15 rpm to ensure uniform deposition of Pt along the fibers. The deposition was maintained at a constant rate of 0.5 Å/s and was precisely controlled to a nominal thickness of 10 nm using an in-situ quartz crystal microbalance with less than 5% error to get the desired Pt mass loading. PtRu was deposited on the as-grown VACNFs from a Pt/Ru 50/50 at% alloy target with a purity of 99.95%. The deposition procedure of PtRu was similar to that of Pt except for the nominal thickness of deposition which was controlled to 21.5 nm to get the desired PtRu mass loading. The Pt/VACNF with a nominal thickness of 10 nm has a Pt loading of 21.5 μg/cm^2 and an overall wt % of 10.8 % and the PtRu/VACNF with a nominal thickness of 21.5 nm has a PGM loading of 43.0 μg/cm^2 and an overall wt % of 19.8 %.

5.2.3 Materials Characterization

The surface morphology of the as-grown VACNF arrays was characterized by a versa 3D dual beam FESEM (FEI, Hillsboro, OR) at a 15 kV accelerating voltage. The microstructure of the Pt/VACNF and PtRu/VACNF was analyzed using a Tecnai F20 XT HRTEM (FEI, Hillsboro, OR) at a 200 kV accelerating voltage. Elemental mapping and analysis were obtained using EDS in the Tecnai Osiris S/TEM (FEI, Hillsboro, OR) at a 200 kV accelerating voltage. Surface composition and chemical environments of the catalysts were obtained using a K-Alpha X-ray photoelectron spectrometer system (Thermo Scientific, Waltham, MA) with a monochromated Al Kα source (1486.7 eV). All the XPS spectra were obtained using a 400 μm spot size. Survey spectra were recorded using a pass energy of 200.0 eV, a step size of 1.00 eV, and a dwell time of 10 ms. The high-resolution spectra were recorded using a pass energy of 50.0 eV, a step size of 0.10 eV, and a dwell time of 50 ms.

5.2.4 Electrochemical Characterization

All the electrochemical measurements were performed in a three-electrode system using the CHI 760D electrochemical workstation (CH Instruments, Austin, TX). A coiled Pt wire was used as the counter electrode, a silver-silver chloride (Ag/AgCl) (1.0 M KCl) reference electrode was used in acidic solutions, and a mercury-mercuric oxide (Hg/HgO) (1.0 M NaOH) reference electrode was used in alkaline solutions. For Pt/VACNF and PtRu/VACNF, the working electrode was prepared by punching out a 6.0 mm diameter discs from the as-prepared samples and mounting it on a PEEK-encased GCE using a conductive silver pasted and dried at 70 ^{o}C for a few hours. For 20 % Pt/C and 75% PtRu/C, the catalyst ink was prepared by mixing a required amount of catalyst powder in a mixture of ethanol, water, and 5 % Nafion to get the catalyst loading similar to that of the VACNF catalysts. Then, the resulting solution was sonicated for 1 h and a 5 μL of the catalyst ink was drop cast onto the 3.0 mm GCE encased in PEEK and dried at room temperature to form a uniform thin catalyst film. Before drop-casting the catalyst ink, the GCE was polished with a 50 nm diameter alumina slurry. The electrolytes used were 0.10 M $HClO_4$ and 0.10 M KOH.

Catalytic activity was evaluated by recording CV between -0.10 to 1.00 V (vs. Ag/AgCl) and -0.70 to 0.50 V (vs. Hg/HgO) at a scan rate of 50 mV/s. For comparison with other studies in literature, the measured electrode potentials vs. Ag/AgCl in 0.10 M $HClO_4$ and vs. Hg/HgO in 0.10 M KOH electrolyte at 25 ^{o}C are converted to the value vs. RHE, by adding 0.281 V and 0.907 V, respectively. The catalyst stability was determined by recording CV for 500 cycles at a scan rate of 50 mV/s. The ECSA of the catalysts was evaluated using the CO stripping experiments.

The electrolyte was first purged with Ar for 10 min to remove any dissolved O_2 species followed by recording an initial CV. Then, the solution was purged with pure CO gas for 5 min while holding the potential at -0.122 V (vs. Ag/AgCl) and -0.80 V (vs. Hg/HgO), respectively. These correspond to 0.159 and 0.107 V vs. RHE, respectively. After that, the purging gas was switched to Ar for about 30 min to remove any dissolved CO species from the electrolyte at a fixed potential of -0.122 V (vs. Ag/AgCl) and -0.80 V (vs. Hg/HgO). The current-potential cycles of the electrode were obtained in the potential range between 0 to 1.30 V (vs. RHE) at a scan rate of 10 mV/s in the presence of Ar.

5.2.5 DFT Calculations

Computation work done by our collaborators Dr. Bin Liu and Mr. Jiayi Xu in the Tim Taylor Department of Chemical Engineering of Kansas State University was used to gain insights into the experimental work. Semi-periodic, spin-polarized DFT calculations were performed using the VASP[28]. The PBE functional based on the GGA method was used to account for the Kohn-Sham electron exchange-correlation interactions[29]. The PAW method was used to represent the ionic cores[30]. The energy cut-off for the geometry optimization was set to 400 eV with a Monkhorst-Pack *k*-point mesh of $1 \times 4 \times 1$ to sample the first Brillouin zone[31]. The break condition for the self-consistent iteration was set to be 1×10^{-6} eV. The ionic relaxations stop when the forces on all atoms are less than 0.05 eV/Å.

The *fishbone* catalyst model was adopted to represent the multi-edge vertically aligned carbon nanofiber architecture[27]. Semi-periodic Pt and Pt-Ru alloy represented by 4-atom Pt_4 and Pt_2Ru_2 were placed at the open edge as shown in Figures 5.3 and 5.5. The CO and OH adsorbates were placed at the top and bridge sites to identify the most stable configurations. Bader charge analyses were carried out to understand the charge transfer between the metal catalyst and its carbon support[32].

The adsorption energies (ΔG_{ads}) were calculated using Equation (1), where E_* refers to the total energy of the adsorbate-free system. The free energy of free OH is estimated with Equation (2) using the gas phase H_2O and H_2 as the reference[33]. The zero-point energy (ZPE) corrections and entropic contributions were estimated using the vibrational frequencies obtained from the simple harmonic approximation[34].

$$\Delta G_{ads} = G_{ads} - E_* - G_{ads\,(g)} \qquad (5.1)$$

$$G_{OH} = G_{H_2O} - \frac{1}{2} G_{H_2} \qquad (5.2)$$

5.3. Results and Discussion

5.3.1 Morphological Analysis

The FESEM image of the as-grown VACNFs with an average diameter of 150 nm is shown in Figure 5.1a. The VACNFs are vertically aligned and well separated from each other, forming a unique brush-like structure. The TEM image in Figure 5.1b shows the uniform deposition of Pt NPs on the VACNF sidewall at a Pt loading of 21.5 μg/cm^2 (relative to the geometric surface area of the graphite paper substrate that the VACNF arrays were grown on). The average particle size was found to be 1.7 ± 0.4 nm as shown by the distribution in Figure C.1a. The high-magnification image of the area highlighted by the red rectangle in Figure 5.1b is shown in Figure 5.1c, which displays the Pt NPs present on top of the graphitic layers of VACNF. The lattice fringe d= 0.34 nm confirms the presence of graphitic layers. This shows that small Pt NPs (highlighted in white circles) are effectively anchored on the graphitic edges instead of basal planes. The TEM image of PtRu/VACNF and the particle size distribution in Figure C.1b show the similar structure of PtRu alloy NPs on the VACNFs sidewall with an average particle size of 2.8 ± 0.6 nm at the PGM loading of 43.0 μg/cm^2.

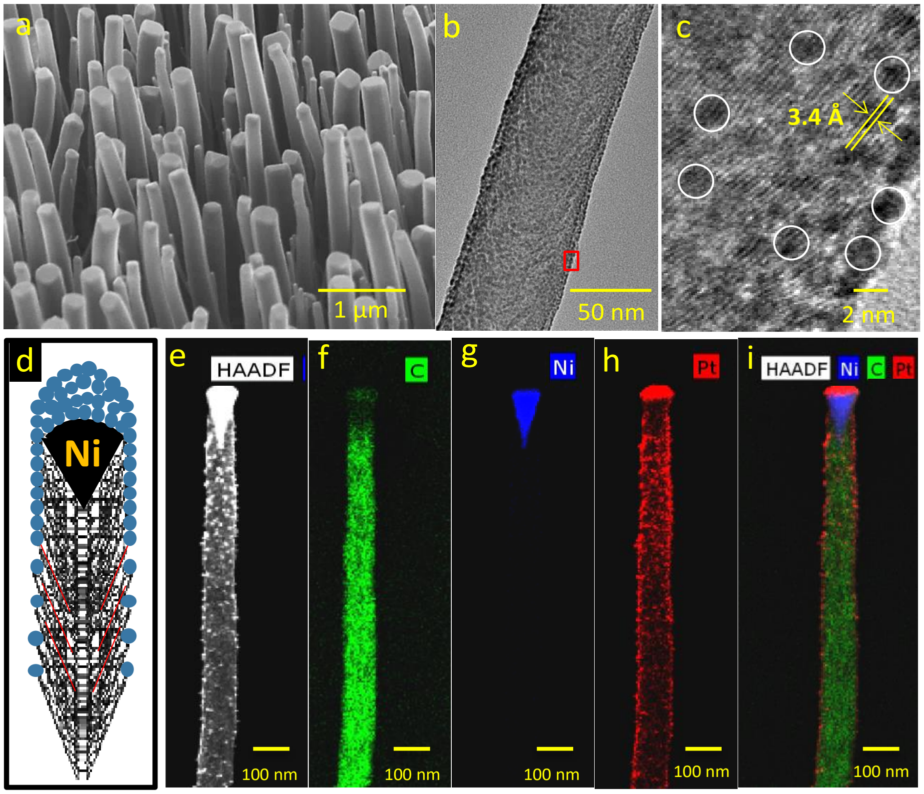

Figure 5.1: (a) FESEM image of VACNF; (b) TEM image of Pt/VACNF (21.5 μg/cm^2 loading); (C) High-magnification TEM image of the red highlighted area of panel (b) showing the lattice fringes of underlying graphitic carbon and Pt nanoparticles (some being highlighted with white circles); (d) Schematic illustration of single VACNF deposited with Pt nanoparticles (blue color); (e) HAADF-STEM image and (f-i) STEM-EDX elemental mapping of C, Ni and Pt in Pt/VACNF.

Figure 5.1d presents the schematic illustration of Pt particles deposited on a single VACNF with the conically stacked microstructures. The presence of C, N, O, and Pt in Pt/VACNF is confirmed by the TEM EDX spectrum shown in Figure C.2. The Cu signal seen in the spectrum comes from the TEM grid used for the analysis. The high-angle annular dark-field (HAADF) STEM image of the Pt/VACNF is shown in Figure 5.1e. EDX elemental mapping of Pt/VACNF in Figures 5.1f-5.1i reveal that C (green) presents throughout the fiber, Ni (blue) presents only at the tip of the fiber with an inverse tear-drop shape, and Pt (red) presents as NPs around the entire fiber except for the thick cap at the very end of the VACNF tip. The Pt NP density slowly decreases moving down the fiber due to shadow effects. The Pt elemental mapping confirmed that the Pt flux can reach deep into the three-dimensional structure even though there was about 20% of the deposited Pt accumulated at the very end of the VACNF tips. The TEM EDX spectrum and elemental mapping of PtRu/VACNF in Figure C.3 display the similar features of PtRu NPs anchored on VACNF sidewalls.

5.3.2 XPS Analysis

The XPS survey spectra for all catalysts presented in Figure C.4 show the principal peaks of C, O, N, and Pt elements. The derived atomic percentage (at%) of all the elements for different catalysts are listed in Table C.1. To further evaluate the chemical environments, high-resolution spectra of C1s, N1s, O1s, and Pt 4f was recorded for bare VACNF, Pt/C and Pt/VACNF as shown in Figures 5.2 and C.5. All the high-resolution spectra were deconvoluted using Gaussian peaks and a Shirley background function. The binding energies (BE) and relative at% of different chemical components derived from the high-resolution spectra of C 1s, O 1s, and N 1s are summarized in Table C.2. The C 1s peak of 20% Pt/C catalyst displayed in Figure 5.2a can be resolved into five subpeaks with BE of 283.13, 284.40, 285.80, 287.63, and 290.73 eV. The peaks at 283.13 (ca. 4.6%) and 284.40 eV (ca. 60.7%) can be assigned to the carbon from the carbide phase[35] and sp^2 hybridized carbon atoms (C=C), respectively[36]. The peaks at 285.80 (ca. 15.1%) and 287.63 eV (ca. 7.4%) are assigned to C-O and C=O bonds indicating the presence of hydroxyl and carbonyl groups, respectively[37]. The peak at 290.73 eV (ca. 12.2%) is assigned to the $\pi - \pi*$ of the shake-up satellite peak from the sp^2 carbon[36]. The C 1s of bare VACNF can be deconvoluted into seven components with binding energies of 283.71, 284.70, 285.82, 286.70, 287.73, 288.70, and 291.48 eV as shown in Figure C.5a. The peaks at 283.71 (ca. 4.4%) and 284.50 (ca. 48.6%) corresponds to Ni-C[38] and sp^2 hybridized carbon atoms (C=C). The peaks at 285.82 (ca. 14.1%) and 286.70 eV (ca. 16.6%) belong to C-O/C=N and C-O-C/C-N bonds which reveals the presence of nitrogen bonding [39, 40], and oxygenated functional groups such as hydroxyl and epoxy[37]. The peaks at 287.73 (ca. 2.7%) and 288.70 eV (ca. 5.6%) belong to C=O and O-C=O bonds indicating the presence of carbonyl and carboxyl groups, respectively[37, 41]. The peak at 291.48 eV (ca. 10.2%) corresponds to the $\pi - \pi*$ of the shake-up satellite peak from the sp^2 C[36, 37]. The deconvolution of the C 1s spectra of the Pt/VACNF shown in Figure 5.2b is almost the same as that of bare VACNF, suggesting that the Pt deposition on the structure does not change the surface chemistry of the VACNFs. However, the decrease in the relative % of carboxyl (-COOH) functional groups (from 5.6% to 3.2%) indicates the binding of the -COOH group with Pt NPs. The COOH group on the VACNF surface can help to strongly anchor the Pt NPs to the sidewalls of VACNFs[41].

The O1s peak of 20% Pt/C accounts for a total of 2.97 at% and it can be smoothly deconvoluted into four fitting curves with peaks at BE of 531.14, 532.29, 533.50, and 535.01 eV as shown in Figure 5.2c. The first two peaks are assigned to the C=O and C-O bonds, which account for 23.4% and 45.1% of oxygen atoms, respectively[36]. The third peak is assigned to the C-O-H/C-O-C bonds accounting for 28.6% of oxygen atoms and the fourth peak is assigned to the physisorbed water on the surface accounting for 2.9% of oxygen atoms[36]. However, the concentration of oxygen on the surface is 6.73 at% and 14.55 at% for bare VACNF and Pt/VACNF, respectively, which is higher than the oxygen concentration of 20 % Pt/C. The O1s peak of bare VACNF shown in Figure C.5b can be divided into four components with BE of 531.28, 532.26, 533.64 and 534.72 eV corresponding to the C=O, C-O, C-O-H/C-O-C bonds, and physisorbed water, which accounts for 20.7, 47.7, 23.0 and 8.6 % of total oxygen atoms, respectively. The O1s peak of Pt/VACNF shown in Figure 5.2d can be separated into three components with BE of 531.20, 532.22, and 533.52 eV corresponding to the C=O, C-O, and C-O-H/C-O-C bonds, which accounts for 36.0, 56.5 and 11.5% of total oxygen, respectively. The N 1s spectrum of bare VACNF consists of five components centered at BE of 398.76, 399.95. 401.13. 402.67 and 405.13 eV as presented in Figure 5.2g with a total of 7.36 at% of nitrogen doping. The first three peaks are ascribed to the pyridinic N, pyrrolic N, graphitic N, and the last two minor components are ascribed to the pyridinic oxide N[42]. Relative % of the pyridinic N, pyrrolic N, graphitic N, and oxidic N are 32.9, 10.9, 34.0, and 22.2% of total nitrogen atoms, respectively. After the Pt deposition, total nitrogen concentration slightly decreased to 6.87 at% and this could be due to the deposited Pt blocking some N. The N1s peak of Pt/VACNF as shown in Figure 5.2h can be deconvoluted into four peaks. The peaks at 398.81 eV, 400.13, and 401.20 eV are allocated to pyridinic N, pyrrolic N, and graphitic N that account for 45.3, 17.6, and 11.1% of total nitrogen, respectively. However, the additional peak at 398.0 eV which was not present in the bare VACNF can be assigned to the Pt-N resulting from the strong interaction between Pt and N[43, 44], which corresponds to a total of 26.0% of the total nitrogen atoms. As indicated by the presence of Pt-N peak, it can be noted that the nitrogen species present in VACNFs successfully anchors the Pt NPs, and the deposited Pt NPs on nitrogen-rich VACNFs can display a higher catalytic activity towards the electro-oxidation of alcohols[45]. The resulting strong metal-support interaction may potentially weaken the binding energy of strongly adsorbed poisonous intermediate carbonaceous species such as CO_{ads}[46, 47], and hence promoting the catalytic activity with lower surface poisoning.

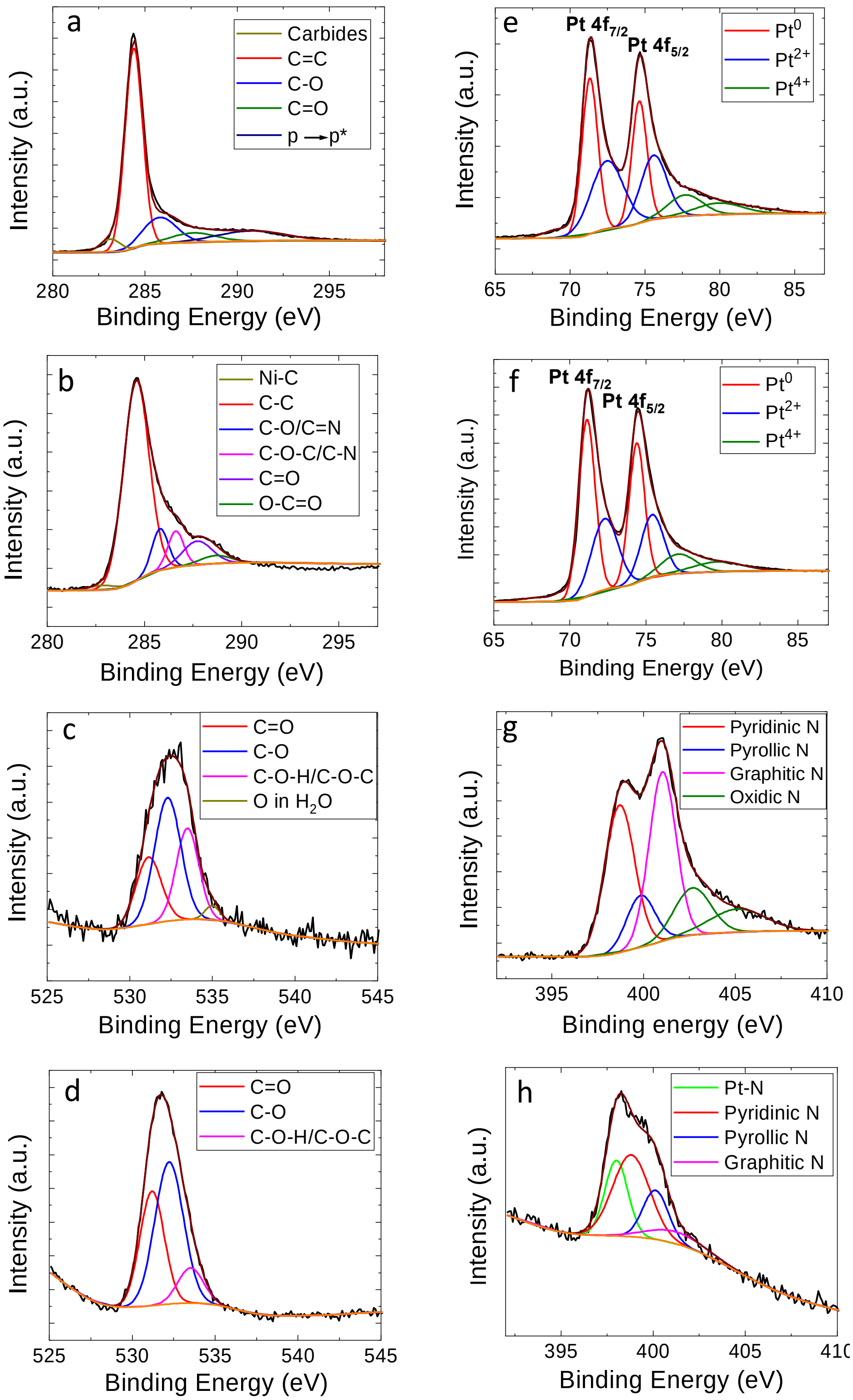

Figure 5.2: (a,b) C 1s, (c,d) O 1s, and (e,f) Pt 4f XPS spectra of Pt/C (panels a, c and e) and Pt/VACNF (panels b, d and f); N 1s XPS spectra of (g) bare VACNF and (h) Pt/VACNF.

Figures 5.2e and 5.2f present the Pt 4f XPS spectra of 20% Pt/C and Pt/VACNF. Each Pt 4f spectrum contains two spin-orbit splits, namely Pt $4f_{7/2}$ and Pt $4f_{5/2}$ with a peak area ratio of 4:3. Table C.3 lists the binding energies and relative area % of different Pt species for both Pt/C and Pt/VACNF catalyst. The measured Pt 4f spectrum of 20% Pt/C can be deconvoluted into 3 sets of doublet peaks with the BE at 71.32 eV and 74.63 eV, 72.47 eV and 75.59 eV, 77.70 eV and 79.90 eV, which can be assigned to Pt^0, Pt^{2+} (PtO or $Pt(OH)_2$), and Pt^{4+} (PtO_2) species, respectively[48]. The Pt 4f spectrum of Pt/VACNF showed a similar feature, but it is important to note that the BE of Pt^0 $4f_{7/2}$ and Pt^0 $4f_{5/2}$ of Pt/VACNF shifted negatively by 0.20 eV and 0.23 eV, respectively, relative to those of Pt/C. The negative shift in the BE of metallic Pt^0 indicates that the Pt/VACNF either has less electron transfer from the Pt to carbon support than the commercial Pt/C catalyst or has electron transfer from C to Pt [23, 49, 50]. The Pt and VACNF interaction could be either donating or accepting electrons depending on the nature of the atomic sites. More insights about the electron transfer mechanism will be given in the DFT section. Furthermore, Figure C.6 summarizes the percentages of the Pt species in different chemical states, i.e. Pt^0, Pt^{2+} and Pt^{4+}, which are 45.6 %, 41.1 %, 13.3% in Pt/C and 53.4 %, 34.5 %, 12.1 % in Pt/VACNF, respectively. Compared to Pt/C, the Pt/VACNF display a higher content of metallic Pt^0, which can be attributed to the difference in Pt deposition processes, i.e. the dry physical deposition by ion beam sputtering versus the wet chemical synthesis in the commercial Pt/C catalyst. The presence of more metallic Pt can increase the adsorption of methanol on the catalyst surface[51, 52].

5.3.3 Modeling of CO and OH binding at the MOR active sites

In our previous study[27], a *fishbone* model has been developed to represent the stacked graphitic edges in VACNFs for DFT calculations. Bader charge analyses (Figure 5.3) reveal that the four Pt atoms (Pt_4) along the graphitic edge in this mode receive electrons from the carbon support (with a charge of about -0.03 e per Pt atom). Thus, it explains why XPS data show the BE of Pt^0 4f peaks shift negatively due to the charge transfer from carbon support to Pt. This finding is also corroborated by the up shift of its Fermi level as shown in Figure 5.4a when compared with the un-supported Pt (111).

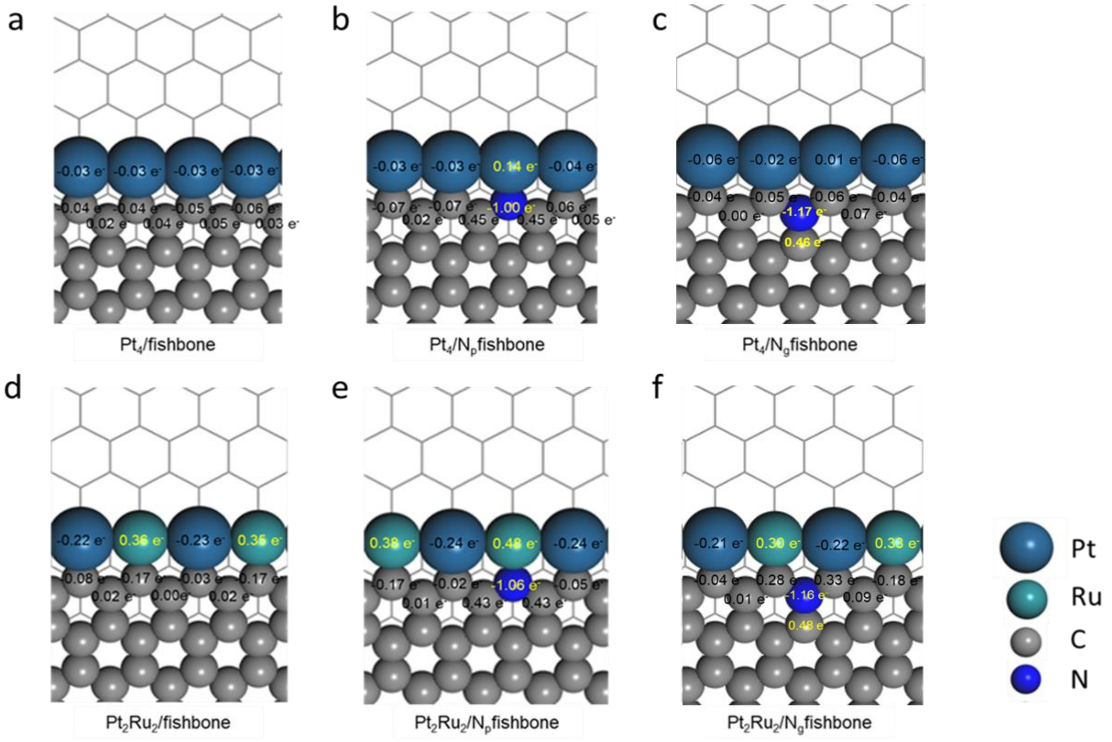

Figure 5.3: Pt_4 (a-c) and Pt_2Ru_2 (d-f) on undoped (panels a and d), N_p-doped (panels b and e) and N_g-doped (panels c and f) graphitic edge of the VACNF carbon support represented by the "fishbone" model.

Table 5.1 summarizes the value of Fermi level, *d*-band center, atomic net charges, adsorption energies for the Pt_4 and Pt_2Ru_2 systems supported on undoped, and N-doped carbon edges. In the presence of pyridinic nitrogen (N_p) species, however, the Pt atom adjacent to the electron-withdrawing N_p becomes positively charged as shown in Figure 5.3b. In the presence of near-edge graphitic nitrogen (N_g), the electron-withdrawing effect on Pt was not observed, as shown in Figure 5.3c. The Bader charge analyses on the Pt_2Ru_2 (Figures 5.3d-f) suggest that the charge transfer occurs primarily between Pt and Ru, as well as Ru and C. Consistent trend has been reported in other Pt-Ru alloy systems[53-55]. In this case, the *d*-band center upshifts for Ru but downshifts for Pt as shown in Table 5.1.

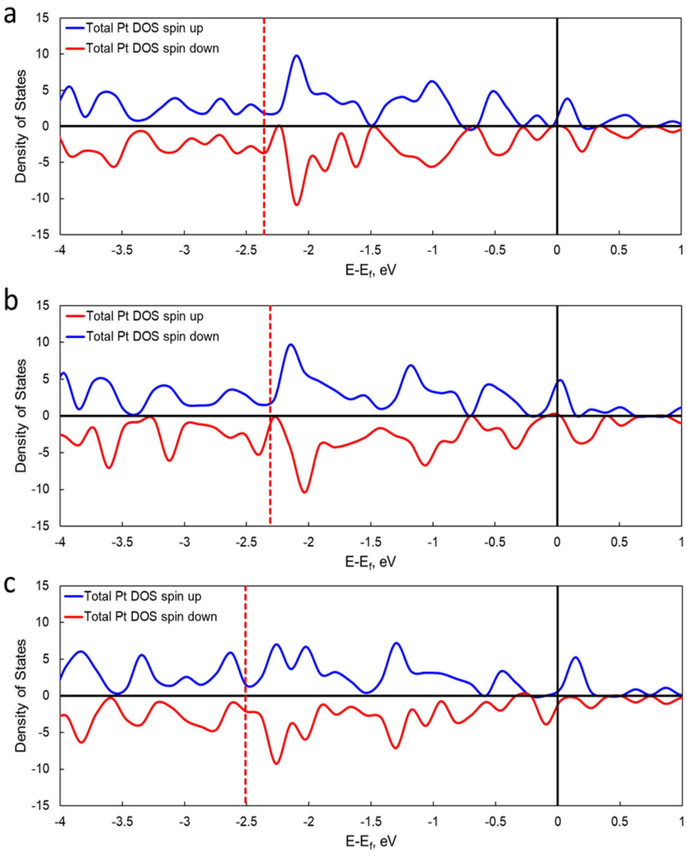

Figure 5.4: Total density of states (DOS) of Pt_4 on (a) undoped, (b) N_p-doped, and (c) N_g-doped graphitic edge of the VACNF carbon support represented by the "fishbone" model. The vertical solid lines indicate Fermi energy, and the dashed lines indicate the corresponding *d*-band center.

Table 5.1: Summary of Fermi level, d-band center, charges, and adsorption energies of Pt_4 and Pt_2Ru_2 supported by undoped, N_p doped, and N_g doped carbon edges.

Models	Fermi level (eV)	Total d-band (eV)	d-band center of Pt (eV)	d-band center of Ru (eV)	Charges on Pt	Charges on Ru	G_{OH} (eV)	G_{CO} (eV)	ΔG_{OH-CO} (eV)
Pt(111)	-2.24	-2.10	-2.10	-	0.00	-	1.02	-1.33	2.35
Pt_4/fishbone	-2.02	-2.36	-2.36	-	-0.03	-	-0.22	-1.79	1.57
Pt_4/N_pfishbone	-1.98	-2.31	-2.31	-	0.01	-	-1.07	-2.83	1.76
Pt_4/N_gfishbone	-1.80	-2.51	-2.51	-	-0.03	-	-0.83	-1.96	1.13
Pt_2Ru_2/fishbone	-1.95	-1.98	-2.66	-1.32	-0.22	0.36	-0.47	-1.87	1.40
Pt_2Ru_2/N_pfishbone	-1.86	-2.07	-2.79	-1.39	-0.24	0.43	-0.55	-1.96	1.41
Pt_2Ru_2/N_gfishbone	-1.81	-2.08	-2.73	-1.44	-0.22	0.32	-0.53	-1.81	1.28

Figure 5.5 also displays the adsorptions of OH and CO on Pt_4 and Pt_2Ru_2. Generally, it is known that adsorbates tend to bind stronger if the PGM *d*-band center shifts toward the Fermi level[56-59]. In this case, Pt_4 supported on the N_p-doped carbon edge shows the highest *d*-band center (see Figure 5.4b), and thus, is expected to bind the most strongly with CO and OH. In fact, the CO and OH adsorption energies (G_{OH}, G_{CO}) at the Pt site both follow the trend of N_p-doped > N_g-doped > undoped in decreasing order. For MOR catalyst design, it is also paramount to mitigate potential poisoning of active sites by intermediate carbonaceous species such as CO. In principle, stronger OH binding is able to effectively compete with CO for the MOR active site and also facilitates the removal of CO via the water-gas shift reaction[60]. It is evident that the local chemical environment in the carbon support can influence the relative adsorption energies between OH and CO (i.e., $\Delta G_{OH-CO} = G_{OH} - G_{CO}$). Despite that the nitrogen dopants enhance both OH and CO binding, the electron-withdrawal by N from Pt impacts more on the binding of OH on PGM sites. Hence, ΔG_{OH-CO} corresponding to the N_g-doped carbon support is smaller than both the undoped support and the N_p-doped support. Further, as shown in Figures 5.5d-f, the Ru top site or Ru-Pt bridge sites are preferred by both OH and CO in the supported Pt_2Ru_2 systems. Both G_{OH} and G_{CO} still follow the trend of N_p-doped > N_g-doped > undoped in the same decreasing order. Moreover, ΔG_{OH-CO} is the smallest for Pt_4 and Pt_2Ru_2 on the N_g-doped VACNF system. The DFT calculations predict that the PGM on N_g-doped VACNFs would give the smallest CO poisoning.

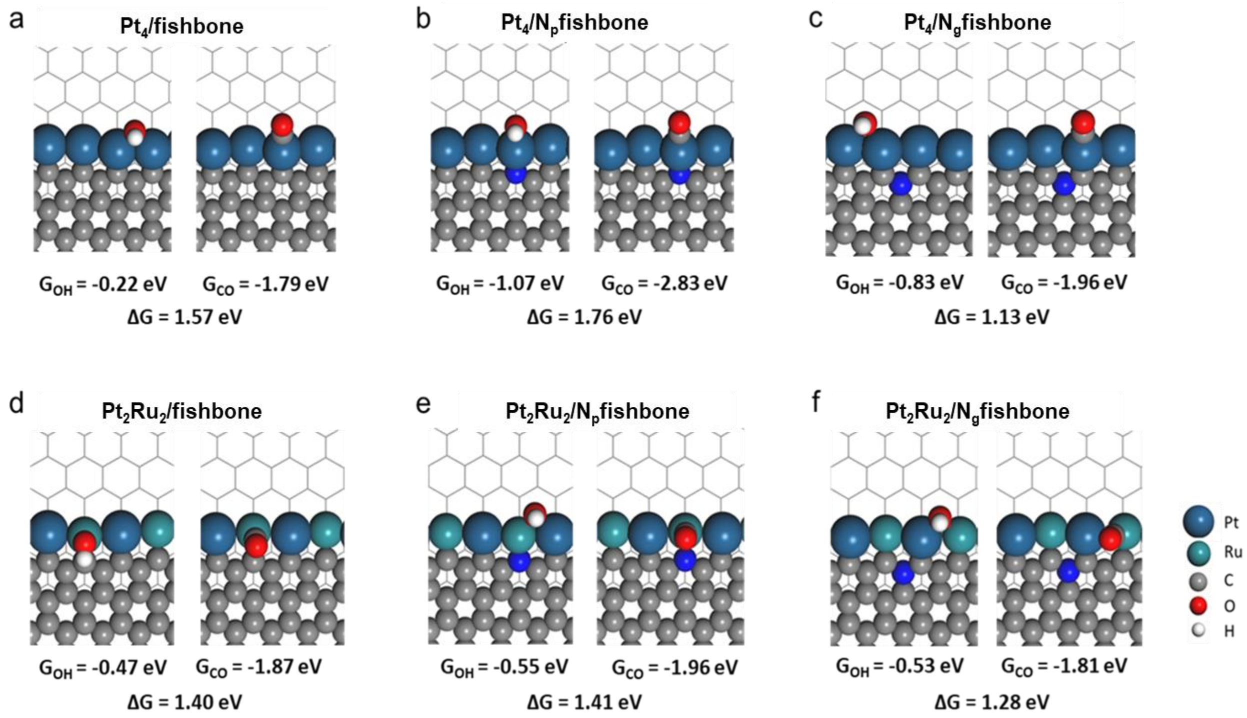

Figure 5.5: Adsorptions of OH and CO on Pt_4 and Pt_2Ru_2 supported on undoped (panels a and d), N_P-doped (panels b and e) and N_g-doped (panels c and f) graphitic edge of the VACNF carbon support represented by the "fishbone" model.

5.3.4 Electrochemical Surface Area Evaluation

The Electrochemical Surface Area (ECSA) of the Pt catalyst can be derived from Cyclic Voltammetry (CV) with two different methods: i) hydrogen underpotential (H_{UPD}) and ii) CO stripping. Figure C.7 illustrates the CV curves of Pt/C (25.6 μg/cm^2), Pt/VACNF (21.5 μg/cm^2), PtRu/C (48.0 μg/cm^2), and PtRu/VACNF (43.0 μg/cm^2) in the potential range from -0.10 to 1.00 V (vs. Ag/AgCl) in Ar-saturated 0.10 M $HClO_4$ and -0.90 to 0.30 V (vs. Hg/HgO) in Ar-saturated 0.10 M KOH solution, respectively, at a scan rate of 50 mV/s. The Pt/VACNF and PtRu/VACNF catalysts showed about 50% to 100% higher capacitive background current than the commercial Pt/C and PtRu/C catalysts, which mainly arises from the porous graphite paper substrate as discussed in our previous paper[27]. This obscures the H_{UPD} features and makes it difficult to derive the ECSA accurately using H_{UPD}. Thus, CO stripping was used as the primary method to determine

ECSA in this study.

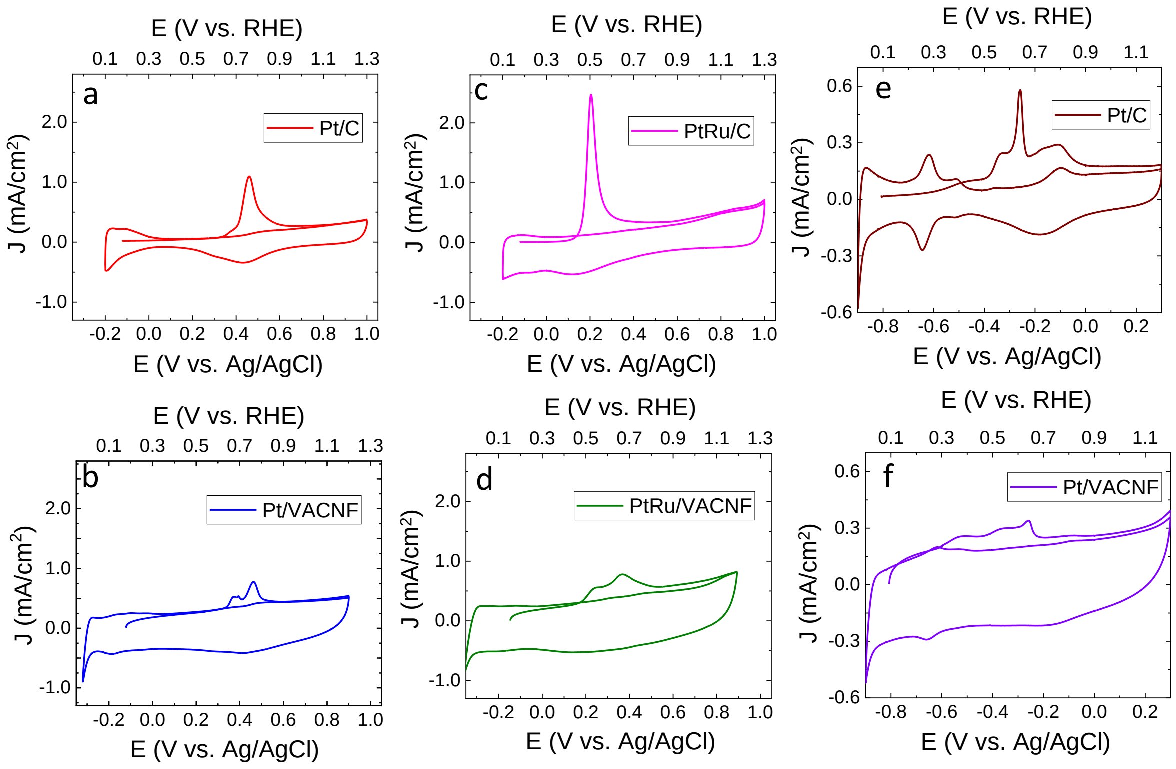

Figure 5.6: Electrochemical CO Stripping curves of (a) Pt/C (25.6 μg/cm^2) , (b) Pt/VACNF (21.5 μg/cm^2), (c) PtRu/C (48.0 μg/cm^2), and (d) PtRu/VACNF (43.0 μg/cm^2) recorded in 0.10 M $HClO_4$ solution at a scan rate of 10 mV/s; Electrochemical CO Stripping curves of (e) Pt/C (25.6 μg/cm^2) and (f) Pt/VACNF (21.5 μg/cm^2) recorded in 0.10 M KOH solution at a scan rate of 10 mV/s.

The CO stripping voltammograms and the subsequent CV curves of Pt/C, Pt/VACNF, PtRu/C, and PtRu/VACNF in 0.10 M $HClO_4$ solution, and Pt/C and Pt/VACNF in 0.10 M KOH solution are presented in Figure 5.6. Figure C.8 displays the first anodic scan from the CO stripping CV curves recorded for all the catalysts in both 0.10 M $HClO_4$ and 0.10 M KOH. For all the catalysts, the absence of hydrogen desorption peaks in the first anodic scan indicates that the Pt sites were predominately covered by adsorbed CO species. The determination of onset potential for CO electro-oxidation in Pt/VACNF and PtRu/VACNF is difficult due to the large capacitive background current. However, useful information can be derived from the CO electro-oxidation peaks.

The CO electro-oxidation on Pt/C takes on a single sharp peak at ~0.46 V (vs. Ag/AgCl) as shown in Figure 5.6a, whereas the CO electro-oxidation on Pt/VACNF is composed of two peaks at ~0.38 V (vs. Ag/AgCl) and ~0.46 V (vs. Ag/AgCl) as shown in Figure 5.6b. The occurrence of the two CO electro-oxidation peaks is a significant characteristic of graphitic carbon supports as previously reported[61]. The two peaks can be assigned to the oxidation of CO adsorbed on the Pt sites interacting with the graphitic (sp^2) carbon (peak at ~0.38 V vs. Ag/AgCl) and disordered (sp^3) carbon (peak at ~0.46 V vs. Ag/AgCl), respectively[61]. The appearance of the new negatively shifted CO stripping peak in Pt/VACNF correlates well with the negative shift in the BE of Pt^0 $4f_{7/2}$ and Pt^0 $4f_{5/2}$. This confirms the easier removal of CO_{ads} species from the catalyst surface. The CO stripping peak of PtRu/C is located at ~0.21 V (vs. Ag/AgCl) as shown in Figure 5.6c, almost 250 mV lower than that of Pt/C. This can be attributed to the fact that a more active metal (like Ru) in proximity can provide reactive OH_{ads} species to CO_{ads}/Pt at a relatively lower potential and hence facilitate oxidizing the adsorbed CO[62]. Figure 5.6d displays the CO stripping curve of PtRu/VACNF consisting of two oxidation peaks at ~0.24 and ~0.36 V (vs. Ag/AgCl) similar to that of Pt/VACNF but at lower potentials resulting from the alloying of Ru with Pt. In contrast, as demonstrated in Figures 5.6e and 5.6f, the CO stripping peaks on Pt/C and Pt/VACNF in 0.10 M KOH solution are completely different from those in 0.10 M $HClO_4$ solution. In the alkaline solution, multiple anodic peaks appear at different potentials which is consistent with the literature[63, 64]. Nevertheless, the CO stripping peaks of Pt/VACNF are at lower potentials than the commercial Pt/C catalyst.

The second anodic scan of the CO stripping CVs of all the catalysts does not show any peaks related to CO electro-oxidation, indicating that the adsorbed CO species were completely oxidized during the first scan. So, the overall CO stripping charge can be calculated by subtracting the second anodic scan from the first scan of CO stripping CVs and integrating the remaining peak area. The ECSA by CO stripping for all the catalysts is calculated using the following equation

$$ECSA_{CO} = \frac{Q_{CO}}{Q_a{}^* \, m_{Pt}} \tag{5.3}$$

where Q_{CO} is the charge associated with the desorption of CO from the Pt active sites, Q_a (420 μC/cm^2) is the charge required to oxidize a monolayer of CO adsorbed on 1 cm^2 of Pt surface and m_{Pt} is the mass loading of platinum. The ECSA values of Pt//C, Pt/VACNF, PtRu/C and PtRu/VACNF in 0.10 M $HClO_4$ solution are 89.6, 41.3, 87.5, and 39.4 m^2/g$_{PGM}$, respectively. The calculated ECSA from the CO stripping charge for the Pt and PtRu catalysts are similar as both Pt and Ru have similar affinities for CO adsorption[65]. The ECSA values of Pt/C and Pt/VACNF in 0.10 M KOH solution are 52.9 and 36.1 m^2/g$_{PGM}$ which is comparatively lower when compared to the values in the acidic medium. This could be due to more OH^- species competing with CO for the available Pt sites in the alkaline medium and hence resulting in the underestimation of ECSA. Since the ECSA values calculated from the acidic medium are representing the maximally available catalyst sites, they are used for normalizing the current density in this study to make consistent comparisons. It is noted that the ECSA values on VACNFs are generally lower than the counterparts on commercial Vulcan carbon supports. This is mainly attributed to the large aggregated PGM caps (~20% total PGM mass) at the VACNF tips due to shadow effects during PGM sputtering as shown in Figures 5.1h and 5.1i. A more uniform PGM NP deposition can be achieved in the future with atomic layer deposition (ALD). In this study, it was found that normalizing the measured MOR current with the ECSA of the PGMs was sufficient to reveal the underlying effects attributed to the catalyst-support interactions.

5.3.5 Electrocatalytic Activity towards the MOR

The catalytic performance towards the MOR is evaluated for the Pt/VACNF and PtRu/VACNF catalysts and benchmarked relative to the commercial Pt/C and PtRu/C catalysts. Figure 5.7 presents the steady-state CV curves recorded in the potential range between 0.10 to 1.00 V (vs. Ag/AgCl) and -0.70 to 0.50 V (vs. Hg/HgO) in Ar saturated 0.10 M $HClO_4$ and 0.10 M KOH solution containing 0.75 M CH_3OH at a scan rate of 50 mV/s for all the catalysts. The CVs of Pt/VACNF and PtRu/VACNF have a significant capacitive contribution from the graphite paper substrate as discussed in our previous paper[27]. Hence, to illustrate the true MOR current density, the capacitive contribution needs to be subtracted from the original CV. Figures C.9a and C.9d present the CV recorded with a bare graphite paper substrate in Ar-saturated 0.10 M $HClO_4$ and 0.10 M KOH solution containing 0.75 M CH_3OH at a scan rate of 50 mV/s with the currents normalized to the geometric area, which serve as the background. The Figures C.9b and C.9c show the CV curves before and after subtracting the background in 0.10 M $HClO_4$ solution and Figures C.9e and C.9f show the CV curves before and after subtracting the background in 0.10 M KOH solution, respectively. It is clear that, after background subtraction, the CVs of the catalysts on VACNFs resemble those observed with the commercial Pt/C and PtRu/C catalysts in Figure 5.7 with the minimum contribution from the bare catalyst support (including the substrate).

The CVs for all the catalysts for MOR are reported in terms of current density after normalizing with the ECSA calculated from the CO stripping experiments. All the CVs in methanol-containing solutions show two characteristic irreversible anodic peaks, one in the forward scan and one at lower potentials in the backward scan. Figure 5.7a presents the CV curves recorded for the Pt/C and Pt/VACNF in Ar-saturated 0.10 M $HClO_4$ solution containing 0.75 M methanol. The forward peak current density (J_f) of Pt/VACNF is 0.71 mA/cm^2, similar to the 0.67 mA/cm^2 observed for Pt/C. However, the onset potential of Pt/VACNF is about 40 mV shifted to a lower potential indicating the faster kinetics of MOR on the Pt/VACNF catalyst. The significant difference between these two catalysts arises from their backward peak current density (J_b) which is calculated to be 0.51 mA/cm^2 for Pt/VACNF and 0.98 mA/cm^2 for Pt/C. In addition to that, the J_b peak of Pt/VACNF appears at about 140 mV more negative potential (i.e. ~0.4 V vs. Ag/AgCl) and the cathodic CV curve below 0.4 V nearly overlaps with that of Pt/C. In common literature, the oxidation peak during the forward scan is attributed to electro-oxidation of methanol and the oxidation peak in the backward scan is attributed to the electro-oxidation of the adsorbed carbonaceous intermediate species (such as CO, CH_2OH, CH_2O, and HCOOH) that have been generated in the previous forward scan and the value of J_f/J_b has been used to represent the catalyst's tolerance to the poisoning intermediate carbonaceous species [66, 67]. The Pt/VACNF has a J_f/J_b value of 1.39 which is much higher than the 0.68 obtained with the commercial Pt/C catalyst. However, several studies indicated that the backward peak (J_b) may be also attributed to the oxidation of methanol by the regenerated Pt surface from the Pt-O_x formed in the previous forward scan[68, 69]. As a result, it was suggested that the J_f/J_b value was not related to the degree of CO tolerance but to the degree of oxophilicity. The CV curves in Figure C.10b shows that the I_f peak is not affected by the upper potential limit while the I_b peak height is quickly reduced and the peak potential is negatively shifted as the upper potential limit is increased, which correlates well with the increase of the degree of oxidation and reduction of Pt nanoparticles as shown in Figure C.10a (without the presence of MeOH). In Pt/VACNF, the lower J_b value and the shift of J_b peak potential by about -140 mV comparing to Pt/C are consistent with the DFT calculations that the adsorption energy of OH (see G_{OH} in Table 1) substantially increases in Pt/VACNF, particularly with N-doping. The presence of nitrogen doping, as confirmed by the XPS analysis, accelerates the formation of OH species by dissociating the water molecules, which is known to promote the oxidation of methanol at a lower potential[49, 52, 70]. In addition, the increased oxygen functional groups on the VACNF surface as observed by XPS could also assist the oxidative removal of adsorbed intermediate carbonaceous species from the catalyst surface[71]. The nitrogen doping and oxygen functional groups together play a major role in keeping the Pt sites available for methanol adsorption. These results are in good agreement with the lower peak potential for CO oxidation observed with the Pt/VACNF catalyst in the CO stripping experiments.

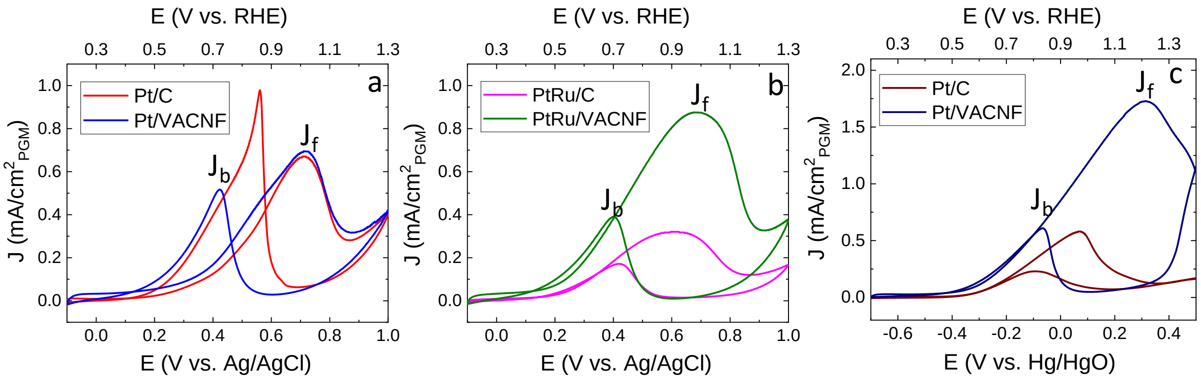

Figure 5.7: Cyclic voltammogram of (a) Pt/C and Pt/VACNF, (b) PtRu/C and PtRu/VACNF recorded in Ar-saturated 0.10 M $HClO_4$ solution with 0.75 M MeOH at a scan rate of 50 mV/s; (c) Cyclic voltammogram of Pt/C and Pt/VACNF recorded in Ar-saturated 0.10 M KOH solution with 0.75 M MeOH at a scan rate of 50 mV/s. The current density (J) is normalized to the electrochemical surface area derived from CO stripping experiments.

The effects of oxophilicity are more evident by comparing the PtRu/C bimetallic catalyst with the Pt/C catalyst. Figure 5.7b displays the CV curves recorded for the PtRu/C and PtRu/VACNF in Ar-saturated 0.10 M $HClO_4$ solution for MOR. The J_b value of PtRu/C is only 0.16 mA/cm^2, which is substantially suppressed from 0.98 mA/cm^2 for the Pt/C catalyst. The J_f value of PtRu/C is about half of that in Pt/C mainly due to the higher PGM loading and higher

ECSA of PtRu/C as shown in Figure 5.6c. The J_f peak potential shifts from ~1.0 V (vs. RHE) for Pt/C to ~0.90 V for PtRu/C, indicating the effects of OH_{ads} on the more oxophilic Ru atoms as reported in the literature[68, 69]. The J_f of PtRu/VACNF is 0.87 mA/cm^2, which is 2.7 folds of that of PtRu/C (0.32 mA/cm^2). The J_b features of PtRu/VACNF, in both peak height and peak potential, are similar to Pt/VACNF. It is interesting that the VACNF support in Pt/VACNF catalyst to a certain degree plays a similar role as the Ru atoms in PtRu/C catalyst.

Figure 5.7c shows the CV curves of Pt/C and Pt/VACNF in Ar-saturated 0.10 M KOH solution containing 0.75 M methanol, which presents similar MOR behavior to those of PtRu catalysts in the acidic media, but with higher J_f and J_b values. The J_f and J_b are 1.72 and 0.60 mA/cm^2 for Pt/VACNF and 0.59 and 0.23 mA/cm^2 for Pt/C. The J_f value of Pt/VACNF in the alkaline media, 1.72 mA/cm^2, is clearly higher than the value of 0.87 mA/cm^2 for PtRu/VACNF in the acidic media. The J_f peak of Pt/C is at the same potential, i.e. ~0.94 – 0.98 V (vs. RHE), in the acid and alkaline solutions while the J_f peak of Pt/VACNF extends from 0.98 V in the acidic solution to 1.20 V (vs. RHE) in the alkaline solution. It is known that the OH^- species in the alkaline media can assist in the removal of the accumulated carbonaceous intermediate species[72], and hence resulting in higher tolerance to poisoning carbonaceous species when compared to the acidic media. Here the formation of surface oxygenated groups on VACNFs likely amplified this effect. On the other hand, Wang *et al.* reported that, in alkaline media, the reactive hydroxyl species preferably adsorb on the Pt surface than the PtRu surface and the surface reactivity of Pt is actually suppressed in the presence of Ru[64]. Hence, alloying of Pt with Ru is not required in alkaline media. It is noteworthy that, in the plots versus RHE, the anodic curve of Pt/VACNF in the alkaline medium is very close to that of the PtRu/VACNF catalyst in the acidic media, which indicates that the VACNF support provides the needed -OH species to remove CO_{ads} similar to the Ru sites.

Interestingly, VACNF support allows the J_f peak to move toward higher potentials by approximately 200 mV. Overall, the Pt/VACNF and PtRu/VACNF catalysts demonstrated higher catalytic activity than Pt/C catalysts in both acidic and alkaline solutions.

5.3.6 Durability of the Catalysts for MOR

The long-term durability of the catalyst for MOR is another important property. Here, the durability of all the catalysts is evaluated by the consecutive CV measurements. As shown in Figure 5.8, after 500 CV cycles, the J_f and J_b display an obvious decrease for all the samples. Table 5.2 lists the ECSA calculated from CO stripping, J_f, J_b, and J_f/J_b ratio of the initial and 500th CV cycle for all the catalysts measured in 0.10 M $HClO_4$ and 0.10 M KOH, respectively. The J_f value of Pt/VACNF and PtRu/VACNF catalysts are higher than the Pt/C and Pt/Ru/C throughout the entire testing period in both acid and alkaline media. In 0.10 M $HClO_4$, the activity of Pt/VACNF degrades similarly to Pt/C as shown in Figures 5.8a and 5.8b. As seen from the elemental mapping, some PGM catalysts are deposited on the Ni NPs at the VACNF tips, which quickly dissolute in the acidic solution, resulting in the loss of ~20% PGM material. However, even after 500 cycles, the ~1.7 nm diameter Pt NPs deposited on the VACNF sidewall remain and able to show similar catalytic activity as the Pt/C catalyst with ~3.8 nm particle size.

Figures 5.8c and 5.8d display the CV curves in 0.10 M $HClO_4$ solution containing 0.75 M methanol for PtRu/C and PtRu/VACNF, respectively. When Ru is added, the PtRu/VACNF showed better durability with only a 10% decay in J_f comparing to the 25% decay of the commercial PtRu/C catalyst. In addition, Pt/VACNF and PtRu/VACNF maintain higher J_f/J_b values (1.39 and 1.08) comparing to the commercial Pt/C and PtRu/C (0.65 and 1.00), respectively, at the 500th CV cycle. The significant drop in the J_f/J_b values of PtRu/VACNF and PtRu/C after the 500 CV cycles is mainly attributed to the Ru dissolution at potentials higher than 0.80 V (vs.

RHE)[72]. Figures 5.8e and 5.8f display the CV curves in 0.10 M KOH solution containing 0.75 M methanol for Pt/C and Pt/VACNF, respectively. The Pt/VACNF shows only 21% decay in the MOR activity after 500 CV cycles, which is much smaller than 46% decay of Pt/C. Also, Pt/VACNF maintains a higher J_f/J_b value compared to that of Pt/C, i.e. 4.81 vs. 1.69. These durability test results indicate that Pt/VACNF and PtRu/VACNF catalysts are more stable and efficient than their commercial counterparts, which is likely due to the increased OH adsorption energy on the N-doped graphitic edges of VACNF support, making them more competitive relative to the adsorption of CO poison.

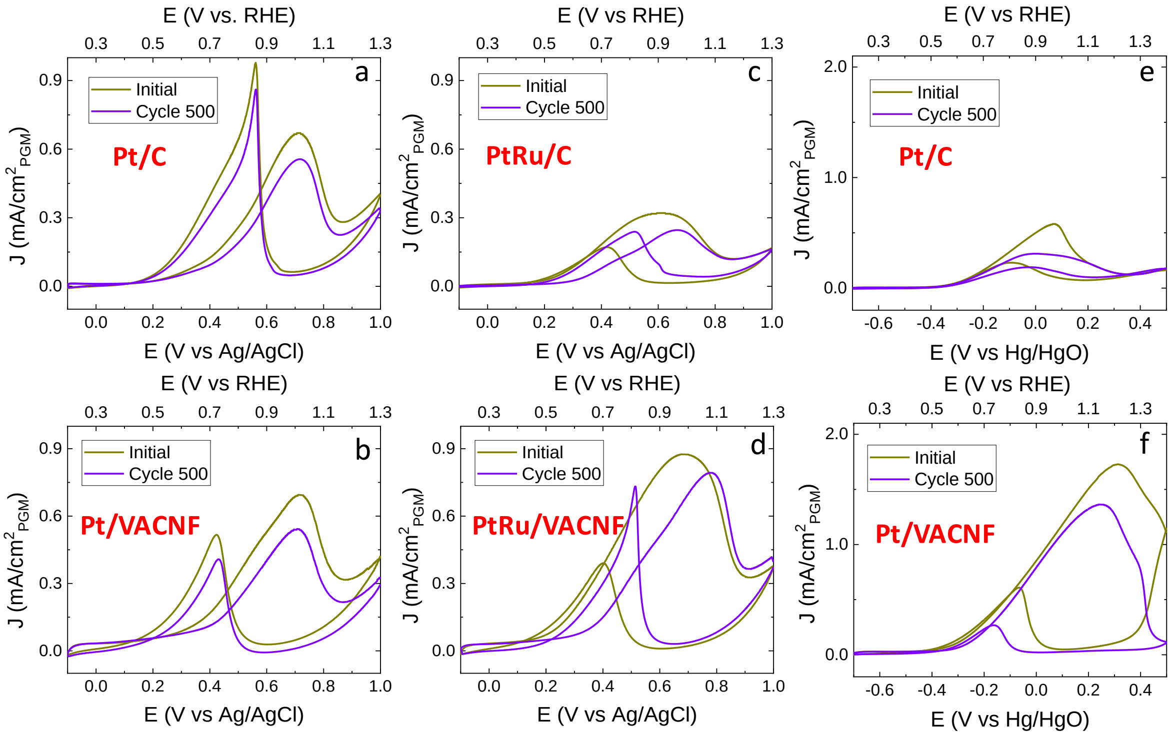

Figure 5.8: Durability test of (a) Pt/C (25.6 μg/cm^2), (b) Pt/VACNF (21.5 μg/cm^2), (c) PtRu/C (48.0 μg/cm^2), and (d) PtRu/VACNF (43.0 μg/cm^2) recorded in Ar-saturated 0.10 M $HClO_4$ solution with 0.75 M MeOH at a scan rate of 50 mV/s; Durability test of (e) Pt/C (25.6 μg/cm^2) and (f) Pt/VACNF (21.5 μg/cm^2) recorded in Ar-saturated 0.10 M KOH solution with 0.75 M MeOH at a scan rate of 50 mV/s. All current densities (J) are normalized to the electrochemical surface area derived from CO stripping experiments.

Table 5.2: Electrochemical surface area (ECSA), forward (J_f) and backward (J_b) peak current density normalized to ECSA, and J_f/J_b for Pt/C, PtRu/C, Pt/VACNF. and PtRu/VACNF measured in different electrolyte solution containing 0.75 M CH_3OH.

Electrolyte (with 0.75 M CH_3OH)	Catalyst	ECSA (m^2/g_{PGM})	J_f (mA/cm^2_{PGM})		J_b(mA/cm^2_{PGM})		J_f/J_b	
			Initial	500th CV	Initial	500th CV	Initial	500th CV
0.1 M $HClO_4$	Pt/C	89.6	0.67	0.56	0.98	0.86	0.68	0.65
	Pt/VACNF	41.3	0.71	0.57	0.51	0.41	1.39	1.39
	PtRu/C	87.5	0.32	0.24	0.17	0.24	1.88	1.00
	PtRu/VACNF	39.4	0.87	0.79	0.39	0.73	2.23	1.08
0.1 M KOH	Pt/C	52.9	0.59	0.23	0.32	0.19	2.56	1.69
	Pt/VACNF	36.1	1.72	0.60	1.35	0.28	2.86	4.81

5.4 Conclusions

The Pt and PtRu catalysts supported on the three-dimensional graphitic carbon support was successfully prepared using ion beam sputtering of PGMs onto PECVD-grown vertically aligned carbon nanofiber arrays. The morphological analyses confirm the anchoring of PGM nanoparticles at the graphitic edges. XPS spectra of the Pt/VACNF catalysts reveal the presence of nitrogen species and oxygen functional groups in the 3D VACNF supports and the presence of strong metal-support interactions. DFT calculations reveal that the electrons are partially transferred from the carbon atoms at the graphitic edges of VACNFs to the Pt atoms while pyridinic and graphitic N-dopants near the graphitic edge of VACNFs withdraw electrons from the attached Pt atoms. The electron transfer between PGM and the edge atoms of VACNF support promotes OH binding over that of CO. As a result, the energy difference between OH_{ads} and CO_{ads} binding is reduced at the Pt catalyst deposited on the N-doped VACNF support, which makes OH more effective in the electro-oxidative removal of CO poison. This has been validated by the CO stripping analyses which exhibit additional CO stripping peaks at lower electrode potentials on the VACNF support.

Cyclic voltammetry measurements of MOR in both acidic and alkaline media further exhibit a higher J_f/J_b ratio and improved stability with N-doped VACNFs. Overall, these results provide new insights into the role of nitrogen-doped three-dimensional graphitic carbon supports in enhancing the MOR catalytic activity.

5.5 References

1. Chu, S.; Majumdar, A., Opportunities and challenges for a sustainable energy future. *Nature* **2012,** *488* (7411), 294-303.
2. An, L.; Zhao, T. S.; Li, Y. S., Carbon-neutral sustainable energy technology: Direct ethanol fuel cells. *Renew. Sust. Energ. Rev.* **2015,** *50*, 1462-1468.
3. Li, X.; Faghri, A., Review and advances of direct methanol fuel cells (DMFCs) part I: Design, fabrication, and testing with high concentration methanol solutions. *J. Power Sources* **2013,** *226*, 223-240.
4. Tiwari, J. N.; Tiwari, R. N.; Singh, G.; Kim, K. S., Recent progress in the development of anode and cathode catalysts for direct methanol fuel cells. *Nano Energy* **2013,** *2* (5), 553-578.
5. Ong, B. C.; Kamarudin, S. K.; Basri, S., Direct liquid fuel cells: A review. *Int. J. Hydrog. Energy* **2017,** *42* (15), 10142-10157.
6. Lee, E.; Kim, S.; Jang, J.-H.; Park, H.-U.; Matin, M. A.; Kim, Y.-T.; Kwon, Y.-U., Effects of particle proximity and composition of Pt–M (M = Mn, Fe, Co) nanoparticles on electrocatalysis in methanol oxidation reaction. *J. Power Sources* **2015,** *294*, 75-81.
7. Cui, X.; Zhu, Y.; Hua, Z.; Feng, J.; Liu, Z.; Chen, L.; Shi, J., SnO2 nanocrystal-decorated mesoporous ZSM-5 as a precious metal-free electrode catalyst for methanol oxidation. *Energy Environ. Sci.* **2015,** *8* (4), 1261-1266.
8. Dong, L.; Gari, R. R. S.; Li, Z.; Craig, M. M.; Hou, S., Graphene-supported platinum and platinum–ruthenium nanoparticles with high electrocatalytic activity for methanol and ethanol oxidation. *Carbon* **2010,** *48* (3), 781-787.
9. Jiang, J.; Aulich, T., High activity and durability of Pt catalyst toward methanol electrooxidation in intermediate temperature alkaline media. *J. Power Sources* **2012,** *209*, 189-194.
10. Xiong, B.; Zhou, Y.; Zhao, Y.; Wang, J.; Chen, X.; O'Hayre, R.; Shao, Z., The use of nitrogen-doped graphene supporting Pt nanoparticles as a catalyst for methanol electrocatalytic oxidation. *Carbon* **2013,** *52*, 181-192.
11. Chen, W.; Cai, J.; Yang, J.; Sartin, M. M.; Chen, Y.-X., The kinetics of methanol oxidation at a Pt film electrode, a combined mass and infrared spectroscopic study. *J. Electroanal. Chem.* **2017,** *800*, 89-98.
12. Ren, X.; Lv, Q.; Liu, L.; Liu, B.; Wang, Y.; Liu, A.; Wu, G., Current progress of Pt and Pt-based electrocatalysts used for fuel cells. *Sust. Energ. Fuels* **2020,** *4* (1), 15-30.

13. Lee, M. J.; Kang, J. S.; Kang, Y. S.; Chung, D. Y.; Shin, H.; Ahn, C.-Y.; Park, S.; Kim, M.-J.; Kim, S.; Lee, K.-S.; Sung, Y.-E., Understanding the Bifunctional Effect for Removal of CO Poisoning: Blend of a Platinum Nanocatalyst and Hydrous Ruthenium Oxide as a Model System. *ACS Catal.* **2016,** *6* (4), 2398-2407.

14. Xue, S.; Deng, W.; Yang, F.; Yang, J.; Amiinu, I. S.; He, D.; Tang, H.; Mu, S., Hexapod PtRuCu Nanocrystalline Alloy for Highly Efficient and Stable Methanol Oxidation. *ACS Catal.* **2018,** *8* (8), 7578-7584.

15. Xiao, Y.; Zhan, G.; Fu, Z.; Pan, Z.; Xiao, C.; Wu, S.; Chen, C.; Hu, G.; Wei, Z., Robust non-carbon titanium nitride nanotubes supported Pt catalyst with enhanced catalytic activity and durability for methanol oxidation reaction. *Electrochim. Acta* **2014,** *141*, 279-285.

16. Huang, H.; Wang, X., Recent progress on carbon-based support materials for electrocatalysts of direct methanol fuel cells. *J. Mater. Chem. A* **2014,** *2* (18), 6266-6291.

17. Fan, J.-J.; Fan, Y.-J.; Wang, R.-X.; Xiang, S.; Tang, H.-G.; Sun, S.-G., A novel strategy for the synthesis of sulfur-doped carbon nanotubes as a highly efficient Pt catalyst support toward the methanol oxidation reaction. *J. Mater. Chem. A* **2017,** *5* (36), 19467-19475.

18. Merati, Z.; Basiri Parsa, J., Enhancement of the catalytic activity of Pt nanoparticles toward methanol electro-oxidation using doped-SnO2 supporting materials. *Appl. Surf. Sci.* **2018,** *435*, 535-542.

19. Shao, Y.; Sui, J.; Yin, G.; Gao, Y., Nitrogen-doped carbon nanostructures and their composites as catalytic materials for proton exchange membrane fuel cell. *Appl. Catal. B* **2008,** *79* (1), 89-99.

20. Zhang, Y.; Liu, Y.; Liu, W.; Li, X.; Mao, L., Synthesis of honeycomb-like mesoporous nitrogen-doped carbon nanospheres as Pt catalyst supports for methanol oxidation in alkaline media. *Appl. Surf. Sci.* **2017,** *407*, 64-71.

21. Yokoyama, K.; Sato, Y.; Hirano, K.; Ohta, H.; Motomiya, K.; Tohji, K.; Sato, Y., Defluorination-assisted nanotube-substitution reaction with ammonia gas for synthesis of nitrogen-doped single-walled carbon nanotubes. *Carbon* **2015,** *94*, 1052-1060.

22. Kundu, S.; Xia, W.; Busser, W.; Becker, M.; Schmidt, D. A.; Havenith, M.; Muhler, M., The formation of nitrogen-containing functional groups on carbon nanotube surfaces: a quantitative XPS and TPD study. *Phys. Chem. Chem. Phys.* **2010,** *12* (17), 4351-4359.

23. Ma, J.-h.; Wang, L.; Mu, X.; Li, L., Nitrogen-doped graphene supported Pt nanoparticles with enhanced performance for methanol oxidation. *Int. J. Hydrog. Energy* **2015,** *40* (6), 2641-2647.

24. Liang, L.; Xiao, M.; Zhu, J.; Ge, J.; Liu, C.; Xing, W., Low-temperature synthesis of nitrogen doped carbon nanotubes as promising catalyst support for methanol oxidation. *J. Energy Chem.* **2019,** *28*, 118-122.

25. Ding, J.; Ma, L.; Gan, M.; Zhan, W.; Zhou, C.; Wei, D.; Han, S.; Shen, J.; Xie, F.; Zhong, X., Facile fabrication of ultrafine Pt nanoparticles supported on 3D macro-/oversized mesoporous N-doped carbon for efficient methanol oxidation. *Int. J. Hydrog. Energy* **2019,** *44* (57), 30388-30400.

26. Melechko, A. V.; Merkulov, V. I.; McKnight, T. E.; Guillorn, M. A.; Klein, K. L.; Lowndes, D. H.; Simpson, M. L., Vertically aligned carbon nanofibers and related structures: Controlled synthesis and directed assembly. *J. Appl. Phys.* **2005,** *97* (4), 041301.
27. Elangovan, A.; Xu, J.; Brown, E.; Liu, B.; Li, J., Fundamental Electrochemical Insights of Vertically Aligned Carbon Nanofiber Architecture as a Catalyst Support for ORR. *J. Electrochem. Soc.* **2020,** *167* (6), 066523.
28. Kresse, G.; Furthmüller, J., Efficient iterative schemes for ab initio total-energy calculations using a plane-wave basis set. *Phys. Rev. B* **1996,** *54* (16), 11169-11186.
29. Perdew, J. P.; Burke, K.; Ernzerhof, M., Generalized Gradient Approximation Made Simple. *Phys. Rev. Lett.* **1996,** *77* (18), 3865-3868.
30. Blöchl, P. E., Projector augmented-wave method. *Phys. Rev. B* **1994,** *50* (24), 17953-17979.
31. Monkhorst, H. J.; Pack, J. D., Special points for Brillouin-zone integrations. *Phys. Rev. B* **1976,** *13* (12), 5188-5192.
32. Yu, M.; Trinkle, D. R., Accurate and efficient algorithm for Bader charge integration. *J. Chem. Phys.* **2011,** *134* (6), 064111.
33. Meng, Y.; Yin, C.; Li, K.; Tang, H.; Wang, Y.; Wu, Z., Improved Oxygen Reduction Activity in Heteronuclear FeCo-Codoped Graphene: A Theoretical Study. *ACS Sustainable Chem. Eng.* **2019,** *7* (20), 17273-17281.
34. Shan, N.; Zhou, M.; Hanchett, M. K.; Chen, J.; Liu, B., Practical principles of density functional theory for catalytic reaction simulations on metal surfaces – from theory to applications. *Mol. Simul.* **2017,** *43* (10-11), 861-885.
35. Krasovskii, P. V.; Malinovskaya, O. S.; Samokhin, A. V.; Blagoveshchenskiy, Y. V.; Kazakov, V. A.; Ashmarin, A. A., XPS study of surface chemistry of tungsten carbides nanopowders produced through DC thermal plasma/hydrogen annealing process. *Appl. Surf. Sci.* **2015,** *339*, 46-54.
36. Ganguly, A.; Sharma, S.; Papakonstantinou, P.; Hamilton, J., Probing the Thermal Deoxygenation of Graphene Oxide Using High-Resolution In Situ X-ray-Based Spectroscopies. *J. Phys. Chem.C* **2011,** *115* (34), 17009-17019.
37. Zhang, L.; Wang, X.; Wang, R.; Hong, M., Structural Evolution from Metal–Organic Framework to Hybrids of Nitrogen-Doped Porous Carbon and Carbon Nanotubes for Enhanced Oxygen Reduction Activity. *Chem. Mater.* **2015,** *27* (22), 7610-7618.
38. Furlan, A.; Lu, J.; Hultman, L.; Jansson, U.; Magnuson, M., Crystallization characteristics and chemical bonding properties of nickel carbide thin film nanocomposites. *J. Condens. Matter Phys.* **2014,** *26* (41), 415501.
39. Zhao, M.; Cao, Y.; Liu, X.; Deng, J.; Li, D.; Gu, H., Effect of nitrogen atomic percentage on N+-bombarded MWCNTs in cytocompatibility and hemocompatibility. *Nanoscale Res. Lett.* **2014,** *9* (1), 142.
40. Bang, G. S.; Shim, G. W.; Shin, G. H.; Jung, D. Y.; Park, H.; Hong, W. G.; Choi, J.; Lee, J.; Choi, S.-Y., Pyridinic-N-Doped Graphene Paper from Perforated Graphene Oxide for Efficient Oxygen Reduction. *ACS Omega* **2018,** *3* (5), 5522-5530.

41. Wang, Y.; He, Q.; Guo, J.; Wei, H.; Ding, K.; Lin, H.; Bhana, S.; Huang, X.; Luo, Z.; Shen, T. D.; Wei, S.; Guo, Z., Carboxyl Multiwalled Carbon-Nanotube-Stabilized Palladium Nanocatalysts toward Improved Methanol Oxidation Reaction. *ChemElectroChem* **2015,** *2* (4), 559-570.

42. Wu, J.; Ma, S.; Sun, J.; Gold, J. I.; Tiwary, C.; Kim, B.; Zhu, L.; Chopra, N.; Odeh, I. N.; Vajtai, R.; Yu, A. Z.; Luo, R.; Lou, J.; Ding, G.; Kenis, P. J. A.; Ajayan, P. M., A metal-free electrocatalyst for carbon dioxide reduction to multi-carbon hydrocarbons and oxygenates. *Nature Commun.* **2016,** *7* (1), 13869.

43. Ma, J.; Habrioux, A.; Luo, Y.; Ramos-Sanchez, G.; Calvillo, L.; Granozzi, G.; Balbuena, P. B.; Alonso-Vante, N., Electronic interaction between platinum nanoparticles and nitrogen-doped reduced graphene oxide: effect on the oxygen reduction reaction. *J. Mater. Chem. A* **2015,** *3* (22), 11891-11904.

44. Peera, S. G.; Arunchander, A.; Sahu, A. K., Platinum nanoparticles supported on nitrogen and fluorine co-doped graphite nanofibers as an excellent and durable oxygen reduction catalyst for polymer electrolyte fuel cells. *Carbon* **2016,** *107*, 667-679.

45. Lei, Z.; An, L.; Dang, L.; Zhao, M.; Shi, J.; Bai, S.; Cao, Y., Highly dispersed platinum supported on nitrogen-containing ordered mesoporous carbon for methanol electrochemical oxidation. *Micropor. Mesopor. Mat.* **2009,** *119* (1), 30-38.

46. Wang, D.; Lu, S.; Xiang, Y.; Jiang, S. P., Self-assembly of HPW on Pt/C nanoparticles with enhanced electrocatalysis activity for fuel cell applications. *Appl. Catal. B* **2011,** *103* (3), 311-317.

47. Chang, J.; Feng, L.; Liu, C.; Xing, W.; Hu, X., Ni2P enhances the activity and durability of the Pt anode catalyst in direct methanol fuel cells. *Energy Environ. Sci.* **2014,** *7* (5), 1628-1632.

48. Matin, M. A.; Lee, E.; Kim, H.; Yoon, W.-S.; Kwon, Y.-U., Rational syntheses of core–shell Fe@(PtRu) nanoparticle electrocatalysts for the methanol oxidation reaction with complete suppression of CO-poisoning and highly enhanced activity. *J. Mater. Chem. A* **2015,** *3* (33), 17154-17164.

49. Zhou, Y.; Neyerlin, K.; Olson, T. S.; Pylypenko, S.; Bult, J.; Dinh, H. N.; Gennett, T.; Shao, Z.; O'Hayre, R., Enhancement of Pt and Pt-alloy fuel cell catalyst activity and durability via nitrogen-modified carbon supports. *Energy Environ. Sci.* **2010,** *3* (10), 1437-1446.

50. Pylypenko, S.; Queen, A.; Olson, T. S.; Dameron, A.; O'Neill, K.; Neyerlin, K. C.; Pivovar, B.; Dinh, H. N.; Ginley, D. S.; Gennett, T.; O'Hayre, R., Tuning Carbon-Based Fuel Cell Catalyst Support Structures via Nitrogen Functionalization. I. Investigation of Structural and Compositional Modification of Highly Oriented Pyrolytic Graphite Model Catalyst Supports as a Function of Nitrogen Implantation Dose. *J. Phys. Chem. C* **2011,** *115* (28), 13667-13675.

51. Xu, H.; Ding, L.-X.; Liang, C.-L.; Tong, Y.-X.; Li, G.-R., High-performance polypyrrole functionalized PtPd electrocatalysts based on PtPd/PPy/PtPd three-layered nanotube arrays for the electrooxidation of small organic molecules. *NPG Asia Mater.* **2013,** *5* (11), e69-e69.

52. Huang, H.; Yang, S.; Vajtai, R.; Wang, X.; Ajayan, P. M., Pt-Decorated 3D Architectures Built from Graphene and Graphitic Carbon Nitride Nanosheets as Efficient Methanol Oxidation Catalysts. *Adv. Mater.* **2014,** *26* (30), 5160-5165.

53. Poh, C. K.; Tian, Z.; Gao, J.; Liu, Z.; Lin, J.; Feng, Y. P.; Su, F., Nanostructured trimetallic Pt/FeRuC, Pt/NiRuC, and Pt/CoRuC catalysts for methanol electrooxidation. *J. Mater. Chem.* **2012,** *22* (27), 13643-13652.

54. Zheng, J.; Cullen, D. A.; Forest, R. V.; Wittkopf, J. A.; Zhuang, Z.; Sheng, W.; Chen, J. G.; Yan, Y., Platinum–Ruthenium Nanotubes and Platinum–Ruthenium Coated Copper Nanowires As Efficient Catalysts for Electro-Oxidation of Methanol. *ACS Catal.* **2015,** *5* (3), 1468-1474.

55. Demiroglu, I.; Yao, K.; Hussein, H. A.; Johnston, R. L., DFT Global Optimization of Gas-Phase Subnanometer Ru–Pt Clusters. *J. Phys. Chem. C* **2017,** *121* (20), 10773-10780.

56. Hammer, B.; Morikawa, Y.; Nørskov, J. K., CO Chemisorption at Metal Surfaces and Overlayers. *Phys. Rev. Lett.* **1996,** *76* (12), 2141-2144.

57. Hammer, B.; Nørskov, J. K., Theoretical surface science and catalysis—calculations and concepts. In *Adv. Catal.*, Academic Press: 2000; Vol. 45, pp 71-129.

58. Koper, M. T. M.; Shubina, T. E.; van Santen, R. A., Periodic Density Functional Study of CO and OH Adsorption on Pt−Ru Alloy Surfaces: Implications for CO Tolerant Fuel Cell Catalysts. *J. Phys. Chem. B* **2002,** *106* (3), 686-692.

59. Xu, J.; Liu, B., Intrinsic properties of nitrogen-rich carbon nitride for oxygen reduction reaction. *Appl. Surf. Sci.* **2020,** *500*, 144020.

60. Kim, S. H.; Nam, S.-W.; Lim, T.-H.; Lee, H.-I., Effect of pretreatment on the activity of Ni catalyst for CO removal reaction by water–gas shift and methanation. *Appl. Catal. B* **2008,** *81* (1), 97-104.

61. Ma, J.; Habrioux, A.; Morais, C.; Lewera, A.; Vogel, W.; Verde-Gómez, Y.; Ramos-Sanchez, G.; Balbuena, P. B.; Alonso-Vante, N., Spectroelectrochemical Probing of the Strong Interaction between Platinum Nanoparticles and Graphitic Domains of Carbon. *ACS Catal.* **2013,** *3* (9), 1940-1950.

62. Zhao, X.; Yin, M.; Ma, L.; Liang, L.; Liu, C.; Liao, J.; Lu, T.; Xing, W., Recent advances in catalysts for direct methanol fuel cells. *Energy Environ. Sci.* **2011,** *4* (8), 2736-2753.

63. Rheinländer, P. J.; Herranz, J.; Durst, J.; Gasteiger, H. A., Kinetics of the Hydrogen Oxidation/Evolution Reaction on Polycrystalline Platinum in Alkaline Electrolyte Reaction Order with Respect to Hydrogen Pressure. *J. Electrochem. Soc.* **2014,** *161* (14), F1448-F1457.

64. Wang, Y.; Wang, G.; Li, G.; Huang, B.; Pan, J.; Liu, Q.; Han, J.; Xiao, L.; Lu, J.; Zhuang, L., Pt–Ru catalyzed hydrogen oxidation in alkaline media: oxophilic effect or electronic effect? *Energy Environ. Sci.* **2015,** *8* (1), 177-181.

65. Scofield, M. E.; Zhou, Y.; Yue, S.; Wang, L.; Su, D.; Tong, X.; Vukmirovic, M. B.; Adzic, R. R.; Wong, S. S., Role of Chemical Composition in the Enhanced Catalytic Activity of Pt-Based Alloyed Ultrathin Nanowires for the Hydrogen Oxidation Reaction under Alkaline Conditions. *ACS Catal.* **2016,** *6* (6), 3895-3908.

66. Mancharan, R.; Goodenough, J. B., Methanol oxidation in acid on ordered NiTi. *J. Mater. Chem. A* **1992,** *2* (8), 875-887.

67. Liang, Y.; Wei, J.; Zhang, X.; Zhang, J.; Jiang, S. P.; Wang, H., Synthesis of Nitrogen-Doped Porous Carbon Nanocubes as a Catalyst Support for Methanol Oxidation. *ChemCatChem* **2016,** *8* (11), 1901-1904.

68. Hofstead-Duffy, A. M.; Chen, D.-J.; Sun, S.-G.; Tong, Y. J., Origin of the current peak of negative scan in the cyclic voltammetry of methanol electro-oxidation on Pt-based electrocatalysts: a revisit to the current ratio criterion. *J. Mater. Chem.* **2012,** *22* (11), 5205-5208.

69. Chung, D. Y.; Lee, K.-J.; Sung, Y.-E., Methanol Electro-Oxidation on the Pt Surface: Revisiting the Cyclic Voltammetry Interpretation. *J. Phys. Chem. C* **2016,** *120* (17), 9028-9035.

70. Zhao, Y.; Nakamura, R.; Kamiya, K.; Nakanishi, S.; Hashimoto, K., Nitrogen-doped carbon nanomaterials as non-metal electrocatalysts for water oxidation. *Nature Commun.* **2013,** *4* (1), 2390.

71. Mu, X.; Xu, Z.; Ma, Y.; Xie, Y.; Mi, H.; Ma, J., Graphene-carbon nanofiber hybrid supported Pt nanoparticles with enhanced catalytic performance for methanol oxidation and oxygen reduction. *Electrochim. Acta* **2017,** *253*, 171-177.

72. Tripković, A. V.; Popović, K. D.; Lović, J. D.; Jovanović, V. M.; Kowal, A., Methanol oxidation at platinum electrodes in alkaline solution: comparison between supported catalysts and model systems. *J. Electroanal. Chem.* **2004,** *572* (1), 119-128.

Chapter 6 - Current and Future Work

6.1 Hybrid g-C_3N_4/NCNTs as a Potential Catalyst for Oxygen Reduction Reaction

As mentioned in Chapter 5, nitrogen species plays an important role in catalyzing the oxygen reduction reaction (ORR). Here, we will be exploring carbon nitride (g-C_3N_4) containing abundant nitrogen moieties with a graphitic sheet-like structure as a potential catalyst for ORR. The g-C_3N_4 has both graphite-like and pyridine-like nitrogen atoms and every carbon atom in the structure is bonded to three nitrogen atoms. g-C_3N_4 has drawn significant attention as a catalyst material for photocatalysis and organic catalysis due to its low cost, tailorable structure, rich surface properties, easy preparation, and high thermal and chemical stability[1]. In spite of numerous advantages g-C_3N_4 by itself cannot be used as a catalyst for ORR due to its poor electrical conductivity ($< 10^{-2}$ S cm^{-1}). The poor electron transfer characteristics of g-C_3N_4 can be improved by using incorporating highly conductive carbon materials. Previous reports have incorporated graphene[2] and nanoporous carbon (CMK-3)[3] with the g-C_3N_4 framework and explored it for ORR. However, the g-C_3N_4 @graphene catalysts catalyzed oxygen using a less effective 2-e^- pathway. We wanted to explore the role of other sp^2 hybridized carbon frameworks such as N-doped carbon nanotubes (N-CNTs) in improving the performance of g-C_3N_4 for ORR.

g-C_3N_4 was synthesized by mixing the required amount of precursor, melamine in 100 ml hot distilled water followed by drying the solution at 100 ^oC for 12 h. After that, the remaining solid powder was calcined in a muffle furnace at 550 ^oC in the air for 2 h to get the final product, which is in yellow color. The N-doped carbon nanotubes were prepared by chemical vapor deposition of aniline over FeMo/Al_2O_3 catalyst as mentioned in the literature[4]. The synthesized N-CNTs was pretreated to remove any impurities or amorphous carbon present in the sample. Briefly, obtained N-CNTs were washed several times in acetone until the extract becomes colorless. Then 6g NCNTs were mixed in 250 ml of 9M HCl solution and left under stirring for 6 h followed by filtrating the solid. At last, the acid treated NCNTs was annealed in nitrogen for 2 h at 400°C. Figure D.1 shows the prepared N-CNTs have a bamboo-like structure with a diameter varying from 20 to 50 nm. The high-resolution N 1s XPS spectra given in Figure D.2 confirms the % nitrogen in both g-C_3N_4 and N-CNTs. The total % of the nitrogen in g-C_3N_4 and N-CNTs is found to be 53.6 and 1.7%, respectively. The high-resolution N1s spectra further confirm that g-C_3N_4 is mostly dominated by pyridinic N. Before testing the activity of g-C_3N_4 with NCNTs, we mixed it with other carbon supports such as carbon black, graphene, and multi-walled carbon nanotubes (MWCNTs).

The catalyst activity was evaluated using a three-electrode system with coiled Pt wire as the counter electrode and Hg/HgO (1.0 M NaOH) as the reference electrode. The working electrode was prepared by drop-casting 5 μL of the catalyst ink on RDE. The ink solution was formed by mixing the required amount of catalyst powder in a mixture of water, ethanol, and 5 wt% Nafion. Figure D.3a shows the CV data recorded for different catalysts in O_2-saturated 0.10 M KOH solution at a scan rate of 50 mV/s. Among all the catalysts, pure g-C_3N_4 (with a loading of 1.2 mg/cm^2) has the lowest oxygen reduction potential (~ -0.522 V vs. Hg/HgO) due to its poor electron transfer capability. As it is coupled with carbon supports in a 70:30 ratio, the oxygen reduction activity increased in the order of carbon black<graphene<MWCNTs<NCNTs. For all the mixed catalysts, the g-C_3N_4 loading was kept constant (~300 µg/cm^2). Figure D.3b shows the LSV data recorded at 1600 rpm for all these catalysts and at a potential of -0.80 V (vs. Hg/HgO), the g-C_3N_4 + NCNTs have a current density of -2.82 mA/cm^2, which is 2.66, 3.09, 6.3, and 6.3 times greater than g-C_3N_4, g-C_3N_4 + Carbon Black, g-C_3N_4 + Graphene, and g-C_3N_4 + MWCNTs,

respectively. Apart from the higher limiting current density, the g-C_3N_4 + NCNTs mixture has a higher onset potential of about ~0.129 V vs. Hg/HgO when compared with other catalysts. However, the measured activity is lower than other reported catalysts in alkaline medium. So, to improve the catalytic activity of g-C_3N_4 + NCNTs the mixture was annealed in N_2 for 2 h at different temperatures (450 ^oC, 500 ^oC, and 550 ^oC).

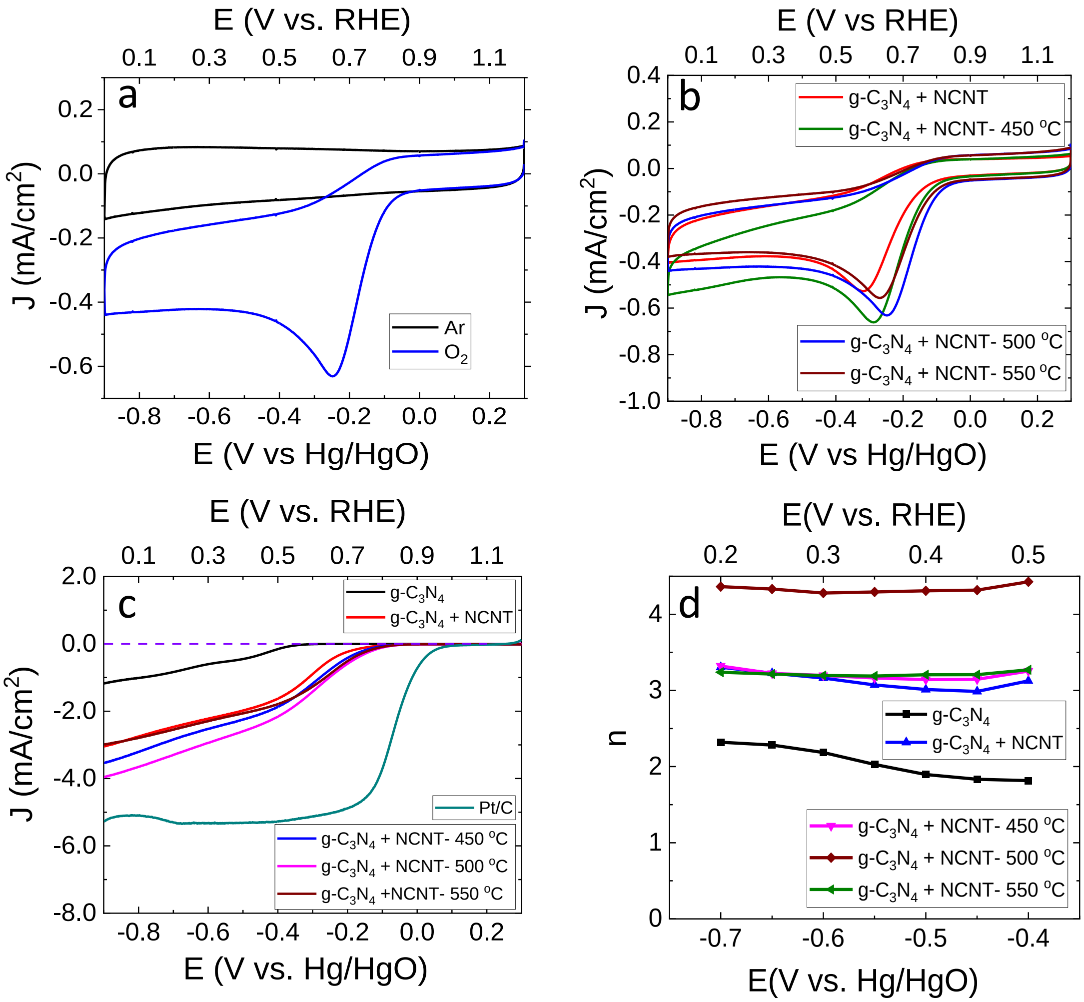

Figure 6.1: (a) CV curve for g-C_3N_4+NCNT- 500 ^oC recorded in Ar-saturated (black line) and O_2-saturated (blue line) 0.10 M KOH solution at a scan rate of 50 mV/s; CV curves for g-C_3N_4+NCNT, g-C_3N_4+NCNT- 450 ^oC, g-C_3N_4+NCNT- 500 ^oC, and g-C_3N_4+NCNT- 550 ^oC 500 ^oC recorded in O_2-saturated 0.10 M KOH solution at a scan rate of 50 mV/s; (c) LSV curves recorded at a scan rate of 10 mV/s and a rotation speed of 1,600 rpm in O_2-saturated 0.10 M KOH solution and (d) plot of E vs n number derived from KL plots for g-C_3N_4, g-C_3N_4+NCNT, g-C_3N_4+NCNT- 450 ^oC, g-C_3N_4+NCNT-500 ^oC, g-C_3N_4+NCNT- 550 ^oC, NCNT, and Pt/C. The purple dash line marks the zero current density.

Figure 6.1a displays the CV curve recorded in Ar- saturated (black line) and O_2-saturated (blue line) 0.10 M KOH solution for g-C_3N_4 + NCNTs- 550 ^oC. As it is seen, the catalyst exhibited no activity in the absence of O_2 and it possesses a reduction peak at ~ -0.522 V vs. Hg/HgO confirming the ORR characteristics in the presence of O_2. Figure 6.1b shows the CV curves recorded in O_2-saturated electrolyte for all the catalysts and the annealing of the catalyst improved the catalytic activity and the activity increases with annealing temperature until 500 ^oC and decreases after 500 ^oC, which can be due to the decomposition of g-C_3N_4. The LSV data recorded at 1600 rpm presented in Figure 6.1c further confirms the higher catalytic activity of g-C_3N_4 + NCNTs- 550 ^oC among all the other catalysts based on g-C_3N_4 with regard to the limiting current density of -3.7 mA/cm^2 and an onset potential of -0.094 V (vs. Hg/HgO). However, the activity is relatively low when compared to the commercial catalyst Pt/C.

Figure D.4 presents the RDE polarization curves (after background correction) recorded from 0.20 to -0.70 V (vs. Hg/HgO) at a series of rotation speed from 500 to 3000 rpm for pure g-C_3N_4, g-C_3N_4+NCNTs, g-C_3N_4+NCNTs-450 ^oC, g-C_3N_4+NCNTs-500 ^oC, and g-C_3N_4+NCNTs-550 ^oC, respectively. The current density increases with the rotation speed as the oxygen flux increases at a higher rotation speed. The KL plot was constructed using the RDE LSV curves recorded at different rpm as shown in Figure D.5. The KL plot at potentials between -0.40 to -0.70 V yields almost parallel lines indicating the first-order kinetics for the ORR. The electron transfer number calculated from the KL plots for pure g-C_3N_4, g-C_3N_4+NCNTs, g-C_3N_4+NCNTs-450 ^oC, g-C_3N_4+NCNTs-500 ^oC, and g-C_3N_4+NCNTs-550 ^oC are between 1.8 to 2.3, 3.1-3.3, 3.2-3.3, 4.3-4.4, and 3.2-3.3, respectively. The increase in n value for the hybrid catalysts confirmed that the addition of NCNTs increased the electrocatalytic activity of the catalyst and catalyzed oxygen reduction through a more efficient 4-e^- pathway. The obtained n value is highest for g-

C_3N_4+NCNTs-500 °C, which validates the higher activity noticed in the CV and LSV data. However, the calculated n value from RDE data is greater than 4 and this can be due to any experimental errors. To confirm that indeed the n value was 4, we further evaluated the activity of g-C_3N_4+NCNTs-500 °C using RRDE analysis.

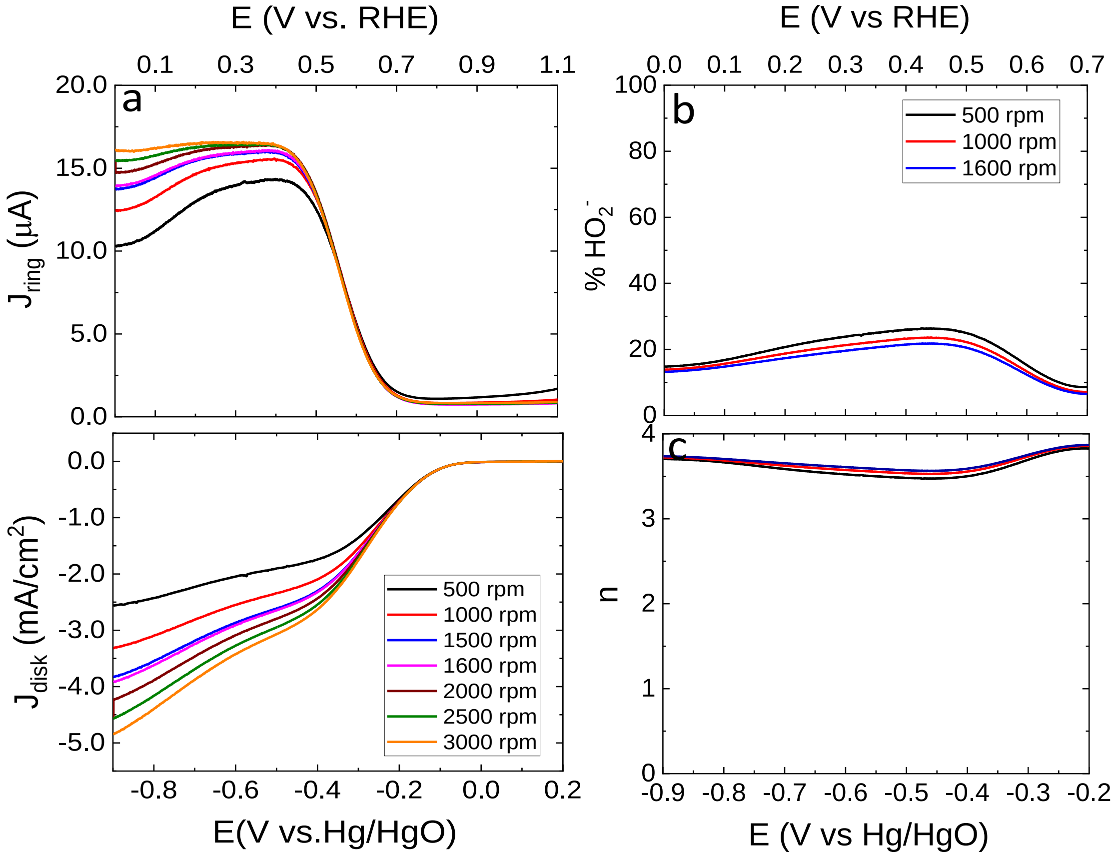

Figure 6.2: (a) RRDE voltammogram of g-C_3N_4+NCNT- 500 °C in O_2-saturated 0.10 M KOH solution recorded at a scan rate of 10 mV/s with different rotation speed from 500 to 3000 rpm. The Ring electrode was kept at a constant potential of 0.30 V (vs Hg/HgO); (b) The percentage of HO_2^- produced and (c) the electron transfer number for g-C_3N_4+NCNT- 500 °C at different rpm.

Figure 6.2 presents the RRDE voltammogram recorded for g-C_3N_4+NCNTs-500 °C in O_2-saturated 0.10 M KOH solution at different rotation speed from 0.20 V to -0.80 V (vs. Hg/HgO). The ring electrode was kept at a constant potential of 0.30 V (vs. Hg/HgO) to record the %HO_2^-

produced by the catalyst. As shown in Figure 6.2c, the overall HO_2^- produced is less than 20% at different rotation speeds. The results from the RRDE analysis confirms that the majority of the reduced O_2 forms OH^-. Figure 6.2c further confirms that the g-C_3N_4+NCNTs-500 ^oC catalyze reduction reaction through a 4-e^- pathway with n = 3.8. The %HO_2^- and n value is calculated using the formula mentioned in Chapter 2.

As mentioned in the previous Chapters, the catalysts catalyzing the cathode reaction (ORR) of fuel cells are susceptible to the oxidation of fuel molecules such as methanol that gets crossover from the anode compartment. This can cause the performance of the ORR catalyst to decrease and hence we want to design catalysts that are not susceptible to the fuel crossover. We tested the methanol tolerance capability of the best performing g-C_3N_4+NCNTs-500 ^oC catalyst using amperometric i-t curve measurement at -0.30 V (vs. Hg/HgO) at a rotation speed of 1600 rpm. The current density was recorded for an initial 300 s, and after that 3 M MeOH was added in a step of 4 ml for every 200 sec to make a final concentration of 0.75 M MeOH. At the end of 1500 s, the g-C_3N_4+NCNTs-500 ^oC lost only about 18% of the initial current density whereas the Pt catalyst lost almost 45% of the current density.

As shown in Figures 6.3b and 6.3c, the g-C_3N_4+NCNTs-500 ^oC showed almost no change in the LSV curve, but in contrast, the Pt/C LSV curve has a huge difference in the presence and absence of methanol. In addition to that, as presented in Figures 6.3d and c, the CV curves recorded in the presence and absence of MeOH for g-C_3N_4+NCNTs-500 ^oC showed almost no difference and the Pt/C catalyst preferred methanol oxidation over oxygen reduction when the MeOH is present in the electrolyte. This shows that the prepared g-C_3N_4+NCNTs-500 ^oC is immune to the methanol oxidation and catalyze oxygen reduction in a mixed environment of oxygen and methanol. Overall, this study evaluates the impact of NCNTs in boosting the catalytic activity of g-C_3N_4 and the heat-treatment temperature in improving the activity of g-C_3N_4+NCNTs hybrid catalyst. In spite of following a 4-e^- pathway and showing good tolerance to methanol crossover, the intrinsic catalytic activity of the synthesized g-C_3N_4+NCNTs-500 °C is still not close to the commercial Pt/C in alkaline medium. In the future, we will try to incorporate transition metals (M=Fe, Ni, Co, Mn, etc.) into the abundant nitrogen moieties present in the g-C_3N_4 catalyst to form potential M-N-C sites that can act as the active sites for catalyzing the ORR.

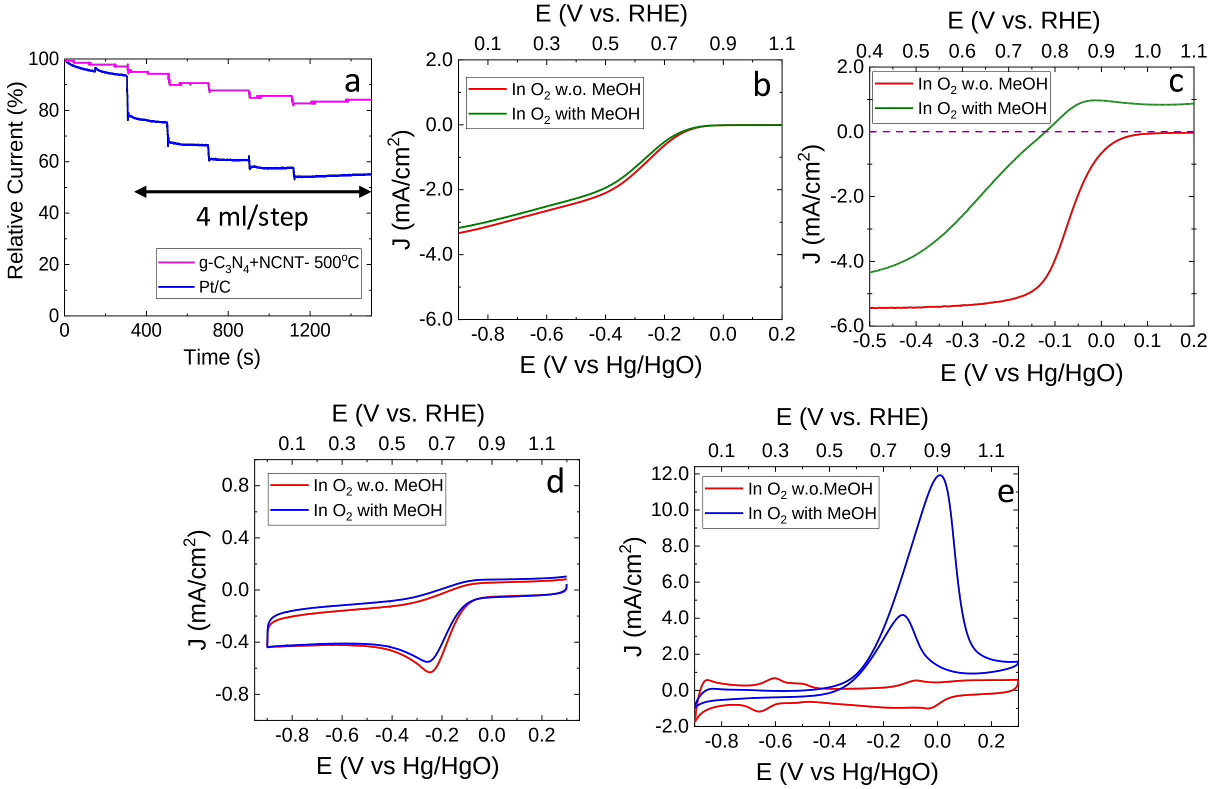

Figure 6.3: (a) Relative current (%) for g-C_3N_4+NCNT- 500 °C and Pt/C derived from amperometric i-t curve recorded at 1,600 rpm in O_2-saturated 0.10 M KOH solution with successive addition of 3.0 M methanol (4 ml for every 200 s) to give the final concentration of 0.75 M at the potential of -0.30 V; LSV curves recorded at a scan rate of 10 mV/s and 1600 rpm in O_2-saturated 0.10 M KOH with and without adding 0.75 M methanol for (b) g-C_3N_4+NCNT- 500 °C and (c) Pt/C; CV curves recorded at a scan rate of 50 mV/s in O_2-saturated 0.10 M KOH with and without adding 0.75 M methanol for (d) g-C_3N_4+NCNT- 500 °C and (e) Pt/C.

6.2 3D Printed MoS_2-rGO for Electrocatalysis of Oxygen Reduction

MoS_2 is a 2D layered material that is similar to graphene and contains edge sites that are preferred for chemisorption of O_2 or H_2 and hence find its application in the electrocatalysis of oxygen reduction and hydrogen evolution[5]. MoS_2 has a high surface area owing to its layered structure and because of the same, they tend to stack together which results in the blocking of active edge sites. Apart from this they also have poor electrical conductivity. These problems can be addressed by combining MoS_2 with carbon materials which can improve the conductivity of MoS_2 and preventing it from stacking[6]. Among different carbon materials, reduced graphene oxide (rGO) is more promising due to its structural and morphological compatibility with rGO, high electrical conductivity, and high mechanical stability.

In collaboration with Dr. Dong Lin of the Department of Mechanical Engineering, the 3D printed MoS_2-rGO was evaluated for the oxygen reduction electrocatalysis. Briefly, a 3D drop-on-demand (DOD) inkjet printing and freeze casting procedure was used[7]. A mixture of ammonium thiomolybdate (ATM) and graphene oxide (GO) was used as the precursor to obtain the 3D printed ATM-GO. The obtained ATM-rGO precursor was annealed at high temperature in 3% H_2/97% Ar mixture to covert the ATM precursor to MoS_2. We annealed the ATM-rGO mixture at two different temperatures 450 °C and 600 °C and evaluated its ORR activity.

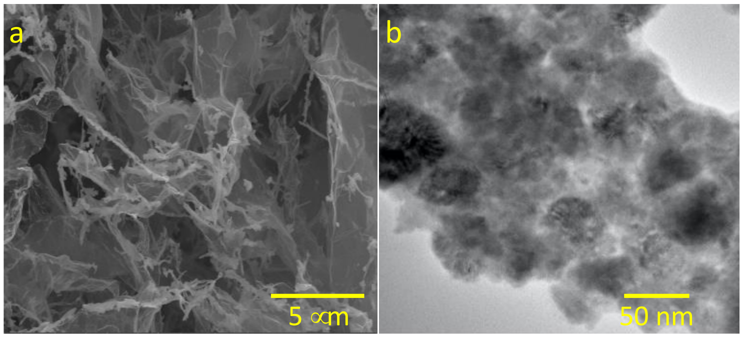

Figure 6.4: (a) SEM and (B) TEM image of MoS_2-rGO@450 °C.

The SEM image in Figure 6.4a illustrates the presence of micron-sized pores present on the wrinkled rGO flakes. The TEM image in Figure 6.4b shows that the thin rGO flakes consist of 10-50 nm diameter darker MoS_2 patches. From TGA analysis, it is found that the 3D printed MoS_2-rGO has around 82% of MoS_2 and 18% of rGO. The electrochemical activity of the material was tested using a three-electrode system with coiled Pt wire as the counter electrode and Hg/HgO (1.0 M NaOH) as the reference electrode. The working electrode was prepared by drop-casting 4 μl of the catalyst ink on RDE. The catalyst ink was prepared by dispersing the 5.0 mg of MoS_2-rGO in water and 5 wt% Nafion mixture to yield a MoS_2 loading of 250 μg/cm^2. The electrocatalytic activity was evaluated using CV and LSV.

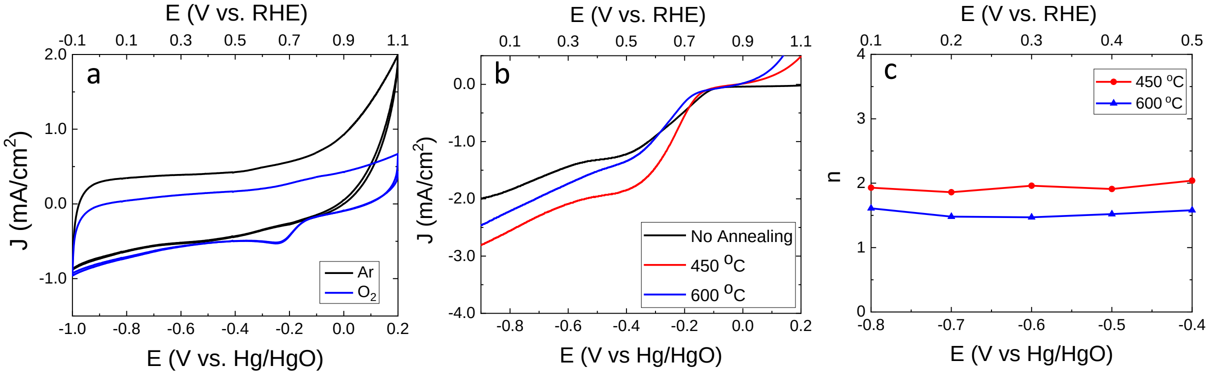

Figure 6.5: (a) CV curves curve for MoS_2-rGO annealed at 450 °C recorded in Ar-saturated (black line) and O_2-saturated (blue line) 0.10 M KOH solution at a scan rate of 50 mV/s; (b) LSV curves of MoS_2-rGO without annealing, annealed at 450 °C, and annealed at 600°C recorded at a scan rate of 10 mV/s and a rotation speed of 1,500 rpm in O_2-saturated 0.10 M KOH solution; (c) Koutecky-Levich plots at a potential of -0.60 V (vs Hg/HgO) for all the catalysts.

Figure 6.5a displays the CV curve recorded in Ar-saturated (black line) and O_2-saturated (blue line) for MoS_2–rGO annealed at 450 °C. It can be seen that in the presence of O_2, the catalyst shows a small reduction peak at -0.210 V (vs. Hg/HgO) owing to the oxygen reduction. The difference in the catalytic activity between the MoS_2-rGO catalyst with and without annealing can be revealed by the LSV curves recorded at 1500 rpm in Figure 6.5b. MoS_2-rGO catalyst annealed at 450°C shows a more positive onset potential (-0.120 V vs. Hg/HgO) and higher limiting current density (-2.6 mA/cm^2) when compared to the one annealed at 600°C and without annealing. As the MoS_2-rGO is annealed the onset potential shifted to more positive with a corresponding increase in current density. The RDE polarization curves were recorded from 500 to 3000 rpm for the MoS_2-rGO without annealing, annealed at 450 °C, and annealed at 600 °C as presented in Figures D.6a-c. The current density increases with the rotation speed in the diffusion-controlled region. Figure D.6d-f shows the KL plot derived from the RDE data for all these catalysts at a potential between -0.40 V to -0.80 V. The parallel lines between different potentials in the KL plot confirms that the ORR reaction follows first-order kinetics and further the n value is calculated for the catalyst annealed at 450 °C and 600 °C. The plot of n vs. potential displayed in Figure 6.5c gives more information about the reaction pathway. MoS_2-rGO annealed at 450 °C and 600 °C possess n = 2.04 and n= ~1.60, respectively. This confirms that the MoS_2-rGO catalyzes ORR through a less effective 2-e$^-$ pathway. Overall the lower activity exhibited by the MoS_2-rGO catalyst could be due to the pH of the electrolyte employed as MoS_2 is not very active in alkaline medium. In the future, we will try to investigate the catalytic activity of 3D printed MoS_2-rGO in acidic medium for ORR and also for HER.

6.3 Catalytic Performance of Pyrolyzed Fe/N-CNF for Oxygen Reduction Reaction

Owing to the high cost of Pt, researchers are exploring alternative ORR catalysts that are completely free from precious metal. Among different candidates, transition metal-nitrogen-carbon catalysts (M-N-C with M = Fe, Co, Mn, and Ni) have attracted huge attention owing to its strong binding with O_2, sufficient active sites to promote ORR kinetics, facile preparation, and their high tolerance to oxidation of fuel[8]. The Fe-N-C catalysts have been regarded as the effective ORR catalysts in the alkaline medium because of its high activity, overall stability, and catalyzing ORR through a 4-e^- pathway[8, 9]. The majority of the previous studies on the Fe-N-C based catalysts employed amorphous carbon alongside nitrogen and metal precursor. We wanted to explore the role of graphitic carbon in creating these Fe-N-C active sites for ORR.

Initially, to prepare the Fe-N/CNF catalyst we employed CNF with a diameter of 20-150 nm containing conical platelets purchased from Sigma Aldrich and adopted a previously reported synthesis procedure using polyaniline and iron chloride[10]. Briefly, 0.4 g CNF was mixed with 2 ml aniline in 100 ml of 0.50 M HCl solution. The mixture was left under stirring for 30 min and then, 1.7 g of ammonium persulfate (APS) in a 4:1 monomer to oxidant ratio mixed in 30 ml of 0.50 M HCl was added dropwise to the mixture to polymerize the aniline and along with this 0.15 g $FeCl_3$ was also added. The addition of APS and $FeCl_3$ happened while maintaining the temperature at 10 ^oC. The solution was left for 24 hours to allow the polymerized PANI to uniformly mix with CNFs. After that, the resulting solution was filtered and vacuum dried at 80 ^oC to get the final product, Fe-PANI-CNF. PANI-CNF was prepared in a similar procedure without the addition of an iron precursor. The Fe-PANI-CNF and PANI-CNF were annealed at 900 ^oC in N_2 for 1 hour. The heat-treated sample was leached in a 0.50 M H_2SO_4 solution at 80 ^oC for 8 hours to remove any impurities or unreacted species from the synthesized material and washed several times in DI water. Finally, the filtered product after acid leaching was dried for 6 hours at 70^oC to obtain the catalyst Fe-N-CNF and N-CNF.

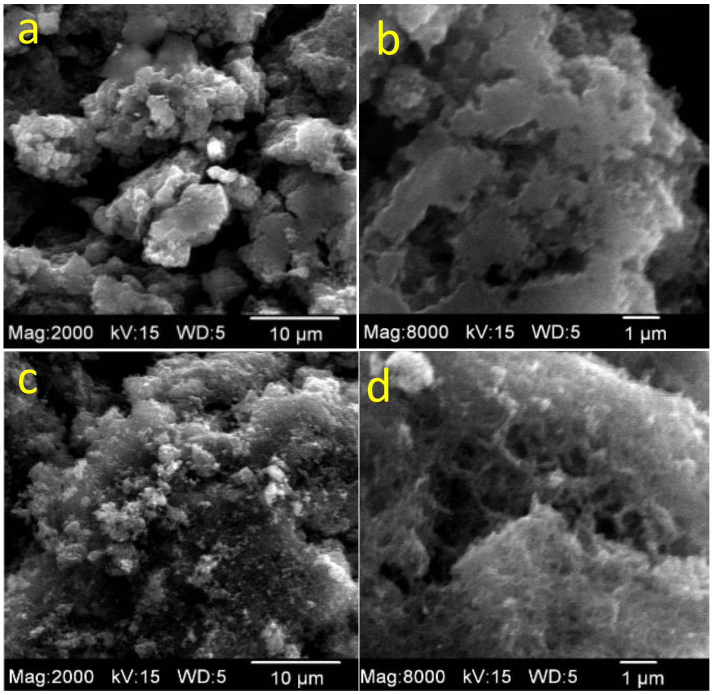

Figure 6.6: FESEM image of Fe-PANI-CNF (a,b) before pyrolysis and (c,d) after pyrolysis.

Figure 6.6 shows the FESEM image taken to confirm the morphological change of the Fe-PANI-CNF before and after pyrolysis. It is clear that before pyrolysis PANI covered the surface of the CNFs and after heat-treatment at 900 ^{o}C there is a change in the surface structure as the deposited PANI decomposes into carbon and nitrogen in which the later get incorporated into the CNFs. Figure D.7 shows the TEM image of the Fe-PANI-CNF catalyst after synthesis. As shown in the TEM image, we can notice that the deposited PANI and $FeCl_3$ did not coat the CNFs uniformly and it is deposited on top of the CNF surface. This confirms that the synthesis procedure needs to be further improved to get the uniformly dispersed Fe-PANI-CNF catalyst. Figure D.8 presents the TEM EDX spectrum and STEM-EDX line profile for the Fe-N-CNF catalyst which confirms the presence of C, N, and Fe. Also, the Fe content in the resulting catalyst is found to be 0.57 at%. Figure D.9 shows the Raman spectra obtained for Fe-PANI-CNF catalysts before and after pyrolysis. The catalyst displayed the D-band and G-band characteristic peaks at ~1340 cm^{-1}

and ~1570 cm^{-1} for the samples in both the conditions. The pyrolyzed Fe-PANI-CNF catalyst has a narrower G band confirming the graphitization of carbon and a high intense D band confirming the presence of carbon defects after heat treatment.

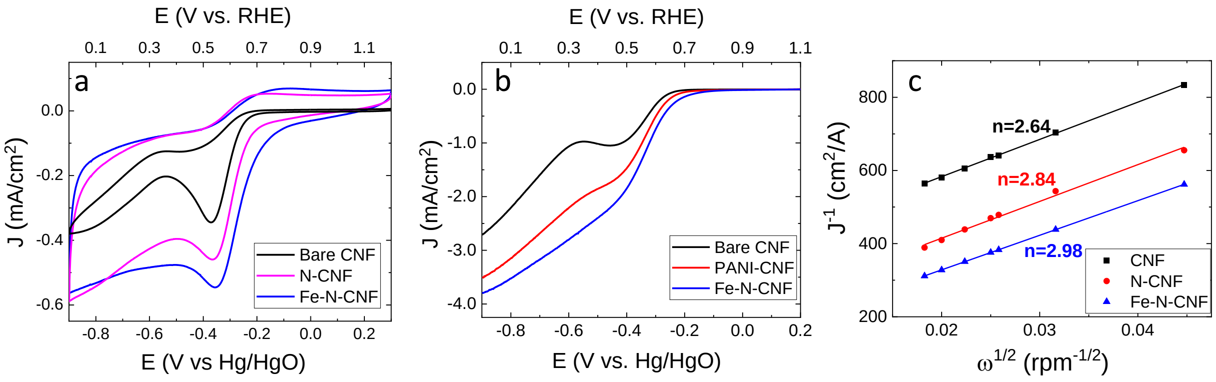

Figure 6.7: (a) CV curves recorded at a scan rate of 50 mV/s and (b) LSV curves recorded at a scan rate of 10 mV/s and a rotation speed of 1,600 rpm in O_2-saturated 0.10 M KOH solution for Bare CNF, PANI/CNF (annealed at 900°C), and Fe-N-CNF; (c) Koutecky-Levich plots at a potential of -0.60 V (vs Hg/HgO) for all the catalysts.

The catalytic performance of the synthesized catalysts was evaluated using a three-electrode system involving coiled Pt wire as the counter electrode and Hg/HgO (1.0 M NaOH) as the reference electrode. The working electrode was prepared by drop-casting 5 µL of the catalyst ink on RDE. The catalyst ink was prepared by dispersing 2.0 mg of the catalyst powder in a mixture of water, ethanol, and 5 wt% Nafion to yield a final catalyst loading of 80 µg/cm^2. The CV curves recorded in O_2-saturated 0.10 M KOH solution are presented in Figure 6.7a and it reveals the ORR activity of the synthesized catalyst. The reduction peak appeared at the same potential for all the catalysts, but the peak intensity is higher for Fe-N-CNF catalysts when compared with the bare CNF and N-CNF. As the Fe was introduced, Fe-N-CNF has an onset potential of ~ -0.180 V vs. Hg/HgO which is positively shifted by 80 mV and 32 mV when compared to the bare CNF and N-CNF without any Fe from the LSV curves recorded at 1600 rpm as shown in Figure 6.7b. Moreover, the current density at 0.80 V (vs. Hg/HgO) increases from -2.2 to -3.25 mA/cm^2 when

N is introduced, and it further increases to -3.54 mA/cm^2 with the incorporation of Fe. The RDE data recorded from 500 to 3000 rpm for bare CNF, N-CNF, and Fe-N-CNF catalysts is presented in Figure D.10 and it confirms that the current density increases with the rotation speed as observed before. The KL plot obtained at -0.60 V (vs. Hg/HgO) predicts the n value to be 2.64, 2.84, and 2.98 for bare CNF, N-CNF, and Fe-N-CNF catalysts, respectively. The increased electron transfer number for the Fe-N-CNF catalyst, when compared with the Fe free N-CNT catalyst further confirms that the formation of Fe-N-C sites in our catalyst improves the ORR. However, the KL results for all the three catalysts suggest that the O_2 reduction is dominated by a 2-e^- pathway. This study confirms that the incorporation of Fe and N increases the ORR activity of CNF but still inferior to the other Fe-N-C catalysts reported in the alkaline medium. We attribute the lower activity of Fe-N-CNF to the very low Fe content in the final catalyst and the employed synthesis procedure. In the future, we plan to extend this study by exploring the ORR activity of the Fe-N-C active site catalysts formed with NCNTs and VACNFs in alkaline medium.

6.4 NiO/N-VACNF Electrocatalyst for Hydrogen Evolution Reaction in Alkaline Media

As discussed in Chapter 4, the plasma annealing of VACNFs at 550 ^{o}C introduced N into the VACNFs and also generated NiO particles of 5 to 30 nm in diameter. This work is focused on employing the N-doped VACNF with NiO particles (NiO/N-VACNF) as an electrocatalyst for hydrogen evolution reaction in the alkaline medium. Recent reports have found that the NiO supported on carbon surface to be an efficient HER electrocatalyst in alkaline medium[11-13]. The HER activity was investigated using a three-electrode system with coiled Pt wire as the counter electrode and Hg/HgO (1.0 M NaOH) as the reference electrode. The working electrode was still prepared by the same method as explained in Chapter 2. The catalytic activity towards HER was evaluated for four different catalysts, namely bare VACNF, VACNF PA 5 min (NiO/N-VACNF (5 min)), VACNF PA 15 min (NiO/N-VACNF (15 min)), and VACNF PA 30 min (NiO/N-VACNF (30 min)).

Figure 6.8a shows the CV curves recorded in Ar-saturated 0.10 M KOH solution for all the four catalysts. It is clear from the CV data that the VACNFs after plasma annealing have a higher HER current density when compared with the bare VACNF and this increase in HER activity can be attributed to the presence of NiO particles on the VACNF surface for the plasma annealed samples. Figure 6.8b shows the LSV curves recorded at 1600 rpm and 10 mV/s scan rate for bare VACNF and three different PA catalysts. To assess the catalytic activity of different catalysts we need to measure the overpotential (η) required to generate a cathodic current density of 5.0 mA/cm^2. Among all the four catalysts the NiO/N-VACNF (15 min) has the smallest overpotential of 268 mV (vs. RHE). The obtained η value of NiO/N-VACNF (15 min) is 6, 55, and 195 mV higher than NiO/N-VACNF (5 min), NiO/N-VACNF (30 min), and bare VACNF respectively. Moreover, at $\eta = 0.5$ V, the NiO-N/VACNF has a cathodic current density of 33 mA/cm^2, which is 1.7, 2.2 and 5.3 times higher than NiO/N-VACNF (5 min), NiO/N-VACNF (30 min), and bare VACNF, respectively. As seen from the CV and LSV data, it is clear that the HER activity is improved in the presence of NiO particles, and the activity increases with the increase in the particle diameter. However, when the VACNF was PA for 30 min, NiO particles with a large diameter of about 15-30 nm are generated on the surface of the VACNF. In addition to that, the diameter of the VACNF decreases as it was annealed for a longer time. So, these two effects added together can cause a decrease in the HER activity when the annealing time increases from 15 to 30 min. The electrode kinetics of HER can be studied using EIS.

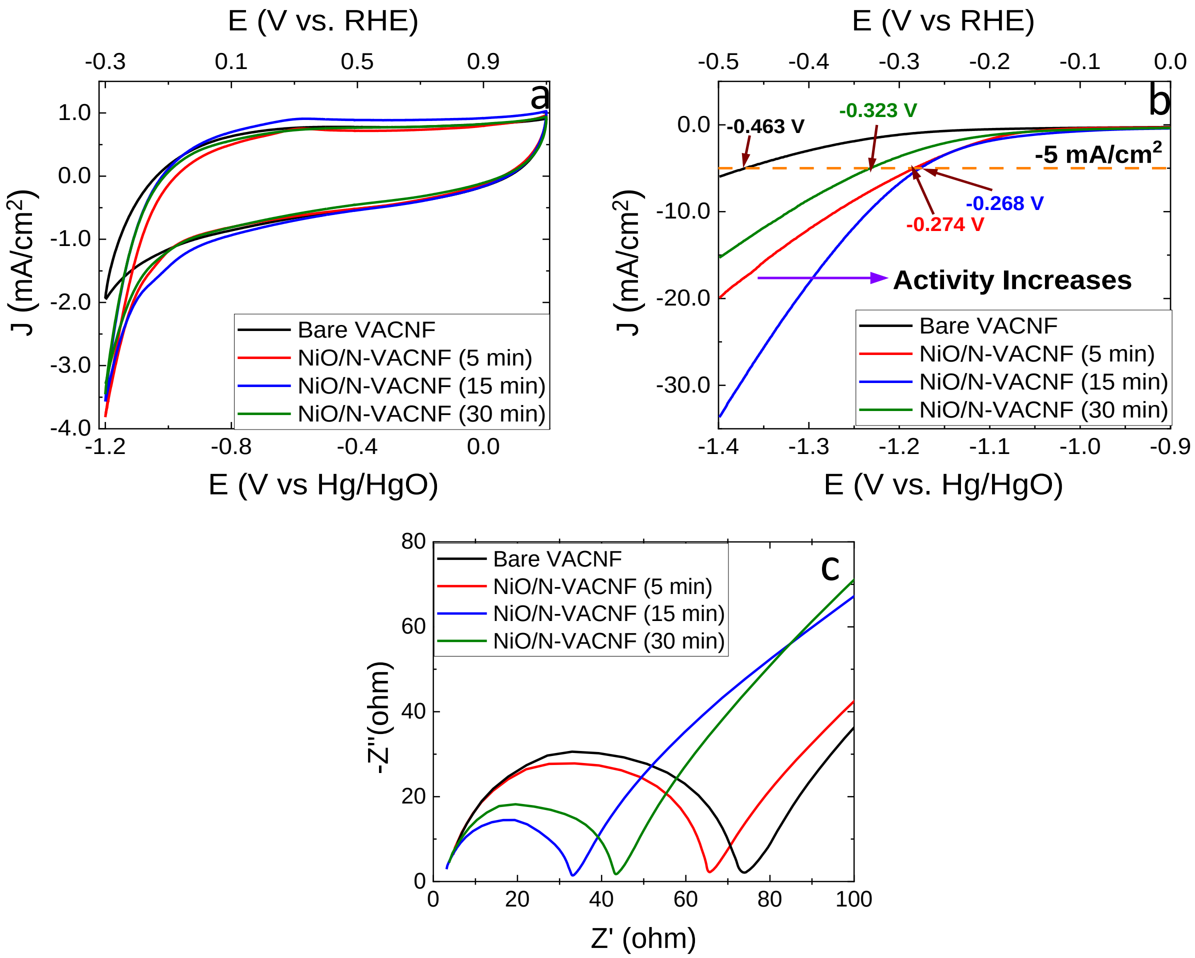

Figure 6.8: (a) CV curves recorded in Ar-saturated 0.10 M KOH solution at a scan rate of 50 mV/s , (b) iR-corrected LSV curves recorded at a scan rate of 10 mV/s and a rotation speed of 1,600 rpm in Ar-saturated 0.10 M KOH solution, and (c) Nyquist plots at η=143 mV in the frequency range from 1 MHZ to 0.01 Hz for bare VACNF, NiO-N/VACNF (5), NiO-N/VACNF (15), and NiO-N/VACNF (30).

Figure 6.8c shows the Nyquist plot (Z'(Re Z) vs. -Z''(Im Z)) obtained at η=143 V vs. RHE in the frequency range from 1.0 MHZ and 0.01 Hz for bare VACNF, NiO/N-VACNF (5 min), NiO/N-VACNF (15 min), and NiO/N-VACNF (30 min). A good HER catalyst should have a semicircle with a smaller radius in the Nyquist plot. Here, the NiO/N-VACNF (15 min) has the smallest semicircle, which means a faster charge transfer rate. This result is in agreement with the increased activity obtained for the NiO-N/VACNF (15 min) from the LSV data. Thus, the presence of NiO particles with a diameter of 10-15 nm increased the catalytic activity of the VACNF catalyst and enhances the charge transfer. This is an ongoing project and we plan to further evaluate the stability of these catalysts towards HER, and further improve the HER catalytic activity by employing plasma annealed VACNFs grown for a longer time.

6.5 References

1. Zheng, Y.; Jiao, Y.; Zhu, Y.; Cai, Q.; Vasileff, A.; Li, L. H.; Han, Y.; Chen, Y.; Qiao, S.-Z., Molecule-Level g-C3N4 Coordinated Transition Metals as a New Class of Electrocatalysts for Oxygen Electrode Reactions. *J. Am. Chem. Soc.* **2017,** *139* (9), 3336-3339.
2. Luo, W.-B.; Chou, S.-L.; Wang, J.-Z.; Zhai, Y.-C.; Liu, H.-K., A Metal-Free, Free-Standing, Macroporous Graphene@g-C3N4 Composite Air Electrode for High-Energy Lithium Oxygen Batteries. *Small* **2015,** *11* (23), 2817-2824.
3. Zheng, Y.; Jiao, Y.; Chen, J.; Liu, J.; Liang, J.; Du, A.; Zhang, W.; Zhu, Z.; Smith, S. C.; Jaroniec, M.; Lu, G. Q.; Qiao, S. Z., Nanoporous Graphitic-C3N4@Carbon Metal-Free Electrocatalysts for Highly Efficient Oxygen Reduction. *J. Am. Chem. Soc.* **2011,** *133* (50), 20116-20119.
4. Cao, Y.; Yu, H.; Tan, J.; Peng, F.; Wang, H.; Li, J.; Zheng, W.; Wong, N.-B., Nitrogen-, phosphorous- and boron-doped carbon nanotubes as catalysts for the aerobic oxidation of cyclohexane. *Carbon* **2013,** *57*, 433-442.
5. Jaramillo, T. F.; Jorgensen, K. P.; Bonde, J.; Nielsen, J. H.; Horch, S.; Chorkendorff, I., Identification of active edge sites for electrochemical H2 evolution from MoS2 nanocatalysts. *Science* **2007,** *317* (5834), 100-2.
6. Du, F.; Chen, Z.; Zhang, Y.; He, H.; Zhou, Y.; Li, T.; Zou, Z., Reduced-graphene-oxide-loaded MoS2‡Ni3S2 nanorod arrays on Ni foam as an efficient and stable electrocatalyst for the hydrogen evolution reaction. *Electrochem. Commun.* **2019,** *99*, 22-26.
7. Brown, E.; Yan, P.; Tekik, H.; Elangovan, A.; Wang, J.; Lin, D.; Li, J., 3D printing of hybrid MoS2-graphene aerogels as highly porous electrode materials for sodium ion battery anodes. *Mater. Des.* **2019,** *170*, 107689.
8. Wang, M.; Yang, Y.; Liu, X.; Pu, Z.; Kou, Z.; Zhu, P.; Mu, S., The role of iron nitrides in the Fe–N–C catalysis system towards the oxygen reduction reaction. *Nanoscale* **2017,** *9* (22), 7641-7649.
9. Wang, W.; Jia, Q.; Mukerjee, S.; Chen, S., Recent Insights into the Oxygen-Reduction Electrocatalysis of Fe/N/C Materials. *ACS Catal.* **2019,** *9* (11), 10126-10141.
10. Wu, G.; More, K. L.; Johnston, C. M.; Zelenay, P., High-Performance Electrocatalysts for Oxygen Reduction Derived from Polyaniline, Iron, and Cobalt. *Science* **2011,** *332* (6028), 443-447.
11. Hoang, V. C.; Dinh, K. N.; Gomes, V. G., Hybrid Ni/NiO composite with N-doped activated carbon from waste cauliflower leaves: A sustainable bifunctional electrocatalyst for efficient water splitting. *Carbon* **2020,** *157*, 515-524.

12. Narwade, S. S.; Mali, S. M.; Digraskar, R. V.; Sapner, V. S.; Sathe, B. R., Ni/NiO@rGO as an efficient bifunctional electrocatalyst for enhanced overall water splitting reactions. *Int. J. Hydrogen Energy* **2019,** *44* (49), 27001-27009.
13. Zhan, W.; Yuan, Y.; Sun, L.; Yuan, Y.; Han, X.; Zhao, Y., Hierarchical NiO@N-Doped Carbon Microspheres with Ultrathin Nanosheet Subunits as Excellent Photocatalysts for Hydrogen Evolution. *Small* **2019,** *15* (22), 1901024.

Chapter 7 - Conclusions

Nanostructured carbon materials will continue to play an important role in enhancing the performance of electrocatalytic reactions in low-temperature fuel cell systems. The dissertation described the role of vertically aligned carbon nanofibers (VACNF) array as an effective catalyst support for oxygen reduction and methanol oxidation reaction. The ability of the VACNFs to strongly anchor the metal nanoparticles, enhance the durability of the electrocatalyst, improve the tolerance towards methanol crossover, induce a faster recovery from CO poisoning, and induce effective removal of reaction intermediates are desirable for an ideal electrocatalyst support.

In Chapter 3, the VACNF array was grown by PECVD and ion-sputtered with different loading (at 6.5, 10.8, 21.5, and 43.0 μg cm^{-2}) of Pt catalysts. The resulting 3D architectured material was employed as an electrocatalyst for the ORR. The linear sweep voltammetry data obtained from such 3D structures on RDE has been found to deviate from the Levich equation which is caused by the raised edge and the roughness at the top surface of the nanostructured VACNF. However, useful information can be extracted from the RDE measurements. The half-wave potential of the Pt/VACNF catalysts is comparable to the benchmark commercial Pt/C catalyst at similar Pt loadings following a 4-e^- ORR pathway. DFT calculations have validated the strong binding of Pt atoms with the graphitic edge sites in Pt/VACNF catalysts and further elucidated the reduction pathway to be a 2-e^- pathway for bare VACNFs and a 4-e^- pathway on Pt/VACNF, respectively. It also, identified that the ORR catalyzed by the Pt/VACNF is thermodynamically more favorable through a dissociative mechanism. The Pt/VACNF catalyst has shown better durability in accelerated stress tests than the commercial Pt/C catalyst at similar loading. Furthermore, the Pt/VACNF catalysts have shown enhanced tolerance to methanol oxidation in the presence of 0.75 M methanol. The Pt/VACNF system has also shown improved capability to recover from CO poisoning.

In Chapter 4, the N-doped VACNF array was prepared by NH_3 plasma annealing at 550 ^{o}C using PECVD and successfully employed as a unique catalyst support to improve the durability of the Pt catalysts towards the ORR. The material analyses identified the morphological change, indicated the presence of NiO particles on the catalyst surface, and confirmed the anchoring of Pt nanoparticles. XPS analysis identified the presence of nitrogen species and different oxygen functionalities present in the VACNFs as a result of plasma annealing. It also confirmed the presence of partial electron transfer between the Pt particles and catalysts support which lead to the strong-metal support interaction. As a result, the Pt particle size was controlled to ~2.3 nm in diameter when attached to N-doped VACNF support. Even with smaller particle size, the Pt/N-VACNF with 43.0 µg/cm^2 Pt loading exhibited only a -16 mV shift in ΔE after 5000 AST cycles indicating a better durability when compared to the Pt/VACNF and Pt/C catalysts. DFT calculations have validated the strong binding of Pt atoms with the pyridinic N-doped edge and confirmed the 4-e$^-$ reduction pathway for Pt/N-VACNF catalyzed ORR. In addition, the Pt/N-VACNF catalysts have shown excellent tolerance to methanol oxidation with the oxygen reduction being more dominant in the full potential range.

In Chapter 5, the Pt and PtRu catalysts supported on the three-dimensional graphitic carbon support was successfully prepared using ion beam sputtering of PGMs onto PECVD-grown vertically aligned carbon nanofiber arrays. XPS analysis confirmed the presence of nitrogen species and oxygen functional groups in the 3D VACNF supports and the presence of strong metal-support interactions in Pt/VACNF. DFT calculations reveal the electron transfer mechanism and it was found to be dependent on the nature of the atomic sites. The electron transfer between PGM and the edge atoms of VACNF support promotes OH binding over that of CO. As a result, the energy difference between OH_{ads} and CO_{ads} binding is reduced at the Pt catalyst deposited on the N-doped VACNF support, which makes OH more effective in the electro-oxidative removal of CO poison. The CO stripping analyses further confirmed the effective removal of CO with the presence of additional CO stripping peaks at lower electrode potentials on the VACNF support. Cyclic voltammetry measurements of Pt/VACNF and PtRu/VACNF presented an enhanced electrocatalytic performance towards the MOR in both acidic and alkaline with higher J_f/J_b ratio indicating a higher degree of oxophilicity. In addition, Pt/VACNF and PtRu /VACNF catalysts with smaller particle sizes (~1.7 nm and 2.8 nm) showed improved stability even after 500 MOR CV cycles with still maintaining a higher J_f/J_b ratio.

In Chapter 6, a short overview of four ongoing studies was mentioned. In the first study, the impact of NCNTs in boosting the catalytic activity of g-C_3N_4 and the heat-treatment temperature in improving the activity of g-C_3N_4+NCNTs hybrid catalyst was successfully explored. The resulting g-C_3N_4+NCNTs-500 ^{o}C catalyst catalyzed ORR through a 4-e^- pathway and showed higher catalytic activity among all the other catalysts prepared using g-C_3N_4. Even though the activity is relatively low when compared to Pt/C, the g-C_3N_4+NCNTs-500 ^{o}C have shown excellent tolerance towards methanol crossover with almost no change in the ORR activity. In the future, significant efforts will be made to incorporate transition metals into the abundant nitrogen moieties, and hence, increasing the intrinsic activity of the hybrid catalyst. In the second study, the 3D printed MoS_2-rGO was successfully evaluated for ORR in alkaline medium. The MoS_2-rGO exhibited lower catalytic activity and catalyzed ORR through a less effective 2-e^- pathway due to the high pH of the electrolyte used. In the future, the 3D printed MoS_2-rGO will be tested for ORR and HER in acidic medium. In the third study, the Fe-N-CNF catalyst was successfully explored towards ORR. The incorporation of Fe and N increased the catalytic activity of CNF and the resulting Fe-N-CNF catalyzed ORR was dominated by a 2-e^- pathway. Due to a very low Fe content, the activity of the Fe-N-CNF catalyst was still inferior to the other reported Fe-N-C catalysts in alkaline medium. In the future, we plan to improve the catalytic activity by increasing the Fe content and extend this study by exploring VACNFs and NCNTs to form Fe-N-C ORR active sites. In the fourth study, the N-doped VACNFs with NiO particles was successfully explored as an HER catalyst. The resulting NiO/N-VACNF (15 min) catalysts had an HER overpotential of ~195 mV lower than the bare VACNF. The presence of NiO particles with a diameter of 10-15 nm increased the catalytic activity of the NiO/N-VACNF (15 min) catalyst and enhanced the charge transfer. We plan to continue this study by evaluating the durability of NiO/N-VACNF catalysts towards HER and further improve the catalytic activity by employing NiO/N-VACNF with longer VACNF.

Appendix A - Supplementary Information for Chapter 3

1) Derivation of limiting current (J_{lim}) and half-wave potentials ($E_{1/2}$):

To compensate for the sloped feature in the LSV curve, the actual limiting current density J_{lim} is derived by extrapolating the kinetic-controlled and diffusion-controlled regions with the tangent drawn. The difference between the current densities of the two intersecting points in the mixed-control regions is counted as J_{lim}. The half-wave potential $E_{1/2}$ is read from the point giving the current density value of $J_{lim}/2$.

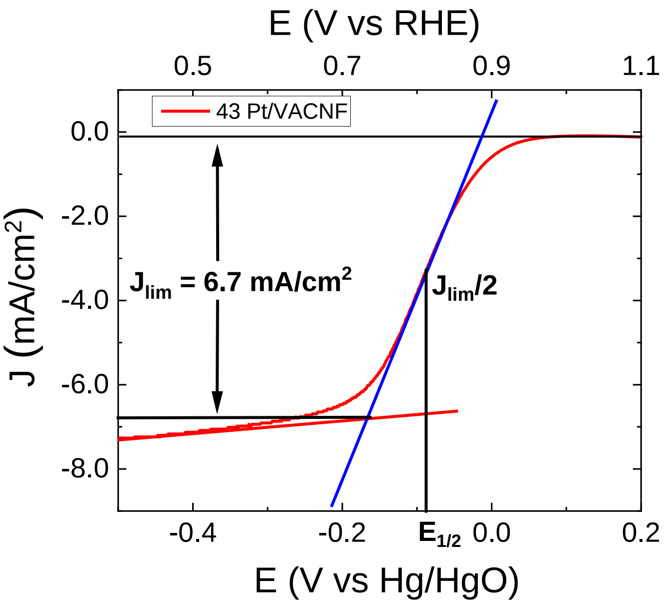

Figure A.1: Extrapolation of the limiting current density J_{lim} and the half-wave potential $E_{1/2}$ from the background subtracted LSV at 1,600 rpm and 10 mV/s for Pt/VACNF with 43.0 μg/cm^2 Pt loading.

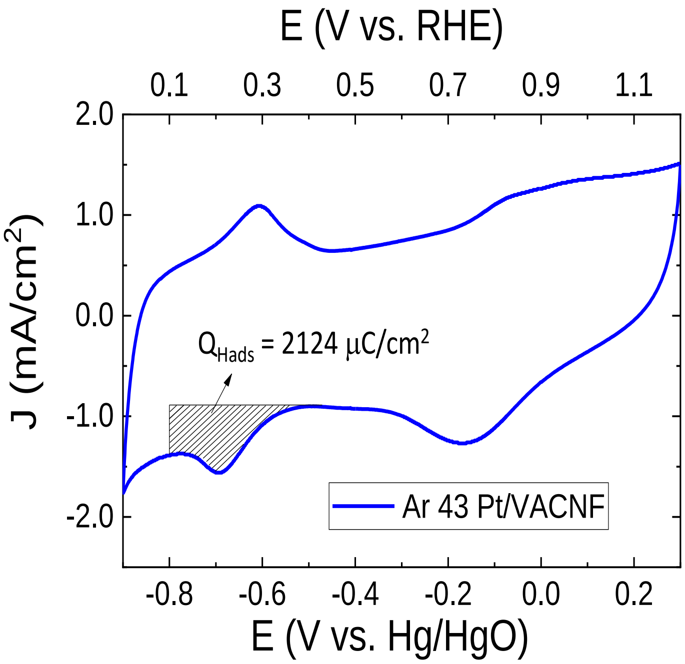

Figure A.2: CV curve of Pt/VACNF (at 43.0 μg/cm^2 Pt loading) showing the calculated area of hydrogen adsorption corresponding to a Pt electrochemical surface area of 23.5 m^2/g. (Reproduced with permission from *J. Electrochem. Soc.* 2020, 167, 066523. © The Electrochemical Society. All rights reserved.)

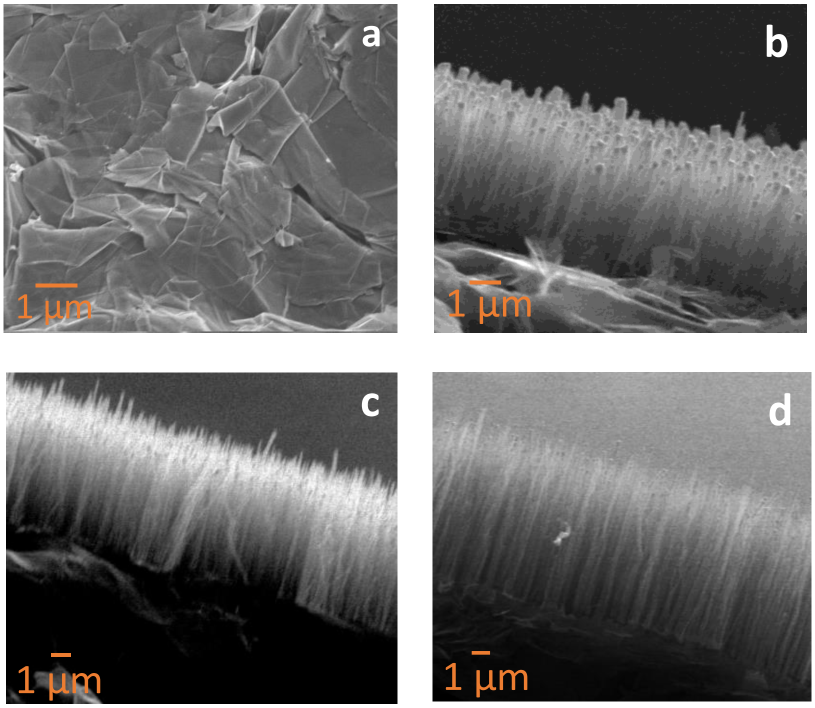

Figure A.3: Low-magnification FESEM images of (a) graphite paper (top view); and VACNF arrays on the graphite paper (cross-sectional view) with PECVD growth time of (b) 30 min, (c) 60 min, and (d) 90 min. (Reproduced with permission from *J. Electrochem. Soc.* 2020, 167, 066523. © The Electrochemical Society. All rights reserved.)

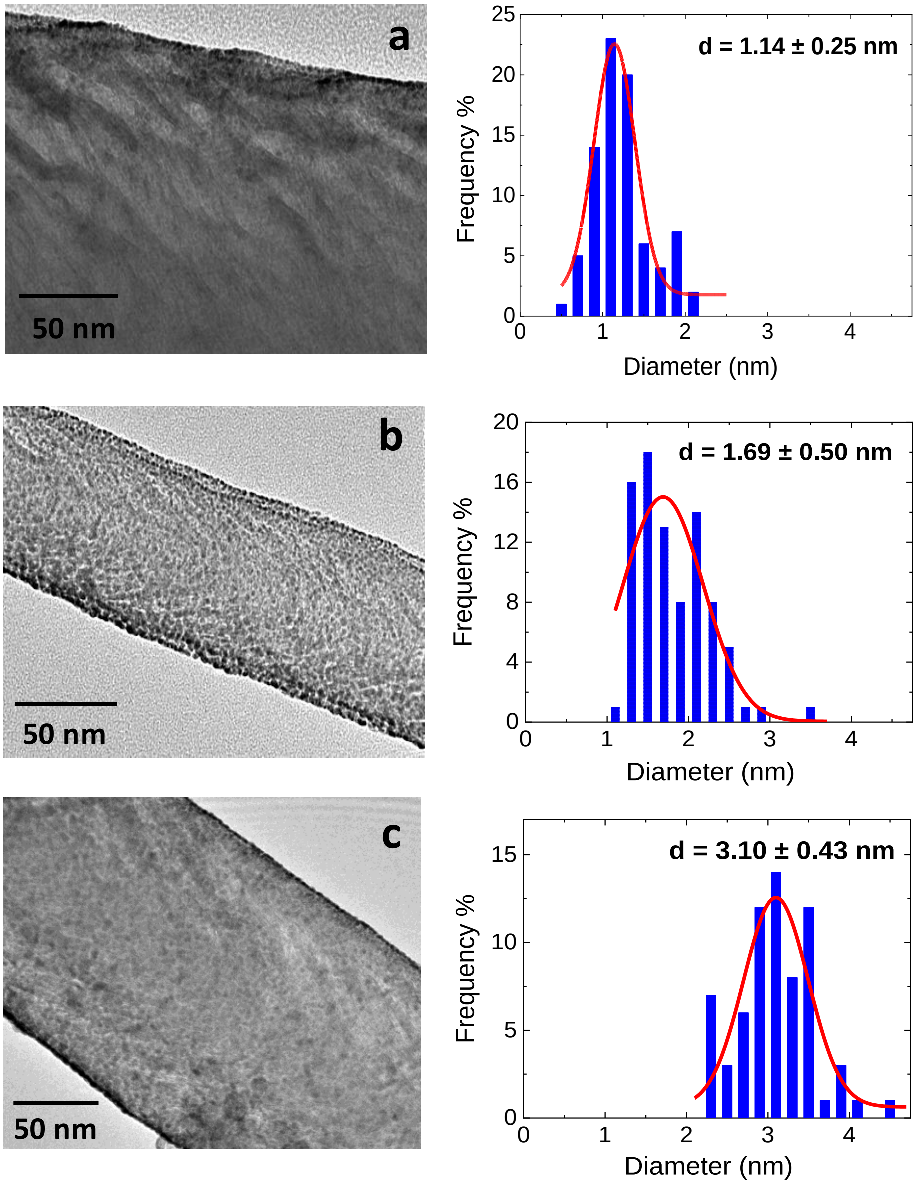

Figure A.4: TEM image of (a) Pt/VACNF (10.8 µg/cm^2); (b) Pt/VACNF (21.5 µg/cm^2) and (c) Pt/VACNF (43.0 µg/cm^2) and corresponding particle size distribution. (Reproduced with permission from *J. Electrochem. Soc.* 2020, 167, 066523. © The Electrochemical Society. All rights reserved.)

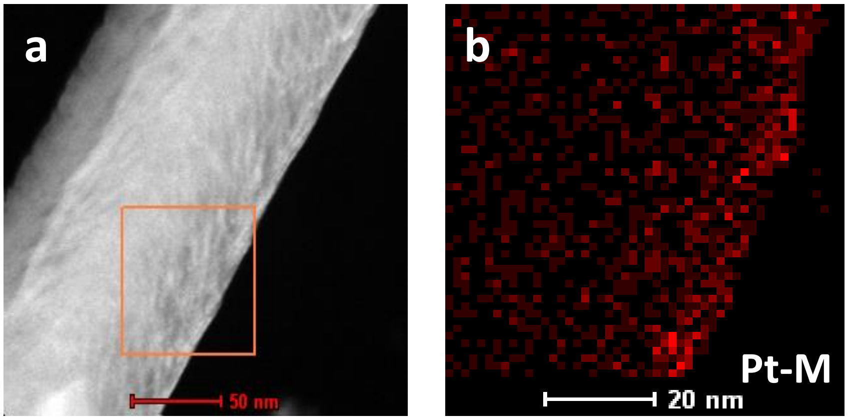

Figure A.5: (a) HAADF–STEM image of the Pt/VACNF with 5.0 nm nominal thickness (10.8 µg/cm^2) Pt loading by ion-beam sputtering, (b) EDS elemental mapping of Pt in the selected region. (Reproduced with permission from *J. Electrochem. Soc.* 2020, 167, 066523. © The Electrochemical Society. All rights reserved.)

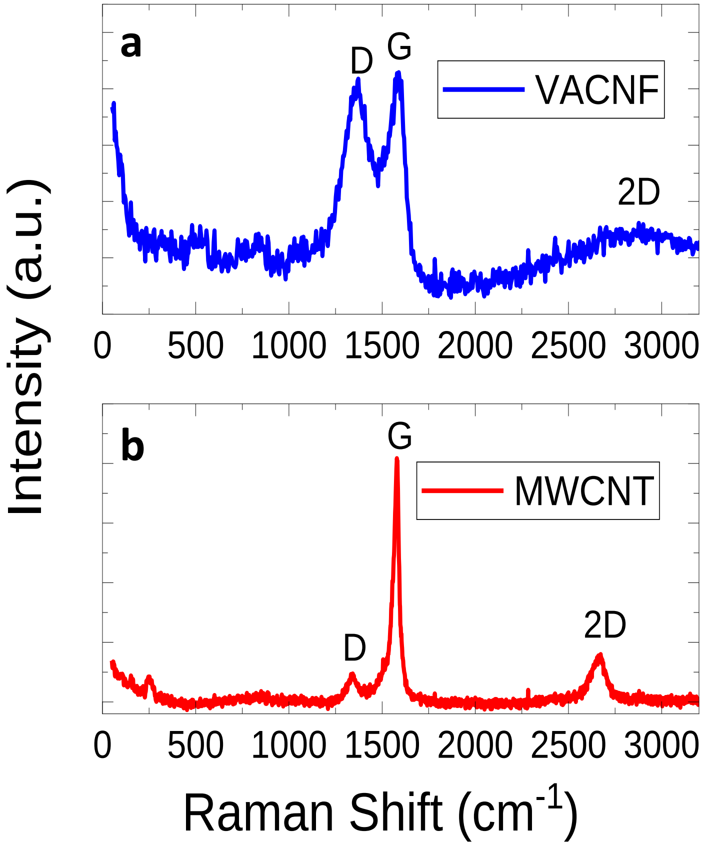

Figure A.6: Raman spectra of (a) bare VACNFs in comparison to (b) ideal multi-walled carbon nanotubes (MWCNTs). The MWCNTs were purchased from Nanostructured & Amorphous Materials Inc. (Katy, TX). (Reproduced with permission from *J. Electrochem. Soc.* 2020, 167, 066523. © The Electrochemical Society. All rights reserved.)

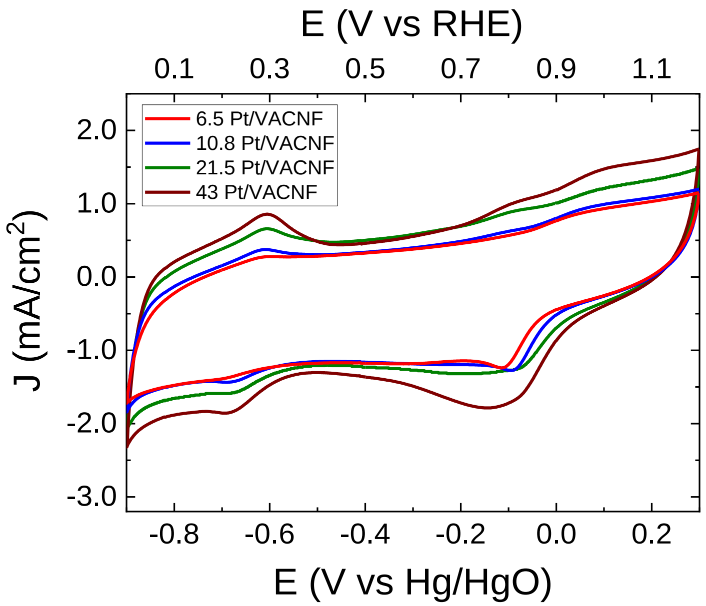

Figure A.7: CV curves recorded at a scan rate of 50 mV/s in O_2-saturated 0.1 M KOH solution for various Pt/VACNF catalysts with different Pt loadings (6.5, 10.8, 21.5 and 43.0 µg/cm^2). (Reproduced with permission from *J. Electrochem. Soc.* 2020, 167, 066523. © The Electrochemical Society. All rights reserved.)

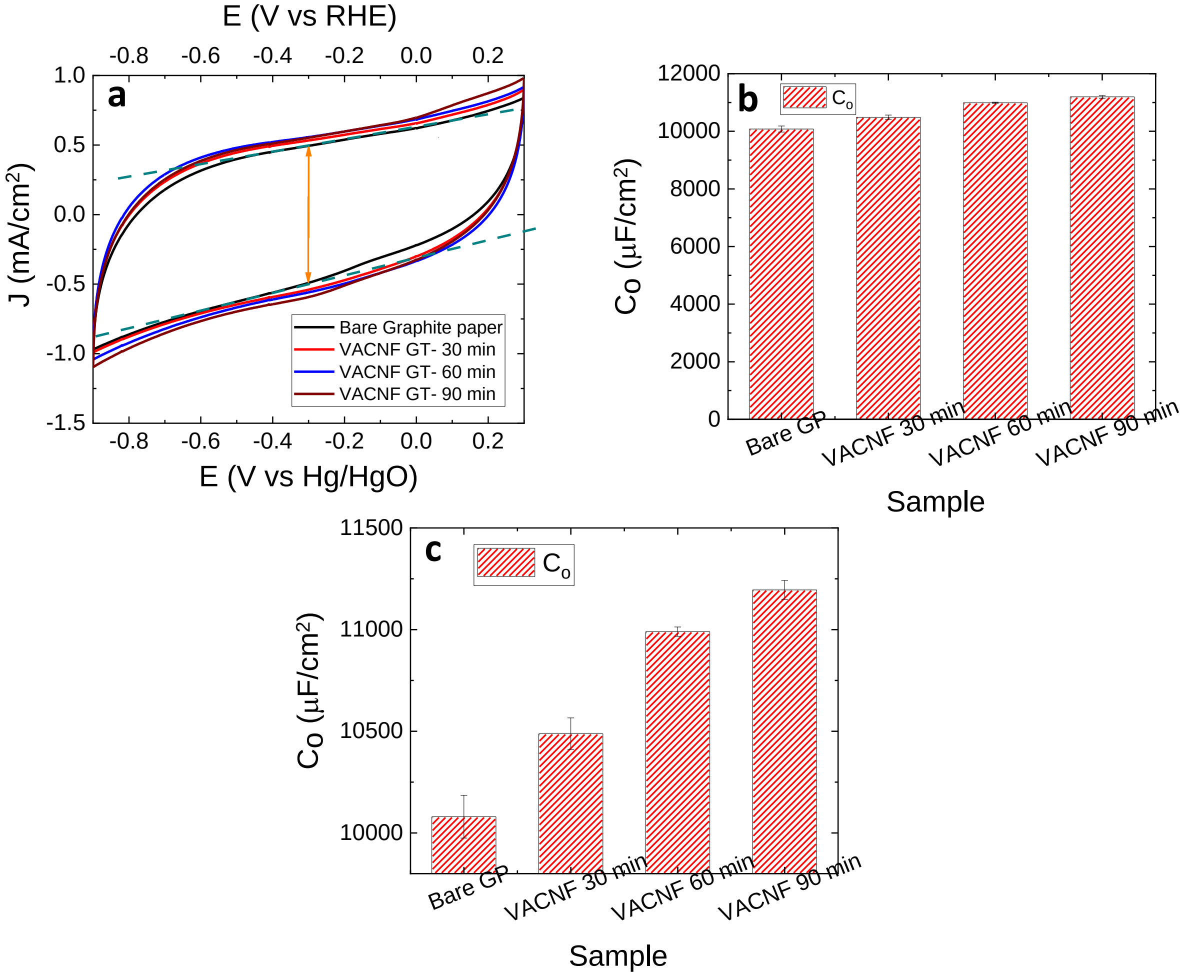

Figure A.8: (a) CV curves recorded at a scan rate of 50 mV/s in Ar-saturated 0.10 M KOH for bare graphite paper and those grown with VACNFs at 30, 60 and 90 min growth time. The dashed lines show the baselines and the orange arrow indicates the current density that was used to calculate the capacitance; (b) Plot of capacitance C_o (μF/cm^2) vs. different samples; (c) Enlarged plot of (b) to show the capacitance variation versus the VACNF length (or growth time). The error bars are calculated by the standard deviation from 3 samples. (Reproduced with permission from *J. Electrochem. Soc.* 2020, 167, 066523. © The Electrochemical Society. All rights reserved.)

Table A.1: The average length and the corresponding capacitance C_o ($\mu F/cm^2$) of VACNFs prepared with different PECVD growth time. (© The Electrochemical Society. Reproduced with permission from *J. Electrochem. Soc.* 2020, 167, 066523. All rights reserved)

Sample	**Average Length (µm)**	**C_0 ($\mu F/cm^2$) (After GP subtraction)**
VACNF – 30 min GT	5	408±78
VACNF – 60 min GT	8	910 ± 23
VACNF – 90 min GT	11	1115±48

*GT represents growth time.

*The C_o for bare graphite paper is 10080 ± 105 $\mu F/cm^2$.

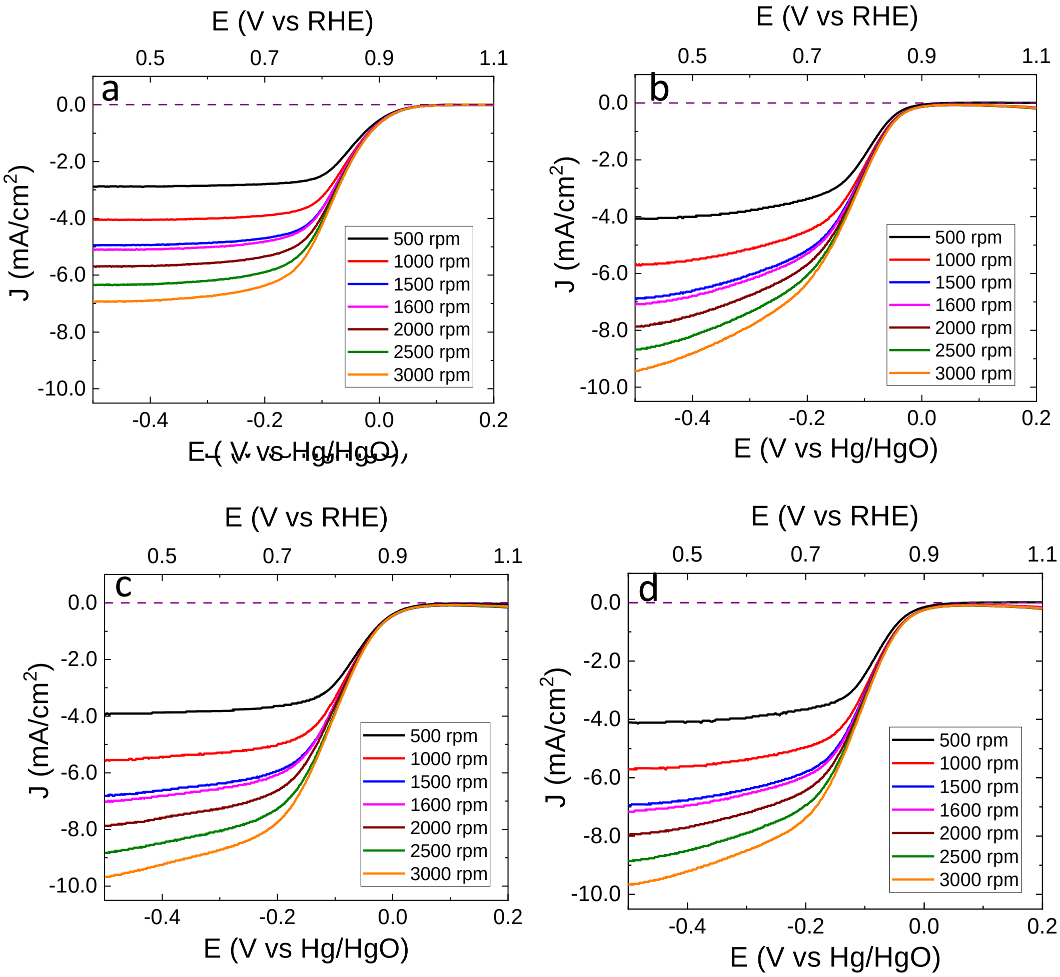

Figure A.9: RDE LSV voltammogram with background corrected for (a) Pt/C (12.8 µg/cm^2 Pt), (b) Pt/VACNF (6.5 µg/cm^2 Pt), (c) Pt/VACNF (10.8 µg/cm^2 Pt), and (d) Pt/VACNF (43.0 µg/cm^2 Pt) recorded in 0.10 M KOH solution at a scan rate of 10 mV/s in the negative direction and at a rotation speed from 500 to 3000 rpm. The purple dash lines mark the zero current density. (Reproduced with permission from *J. Electrochem. Soc.* 2020, 167, 066523. © The Electrochemical Society. All rights reserved.)

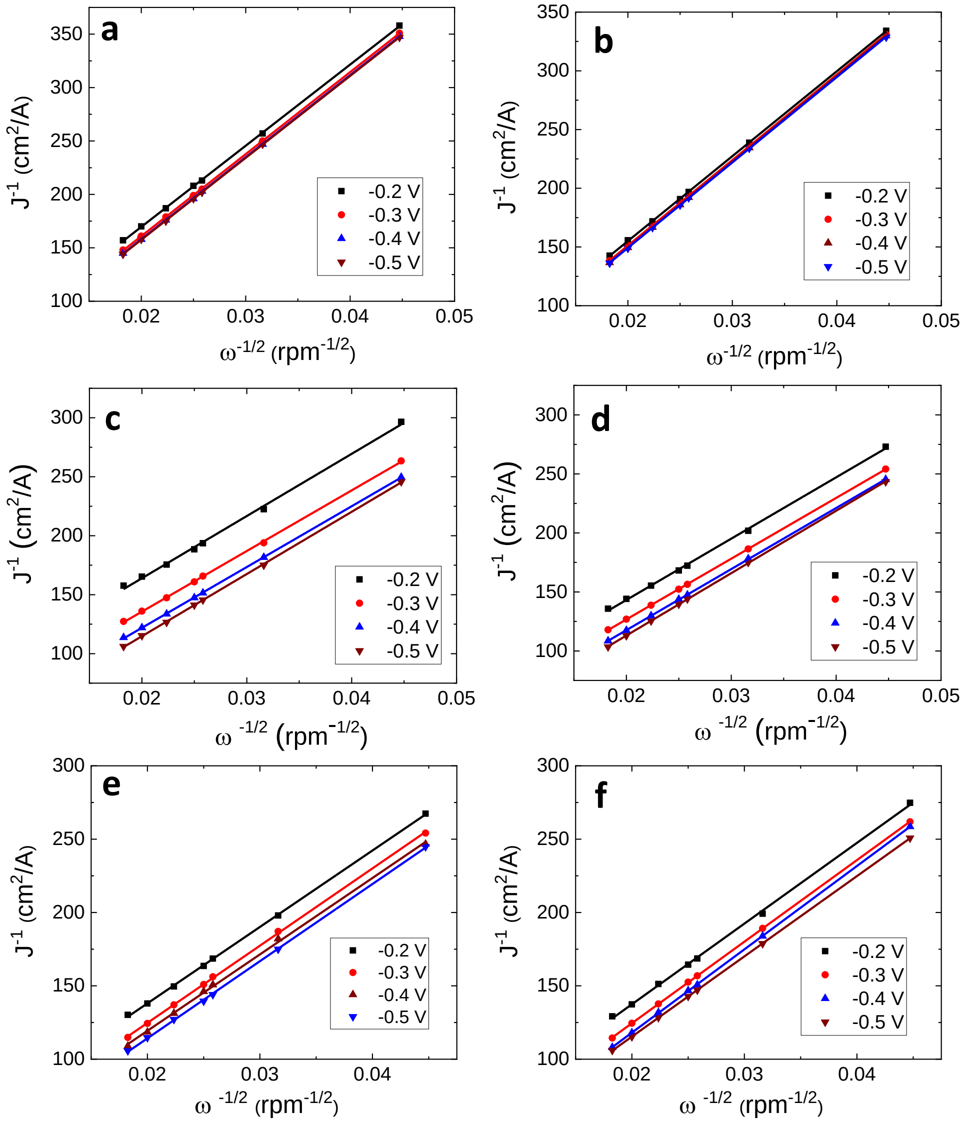

Figure A.10: Koutecky-Levich plots of (a) Pt/C (12.8 μg/cm^2 Pt), (b) Pt/C (25.6 μg/cm^2 Pt), (c) Pt/VACNF (6.5 μg/cm^2 Pt), (d) Pt/VACNF (10.8 μg/cm^2 Pt), (e) Pt/VACNF (21.5 μg/cm^2 Pt), and (f) Pt/VACNF (43.0 μg/cm^2 Pt). (Reproduced with permission from *J. Electrochem. Soc.* 2020, 167, 066523. © The Electrochemical Society. All rights reserved.)

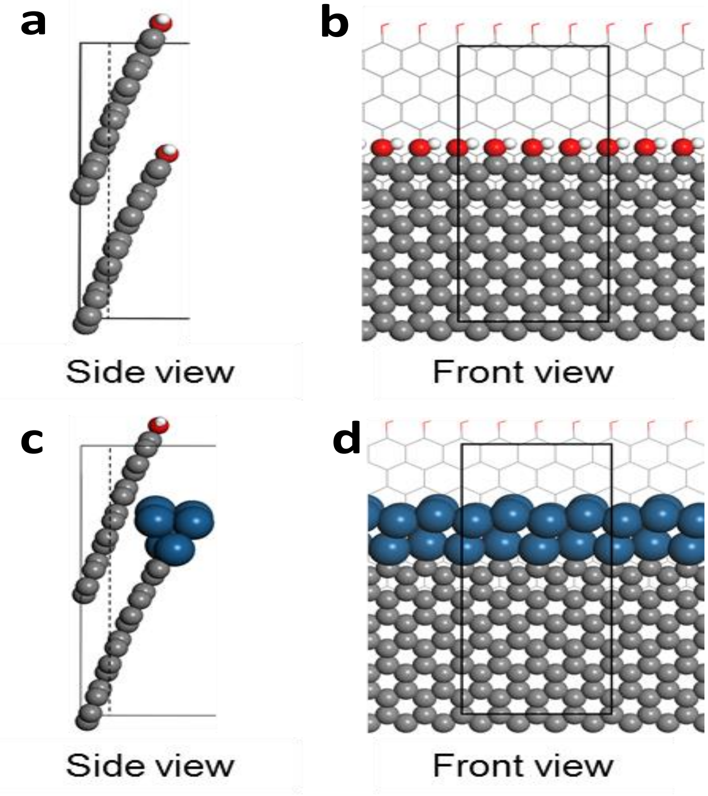

Figure A.11: Side and front views of the molecular models representing the fishbone-type bare VACNFs (a and b), and Pt/VACNFs (c and d) used in this work. Periodic boundaries are indicated by black lines. Color code: white – H, red – O, grey – C, and blue – Pt. (Reproduced with permission from *J. Electrochem. Soc.* 2020, 167, 066523. © The Electrochemical Society. All rights reserved.)

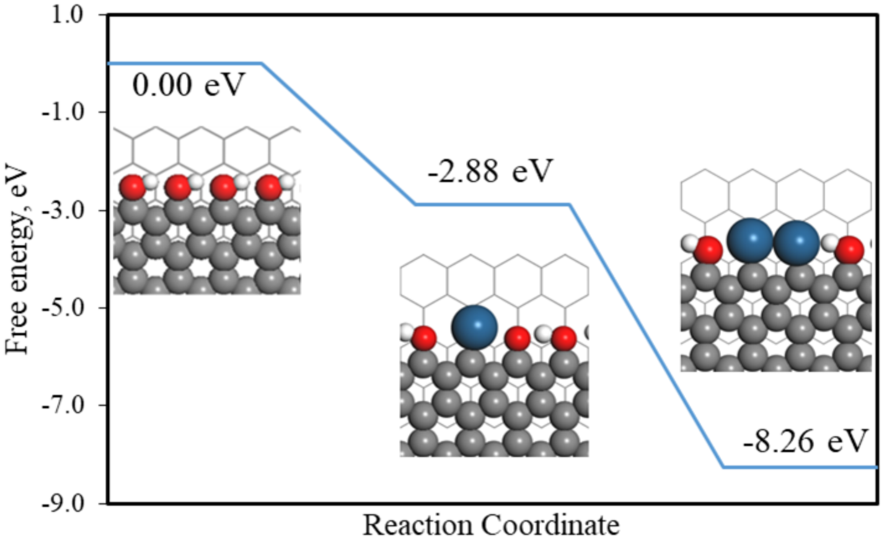

Figure A.12: Free energy profiles for Pt deposition on the VACNF edge, which indicates free energy change of depositing another Pt at carbon edge. Color code: white – H, red – O, gray – C, and blue – Pt. (Reproduced with permission from *J. Electrochem. Soc.* 2020, 167, 066523. © The Electrochemical Society. All rights reserved.)

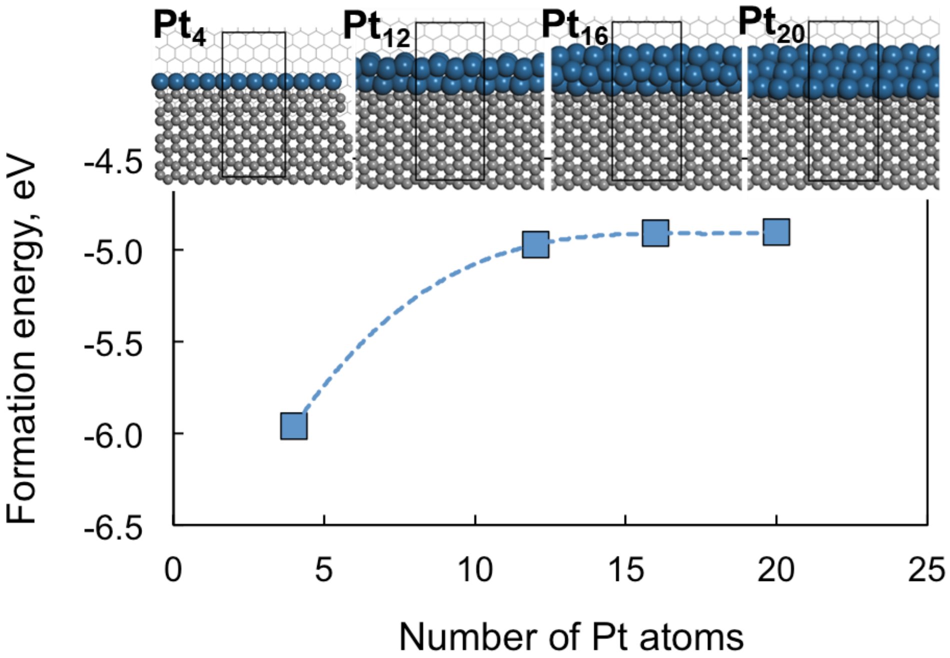

Figure A.13: Models of Pt clusters consisting of Pt4, Pt 12, Pt 16, and Pt 20 on the VACNF edges. Numerical values represent the formation free energies on the per Pt atom basis. Color code: gray – C, and blue – Pt. (Reproduced with permission from *J. Electrochem. Soc.* 2020, 167, 066523. © The Electrochemical Society. All rights reserved.)

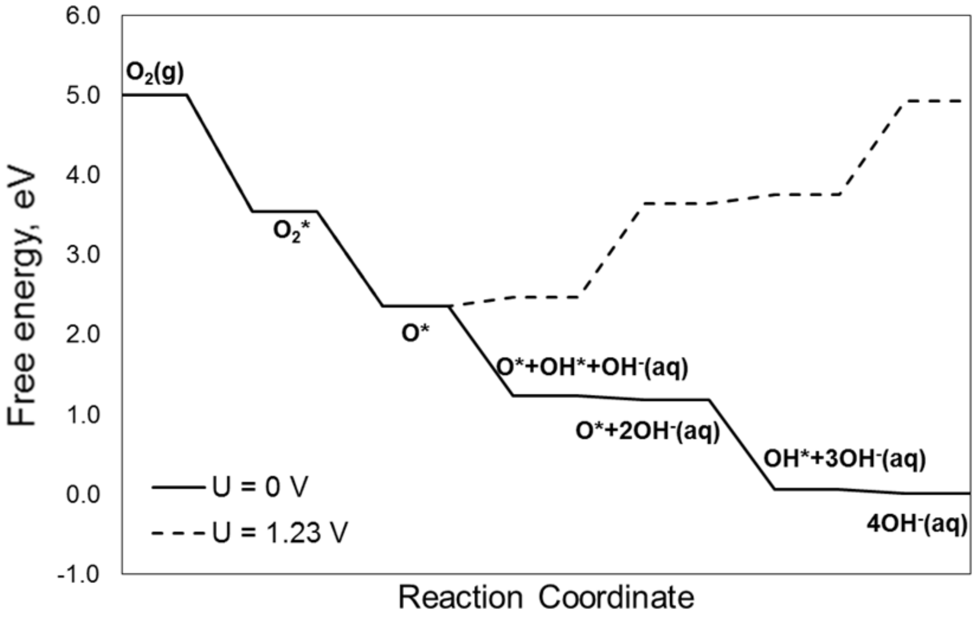

Figure A.14: Free energy profiles of the 4-e$^-$ ORR dissociative pathway at the 0 V applied potential (solid line) and at the 1.23 V applied potential (dashed line). (Reproduced with permission from *J. Electrochem. Soc.* 2020, 167, 066523. © The Electrochemical Society. All rights reserved.)

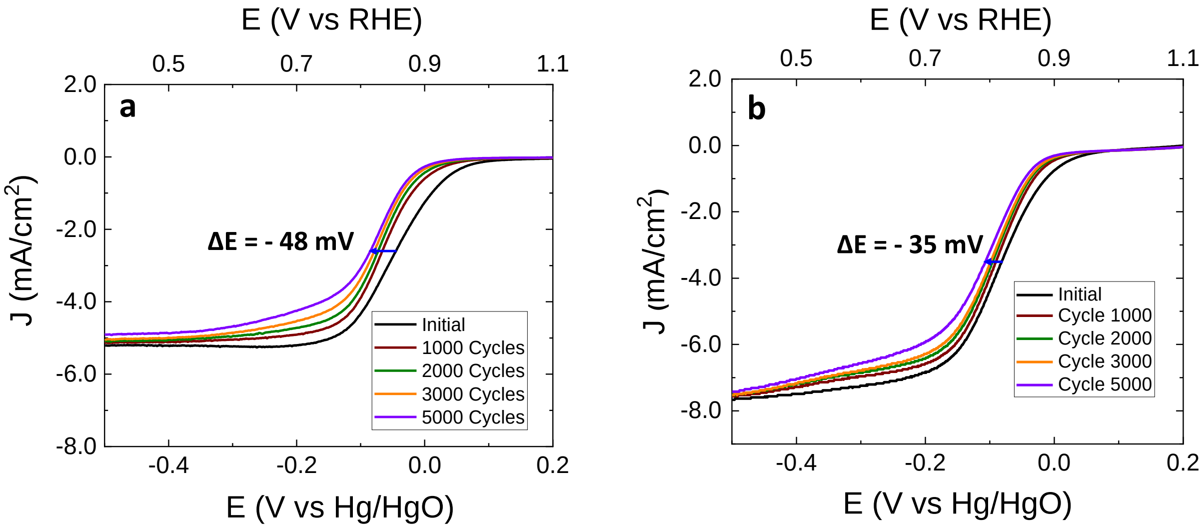

Figure A.15: LSV curves of (a) Pt/C (51.2 µg/cm^2) and (b) Pt/VACNF (43.0 µg/cm^2) after every 1000 AST cycles in O_2-saturated 0.10 M KOH solution at a scan rate of 10 mV/s and a rotation speed of 1600 rpm. (Reproduced with permission from *J. Electrochem. Soc.* 2020, 167, 066523. © The Electrochemical Society. All rights reserved.)

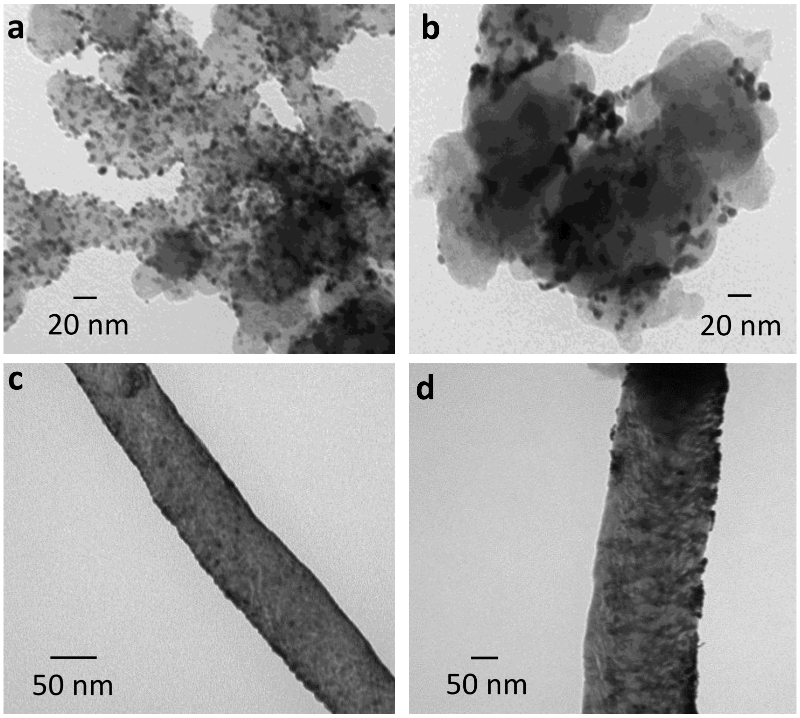

Figure A.16: TEM images of Pt/C (78.5 μg/cm^2) (a) before and (b) after 5,000 AST cycles, and Pt/VACNF (86.0 μg/cm^2) (c) before and (d) after 5,000 AST cycles. (Reproduced with permission from *J. Electrochem. Soc.* 2020, 167, 066523. © The Electrochemical Society. All rights reserved.)

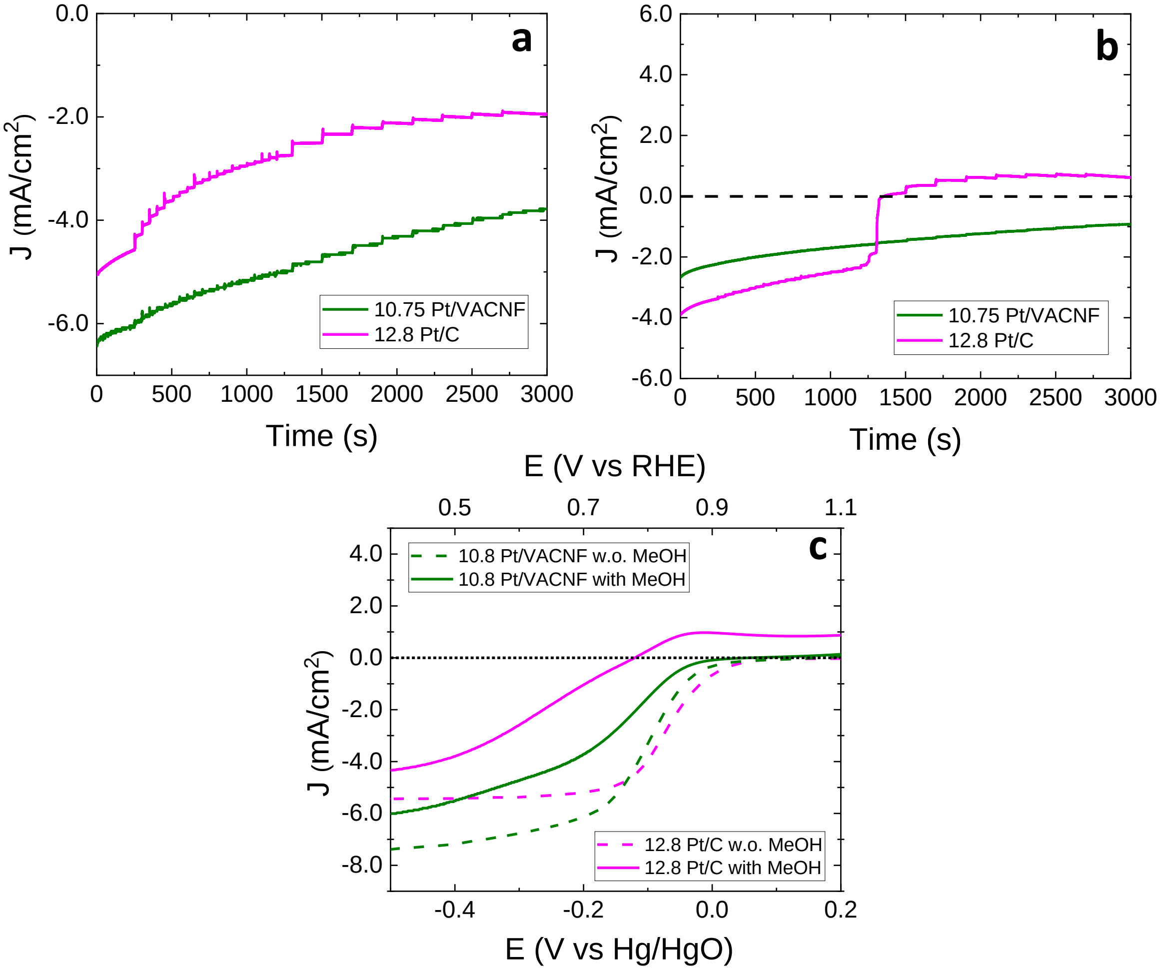

Figure A.17: Amperometric *j-t* curve of Pt/C (12.8 µg/cm^2 Pt) and Pt/VACNF (10.8 µg/cm^2 Pt) recorded at 1,600 rpm in O_2-saturated 0.10 M KOH solution with successive addition of 3.0 M methanol to give the final concentration of 0.75 M at the potential of (a) -0.3 V and (b) -0.1 V (vs. Hg/HgO); (c) LSV curves recorded at a scan rate of 10 mV/s and 1,600 rpm with and without adding 0.75 M methanol. (Reproduced with permission from *J. Electrochem. Soc.* 2020, 167, 066523. © The Electrochemical Society. All rights reserved.)

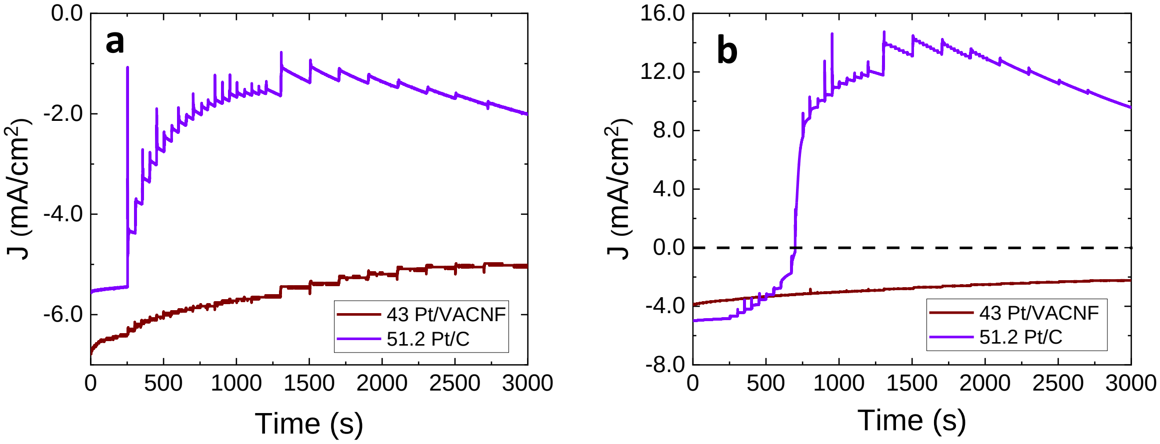

Figure A.18: Amperometric *j-t* curve of Pt/C (51.2 µg/cm^2) and Pt/VACNF (43.0 µg/cm^2) recorded at 1,600 rpm in O_2-saturated 0.10 M KOH solution with successive addition of 3.0 M methanol to give the final concentration of 0.75 M at a potential of (a) -0.3 V and (b) -0.1 V (vs. Hg/HgO). (Reproduced with permission from *J. Electrochem. Soc.* 2020, 167, 066523. © The Electrochemical Society. All rights reserved.)

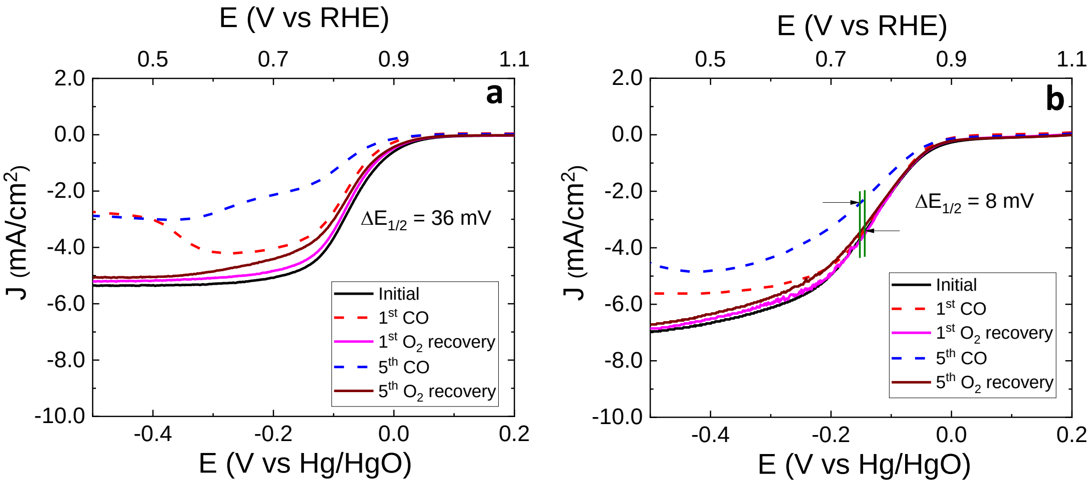

Figure A.19: LSV curves recorded at a scan rate of 10 mV/s and 1,600 rpm in 0.10 M KOH purged with pure O_2 (Initial), 10 % CO and 90% O_2 (1st CO), and re-purged with pure O_2 (1st O_2 recovery) of (a) Pt/C (12.8 µg/cm^2 Pt) and (b) Pt/VACNF (10.8 µg/cm^2 Pt). The experiments are repeated 5 times and data from the first and fifth sets are presented. (Reproduced with permission from *J. Electrochem. Soc.* 2020, 167, 066523. © The Electrochemical Society. All rights reserved.)

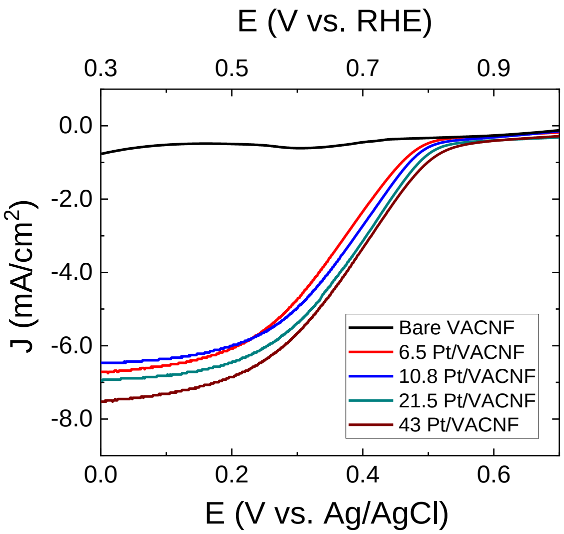

Figure A.20: LSV curves recorded at a scan rate of 10 mV/s and a rotation speed of 1,600 rpm in O_2 saturated 0.1 M $HClO_4$ solution for bare VACNF and Pt/VACNF catalysts with different Pt loadings (6.5, 10.8, 21.5 and 43.0 µg/cm^2 Pt).

The Pt/VACNF catalysts have also been investigated in an acidic medium. Figure A.20 presents the LSVs recorded at 1,600 rpm for bare VACNF and Pt/VACNF catalysts (at 6.5, 10.8, 21.5 and 43.0 µg/cm^2 Pt loading) in O_2 saturated 0.10 M $HClO_4$ solution. Even though the contribution to ORR by the bare VACNF is substantially smaller in the acidic medium, the overall properties of Pt/VACNF catalysts are similar in both acidic and alkaline conditions. The J_{lim} values of all Pt/VACNF catalysts in 0.10 M $HClO_4$ solution are higher than the theoretical value, but the J_{lim} at the low Pt loading is slightly smaller than that in alkaline medium. The change in $E_{1/2}$ with respect to the Pt loading is similar in both media. The half-wave potential $E_{1/2}$ (vs. RHE) in the acidic medium, however, shifts by about -140 mV comparing to those in the alkaline medium.

Appendix B - Supplementary Information for Chapter 4

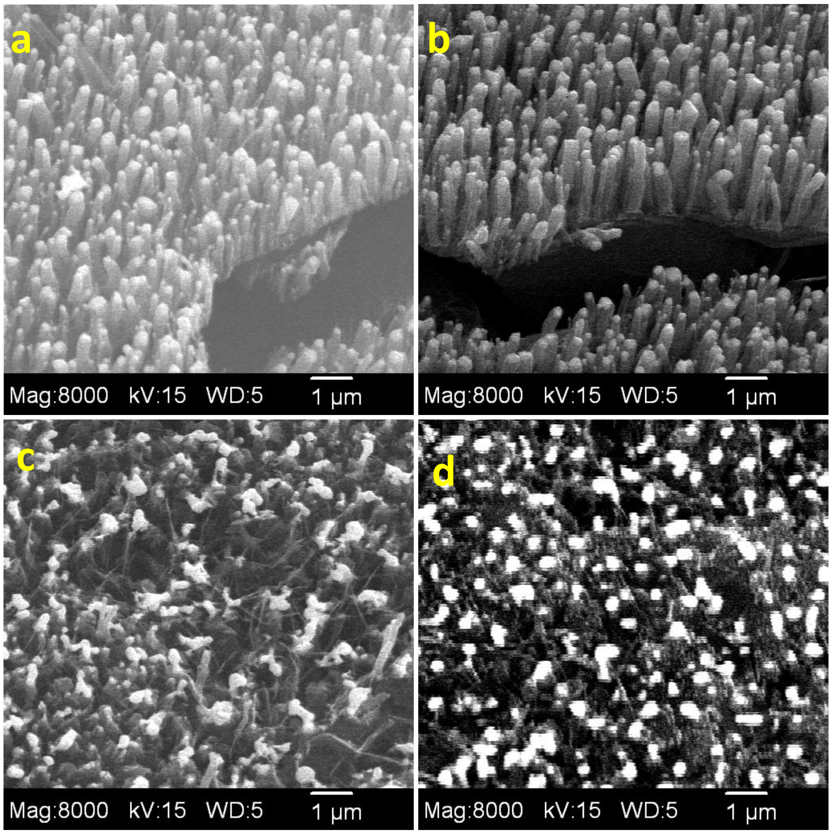

Figure B.1: FESEM images of VACNFs (a) as-grown and thermal annealed for 1 h at (b) 650 ^{o}C, (c) 700 ^{o}C, and (d) 800 ^{o}C.

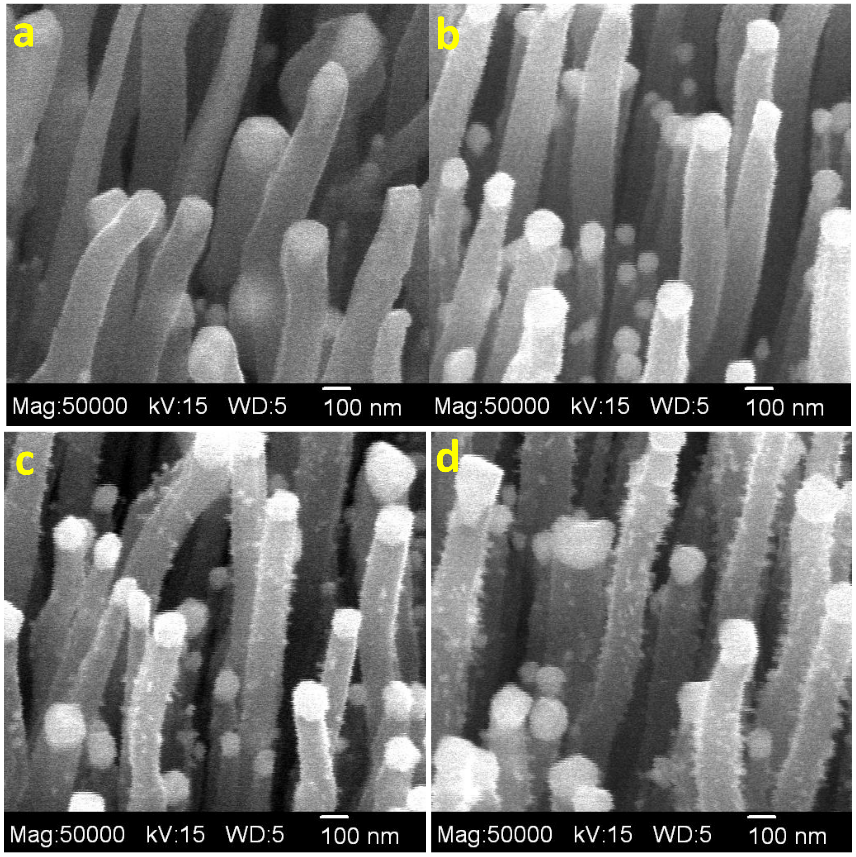

Figure B.2: FESEM images of VACNFs (a) as-grown and plasma annealed for 5 min at (b) 550 ^{o}C, (c) 600 ^{o}C, and (d) 650 ^{o}C.

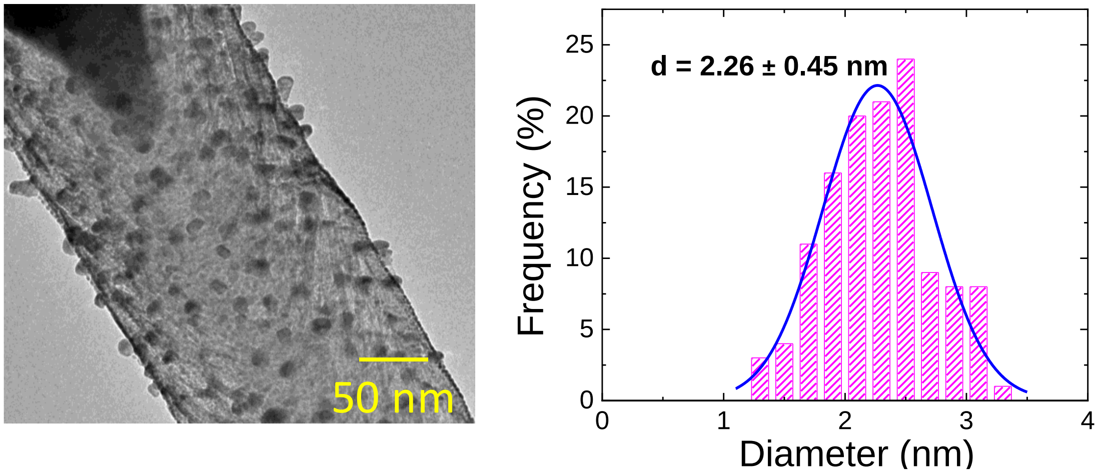

Figure B.3: TEM image of Pt/N-VACNF PA 5 min (43.0 µg/cm^2) with the corresponding particle size distribution.

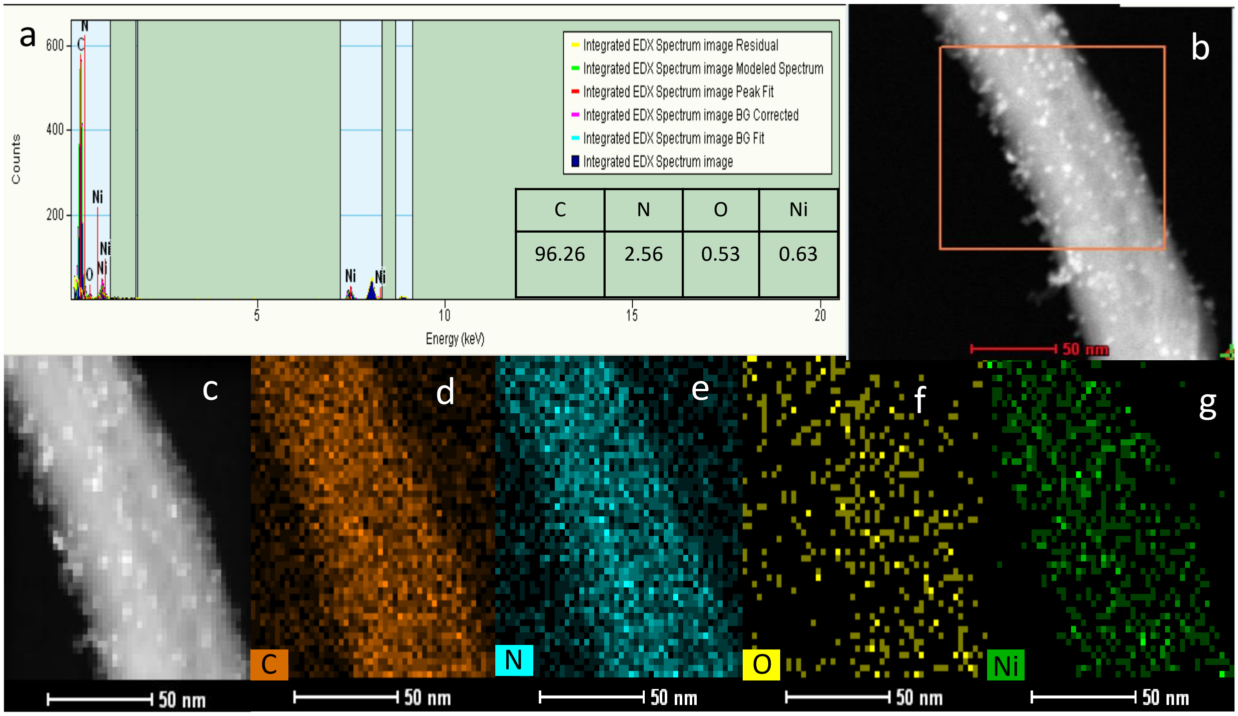

Figure B.4: (a) TEM-EDX spectrum and (b) HAADF-STEM image showing the selected area for EDX analysis of N-VACNF (PA 5 min); (c) HAADF-STEM image and (d-g) STEM-EDX mapping for all the elements of N-VACNF (PA 5 min). The inset table in (a) shows the atomic % of different elements.

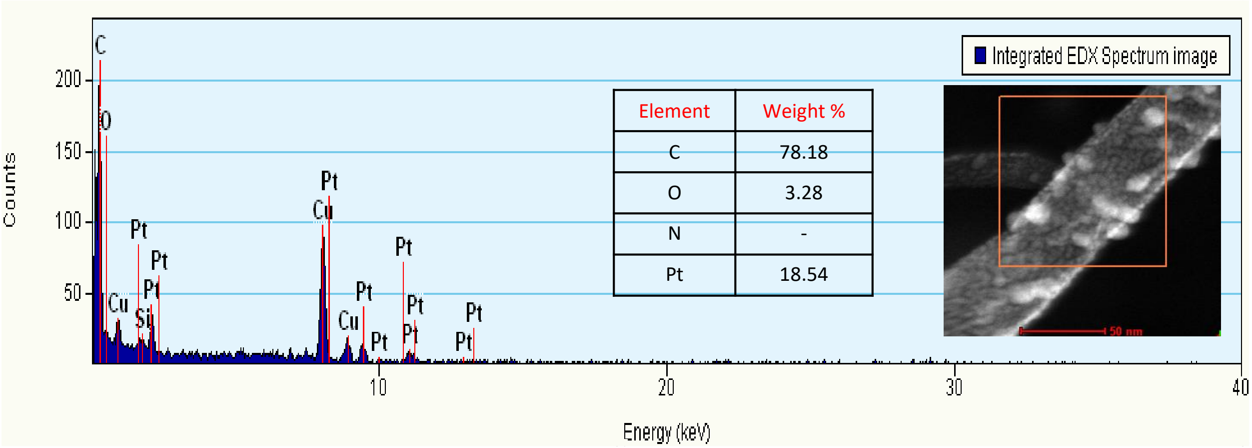

Element	Weight %
C	78.18
O	3.28
N	-
Pt	18.54

Figure B.5: TEM-EDX spectrum of Pt/N-VACNF PA 5 min (43.0 μg/cm^2). The orange rectangle in inset HAADF-STEM image shows the selected area for EDX analysis. The inset table shows the weight % of different elements.

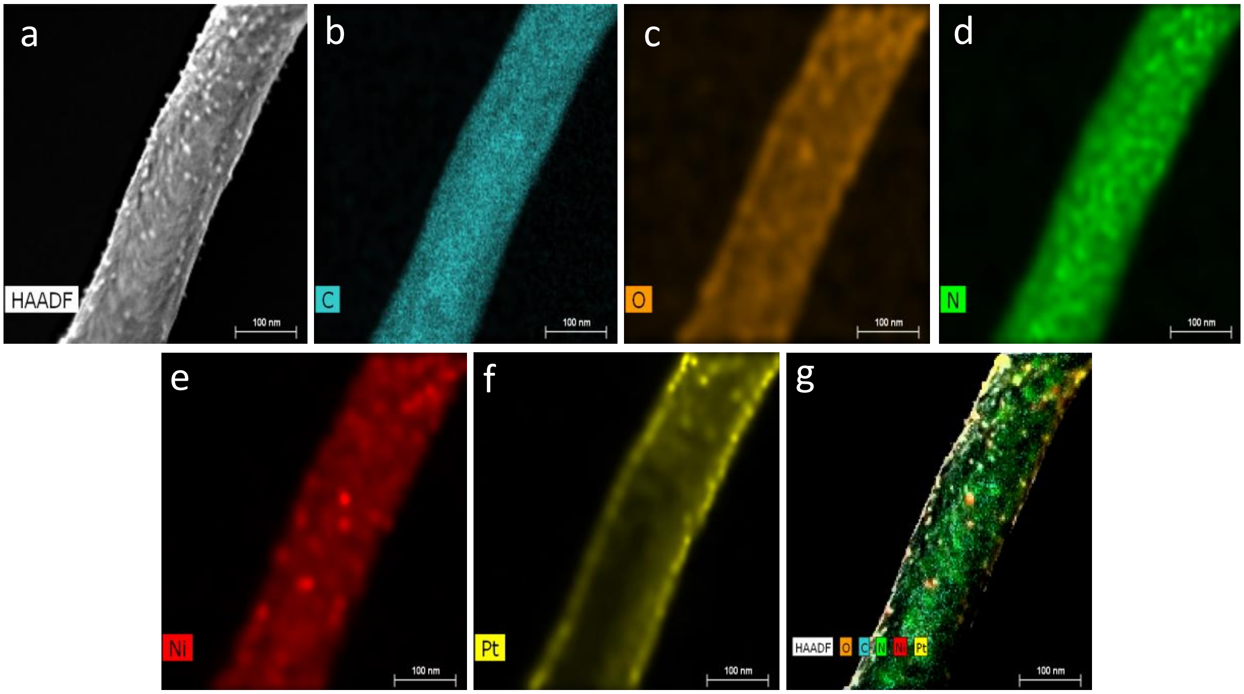

Figure B.6: (a) HAADF-STEM image and (b-g) STEM-EDX elemental mapping of Pt/N-VACNF PA 5 min (43.0 μg/cm^2).

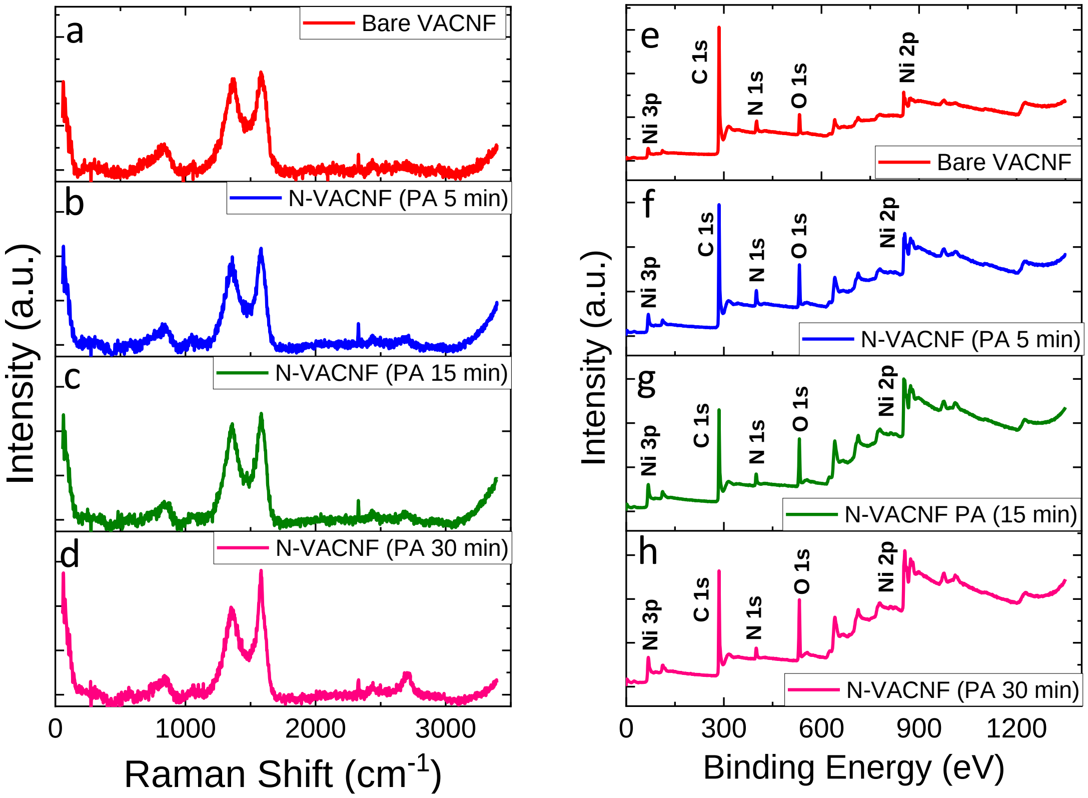

Figure B.7: (a-d) Raman spectra and (e-h) XPS survey spectra of bare VACNF, N-VACNF (PA 5 min), N-VACNF (PA 15 min), and N-VACNF (PA 30 min).

Table B.1: Atomic Percentage (at %) of the elemental species from the XPS survey spectra.

Catalyst	**at %**			
	C	**N**	**O**	**Pt**
Bare VACNF	85.9	7.4	6.7	-
VACNF PA 5 min	78.9	8.5	12.6	-
VACNF PA 15 min	74.7	8.6	16.7	-
VACNF PA 30 min	73.6	7.4	19.0	-
Pt/N-VACNF	49.1	5.1	21.4	24.4
Pt/C	93.8	3.0	-	3.2

Table B.2: Binding energies (BE) and integrated relative area % of individual chemical component from N 1s and O 1s XPS spectra of Bare VACNF, N-VACNF (PA 5min), N-VACNF (PA 15 min), and N-VACNF (PA 30 min).

XPS Spectra	Species	Bare VACNF		N-VACNF (PA 5 min)		N-VACNF (PA 15 min)		N-VACNF (PA 30 min)	
		BE (eV)	Relative Area %	BE (eV)	Relative Area %	BE (eV)	Relative Area %	BE (eV)	Relative Area %
N 1s	Pyridinic N	398.76	32.9	398.78	45.2	398.70	53.1	398.54	49.1
	Pyrrolic N	399.95	10.9	399.88	16.8	399.81	19.4	400.05	26.1
	Graphitic N	401.13	34.0	401.04	27.4	401.15	16.4	401.19	15.0
	Oxidic N	402.67, 405.13	22.2	403.46,405.43	10.6	403.28	12.1	403.75	9.8
O 1s	NiO	-	-	529.58	10.3	529.58	15.0	529.68	16.4
	C=O	531.28	20.7	531.30	24.1	531.24	26.4	531.20	17.3
	C-O	532.26	47.7	532.28	53.1	532.20	43.6	532.14	53.2
	C-O-H	533.64	23.0	533.86	12.5	533.64	15	533.64	13.1
	O in H_2O	534.72	8.6	-	-	-	-	-	-

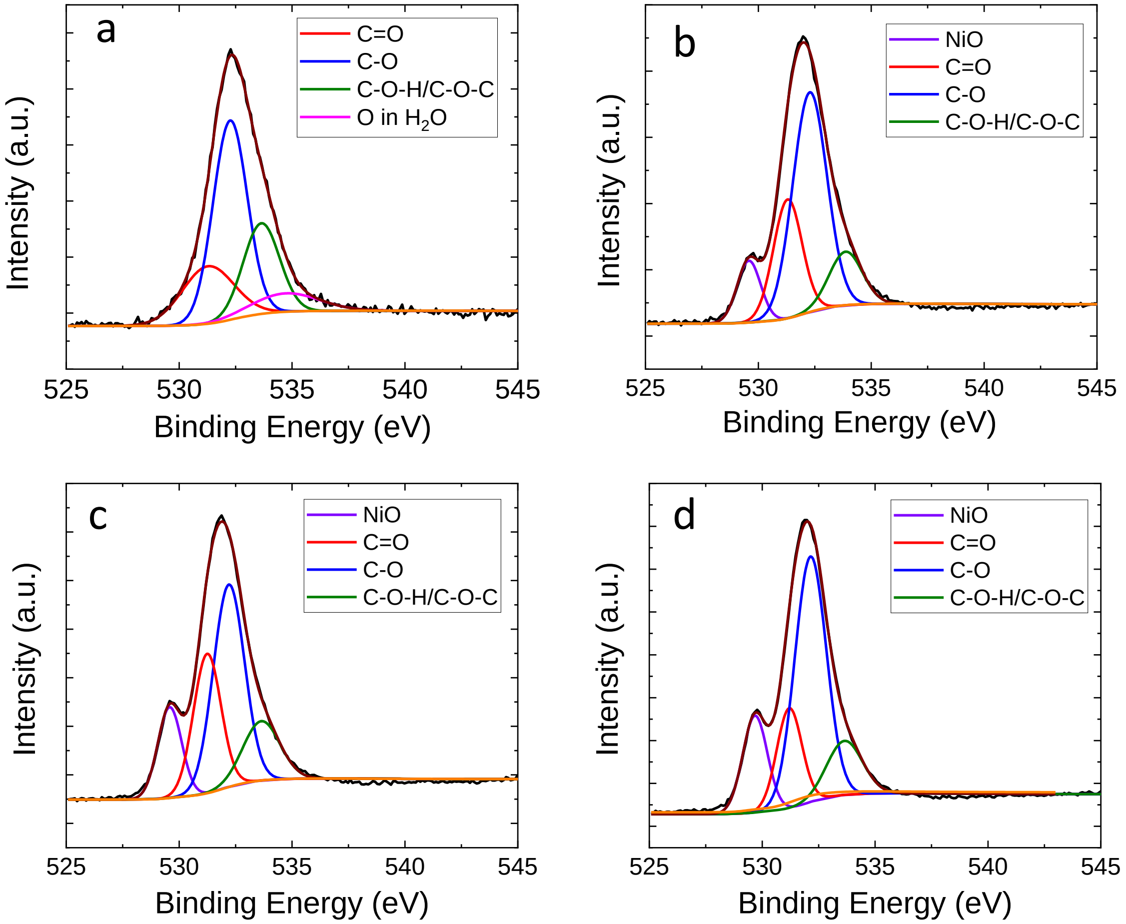

Figure B.8: O 1s XPS spectra of bare VACNF and VACNF samples plasma annealed at 550 °C for (b) 5 min, (c) 15 min, and (d) 30 min.

Table B.3: Binding energies (BE) and integrated relative area % for each species of Pt/C and Pt/N-VACNF from Pt 4f XPS spectra.

Sample	Species	BE (eV)		Relative area %
		Pt $4f_{7/2}$	Pt $4f_{5/2}$	
Pt/C	Pt^0	71.32	74.63	45.6
	Pt^{2+}	72.47	75.59	41.1
	Pt^{4+}	77.70	79.90	13.3
Pt/N-VACNF	Pt^0	71.13	74.41	57.2
	Pt^{2+}	72.50	75.48	30.2
	Pt^{4+}	77.07	79.49	12.6

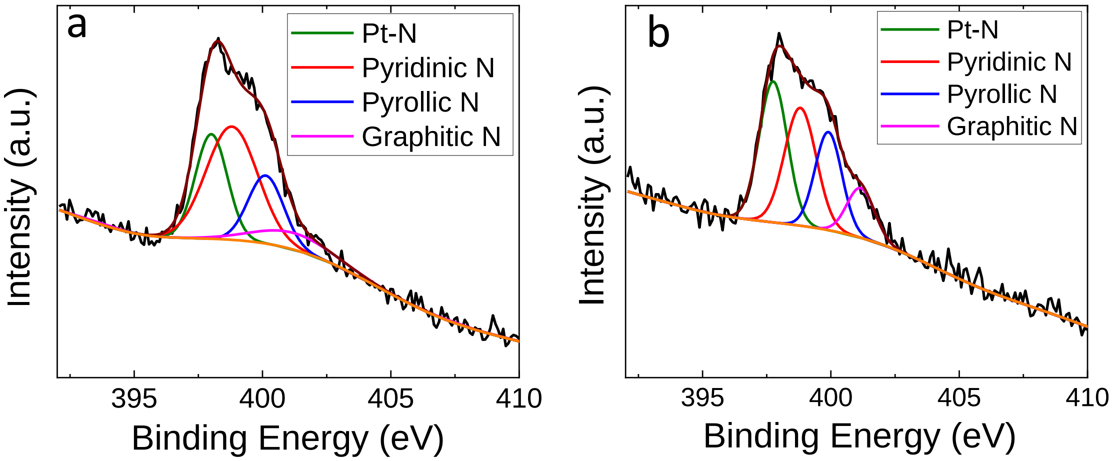

Species	Pt/VACNF		Pt/N-VACNF	
	BE (eV)	Relative Area %	BE (eV)	Relative Area %
Pt-N	398.00	26.0	397.75	33.9
Pyridinic N	398.81	45.3	398.80	31.8
Pyrrolic N	400.13	17.6	399.90	22.5
Graphitic N	401.20	11.1	401.16	11.8

Figure B.9: N 1s XPS spectra of (a) Pt-/VACNF (43.0 μg/cm^2) and (b) Pt/N-VACNF PA 5 min (43.0 μg/cm^2).

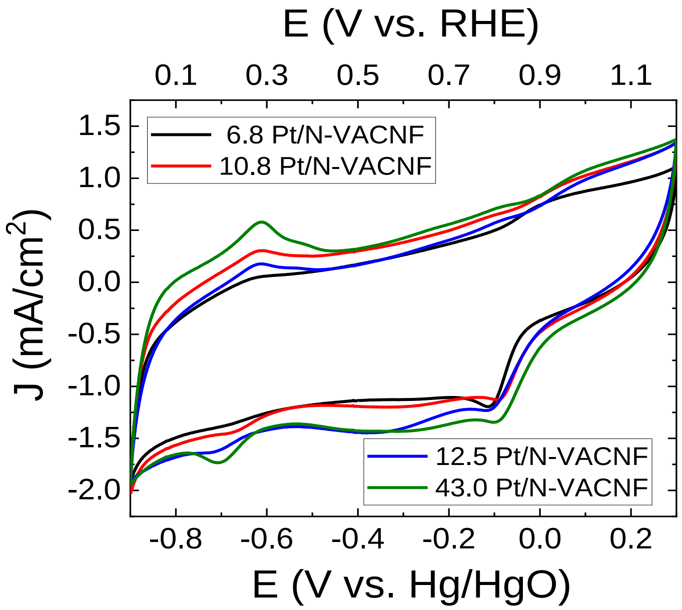

Figure B.10: CV curves recorded at a scan rate of 50 mV/s in O_2 saturated 0.10 M KOH solution for N-VACNF (PA 5 min) catalysts with different Pt loadings (6.5, 10.8, 21.5 and 43.0 µg/cm^2).

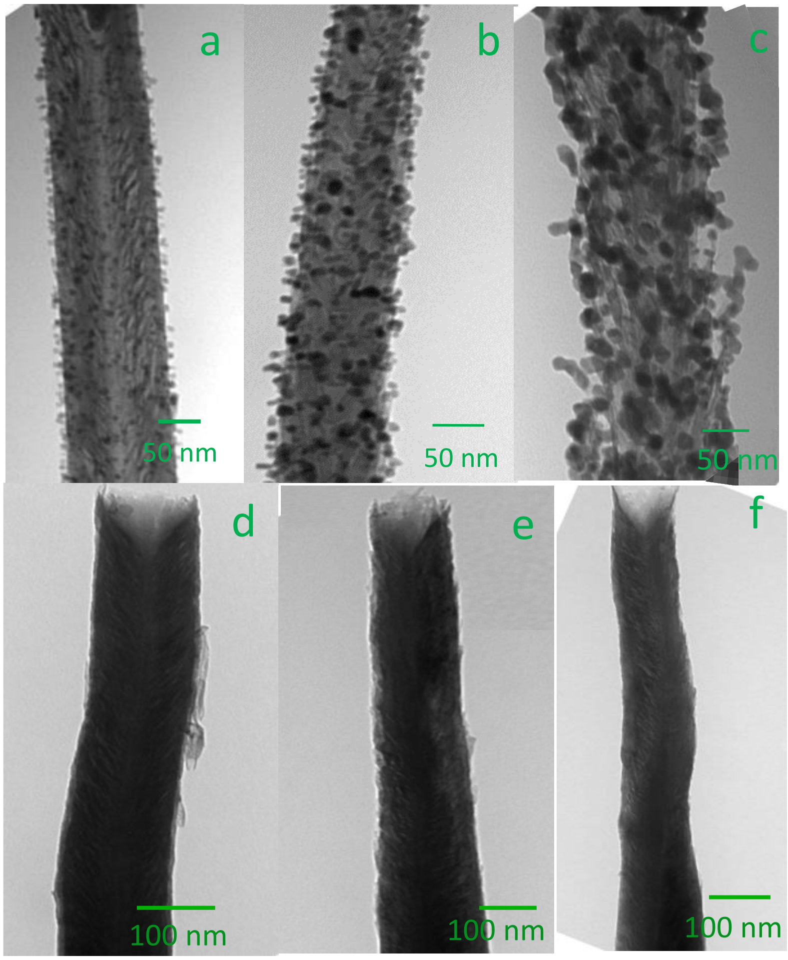

Figure B.11: TEM image of N-VACNF (PA 5 min), N-VACNF (PA 15 min), and N-VACNF (PA 30 min) (a-c) as-prepared and (d-f) after treatment in HNO_3.

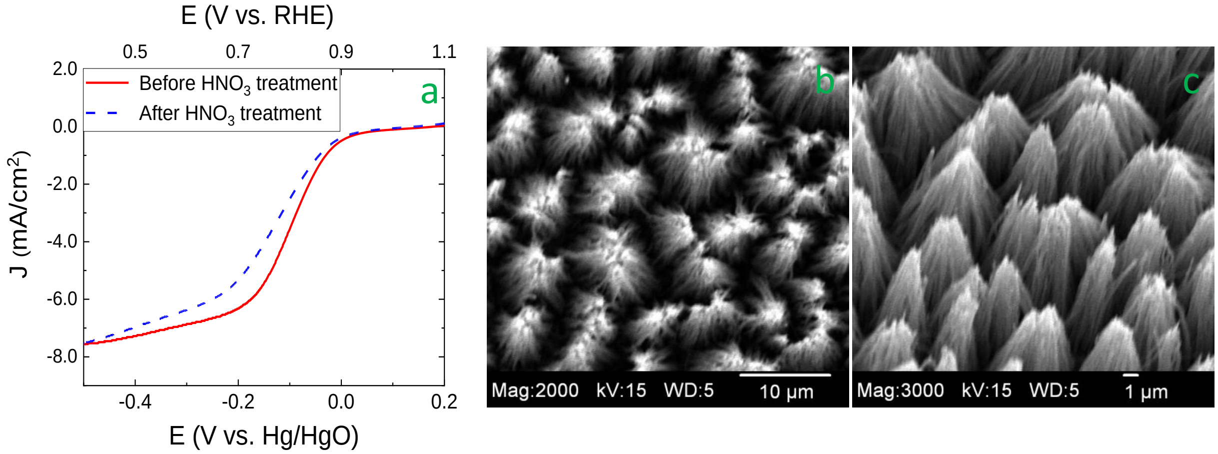

Figure B.12: (c) LSV recorded at 1600 rpm in O_2-saturated 0.10 M KOH solution with Pt sputtered without any treatment in HNO_3 and after treatment in HNO_3 for Pt/N-VACNF PA 5 min (43.0 μg/cm^2); (a and b) FESEM image of N-VACNF (PA 5 min) after contact with solution.

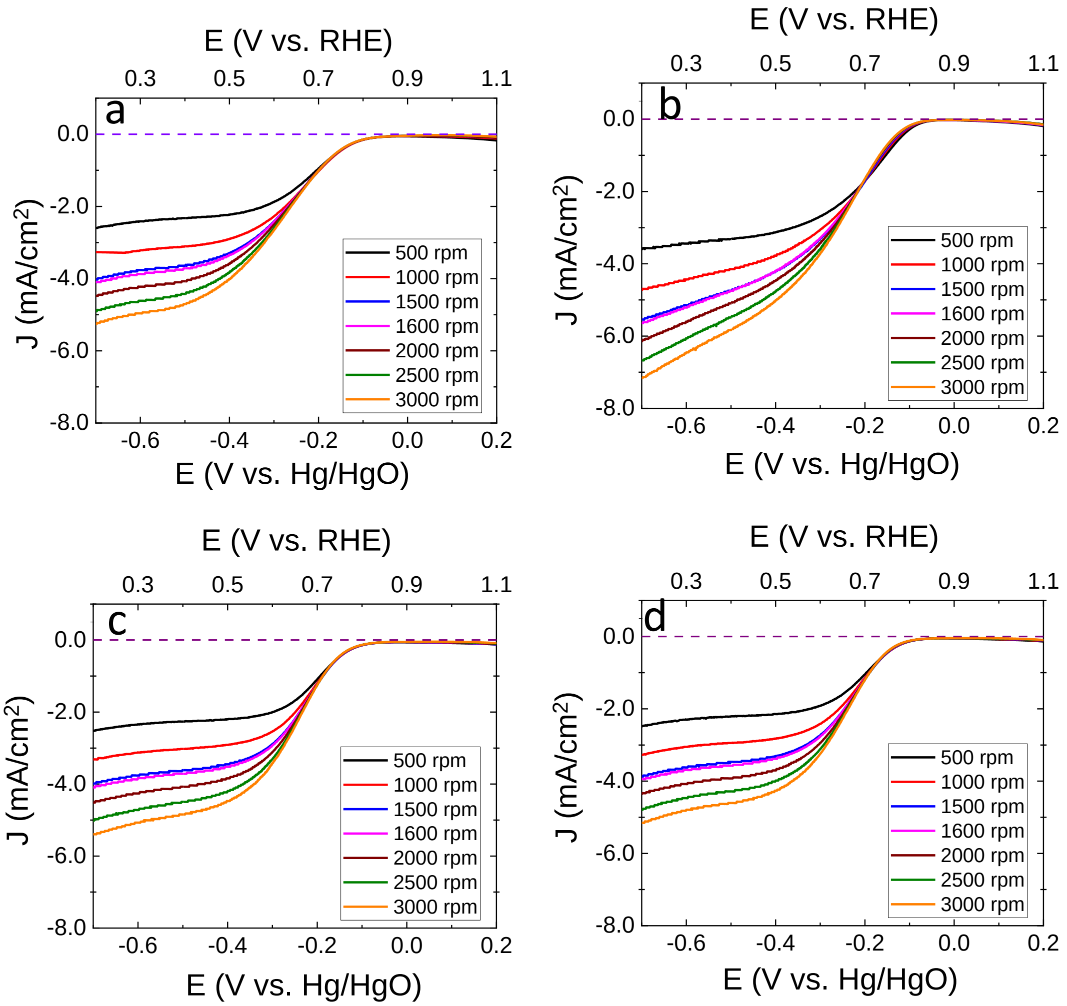

Figure B.13: RDE LSV voltammogram of (a) bare VACNF, (b) N-VACNF (PA 5 min), (c) N-VACNF (PA 15 min), and (d) N-VACNF (PA 30 min) in O_2-saturated 0.10 M KOH solution at a scan rate of 10 mV/s and at a rotation speed from 500 to 3000 rpm. The purple dash-line marks the zero current density.

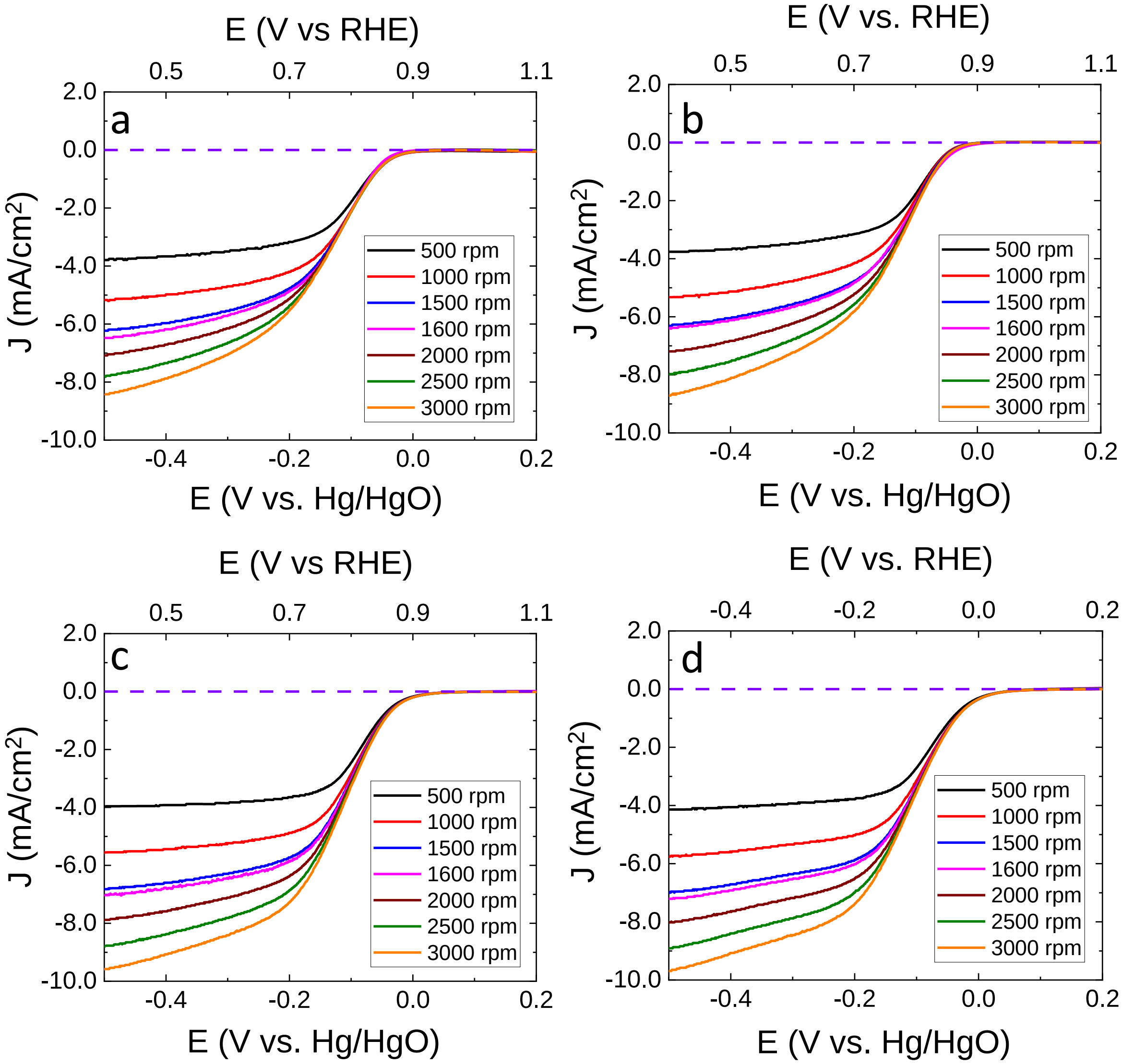

Figure B.14: RDE LSV voltammogram of (a) Pt/N-VACNF (6.5 μg/cm^2 Pt), (b) Pt/N-VACNF (10.8 μg/cm^2 Pt), (c) Pt/N-VACNF (21.5 μg/cm^2 Pt), and (d) Pt/N-VACNF (43.0 μg/cm^2 Pt) in O_2-saturated 0.10 M KOH solution at a scan rate of 10 mV/s and at a rotation speed from 500 to 3000 rpm. The purple dash-line marks the zero current density.

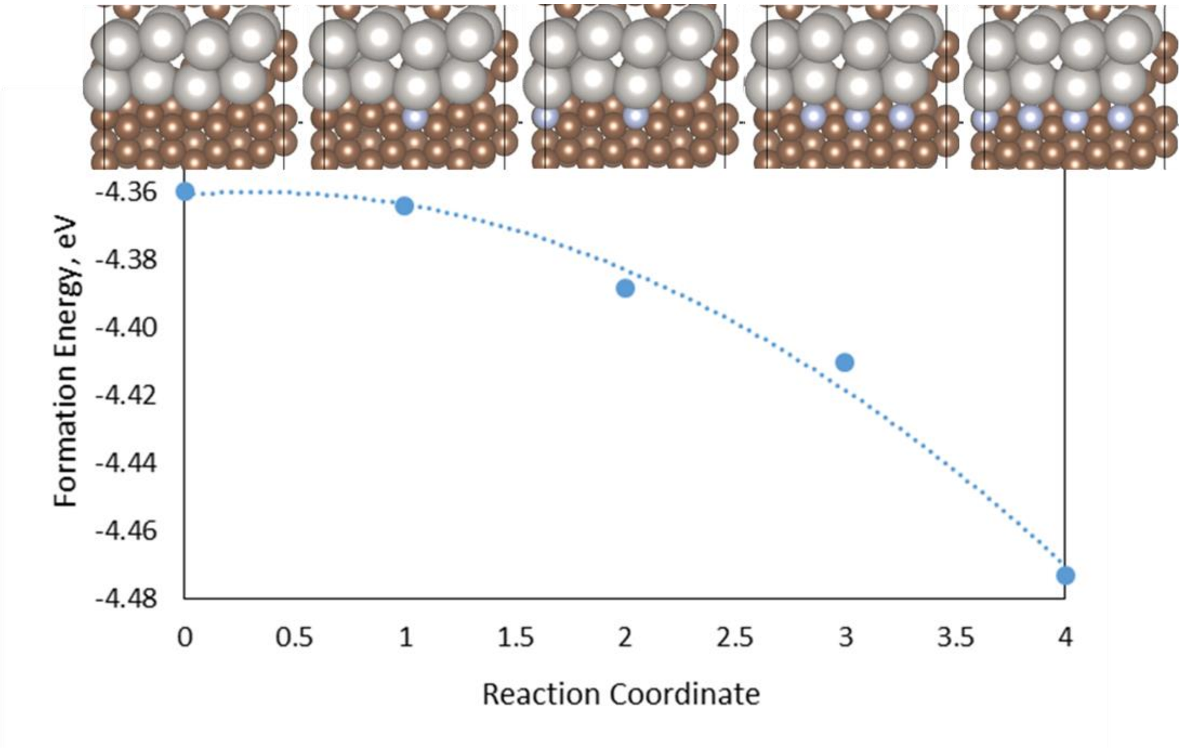

Figure B.15: Stability analysis of Pt particles over pyridinic nitrogen doped edge.

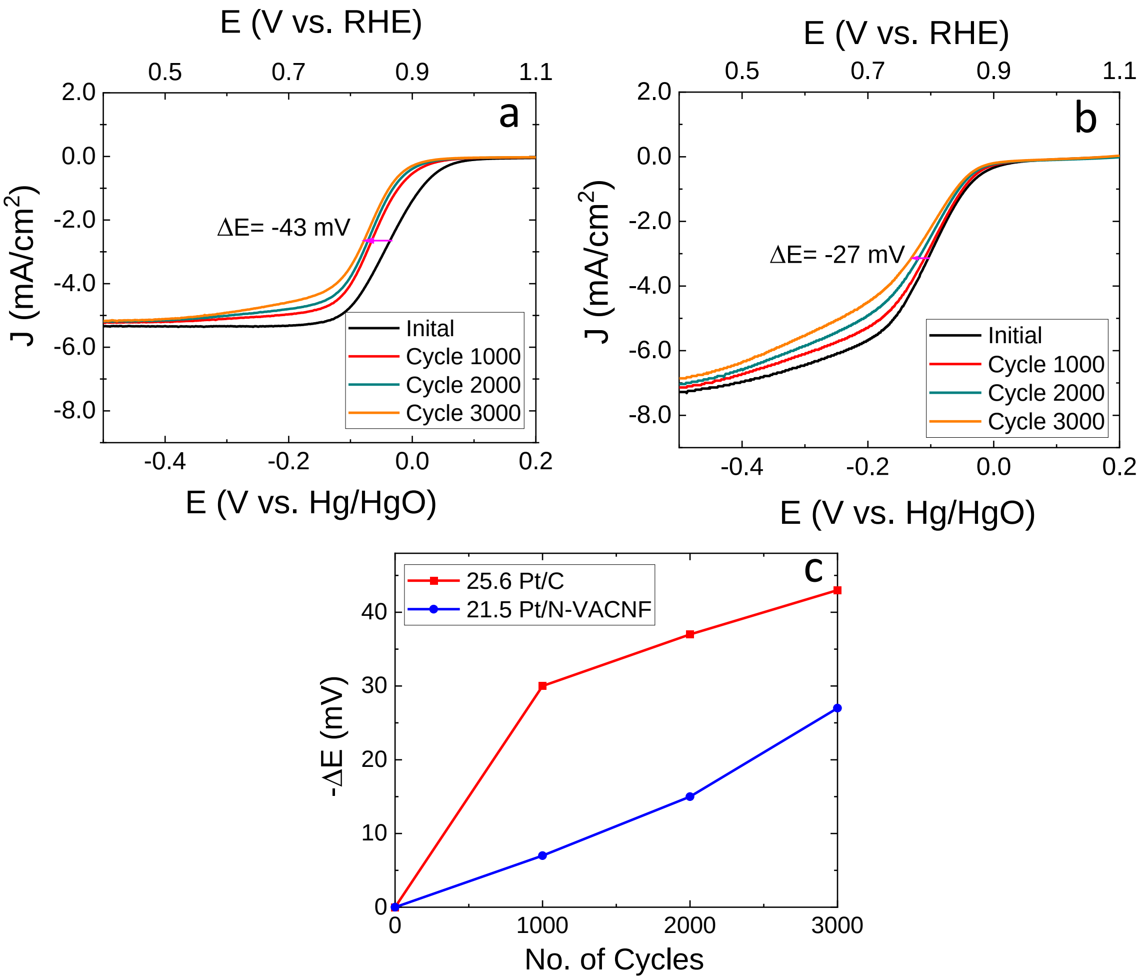

Figure B.16: LSV curves of (a) Pt/C (25.6 μg/cm^2) and (b) Pt/N-VACNF (21.5 μg/cm^2) after every 1000 AST cycles in O_2-saturated 0.10 M KOH solution at a scan rate of 10 mV/s and a rotation speed of 1600 rpm; (c) Change in the half-wave potential of the LSV curves vs. the number of AST cycles for both the catalysts.

Appendix C - Supplementary Information for Chapter 5

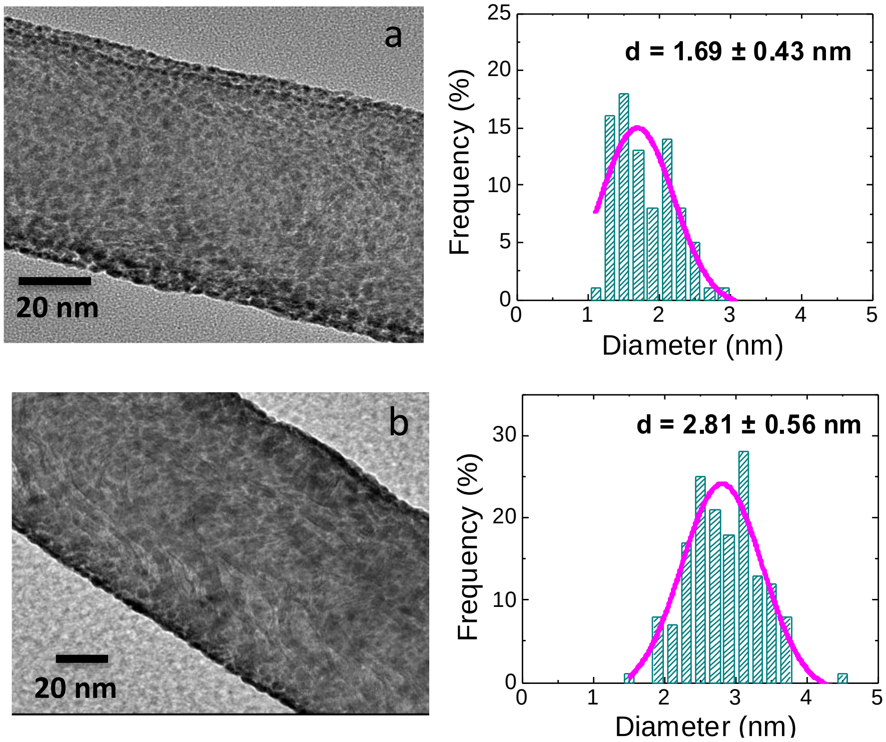

Figure C.1: TEM image of (a) Pt/VACNF (21.5 µg/cm^2) and (b) PtRu/VACNF (43.0 µg/cm^2) with their corresponding particle size distribution.

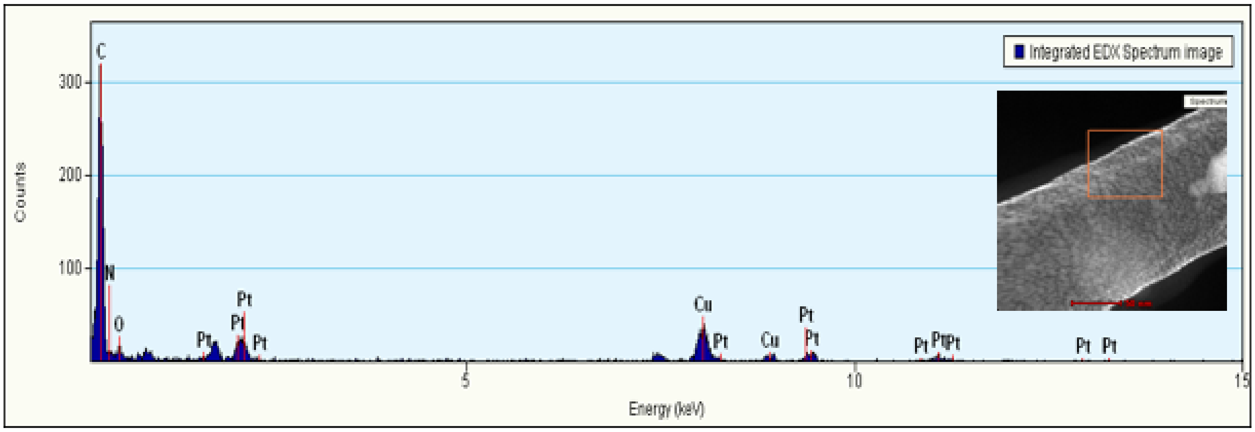

Figure C.2: TEM EDX spectrum of Pt/VACNF (21.5 µg/cm^2). The orange rectangle in the inset HAADF image shows the selected EDX analysis area.

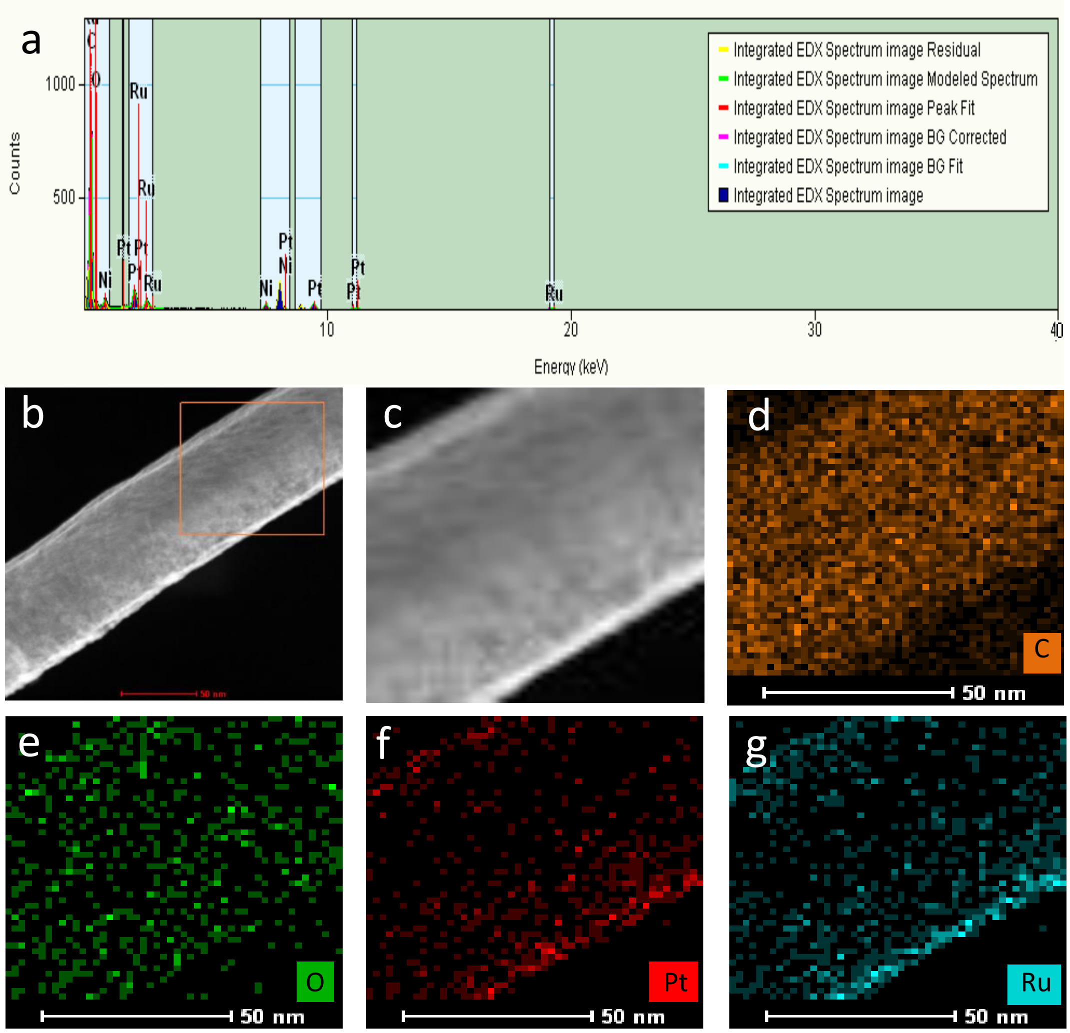

Figure C.3: (a) TEM-EDX spectrum and (b) HAADF-STEM image showing the selected area for EDX analysis of PtRu/VACNF (43.0 µg/cm^2); (c) HAADF-STEM image and (c-g) STEM-EDX mapping of PtRu/VACNF (43.0 µg/cm^2) for the following elements: C, O, Pt, and Ru.

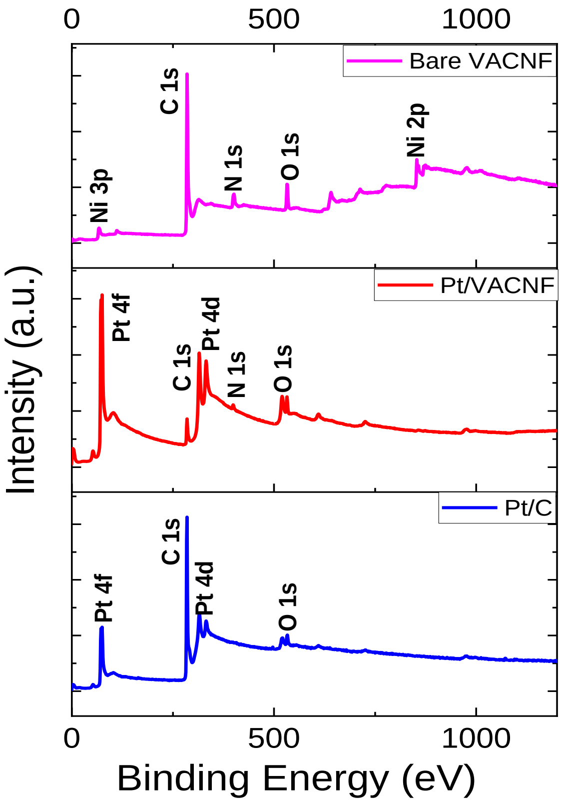

Figure C.4: XPS survey spectra of (a) bare VACNF, (b) Pt/VACNF, and (c) Pt/C.

Table C.1: Atomic Percentage (at %) of the elemental species from the XPS survey spectra.

Catalyst	**At %**			
	C	**O**	**N**	**Pt**
Bare VACNF	85.9	6.7	7.4	-
Pt/VACNF	50.7	14.5	6.9	27.9
Pt/C	93.8	3.0	-	3.2

Table C.2: Binding energies and relative integrated area % of individual chemical component from C 1s, O 1s and N1s XPS spectra of bare VACNF, Pt/VACNF, and Pt/C .

XPS Spectra	Species	Bare VACNF		Pt/VACNF		Pt/C	
		Binding Energy (eV)	Relative Area %	Binding Energy (eV)	Relative Area %	Binding Energy (eV)	Relative Area %
C 1s	Carbides	283.71	2.2	283.42	1.5	283.13	4.6
	sp^2 C	284.50	48.6	284.58	69.0	284.40	60.7
	C-O/C=N	285.82	14.1	285.80	9.2	285.80	15.1
	O-C-O/C-N	286.70	16.6	286.60	7.8	-	-
	C=O	287.73	2.7	287.71	9.3	287.63	7.4
	O-C=O	288.70	5.6	288.77	3.2	-	-
	p→p*	291.48	10.2	-	-	290.73	12.2
O 1s	C=O	531.28	20.7	531.20	36.0	531.14	23.4
	C-O	532.26	47.7	532.22	52.5	532.29	45.1
	O-H	533.64	23.0	533.52	11.5	533.50	28.6
	O in H_2O	534.72	8.6	-	-	535.01	2.9
N 1s	Pt-N	-	-	398.00	26.0	-	-
	Pyridinic N	398.76	32.9	398.81	45.3	-	-
	Pyrrolic N	399.95	10.9	400.13	17.6	-	-
	Graphitic N	401.13	34.0	401.20	11.1	-	-
	Oxidic N	402.67, 405.13	22.2	-	-	-	-

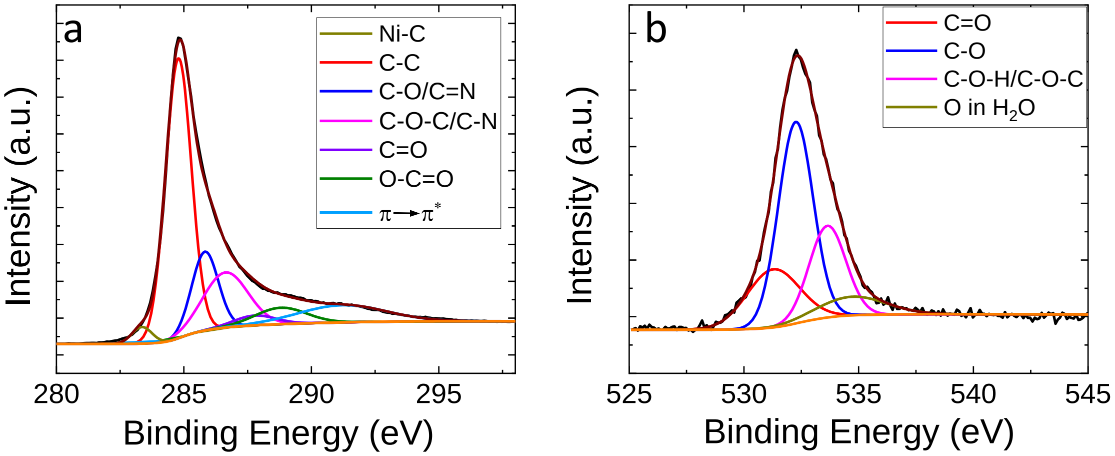

Figure C.5: (a) C 1s and (b) O 1s XPS spectra of bare VACNF.

Table C.3: Binding energies and relative integrated area for each species in Pt/C and Pt/VACNF from Pt 4f XPS spectra.

Sample	Species	Binding energy (eV)		Relative area %
		Pt $4f_{7/2}$	Pt $4f_{5/2}$	
Pt/C	Pt^0	71.32	74.63	45.6
	Pt^{2+}	72.47	75.59	41.1
	Pt^{4+}	77.70	79.90	13.3
Pt/VACNF	Pt^0	71.12	74.40	53.4
	Pt^{2+}	72.30	75.41	34.5
	Pt^{4+}	77.13	79.73	12.1

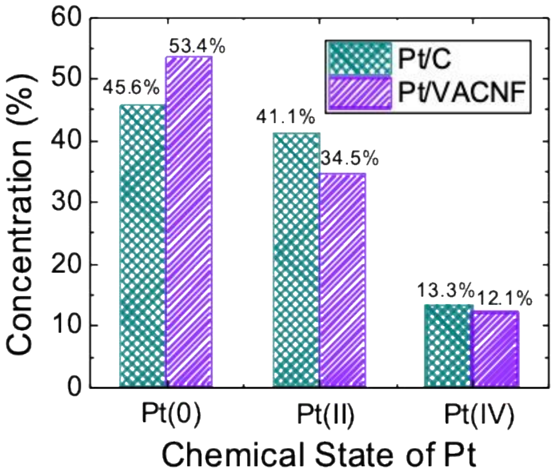

Figure C.6: Plot of chemical state of Pt vs. their corresponding relative % concentration derived from Pt 4f spectra of Pt/C and Pt/VACNF

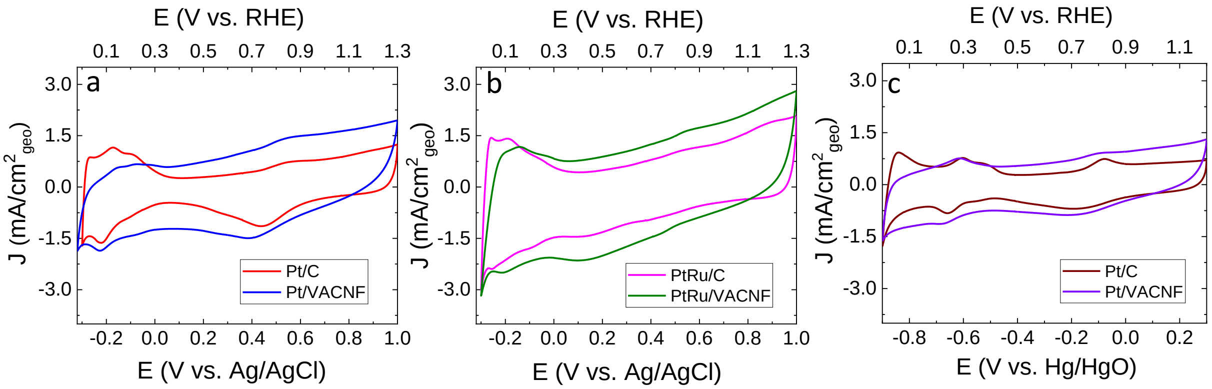

Figure C.7: Cyclic voltammogram of (a) Pt/C (25.6 µg/cm^2), Pt/VACNF (21.5 µg/cm^2) and (b) PtRu/C VACNF (48.0 µg/cm^2), PtRu/VACNF (43.0 µg/cm^2) recorded in Ar saturated 0.10 M $HClO_4$ solution at a scan rate of 50 mV/s; (c) Cyclic voltammogram of Pt/C (25.6 µg/cm^2) and Pt/VACNF (21.5 µg/cm^2) recorded in Ar saturated 0.10 M KOH solution at a scan rate of 50 mV/s.

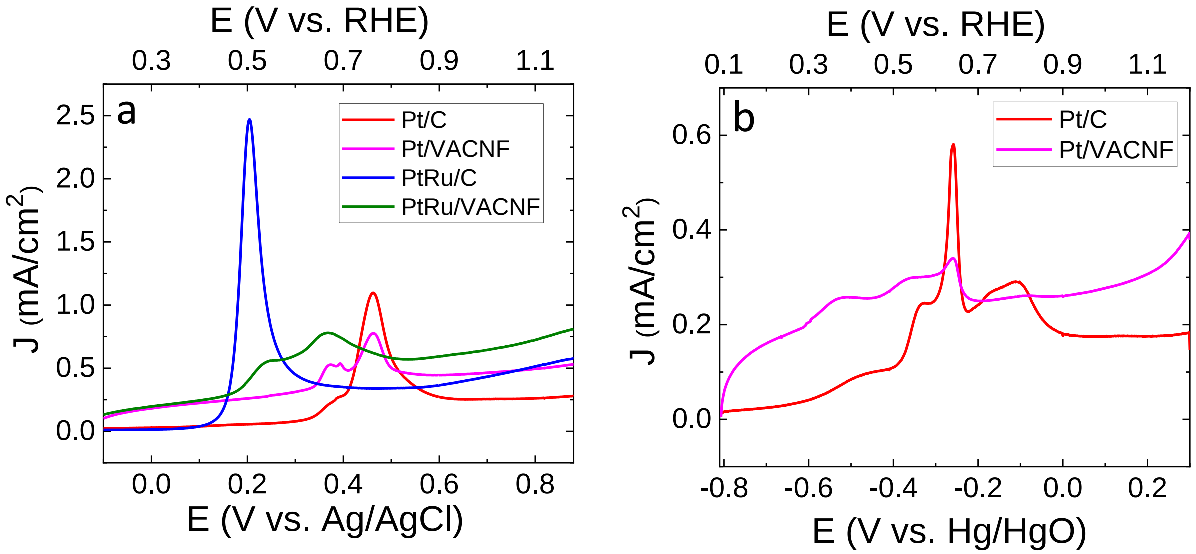

Figure C.8: First anodic scan of CO Stripping curves of (a) Pt/C (25.6 µg/cm^2), (b) Pt/VACNF (21.5 µg/cm^2), (c) PtRu/C (48.0 µg/cm^2), and (d) PtRu/VACNF (43.0 µg/cm^2) recorded in 0.10 M $HClO_4$ solution at a scan rate of 10 mV/s; First anodic scan of CO Stripping curves of (e) Pt/C (25.6 µg/cm^2) and (f) Pt/VACNF (21.5 µg/cm^2) recorded in 0.10 M KOH solution at a scan rate of 10 mV/s. All current densities were relative to the geometric surface area of electrodes.

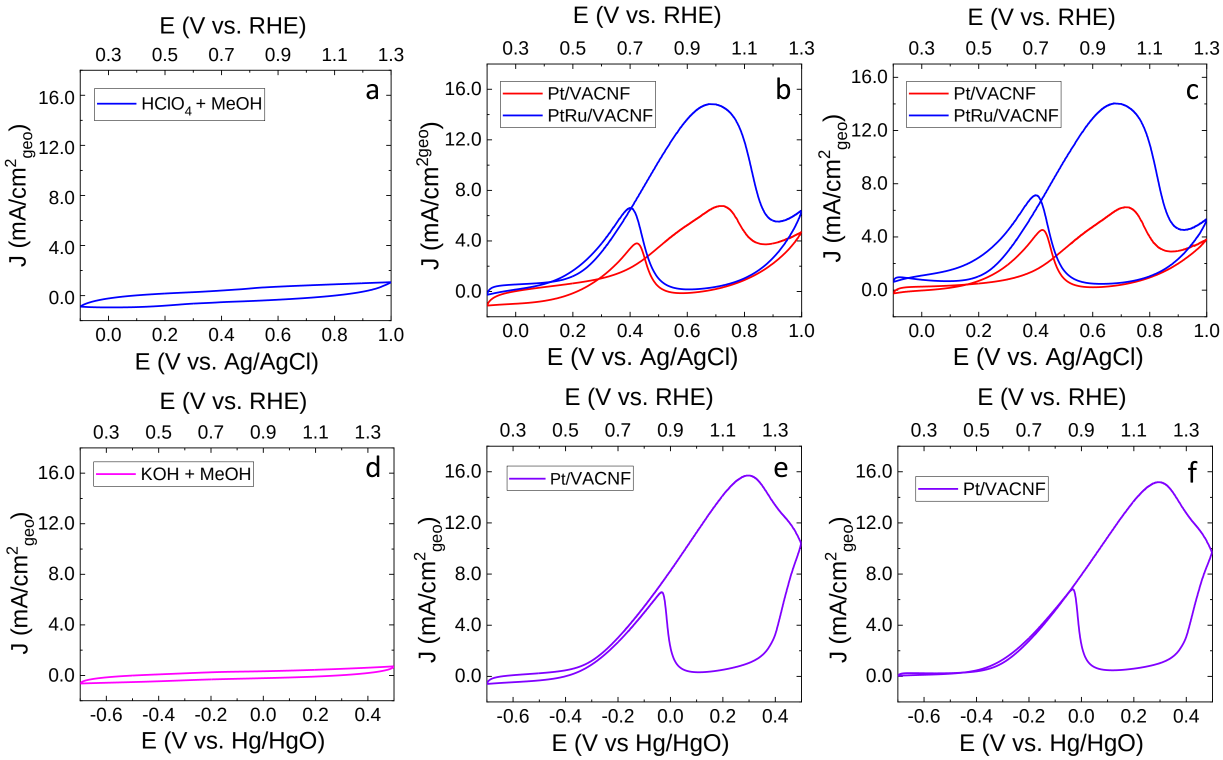

Figure C.9: Cyclic voltammograms in Ar-purged 0.10 M $HClO_4$ containing 0.75 M MeOH: (a) with a bare graphite paper electrode; and with Pt/VACNF and PtRu/VACNF electrodes (b) before and (c) after subtracting the background in (a); Cyclic voltammograms in Ar-purged 0.10 M KOH containing 0.75 M MeOH: (d) with a bare graphite paper electrode; and with a Pt/VACNF electrode (e) before and (f) after subtracting the background in (d). All CVs are recorded at 50 mV/s scan rate. All current densities were relative to the geometric surface area of electrodes.

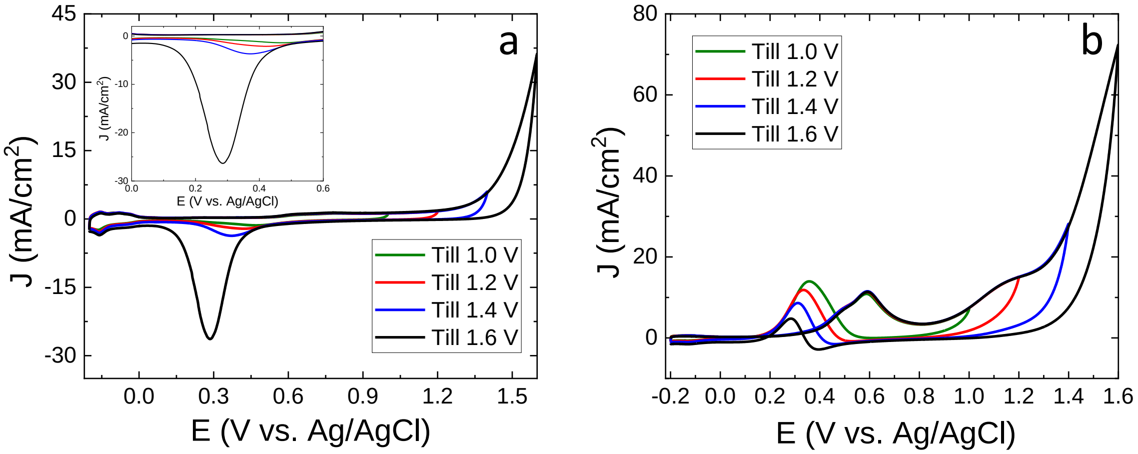

Anodic Potential Limit	Till 1.0 V	Till 1.2 V	Till 1.4 V	Till 1.6 V
PtO Reduction Charge (μC/cm^2)	6210	9670	14200	77800

Figure C.10: Cyclic voltammograms of Pt/C recorded at 50 mV/s scan rate with different anodic potential limit in Ar-purged 0.5 M H$_2$SO$_4$ (a) without and (b) with 0.35 M MeOH. The PtO reduction charge was calculated from Figure C.10a.

Appendix D - Supplementary Information for Chapter 6

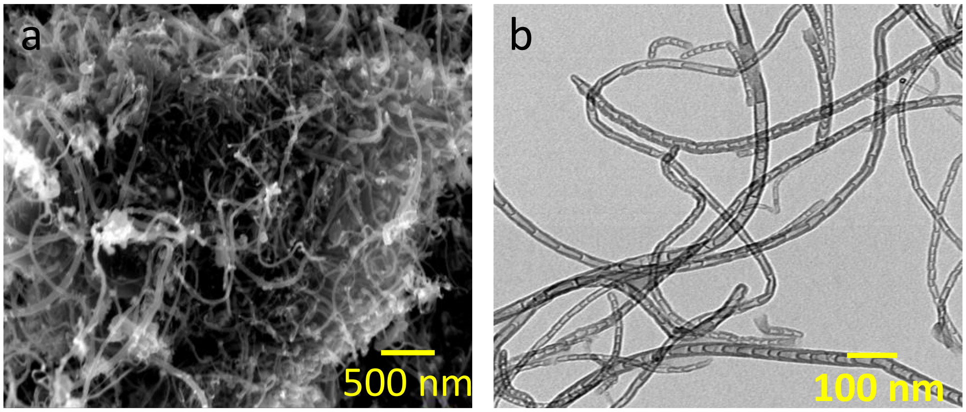

Figure D.1: (a) SEM and (b) TEM image of NCNT.

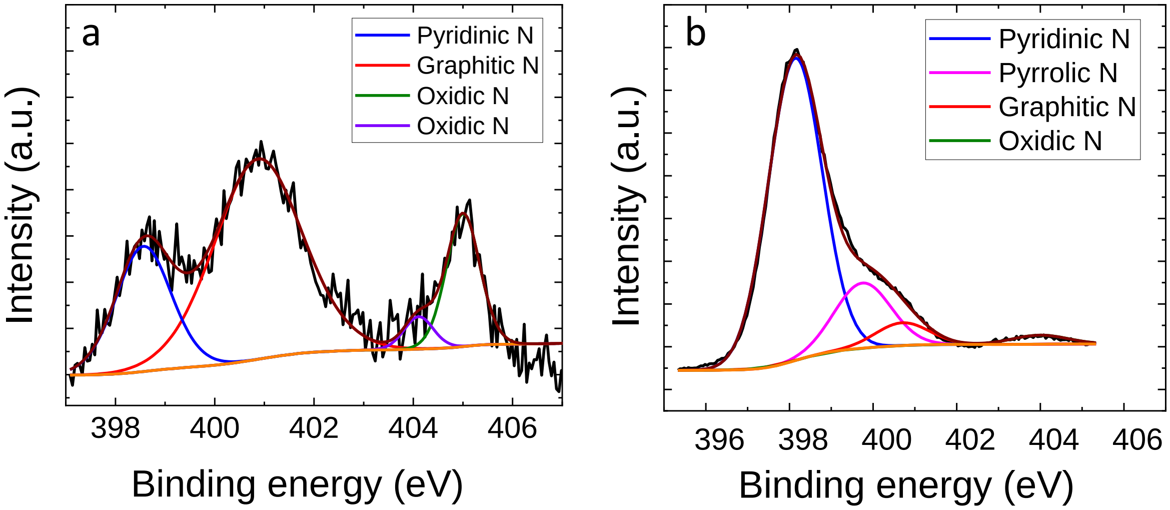

	Pyridinic N	**Pyrrolic N**	**Graphitic N**	**Oxidic N**
NCNTs	0.4	-	1.0	0.3
g-C_3N_4	40.4	9.0	3.0	1.2

Figure D.2: N 1s XPS Spectra of (a) N-CNF and (b) g-C_3N_4.

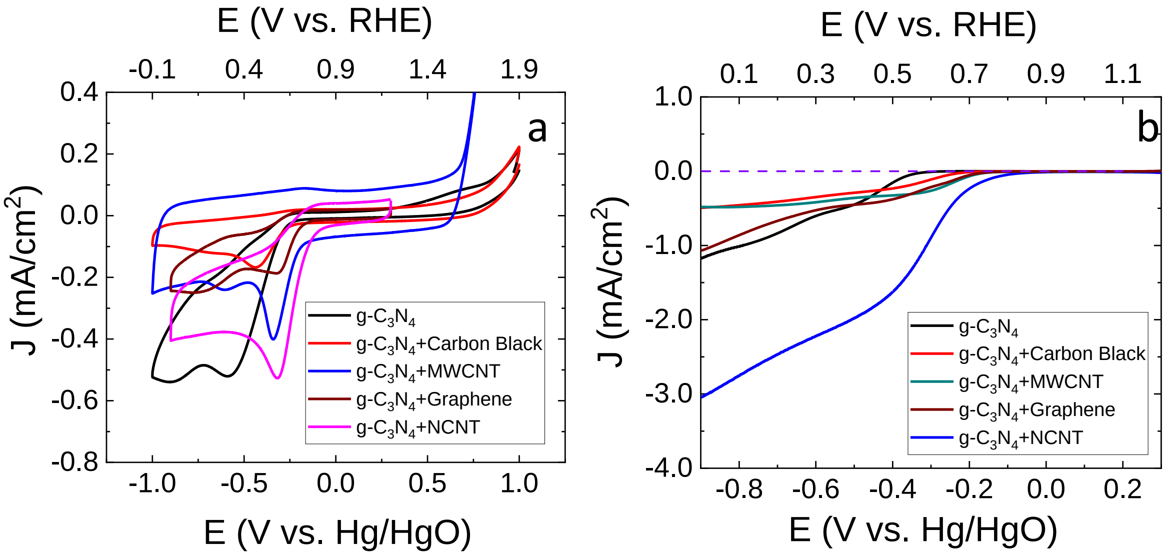

Figure D.3: (a) CV curves recorded in O_2-saturated 0.10 M KOH solution at a scan rate of 50 mV/s and (b) LSV curves recorded at a scan rate of 10 mV/s and a rotation speed of 1,600 rpm in O_2-saturated 0.10 M KOH solution for g-C_3N_4, g-C_3N_4+Carbon Black, g-C_3N_4+MWCNT, g-C_3N_4+Graphene, and g-C_3N_4+NCNT. The purple dash line marks the zero current density.

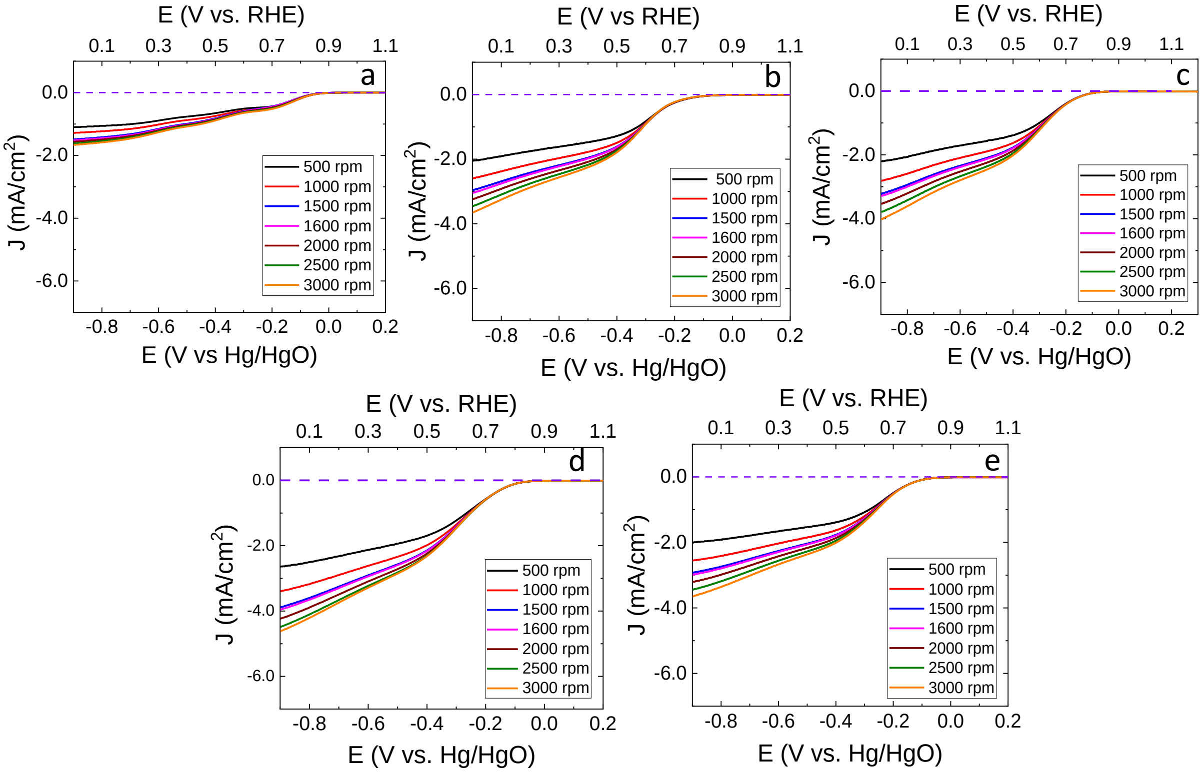

Figure D.4: RDE LSV voltammogram for (a) g-C_3N_4, (b) g-C_3N_4+NCNT, (c) g-C_3N_4+NCNT-450 °C, (d) g-C_3N_4+NCNT- 500 °C, and (e) g-C_3N_4+NCNT- 550 °C with background corrected recorded in 0.10 M KOH solution at a scan rate of 10 mV/s in the negative direction and at a rotation speed from 500 to 3000 rpm. The purple dash lines mark the zero current density.

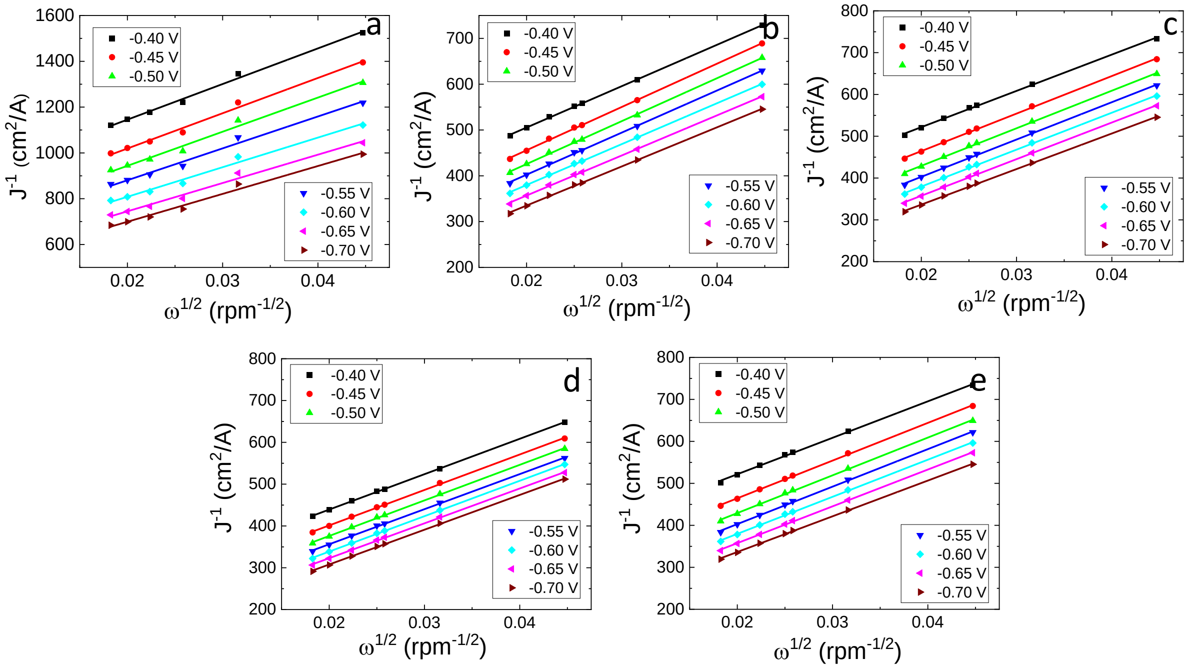

Figure D.5: Koutecky-Levich plots at different potentials for (a) g-C_3N_4, (b) g-C_3N_4+NCNT, (c) g-C_3N_4+NCNT- 450 °C, (d) g-C_3N_4+NCNT- 500 °C, and (e) g-C_3N_4+NCNT- 550 °C. (The current density at each potential was calculated by subtracting the background contribution measured in Ar).

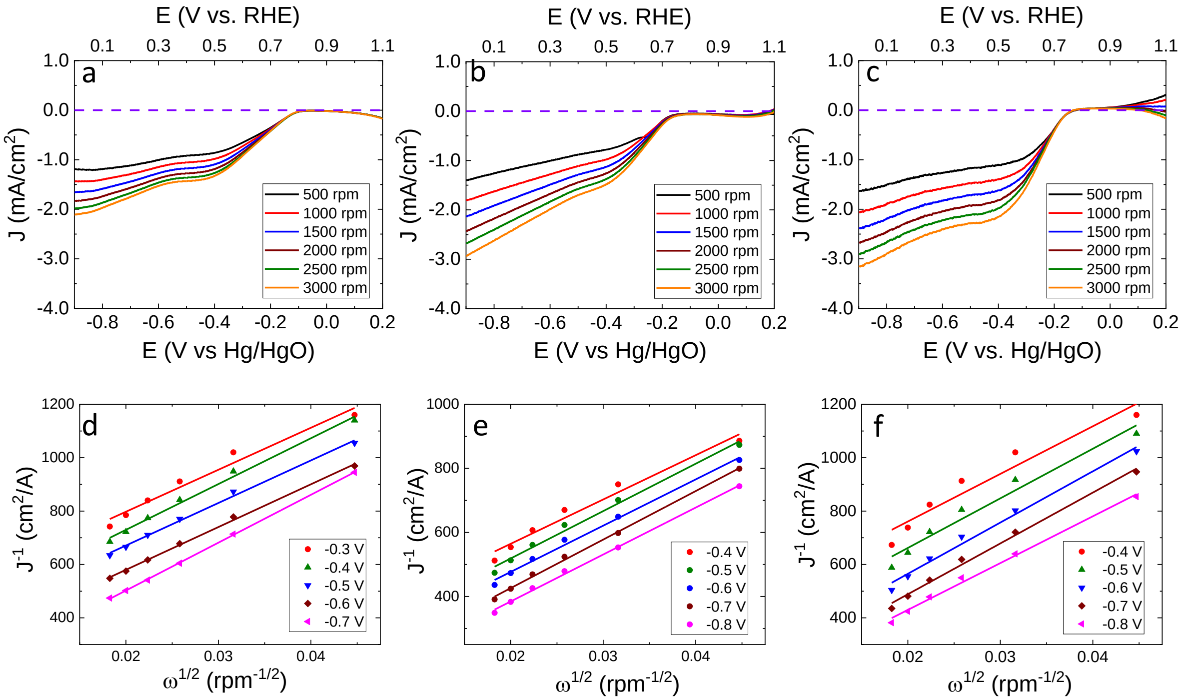

Figure D.6: RDE LSV voltammogram of MoS$_2$-rGO (a) No annealing, (b) annealed at 450 °C, and (c) annealed at 600 °C with background corrected recorded in 0.10 M KOH solution at a scan rate of 10 mV/s in the negative direction and at a rotation speed from 500 to 3000 rpm. The purple dash lines mark the zero current density; Koutecky-Levich plots at different potentials for MoS$_2$-rGO (d) No annealing, (e) annealed at 450 °C, and (f) annealed at 600 °C (The current density at each potential was calculated by subtracting the background contribution measured in Ar).

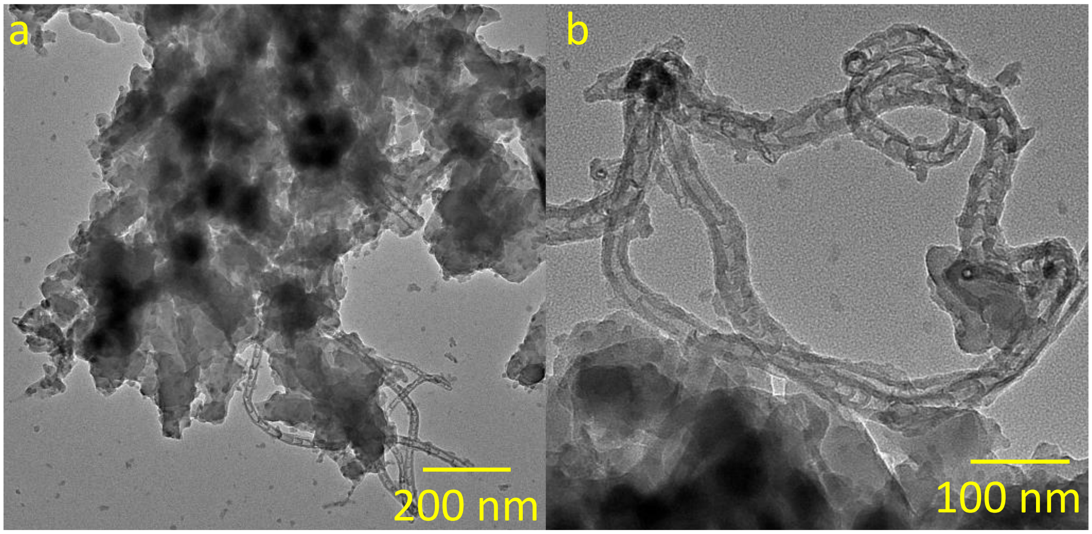

Figure D.7: TEM image of Fe-PANI-CNF after synthesis.

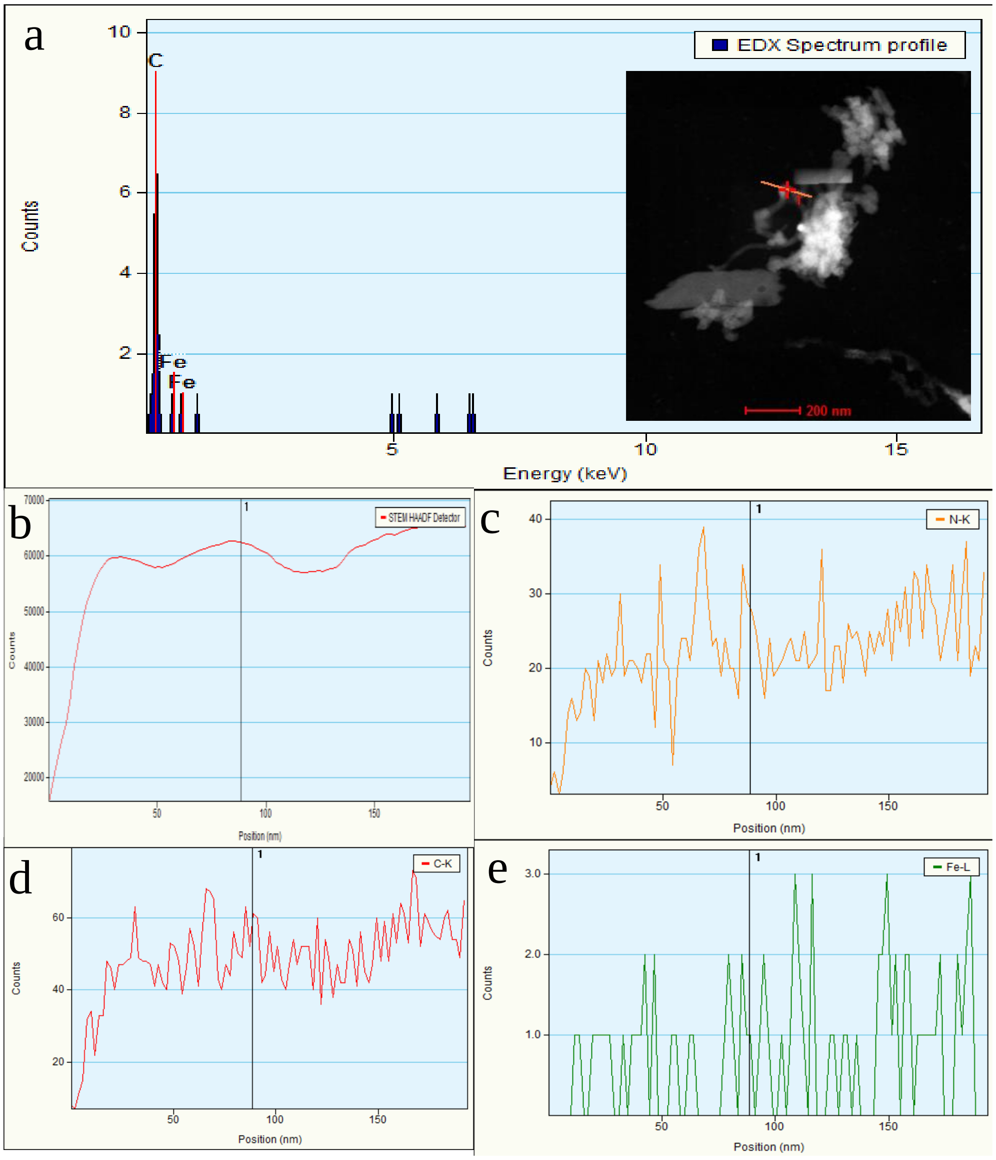

Figure D.8: (a) TEM-EDX spectrum and (b-e) STEM-EDX line profile of Fe-N-CNF annealed at 900 ^{o}C.

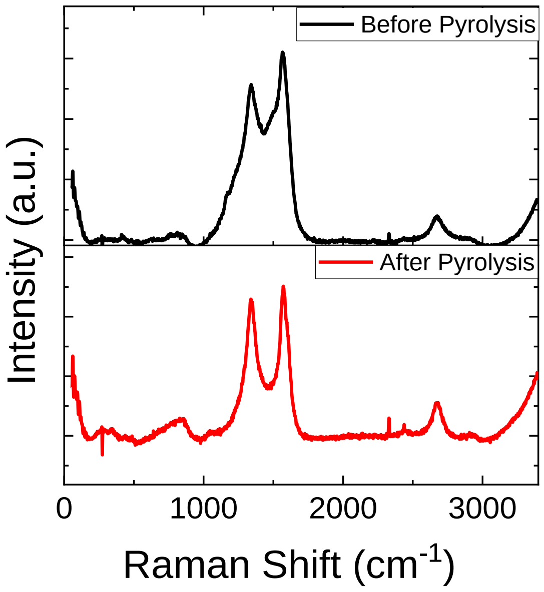

Figure D.9: Raman Spectra of Fe-PANI-CNF catalysts before and after pyrolysis.

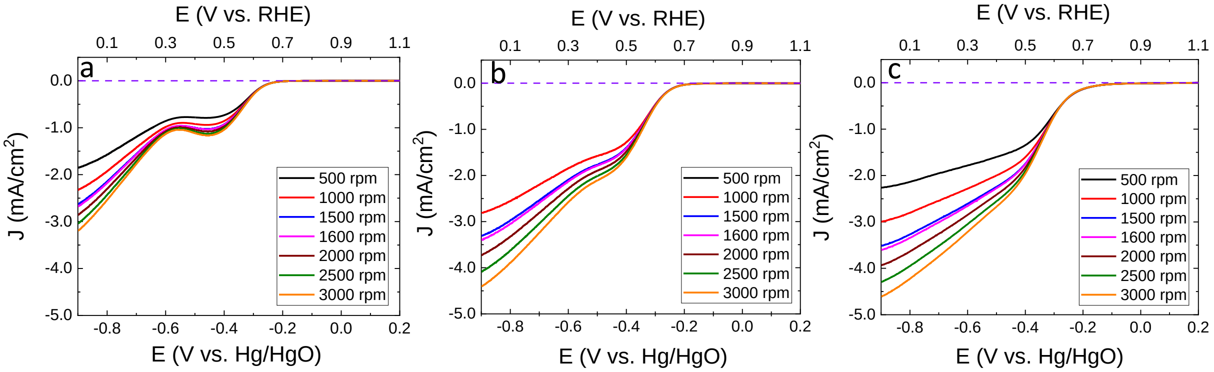

Figure D.10: RDE LSV voltammogram of (a) bare CNF, (b) N-CNF, and (c) Fe-N-CNF with background corrected recorded in 0.10 M KOH solution at a scan rate of 10 mV/s in the negative direction and at a rotation speed from 500 to 3000 rpm. The purple dash lines mark the zero current density

Appendix E - Publications and Presentations

Publications:

- **Ayyappan Elangovan,** Jiayi Xu, Archana Sekar, Bin Liu, Jun Li. Enhancing Methanol Oxidation Reaction with Platinum-based Catalysts Using a N-Doped Three-dimensional Graphitic Carbon Support. **(Submitted to ChemCatChem)**

- Jiayi Xu, **Ayyappan Elangovan,** Jun Li, Bin Liu. Graphene-Based Dual-Metal Sites for Oxygen Reduction Reaction: A Theoretical Study. **(Submitted to Physical Chemistry Chemical Physics)**

- **Ayyappan Elangovan**, Jiayi Xu, Emery Brown, Bin Liu, Jun Li. Fundamental Electrochemical Insights of Vertically Aligned Carbon Nanofiber Architecture as a Unique Catalyst Support for ORR, ***Journal of the Electrochemical Society***, 2020, 167, 066523.

- Yazhou Chen, **Ayyappan Elangovan**, Danli Zeng, Yunfeng Zhang, Hanzhong Ke, Jun Li, Yubao Sun, Hansong Cheng. Vertically Aligned Carbon Nanofibers on Cu Foil as a 3D Current Collector for Reversible Li Plating/Stripping toward High-Performance Li–S Batteries, ***Advanced Functional Materials***, 2019, 1906444.

- Emery Brown, Pengli Yan, Halil Tekik, **Ayyappan Elangovan**, Jian Wang, Dong Lin, Jun Li. 3D printing of Hybrid MoS_2-Graphene Aerogels a highly Porous Electrode Materials for Sodium Ion Battery anodes, ***Materials & Design,*** 2019, 170, 107689.

- Emery Brown, Jagaran Acharya, **Ayyappan Elangovan**, Judy Wu, Jun Li. Disordered Bilayered $V_2O_5.nH_2O$ Shells Deposited on Vertically Aligned Carbon Nanofiber Arrays as Stable High-Capacity Sodium Ion Battery Cathodes, ***Energy Technology***, 2018, 6, 2438-2449.

- Emery Brown, Seok-Hwan Park, **Ayyappan Elangovan**, Yue Yuan, Jooyoun Kim, Xiuzhi Susan Sun, Xiaoming Zhang, Guohong Wang, Jun Li. Facilitating High-Capacity V_2O_5 Cathodes with Stable Two and Three Li^+ Insertion Using a Hybrid Membrane Structure Consisting of Amorphous V_2O_5 Shells Coaxially Deposited on Electrospun Carbon Nanofibers, ***Electrochimica Acta***, 2018, 269, 144-154.

- S Anantharaj, K Sakthikumar, **Ayyappan Elangovan**, G Ravi, T Karthik, Subrata Kundu. Ultra-small rhenium nanoparticles immobilized on DNA scaffolds: An excellent material for surface enhanced Raman scattering and catalysis studies, ***Journal of Colloid and Interface Science***, 2016, 483, 360-373.

- S Anantharaj, U Nithiyanantham, Sivasankara Rao Ede, **E Ayyappan**, Subrata Kundu. Pi-Stacking intercalation and reductant assisted stabilization of osmium organosol for catalysis and SERS application, ***RSC Advances***, 2015, 5, 11850-11860.

Conference Presentations:

- **Ayyappan Elangovan,** Jiayi Xu, Bin Liu, Jun Li, "*Platinum Anchored Vertically Aligned Carbon Nanofibers as a Bifunctional Electrocatalyst for Oxygen Reduction and Methanol Oxidation Reaction",* The 54th Annual ACS Midwest Regional Meeting 2019 (Wichita, KS, USA).

- **Ayyappan Elangovan,** Jiayi Xu, Bin Liu, Jun Li, "*Platinum Anchored on Vertically Aligned Carbon Nanofibers for catalysis of Oxygen Reduction Reaction",* The Designing Molecules Workshop and Conference, 2019 (Manhattan, KS, USA).

- **Ayyappan Elangovan**, Jun Li, "*Vertically Aligned Carbon Nanofibers with Reduced Pt Loading as a Highly Active and Methanol Tolerant Cathode Electrocatalyst in PEMFC",* The 257th ACS National Meeting & Exposition 2019 (Orlando, FL, USA).

- **Ayyappan Elangovan**, Jun Li, "*Vertically Aligned Carbon Nanofibers with Ultra-low Platinum Loading for Oxygen Reduction Reaction",* The 52nd Annual ACS Midwest Regional Meeting 2017 (Lawrence, KS, USA).

Awards and Scholarships:

- Meloan Award for Outstanding Research in Analytical Chemistry (2020)

- International Leadership Award by K-State Alumni Association (2020)

- Graduate Award Symposium Winner at The 54th ACS Midwest Regional Meeting (2020)

- Arts and Science Travel Scholarship (2019)

- Graduate School Travel Award (2019)

- Phi Lambda Upsilon Travel Award (2019)

- International Student Scholarship by K-State Alumni Association (2018)